Precision measurement of the cosmic-ray electron and positron fluxes as a function of time and energy with the Alpha Magnetic Spectrometer on the International Space Station

Von der Fakultät für Mathematik, Informatik und Naturwissenschaften der RWTH Aachen University zur Erlangung des akademischen Grades eines Doktors der Naturwissenschaften genehmigte Dissertation

vorgelegt von

Diplom-Physiker
Nikolas Zimmermann

aus
Köln

Berichter: Universitätsprofessor Dr. rer. nat. Stefan Schael
Universitätsprofessor Dr. rer. nat. Christopher Wiebusch

Tag der mündlichen Prüfung: 17. Februar 2020

RWTH Aachen University
1. Physikalisches Institut B

Precision measurement of the cosmic-ray electron and positron fluxes as a function of time and energy with the Alpha Magnetic Spectrometer on the International Space Station

PhD Thesis
September 2019

by

Diplom-Physiker
Nikolas Zimmermann

Supervisors: Prof. Dr. Stefan Schael
Prof. Dr. Christopher Wiebusch

Eidesstattliche Erklärung

Nikolas Zimmermann erklärt hiermit, dass diese Dissertation und die darin dargelegten Inhalte die eigenen sind und selbstständig, als Ergebnis der eigenen originären Forschung, generiert wurden.

Hiermit erkläre ich an Eides statt

1. Diese Arbeit wurde vollständig oder größtenteils in der Phase als Doktorand dieser Fakultät und Universität angefertigt;
2. Sofern irgendein Bestandteil dieser Dissertation zuvor für einen akademischen Abschluss oder eine andere Qualifikation an dieser oder einer anderen Institution verwendet wurde, wurde dies klar angezeigt;
3. Wenn immer andere eigene- oder Veröffentlichungen Dritter herangezogen wurden, wurden diese klar benannt;
4. Wenn aus anderen eigenen- oder Veröffentlichungen Dritter zitiert wurde, wurde stets die Quelle hierfür angegeben. Diese Dissertation ist vollständig meine eigene Arbeit, mit der Ausnahme solcher Zitate;
5. Alle wesentlichen Quellen von Unterstützung wurden benannt;
6. Wenn immer ein Teil dieser Dissertation auf der Zusammenarbeit mit anderen basiert, wurde von mir klar gekennzeichnet, was von anderen und was von mir selbst erarbeitet wurde;
7. Teile dieser Arbeit wurden zuvor veröffentlicht und zwar in: Physical Review Letters (**121** 051102, 2018)

Aachen, 27. Februar 2020

Abstract

Precision measurement of the cosmic-ray electron and positron fluxes as a function of time and energy with the Alpha Magnetic Spectrometer on the International Space Station

This thesis presents an analysis of the cosmic-ray electron and positron flux using the AMS-02 detector on the International Space Station as a function of time and energy. The time-averaged flux is integrated over 6.5 years of AMS-02 science data and provides the electron and positron flux with unprecedented accuracy, covering the energy range from 0.5 GeV to 1 TeV. In total 28.39 million events were identified as electrons and 1.95 million as positrons. For each of the 88 Bartels rotation periods (27 days), within the 6.5 years, an individual electron and positron flux is derived spanning the energy range from 1 – 50 GeV.

The challenge of the analysis is to extract the small electron and positron signal in the overwhelming proton background present in cosmic rays. A detailed description of the analysis techniques is presented, including a thorough derivation of the systematic uncertainties.

The main motivation for measuring the cosmic-ray electron and positron flux in a time-averaged way is to explore the energy dependence up to high energies in detail and search for structures in the spectrum. The traditional understanding is that electrons are primary cosmic rays, whereas positrons are believed to be secondaries, produced by collisions of primary protons with the interstellar medium. A clear deviation from the traditional understanding was discovered: the positron flux cannot be described by a single power law, nor by the sum of two power laws. The secondary production term plus an additional source term, with a finite cut-off energy, is necessary to describe the positron data. Above the cut-off energy, the positron flux is rapidly decreasing. The cut-off is established with a significance of 4σ, providing strong evidence that a new source of cosmic-ray positrons was discovered, which is responsible for the rise of the positron flux, and its decrease at high energies when the source term contribution is vanishing. The origin of the source term remains unclear: both astrophysical sources, such as pulsars, and dark-matter annihilation are candidates to describe the positron flux data.

The majority of the electrons is believed to come from one of the several astrophysical sources, each making a power law contribution to the electron flux. The electron flux was found to be well described by the sum of two power laws over the whole energy range, supporting the observation that more than one astrophysical source is responsible for the measured electron flux.

For the first time, the charge-sign dependent modulation during solar maximum has been investigated by electrons and positrons alone, using the time-dependent fluxes derived in this thesis. Short-term effects such as Forbush decreases and solar flares were identified simultaneously in the electron and positron flux that cancel in the positron/electron ratio. Long-term effects are revealed in the positron/electron ratio: A smooth transition from one value to another, after the polarity reversal of the solar magnetic field in July 2013. The transition magnitude is decreasing as a function of energy, which was predicated by solar modulation models that incorporate drift effects. This novel dataset allows one to build sophisticated models of solar modulation that can predict the time-dependence of both the electron and positron flux in future. This knowledge will allow a precise modelling of the interstellar electron flux and positron flux from low energies in the GeV regime up to the TeV regime.

Zusammenfassung

Präzisionsmessung der kosmischen Elektron- und Positronflüsse als Funktion der Zeit und Energie mit dem Alpha Magnetic Spectrometer auf der Internationalen Raumstation

In der vorliegenden Dissertation wird die Analyse der kosmischen Elektron- und Positronflüsse, gemessen mit dem AMS-02 Detektor auf der Internationalen Raumstation, in zwei Varianten vorgestellt: zeitgemittelt und zeitabhängig. Die zeitgemittelten Flüsse decken 6.5 Jahre AMS-02 Daten ab und erlauben es die Elektron- und Positronflüsse mit unerreichter Präzision zu messen, im Energieintervall von 0.5 GeV bis 1 TeV. Insgesamt 28.39 Millionen Ereignisse wurden als Elektronen identifiziert und 1.95 Millionen als Positronen. Für jede der 88 Sonnenrotationsperioden ("Bartels rotation") innerhalb der 6.5 Jahre wird zusätzlich jeweils ein Elektron- und ein Positronfluss bestimmt im Energieintervall von 1 – 50 GeV.

Die Herausforderung der Analyse bestand darin, das kleine Elektronen- und Positronensignal aus dem großen Protonenuntergrund zu extrahieren, der die kosmische Strahlung dominiert. Eine detaillierte Beschreibung der Analysetechniken, sowie eine gründliche Diskussion aller relevanten systematischen Unsicherheiten wird präsentiert.

Die Messung der zeitgemittelten kosmischen Elektron- und Positronflüsse erlaubt es die Spektren bis zu den höchsten Energien im Detail zu untersuchen und nach unbekannten Strukturen in der Energieabhängigkeit zu suchen. Nach traditionellem Verständnis sind Elektronen primäre kosmische Teilchen und Positronen sekundäre, die erst bei der Kollision von primären Protonen mit der Materie im interstellaren Raum entstehen. Eine klare Abweichung vom traditionellen Verständnis wurde beobachtet: Der Positronfluss lässt sich nicht als Potenzgesetz oder als Summe von zwei Potenzgesetzen beschreiben. Die Summe eines Potenzgesetzes mit einem zusätzlichem Quellterm, der zu hohen Energien exponentiell abfällt, beschreibt den gemessenen Positronfluss. Oberhalb der Energiegrenze verliert der Quellterm seine Bedeutung und der Positronfluss fällt stark ab. Die Existenz einer solchen Energiegrenze wurde mit einer Signifikanz von 4σ bestimmt, was ein klarer Hinweis auf eine neue Quelle von kosmischen Positronen ist. Der Ursprung des Quellterms ist unbekannt: Es könnte sich um eine astrophysikalisches Quelle, wie einen Pulsar, handeln oder die Signatur eines annihilierenden dunkle Materie Teilchens.

Der Großteil der Elektronen sollte von einer der bekannten astrophysikalischen Quellen kommen, wobei das Spektrum jeder Quelle mit einem Potenzgesetz zum gemessenen Elektronfluss beiträgt. Der Elektronfluss lässt sich als Summe von nur zwei Potenzgesetzen über den gesamten Energiebereich beschreiben, welches die Beobachtung stützt, dass mehr als eine astrophysikalsiche Quelle zum gemessenen Elektronfluss beiträgt.

Zum ersten Mal konnte die Ladungsabhängigkeit der solaren Modulation allein mit Elektronen und Positronen untersucht werden. Effekte auf kurzen Zeitskalen, wie der "Forbush-Effekt" oder Sonneneruptionen lassen sich sowohl in Elektronen als auch Positronen zeitgleich identifizieren. Diese kurzzeitigen Effekte heben sich auf, wenn man das Verhältnis Positronen zu Elektronen betrachtet und ein klarer Langzeiteffekt bleibt übrig: der Übergang von einem Plateau zu einem anderen, nach der Polaritätsänderung des Sonnenmagnetfeldes im Juli 2013. Die Amplitude des Übergangs nimmt als

Funktion der Energie ab und deckt sich daher mit Vorhersagen von Modellen der solaren Modulation, die Drifteffekte berücksichtigen. Die zeitabhängigen Flüsse erlauben es detaillierte Modelle der solaren Modulation zu entwickeln, die es ermöglichen werden, die zukünftige Zeitabhängigkeit der Elektron- und Positronflüsse vorherzusagen. Damit können dann fundierte Modelle der interstellaren Elektron- und Positronflüsse erstellt werden, die den gesamten Energiebereich von wenigen GeV bis zu TeV Energien beschreiben.

Contents

CHAPTER 1

Introduction

"... In order to make further progress, particularly in the field of cosmic rays, it will be necessary to apply all our resources and apparatus simultaneously and side-by-side; an effort which has not yet been made, or at least, only to a limited extent..."

- Victor F. Hess, *Nobel Lecture - 1936*

The search for the fundamental building blocks of nature, their construction principles and the understanding of their interactions occupied generations of particle physicists. Nowadays large accelerators, such as the Large Hadron Collider (LHC) at CERN, are used to collide particles: the collision products are analyzed using sophisticated detectors. The decades of effort lead to the construction of a fundamental model, the *Standard Model*, describing the fundamental forces in the Universe including their interactions on the smallest length scales. The *Standard Model* was tested countless times and is the most accurate description of the microscopic structure of nature today.

However the ultimate laboratory to study particles at the highest possible energies is the Universe itself. In 1912 Victor F. Hess discovered the cosmic rays, when he found that an electroscope discharged more rapidly as he ascended in a balloon. He attributed this to a source of radiation entering the atmosphere from above, and in 1936 was awarded the Nobel prize for his discovery. The famous quote from his Nobel Lecture - see above - paved the way for numerous experiments in the field of cosmic rays, which all share the same goal: unveil the nature of cosmic rays, trace down their origin to gain understanding of the fundamental physics behind cosmic rays, such as the production and propagation mechanisms.

It was clear to physicists since the discovery of cosmic rays that the best place to study cosmic rays is not the Earth itself, since the atmosphere disturbs the measurement. However it took more than half a century until a unique, space-borne experiment was proposed in 1994: the Alpha Magnetic Spectrometer (AMS) [Ahlen1994], to be installed on the International Space Station (ISS). Previously only balloon-borne experiments were used to probe cosmic rays above the atmosphere, which are unable to provide true long term measurements of the cosmic rays.

The precursor experiment AMS-01 flew on the shuttle Discovery on the STS-91 mission, from June, 2^{nd} to June 12^{th} 1998 demonstrating that it is possible to operate a particle physics detector in space, which was believed to be extremely hard to realize, due to the harsh environment: enormous mechanical stress during the launch on a rocket, ever changing temperature conditions, power consumption, etc.

The precursor experiment was successful, and already generated several interesting scientific results, see e.g. Refs. [Alcaraz2000; Aguilar2007].

After more than a decade of research and construction AMS-02 was launched into space with the Space Shuttle STS-134 mission and installed onboard the ISS on May, 19$^{\text{th}}$ 2011, to perform a long duration mission of fundamental physics research in space. The primary scientific goal is to measure the composition and energy spectra of charged cosmic rays, to look for primordial anti-matter and to explore the nature of dark matter.

In this thesis, the precision measurement of the time dependence induced by solar activity on electron and positron fluxes at energies between 1 – 50 GeV is presented and a measurement of the time-averaged electron and positron fluxes between 0.5 – 1,000 GeV based on 6.5 years of AMS-02 science data. Electrons (e^-) and positrons (e^+) are a rare component of the cosmic rays since they present only ≈ 1 % and ≈ 0.1 % of the total cosmic-ray flux, which is dominated by protons (≈ 90 %) and helium (≈ 8 %). It is therefore challenging to extract the $e^{\pm}$ signal from the overwhelming proton and helium background.

The time-dependent fluxes allow for comprehensive studies of the energy and charge-sign dependence on the time scale of months, related to solar activity [Potgieter1993a; Potgieter1993b; Gopalswamy2003], and long-term effects related to the periodic 22 year cycle of the heliospheric magnetic field [Ferreira2003].

Time-dependent structures in the energy spectra of all cosmic rays emerge from solar modulation when charged particles enter the heliosphere [Potgieter2013] - whereas interstellar charged cosmic rays are thought to be stable on the time scale of decades [Strong1998; Maurin2001].

Solar modulation involves convective, diffusive, particle drift, and adiabatic energy loss processes. It is well established that only the drift motion induces a dependence of solar modulation on the cosmic-ray particle charge sign [Potgieter2014]. Measuring the electron and positron fluxes simultaneously with high statistics offers a unique way to study charge-sign dependent solar modulation effects.

Furthermore the understanding of low-energy variations of the fluxes is important when modelling the high-energy part of the fluxes, since the effect of solar modulation alters the energy dependence of cosmic-ray fluxes up to ≈ 20 GeV, which will be shown in this thesis. Therefore to derive cosmic-ray flux models describing the full energy range 0.5 – 1,000 GeV, the low-energy variations need to be taken into account, properly.

In Chapter 2 an overview of the cosmic-ray physics is given, followed by an introduction to the AMS-02 instrument in Chapter 3. A detailed presentation of the analysis techniques, the arising challenges and the systematic uncertainties associated with the measurement is given in Chapter 4. A presentation and discussion of the results in Chapter 5 and a short summary in Chapter 6 will conclude this dissertation.

CHAPTER 2

Cosmic rays

The term *cosmic rays* refers to high energy charged particles and γ-rays with extraterrestrial origin. Charged cosmic rays mainly consist of protons ($\approx 90\,\%$), helium ($\approx 8\,\%$), electrons ($\approx 1\,\%$) and heavy nuclei ($\approx 1\,\%$) and a small fraction of anti-matter, such as positrons (see Section 2.1).

This chapter focuses on charged particles, especially electrons and positrons produced from outside the solar system, which is the topic of this thesis. Charged cosmic rays are messengers for the Universe, encoding information about their origin and travel through the Universe, before reaching Earth. The fluxes of cosmic rays were extensively studied during the past century, but the origin as well as the production mechanism is still not completely understood. The leading explanation of the production of cosmic rays is the *supernova* scenario, which will be described in Section 2.2.

The understanding of the propagation is important, since cosmic rays travel a long distance and continuously interact with the Interstellar Medium (ISM) (Section 2.3), the Sun's magnetic field (Section 2.4) and the magnetic field of the Earth (Section 2.5) before they eventually reach Earth.

Apart from understanding their origin, the study on cosmic-ray production and propagation helps to understand the composition of the Universe, especially at early times, right after the *Big Bang* [Mathews2017]. Many observations suggest that the observable matter only consists of $\approx 5\,\%$ of the mass-energy density of Universe [Akrami2018]. Part of the missing mass-energy density can be attributed to *Dark Matter*. Indirect dark matter searches, probing their existence by searching for the product of their decay and annihilation, will be briefly explained in Section 2.7.2.

2.1 Composition and energy dependence

Figure 2.1 shows an overview of the cosmic-ray measurements of the past two decades. Cosmic rays are categorized in two main categories: **Primaries** and **Secondaries**. Primary cosmic rays are particles produced and accelerated at their sources, whereas secondary cosmic rays are produced by primaries interacting with the ISM during propagation. A detailed introduction on cosmic rays can be found in Ref. [Longair2011].

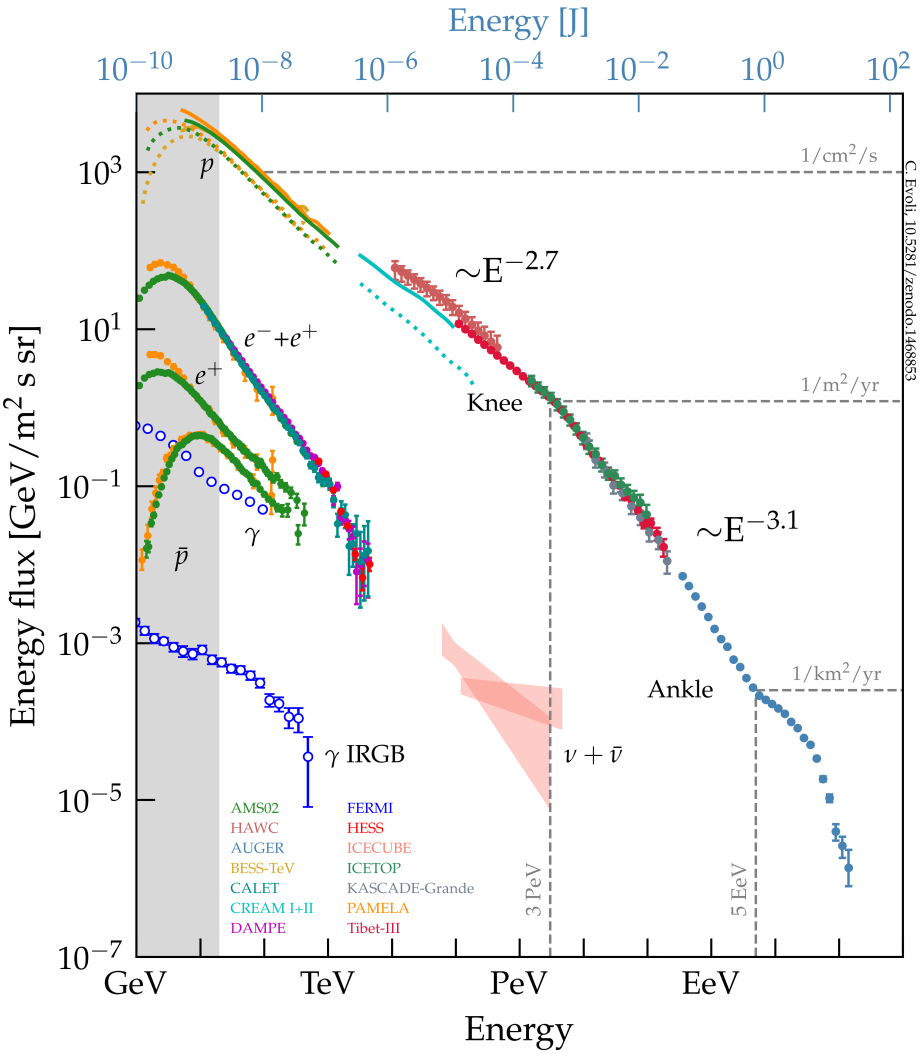

Figure 2.1: The cosmic-ray energy spectrum. Credit: Ref. [Evoli2018]

The energy dependence for most of the cosmic rays follows a power law:

$$\frac{\mathrm{dN}}{\mathrm{dE}} \propto E^{-\gamma}, \tag{2.1}$$

where γ is the *spectral index*. The overall cosmic-ray flux is well described with a spectral index of $\gamma \approx 2.7$ for energies between ≈ 1 GeV and ≈ 3 PeV (*knee*), as shown in Fig. 2.1. Above the *knee* the spectral index softens to $\gamma \approx 3.1$, until the *ankle* is reached at around ≈ 1 EeV.

The transitions of the spectral index is believed to originate in differences in the acceleration and propagation processes, which will be discussed in the following sections.

2.2 Production and acceleration

Since the first detection of cosmic rays early in the 20$^{\text{th}}$ century there have been many efforts to find out the origin of these particles and their production mechanism. An intrinsic problem is that charged cosmic rays are deflected in the interstellar and intergalactic magnetic field, which makes it impossible to precisely track down their origin. However cosmic rays at energies above 10^5 TeV are most likely to have an extragalactic origin – see recent anisotropy studies from the Auger Collaboration in Ref. [Aab2017].

Particles relevant to the measurement with space-born experiments, such as AMS-02, are mainly of galactic origin. The most compelling scenario for the production of Galactic cosmic rays are *supernovae*.

A supernova [Bethe2003] is a powerful and luminous stellar explosion, with an optical luminosity comparable to that of an entire Galaxy, lasting for weeks or longer.

According to Ref. [Raffelt2002] there are two entirely different classes of supernovae. One physical class are the type Ia Supernova (SN) explosions. These are thought to occur, when a carbon-oxygen white dwarf accretes matter from a companion star until it reaches the Chandrasekhar limit [Chandrasekhar1932] ($M \gtrapprox 1.45 \cdot M_\odot$) and begins to collapse. This triggers a nuclear explosion, powered by the fusion of carbon and oxygen to heavier nuclei. The explosion disrupts the original star ("progenitor") entirely. This process is called *thermonuclear supernova*.

The other class of supernova explosions mark the evolutionary end of massive stars with a mass of more than $8 \cdot M_\odot$. Such stars exhibit an onion structure with several burning shells and an iron core. The iron cores is supported by electron degeneracy pressure, strongly cooled via neutrinos, and surrounded by burning shells of Si, O, C, etc. The complex Si shell burning continues to grow iron cores up to the Chandrasekhar limit. Once an iron core attains this critical mass, an unstable gravitational collapse starts [Raffelt2002; Bethe2003], leading to a massive explosion. The progenitor either collapses to a neutron star or a black hole, or it is completely destroyed. This processed is called *hydrodynamic supernova*.

Thermonuclear supernovae occur typically once per 300 years, whereas hydrodynamic supernovae happen once per 30 to 50 years in our Galaxy. Energy is released by supernovae into space with an average rate of $\approx 10^{42}\,\text{erg}\,\text{s}^{-1}$. Only a few percent of the energy would be necessary to accelerate primary particles up to $\approx 10^{20}$ eV to describe the observed flux, outlined in Fig. 2.1.

According to Refs. [Berezhko2008; Blasi2011] particles are accelerated in the shock wave inside the Supernova Remnants (SNRs). The acceleration mechanism that is usually assumed to work in SNRs is Diffusive Shock Acceleration (DSA) [Bell1978; Blandford1987], converting 10 – 20 % of the kinetic energy of the supernova shell into cosmic rays.

The DSA mechanism produces power law energy spectra, consistent with the observations (Fig. 2.1) and is therefore the leading candidate to describe the cosmic-ray spectra. Furthermore recent observation of several SNRs provide strong evidence that charged particles are accelerated in the shock of SNRs [Uchiyama2007; CassamChenai2008; Abdo2010].

2.3 Propagation through the interstellar medium

When charged cosmic rays travel through the Galaxy, their spectra and their composition changes due to a variety of physical processes that take place. Hadronic interactions of primary protons and nuclei

with the ISM create secondary charged particles and γ-rays by π^0 production. Electrons/positrons lose energy by bremsstrahlung (interaction with the ISM), by synchrotron radiation (interaction with the Galactic magnetic field), as well as inverse Compton scattering (scattering on the photons of the Cosmic Microwave Background (CMB) [Penzias1965]).

Due to their charge, charged cosmic rays are scattered on magneto-hydrodynamic waves and discontinuities, which implies that their trajectories do not follow straight lines. On large scales, charged particles effectively perform a random walk, and therefore, a diffusion model is the appropriate approximative description of the propagation process.

The diffusion model with the inclusion of convection provides the most adequate description of cosmic-ray transport in the Galaxy at energies below $\approx 10^{17}$ eV, as described in Ref. [Strong2007]. A general way to describe cosmic-ray propagation for a particular species is given by:

$$\begin{aligned}\frac{\partial\psi(\vec{r},p,t)}{\partial t} &= q(\vec{r},p,t) + \vec{\nabla}\cdot(D_{xx}\vec{\nabla}\psi - \vec{V}\psi) \\ &+ \frac{\partial}{\partial p}p^2 D_{pp}\frac{\partial}{\partial p}\frac{1}{p^2}\psi - \frac{\partial}{\partial p}\left[\dot{p}\psi - \frac{p}{3}(\vec{\nabla}\cdot\vec{V})\psi\right] - \frac{1}{\tau_f}\psi - \frac{1}{\tau_r}\psi,\end{aligned} \tag{2.2}$$

where $\psi(\vec{r},p,t)$ is the cosmic-ray density per unit of total particle momentum p at position $\vec{r}$, $\psi(p)\,\mathrm{d}p = 4\phi p^2 f(\vec{p})\,\mathrm{d}p$ in terms of phase-space density $f(\vec{p})$. The terms on the right hand side of Eq. (2.2) are explained in the following:

1. $q(\vec{r},p)$ is the **source term** including primary, spallation and decay contribution. The injection spectrum of nucleons is assumed to be a power law in momentum, $\mathrm{d}q(p)/\mathrm{d}p \propto p^{-\gamma}$.

2. D_{xx} is the **spatial diffusion coefficient**. Typical numeric values are $D_{xx} \approx 3\times10^{28}\,\mathrm{cm^2\,s^{-1}}$ – $5\times10^{28}\,\mathrm{cm^2\,s^{-1}}$ at $1\,\mathrm{GeV}/n$. D_{xx} increases with rigidity as R^α, where α is in the range $0.3 - 0.6$, depending on the empirical diffusion model.

3. Galactic winds give rise to a **convective transport** of charged particles and are described by the convection velocity $\vec{V}$. $\vec{V}$ is assumed to increase linearly with the distance from the Galactic plane, implying a constant adiabatic energy loss.

4. Besides the spatial diffusion, the scattering of charged particles on randomly moving magneto-hydrodynamic waves leads to stochastic reacceleration. The **diffuse reacceleration** is described as diffusion in momentum space and is determined by the coefficient D_{pp}. The relation between the diffusion coefficient D_{pp} and the spatial diffusion coefficient D_{xx} is approximated by

$$D_{pp} = \frac{p^2 v_A^2}{9 D_{xx}},$$

   where the Alfvén speed v_A [Alfven1942] describes the characteristic velocity of the weak disturbances propagating in a magnetic field. Typical values are $v_A \approx 30\,\mathrm{km\,s^{-1}}$.

5. $\dot{p} = \mathrm{d}p/\mathrm{d}t$ is the **momentum gain or loss rate**, and the term involving $\vec{\nabla}\cdot\vec{V}$ describes **adiabatic momentum gain or loss** in the non-uniform flow of gas with a frozen-in magnetic field whose inhomogeneities scatter the cosmic rays.

6. τ_f is the time scale for loss by **fragmentation**, and τ_r is the time scale for **radioactive decay**.

The best approach to solve the cosmic-ray propagation equation is to use a state of the art numerical model, such as Galprop [Moskalenko1997; Strong1998; Moskalenko2002; Ptuskin2006; Strong2007], which aims to give simultaneous predictions of all relevant observations, while incorporating as much as current information as possible, e.g. on source distribution and the galactic structure.

To compare the predictions of the Galprop model with the fluxes measured at Earth, e.g. using AMS-02, one first has to consider the interactions of the cosmic rays with the solar wind and the magnetic field of the Earth, which will be explained in the following sections.

2.4 Propagation through the heliosphere

When charged cosmic rays enter the solar system, they interact with the magnetic field originating from the Sun, as illustrated in Fig. 2.2. Furthermore the Sun emits a stream of charged particles from its upper atmosphere - the **solar wind**. It is a plasma mostly consisting of electrons, protons and alpha particles with a kinetic energy between 0.5 – 10 keV. The plasma is highly electrically conductive, meaning the magnetic field lines and the plasma flows are effectively "frozen" together. The magnetic pressure greatly exceeds the plasma pressure and thus the plasma is structured and confined by the magnetic field. The magnetic field is effectively carried out up to the termination shock where the plasma slows down to subsonic speed: the coronal magnetic field is dragged out by the solar wind and forms the **Heliospheric Magnetic Field (HMF)** [Owens2013].

The structure and dynamics of the HMF are key to understanding and forecasting space weather, as the HMF directly couples the Sun with planetary magnetospheres, as well as directing the flow of charged particles through the heliosphere.

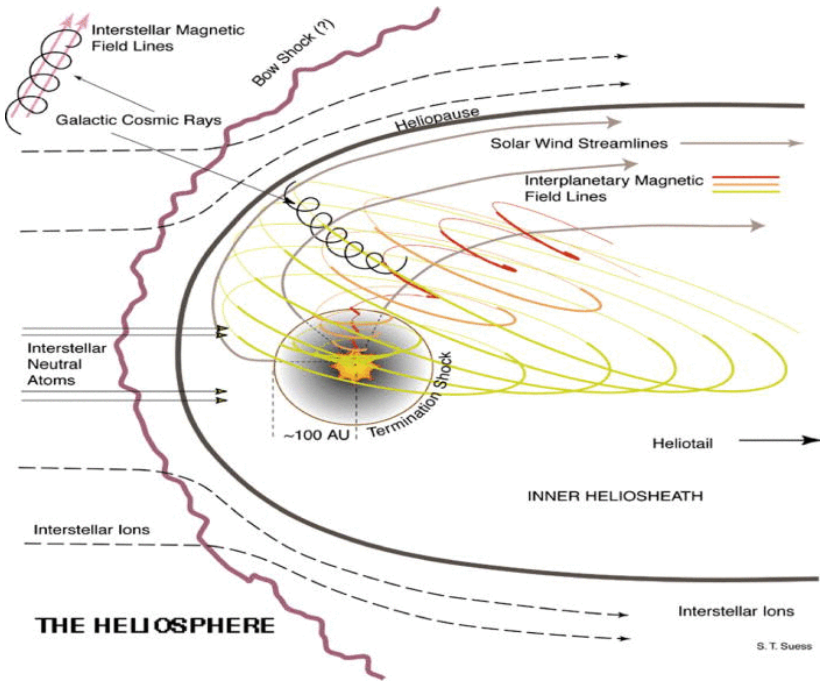

Figure 2.2: Sketch of the heliosphere. Credit: S. T. Suess.

The magnetic field boundary separating oppositely directed magnetic field lines originating from the northern and southern poles of the Sun is carried out by the solar wind to form the **Heliospheric Current Sheet (HCS)**, a large scale boundary which extends throughout the Sun's equatorial plane in the heliosphere. A small electrical current ($I \approx 10^{-10}\,A\,m^{-2}$) flows within the current sheet, which is approximately $\approx$ 10,000 km thick near the orbit of the Earth.

The shape results from the influence of the Sun's rotating magnetic field on the plasma in the interplanetary medium, as illustrated in Fig. 2.3. The current sheet evolves slowly, over timescales of months, as the Sun's magnetic field changes in response to the emergence and decay of solar active regions, disrupted on short time scales by e.g. Coronal Mass Ejections (CME) [Gopalswamy2003]. An essential feature of the HCS is the tilt of the Sun's magnetic dipole with respect to the rotation axis, characterized by the **Tilt Angle θ_t**. The tilt angle is strongly correlated with the Sun's magnetic activity: a small tilt angle ($\approx 5°$) corresponds to quiet periods and a large title angle to active periods.

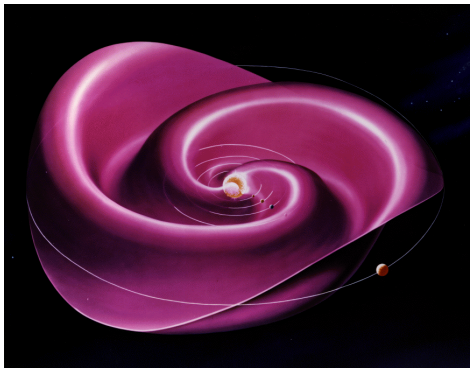

Figure 2.3: Heliospheric current sheet. Credit: NASA GSFC.

The magnetic activity of the Sun follows a nearly periodic 11 year cycle [Ferreira2003], where the magnetic field configuration oscillates between a toroidal and a polodial configuration [Babcock1961]. The strength of the solar radiation, the amount of coronal mass ejections, the number of sunspots, the number of solar flares, etc. are all modulated by the magnetic activity of the Sun, from active to quiet periods with a periodicity of 11 years. Cosmic-ray particles entering the heliosphere are scattered on the HMF, similar to the scattering on the galactic magnetic field, when cosmic rays travel through the ISM. To understand the predictions from galactic propagation models (e.g. Galprop, see Section 2.3), the solar modulation needs to be taken into account.

A simple model was proposed in Ref. [Gleeson1968], describing solar modulation as diffusion through the HMF, including convection by the outward motion of the solar wind and adiabatic declaration of the cosmic rays. In the *force-field approximation*, that is used for the modelling of the measured fluxes in this thesis (Chapter 5), the effect of solar modulation can be described by a single parameter, the fisk potential ϕ, that depends on the solar wind speed $V(\vec{r},t)$ and the diffusion coefficient κ as given by:

$$\phi(\vec{r},t) = \frac{(E+m)T}{3E} \int_{r_E}^{r_b} \frac{V(x,t)}{\kappa(x,E,t)}\,\mathrm{d}x, \tag{2.3}$$

where E is the total energy, T the kinetic energy and m the mass of a cosmic-ray particle. The

integral is evaluated from the location of the Earth r_E to the boundary of the heliosphere r_b. The interstellar cosmic-ray flux J_{IS} is related to the locally observed flux J by:

$$J(E) = \frac{E^2 - m^2}{(E + |Z|\,\phi)^2 - m^2} \cdot J_{\mathrm{IS}}(E + |Z|\,\phi), \tag{2.4}$$

where Z is the charge of the cosmic-ray particle. The modulation parameter ϕ has the dimension of a rigidity and is of the order of $\approx 500\,\mathrm{MV}$. ϕ is a model dependent quantity and changes with time over a solar cycle. Furthermore it has to be derived for each cosmic-ray species individually. The simple description allows one to easily treat the solar modulation when modelling the energy dependence of cosmic-ray spectra, in an approximative way.

2.5 Propagation through the magnetosphere

The Earth's magnetosphere is the final barrier for cosmic-ray particles, before they can be measured at Earth or in low orbits, such as the orbit of the ISS. Low energetic particles cannot penetrate the magnetosphere and get deflected away from Earth. This effect is known as **geomagnetic cut-off**. For a dipole field, Størmer derived an axial symmetric cone towards east direction in which positively charged particles below a specific rigidity cannot enter (*forbidden cone*), as illustrated in Fig. 2.4. The size of the *forbidden cone* depends on the energy of the particle, a low energetic cosmic-ray particle corresponds to a large *forbidden cone*. For negatively charged particles the cones are mirrored: the *forbidden cone* points towards the west direction.

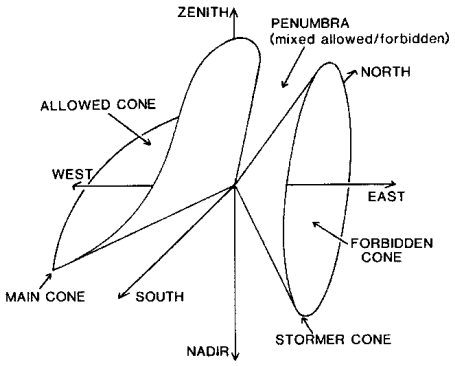

Figure 2.4: The geomagnetic cutoff as defined by Størmer [Stoermer1956]. Credit: Ref. [Smart2005]

The minimum rigidity needed to penetrate the magnetosphere is called the cut-off rigidity R_c. Following Ref. [Smart2005], the magnetic field can be modelled as dipole field in the vicinity of the Earth and the cut-off rigidity is given by:

$$R_c = \frac{M \cos^4 \lambda}{r^2 \left(1 + \sqrt{1 - \sin\epsilon \sin\delta \cos^3 \lambda}\right)^2}, \tag{2.5}$$

where M is the dipole moment, λ is the magnetic latitude, ϵ is zenith angle, δ the azimuthal angle to the north and r is the distance from the dipole center.

For particles entering radially to the dipole the vertical cut-off rigidity R_{vc} can be approximated as: $R_{vc} = 14.9 \cos^4 \lambda / r^2$, where r is in unit of earth radii.

Since the cut-off depends on the latitude λ of the observer, the cut-off rigidity R_c is lowest near the magnetic poles. For particles arriving from any given direction, the cut-off depends on the azimuthal angle δ as well, leading to the **east-west effect** [Ogawa1950]. A positively charged particle at the same zenith angle has a higher cut-off from the east direction then for a negatively charged particle, and vice versa.

The geomagnetic cut-off effect must be taken into account when analyzing the fluxes, measured by AMS-02. AMS-02 is orbiting onboard the ISS between ± 52° latitude, with particle rates that vary from a few hundred Hz up to 2,000 Hz close to the geomagnetic poles. The geomagnetic cut-off rigidity R_c, computed using the Størmer formula (2.5) is shown in Fig. 2.5 as function of the geomagnetic longitude/latitude of the ISS.

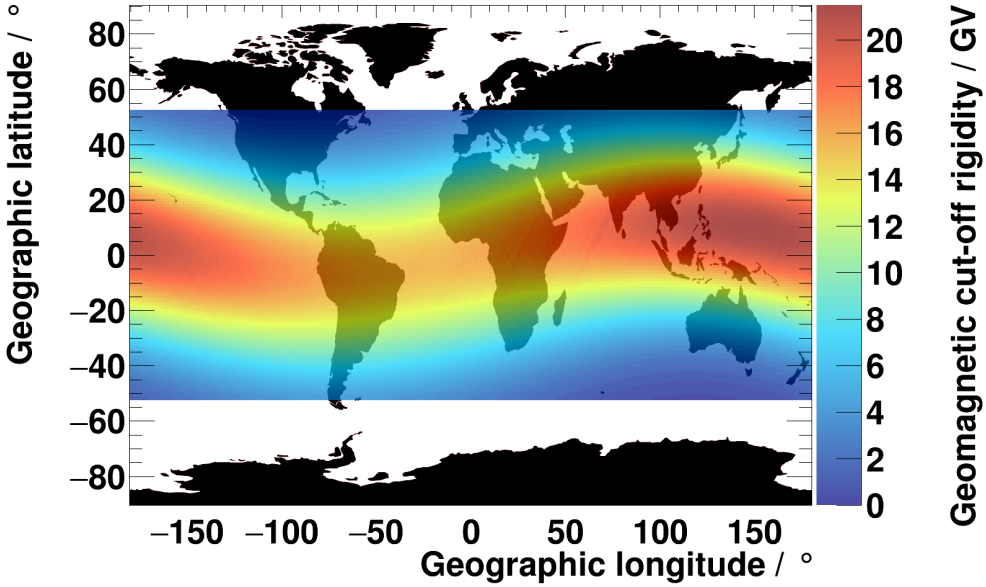

Figure 2.5: The plots shows the geomagnetic cut-off rigidity as function of the geomagnetic longitude/latitude.

It is evident that low energetic particles can only be measured with AMS-02 near the pole regions, never in the equatorial region, where the cut-off rigidity is high. Particles above ≈ 25 GeV can be detected at any longitude/latitude. In order to measure primary cosmic rays, all particles must be excluded from analysis, whose energy is smaller than the geomagnetic cut-off rigidity at a given geographic longitude/latitude.

2.6 Electron and positron specific propagation aspects

In this section the electron and positron specific propagation aspects will be reviewed, since the electron and positron flux analysis in the main topic of this thesis. The spallation and decay terms in the propagation equation Eq. (2.2) are irrelevant for electrons or positrons, since there are no hadronic interactions.

As described in Ref. [Longair2011], the main energy loss processes for electrons and positrons are *synchrotron radiation* and *inverse Compton scattering*. The energy loss rate, in the ultra-relativistic limit $v \rightarrow c$, is given by:

$$\begin{aligned} -\left(\frac{\mathrm{d}E}{\mathrm{d}t}\right)_{\text{synch}} &= \frac{4}{3}\sigma_T c\gamma^2 U_{\text{mag}} \approx 6.6\times 10^4 \gamma^2 B^2, \\ -\left(\frac{\mathrm{d}E}{\mathrm{d}t}\right)_{\text{IC}} &= \frac{4}{3}\sigma_T c\gamma^2 U_{\text{rad}}, \end{aligned} \tag{2.6}$$

for the *synchrotron radiation* and the *inverse Compton scattering* process, respectively. σ_T denotes the Thomson cross-section, γ the Lorentz factor and U the energy density of the radiation fields. Typical values are $B \approx 3\times 10^{-10}\,\mathrm{T}$, $U_{\text{rad}} \approx 6\times 10^5\,\mathrm{eV\,m^{-3}}$ and $U_{\text{rad}} \approx 3\cdot U_{\text{mag}}$.

Inverse Compton losses and synchrotron losses are equally important for high energy electrons and positrons in the Galaxy. Due to their small mass, electrons and positrons lose energy much faster compared to protons and other heavy nuclei.

According to numerical simulations (see Ref. [Panov2013]) a $\approx 1\,\mathrm{TeV}$ electron or positron has a maximum life time of $\tau \approx 1\times 10^5$ years and a mean diffusion distance of only $\approx 1\,\mathrm{kpc}$. This suggests that the high energy electrons and positrons measured at Earth, must come from nearby regions in the Galaxy.

2.7 Electron and positron source candidates

As described in Section 2.2, supernova remnants are widely believed to be responsible for the origin of cosmic rays, as charged particles are accelerated in their strong shock wave. The main evidence for this assumption comes from the observation of radio and γ-ray emission from SNRs [Kobayashi2004]. The radio emission stems from the synchrotron radiation of electrons in a strong magnetic field [Katz-Stone2000], wheres γ-ray emission has two possible sources: inverse Compton scattering [Aharonian2006] and the neutral pion decay [Ackermann2013].

Only electrons are expected to be accelerated within SNRs, not positrons. The flux of electrons injected into the ISM from SNRs can be described as a power law: $\phi_{e^-,\,\text{SNR}}(E) = A_{\text{SNR}} E^{-\gamma_{\text{SNR}}}$, where $\gamma_{\text{SNR}} \approx 2$. The flux after propagation through the ISM changes its energy dependence: $\tilde{\phi}_{e^-,\,\text{SNR}}(E) = A_{\text{SNR}} E^{-\gamma_{\text{SNR}}-\delta}$, where $\delta \approx 1$ due to energy losses during propagation.

These assumptions reproduce the measured fluxes at Earth: the electron flux at energies between $\approx 10\,\mathrm{GeV}$ up to the TeV regime are known to follow a power law with a spectral index $\gamma \approx 3$ [Aguilar2019a]. Therefore electrons are considered as primary cosmic rays.

Positrons, on the other hand, are considered as secondary cosmic rays, since they are believed to be produced in collisions of primary protons with the ISM [Shen1968]. This leads to the creation of charged pion pairs, which further decay into electron and positron pairs:

$$\begin{aligned} \pi^- &\Rightarrow \mu^- + \bar{\nu_\mu}, \qquad & \mu^- &\Rightarrow e^- + \bar{\nu_e} + \nu_\mu \\ \pi^+ &\Rightarrow \mu^+ + \nu_\mu, \qquad & \mu^+ &\Rightarrow e^+ + \nu_e + \bar{\nu_\mu} \end{aligned}$$

These processes produce equal amounts of electrons and positrons following power laws:

$$\phi_{e^+,\,\text{sec}}(E) = A_{\text{sec}} E^{-\gamma_{\text{sec}}}; \qquad \phi_{e^-,\,\text{sec}}(E) = A_{\text{sec}} E^{-\gamma_{\text{sec}}} \tag{2.7}$$

This scenario would lead to a positron flux and a positron fraction (ratio of positrons over positrons and electrons) that would monotonically decrease with energy, in contrary to recent observations by PAMELA [Adriani2009] and AMS-02 [Aguilar2013]. Therefore an additional source of positrons must exist, besides the component associated with secondary production.

Astrophysical sources such as *pulsars* or *dark matter* annihilation are possible candidates for positron sources, which will be explained in the following sections.

2.7.1 Pulsars

A *pulsar* is a rotating neutron star with a strong magnetic field that emits a beam of electromagnetic radiation [Hewish1968]. This radiation can be observed only when the beam of emission is pointing towards Earth and is responsible for the pulsed appearance of the emission. The electromagnetic radiation originates from the rotational energy of the neutron star, generating an electrical field from the movement of the magnetic field. The protons and electrons from the surface of the star are accelerated and create an electromagnetic beam originating from the poles of the magnetic field. The rotation periods of the pulsar are regular and the duration ranges from milliseconds to seconds, depending on the age of the pulsar and its power. Due to the electromagnetic emission the rotation slows down over time.

A pulsar is an additional source of electrons and positrons, as the electrons extracted from the star surface propagate outwards the magnetic field lines and emit high energy photons, which can convert into additional electron and positron pairs. These pairs can escape the magnetosphere and are injected into the ISM.

According to Ref. [Hooper2009], the spectra from pulsars is harder than the secondary positron spectra and has a specific cut-off energy E_{cutoff}, up to which the given pulsar can accelerate particles:

$$\begin{aligned} \phi_{e^+,\,\text{pul}}(E) &= A_{\text{pul}} E^{-\gamma_{\text{pul}}} E^{-E/E_{\text{cutoff}}} \\ \phi_{e^-,\,\text{pul}}(E) &= A_{\text{pul}} E^{-\gamma_{\text{pul}}} E^{-E/E_{\text{cutoff}}} \end{aligned} \tag{2.8}$$

The sum of the positron flux from secondary production (Eq. (2.7)) and the positron flux from pulsars (Eq. (2.8)) leads to a spectrum, which has an additional rise from GeV energies onwards, that gradually diminishes up to the TeV regime. This observation makes *pulsars* a promising candidate to explain the observed rise in the positron flux. According to Ref. [Verbiest2012] there are a few candidate pulsars within the region of interest of ≈ 1 kpc, as described in Section 2.6.

However also *dark matter* annihilation can lead to a similar rise in the positron flux, which will be shown in the following section.

2.7.2 Dark matter

There is overwhelming evidence for the existence of a non-luminous form of matter, *dark matter*, from the observation of galactic rotation curves [Rubin1970], the gravitational lensing effect [Einstein1936], and the CMB [Akrami2018]. According to recent CMB studies, dark matter makes up $\approx 85\,\%$ ($\Omega_c/(\Omega_b + \Omega_c)$, according to ΛCDM model, see Ref. [Akrami2018]) of the total matter in the universe.

Almost nine decades have passed since the first suggestion of Zwicky that a non-luminous form of matter must exist, to explain the observations of rotation curves of galaxies. The rotation curve of a Galaxy describes the rotation velocity $v(r)$ of objects at a distance r from the galactic centre. It it based on measurements of the Doppler shift of emissions or absorption lines. If all matter in a Galaxy

were located in the luminous disc, the rotation velocity would be $v(r) \propto r^{-1/2}$, in accordance with Keplers third law. However the rotation curves were observed to be flat, $v = \text{const.}$, consistent with a mass distribution of $\rho \propto r^{-2}$ that must extend beyond the visible disc. This fact gave rise to the idea that a non-luminous form of matter, *dark matter*, forms halos around the discs of galaxies.

The nature of dark matter still remains unexplained and constitutes one of the most exciting questions in fundamental physics today. Most attempts to explain dark matter propose that it is made of one or more new particles. The hunt for dark matter is an ongoing effort on both the experimental and on the theoretical side. It is widely accepted that any candidate for dark matter must be only weakly interacting, otherwise it would have been detected already after decades of direct [Sumner2011] and indirect [Gaskins2016] searches. Furthermore it must be stable on cosmological timescales, or it would be long gone today - in contrary to astronomical observations.

Many dark matter candidates were proposed, such as *sterile neutrinos* [Boyarsky2019], *gravitinos* [Steffen2006], *axions* [Duffy2009], *Kaluza-Klein dark matter* [Cheng2002] and *Weakly Interacting Massive Particles (WIMPs)* [Roszkowski2017], to name the most common candidates.

According to Ref. [Bergstrom2013], the annihilation of WIMP dark matter particles produce equal amounts of electrons and positrons. For the annihilation/decay process the injected spectrum of cosmic-ray electrons or positrons per volume and time is given by:

$$\begin{aligned} Q_{\text{annihilation}} &= \frac{1}{2}\langle\sigma v\rangle(\rho_\chi/m_\chi)^2\frac{\mathrm{d}N}{\mathrm{d}E}, \\ Q_{\text{decay}} &= \Gamma\rho_\chi/m_\chi\frac{\mathrm{d}N}{\mathrm{d}E}, \end{aligned} \tag{2.9}$$

where $\langle\sigma v\rangle$ is the velocity-averaged annihilation rate, Γ the decay rate, ρ_χ the dark matter density, m_χ the dark matter mass and $\mathrm{d}N/\mathrm{d}E$, the spectrum of electrons or positrons produced per annihilation/decay.

Electrons/positrons from dark matter annihilation or decay typically result from the decay of hadronic final states, like $\pi^\pm$, or the leptonic decay of $\tau^\pm$ or $\mu^\pm$. In the first case, the high multiplicity of the processes will produce a continuous and smooth spectra over a wide energy range. The direct production of electrons and positrons will result in a characteristic spectrum, with a sharp edge-like feature at $E = m_\chi$ (for annihilation) or $E = \frac{1}{2}m_\chi$ (for decay).

As shown in Ref. [Bergstrom2013], this can explain a rise in the positron fraction (and the positron flux), just like the pulsar hypothesis can. Therefore high precision data up to the highest energies is vital to search for edge-like structures in the positron flux, which is one of the goals for this thesis.

CHAPTER 3

Detector

The AMS-02 detector is a general purpose magnetic spectrometer with a large acceptance [Ahlen1994; Kounine2011b]. It was launched to space using the Space Shuttle *Endeavor* during the *STS-134* mission on May 16th 2011. On May 19th 2011 it was installed on the ISS.

It operates in a low earth orbit, with an orbital plane inclination of 51.6° with respect to the Earth's equator. AMS-02 completes approximately 16 orbits of data taking every day, delivering a stable performance since its installation and high-quality data [Ting2013].

The dimensions of the detector are approximately 5 m × 5 m × 4 m and the total weight is 7,500 kg. A schematic view of the instrument is shown in Fig. 3.1.

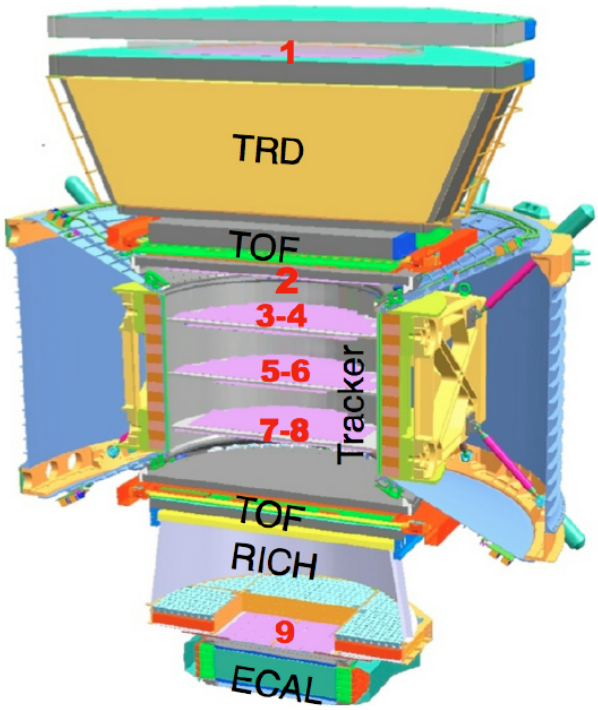

Figure 3.1: Schematic view of the AMS-02 detector. Credit: Ref. [AmsWebsite]

The key subdetectors to measure the electron and the positron flux are:

1. **Silicon tracker** together with the **magnet** (Sections 3.1 and 3.2), to separate negatively from positively charged particles

2. **Transition Radiation Detector** (Section 3.4), to distinguish electrons and positrons from protons

3. **Electromagnetic calorimeter** (Section 3.5, to measure the electron or positron energy and to discriminate protons from electrons or positrons by their shower shape

The strength of AMS-02 is the redundancy of the energy, momentum and charge measurements. Various subdetectors can be combined in the data analysis, to select pure samples of cosmic-ray particles, e.g. positrons separated from the overwhelming proton background, which is thousand times larger than the amount of positrons.

3.1 Magnet

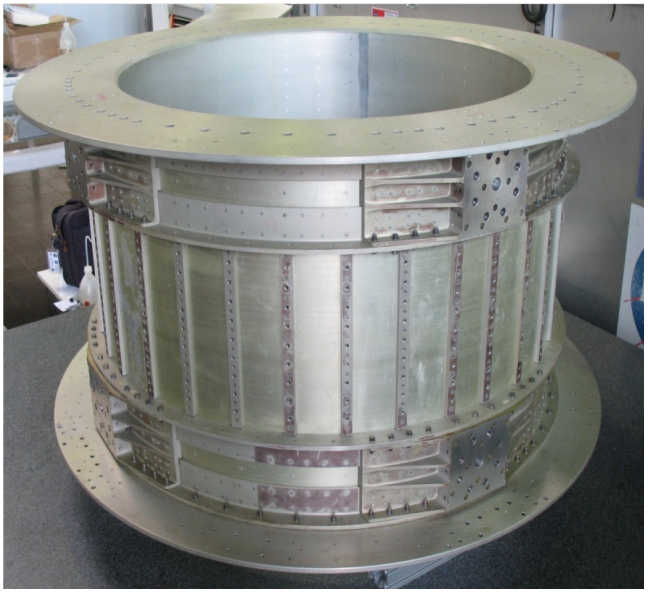

Figure 3.2: Picture of the permanent magnet used in AMS-02. Credit: Ref. [AmsWebsite]

The magnet [Luebelsmeyer2011], shown in Fig. 3.2, is made of 64 high-grade Nd-Fe-B sectors assembled in a cylindrical shell structure - 0.8 m long - with an inner diameter of 1.1 m. The magnet produces a field of 1.4 kG in the X direction at the center of the magnet and negligible dipole moment outside the magnet. The dipole moment outside of the magnet needs to vanish to eliminate the effect of torque on the ISS.

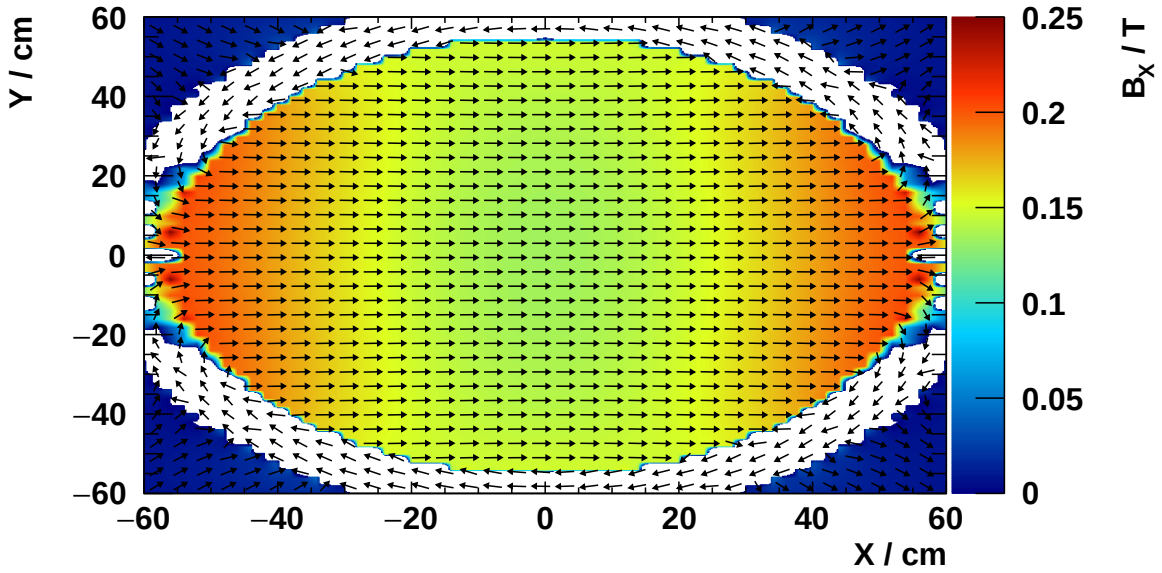

Figure 3.3: Visualization of the magnetic field in X-Y direction of the AMS-02 permanent magnet at $Z = 0$ cm (center of AMS). Credit: B. Beischer.

Figure 3.3 shows the X-Y view of the magnetic field at $Z = 0$ cm (center of AMS), as implemented in the AMS-02 reconstruction software. The magnetic field of the permanent magnet was measured in 1997 and re-measured in 2010 in 120,000 locations. The deviation of the field from both measurements is smaller than 1 % in all locations [AmsWebsite]. The AMS reference coordinate system is aligned with the center of the magnet, such that the x-axis is parallel to the magnetic field line in the center. Since the z-axis points vertically, the Y-Z projection is the bending plane for incident particles.

3.2 Tracker

The AMS-02 tracker [Hass2004; Haino2013] is composed of 2284 double-sided silicon micro-strip detectors, with dimensions of 72 mm × 41 mm × 0.3 mm, covering an effective area of 6.4 m^2.

The high resistivity n-type sensors are inversely biased with an voltage of 80 V. A traversing particle creates electron/hole pairs in the sensors, as illustrated in Fig. 3.4. The drifted electron/hole pairs are collected by the p^+ strip with an implantation pitch of 27.5 µm on one side (**S side** or **y-side**) and the n^+ strip with an implantation pitch of 104 µm oriented orthogonally on the other side (**K side** or **x-side**).

7 to 15 silicon sensors are grouped together on a *Ladder*, forming the building block of the AMS-02 tracker. Each ladder has 1024 readout channels, 640 for the p^+ strips and 384 for the n^+ strips. All strips on the S side are readout independently, whereas the K side strips are bonded together: the same strips on different sensors are linked together, to reduce the overall amount of readout channels. This introduces an ambiguity on the K side, used to measured the non-bending plane coordinate, that needs to be resolved during event reconstruction.

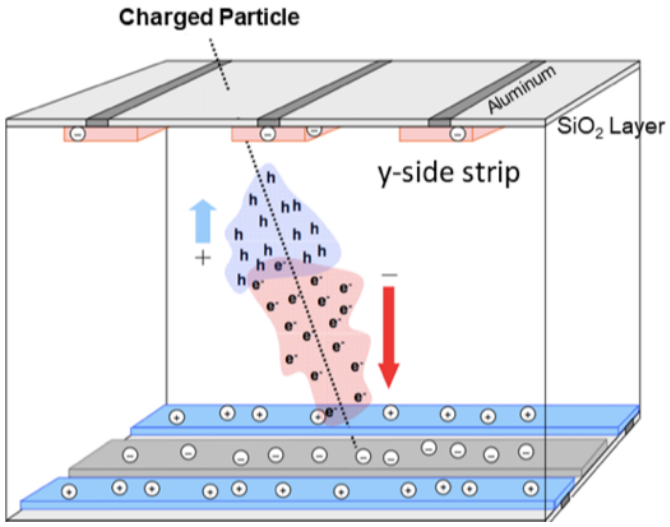

Figure 3.4: Schematic of the measurement principle of the "S side" silicon sensor. Credit: Ref. [AmsWebsite]

In total, there are 192 ladders arranged in nine layers, mounted on six mechanical supporting planes, placed at different vertical positions in the detector, as shown in Fig. 3.5. Six layers are arranged into three double-sided planes (layer 3 to layer 8) placed inside the magnet, together with another single-sided plane (layer 2). The two remaining single-sided planes (layer 1 and layer 9) are placed at the top and the bottom of the instrument, increasing the lever arm for the sagitta measurement.

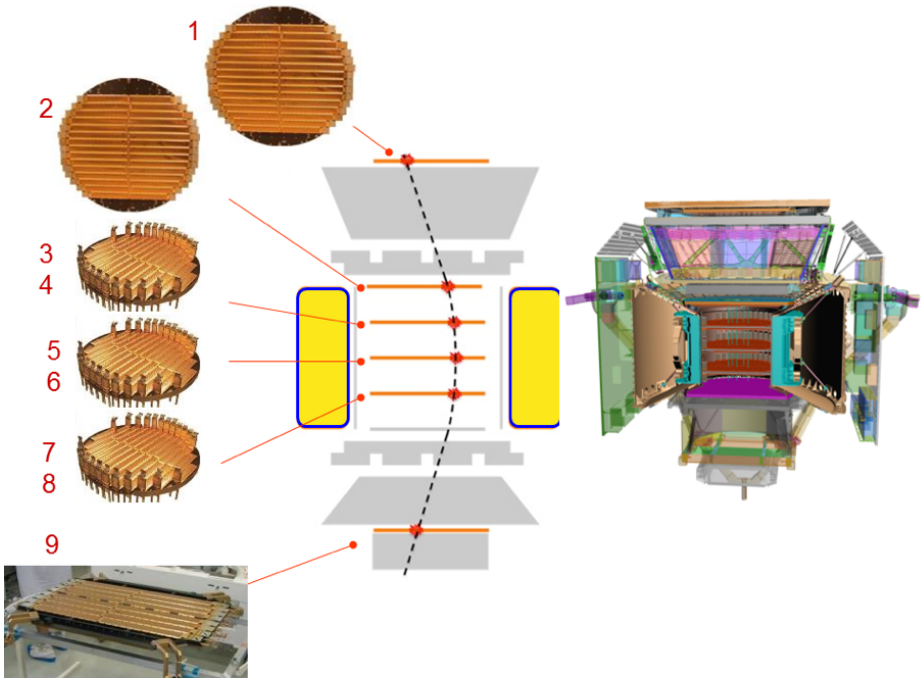

Figure 3.5: Schematic of the tracker showing the locations of the nine tracker planes. Credit: Ref. [AmsWebsite]

The silicon sensors allows one to measure the particle position on the silicon surface, with an accuracy better than 10 µm in y-direction (S side) and 30 µm in x-direction (K side). Moreover, the deposited ionization energy is proportional to the square of the particle charge ($I \propto Z^2$) and can therefore be used to identify the type of the particle. Furthermore due to the magnetic field, any charged particle traversing AMS-02 is bent and thus the charge sign can be reconstructed from a measurement of the curvature of the trajectory.

The inner tracker (formed by layer 2 to 8) is held stable by a carbon fiber structure with negligible coefficient of thermal expansion. The stability of the inner tracker is monitored using the Tracker Alignment System (TAS), which consists of 20 infrared laser beams that penetrate layers 2 through 8 and provide sub-micrometer position measurements. Using cosmic rays over a two-minute window, the position of layer 1 is aligned with a precision of 5 µm with respect to the inner tracker and layer 9 with a precision of 6 µm. The alignment stability of layer 1 and layer 9 over seven years is shown in Fig. 3.6. The stability[1] is 2.2 µm for layer 1 and 2.3 µm for layer 9.

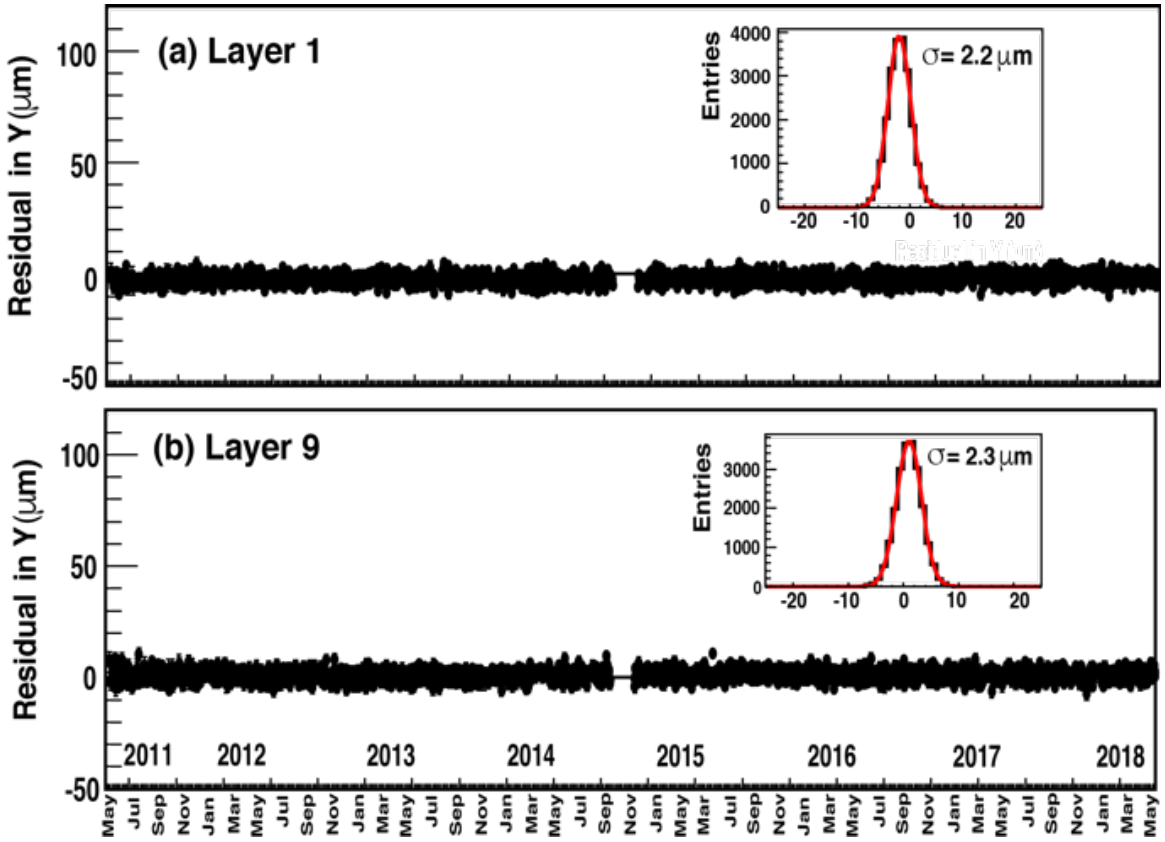

Figure 3.6: Schematic of the measurement principles of the silicon tracker. Credit: Ref. [AmsWebsite]

Together with the magnet (Section 3.1), the tracker provides a maximum detectable rigidity of 2 TV on average for $Z = 1$ particles, over tracker planes 1-9, where rigidity is the momentum divided by the charge. Furthermore each layer of the tracker also provides an independent measurement of Z. The charge resolution of the layers of the inner tracker together is $\Delta Z = 0.05$ for $Z = 1$ particles.

[1] In October and November 2014, the tracker was partially switched off due to detector studies.

3.3 Time Of Flight (TOF)

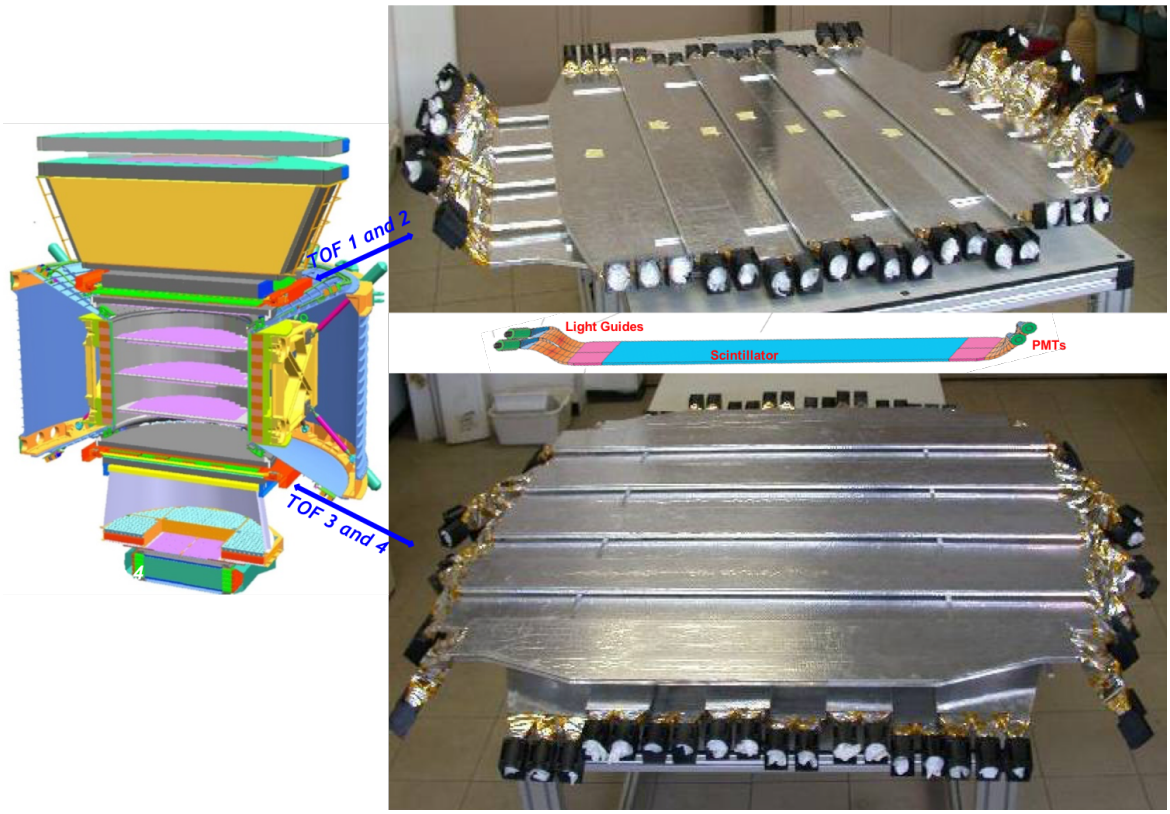

Figure 3.7: Picture of the Time-Of-Flight system. The upper and low TOF, each consists of two planes. Credit: Ref. [AmsWebsite]

Two planes of Time Of Flight (TOF) counters, shown in Fig. 3.7, are located above the magnet, forming the "Upper TOF" and two planes below the magnet forming the "Lower TOF". Each plane contains eight or ten scintillating paddles. Each paddle is equipped with two or three photomultiplier tubes on each end. To ensure efficient detection of traversing particles, the paddles in each plane overlaps with the adjacent ones by 5 mm.

The coincidence of signals from all four planes provides the main trigger (Section 3.8) for charged particles. By taking the time difference between signals from the upper and lower TOF planes a precise measurement of the particle velocity can be obtained: the average time resolution is ≈ 160 ps for $Z = 1$ particles.

While the ionization energy deposition in the TOF counters by nuclei is proportional to Z^2, the scintillator light output slowly saturates and the Z dependence becomes almost linear as described by Birks law [Bindi2014]. The charge resolution was measured to be $\Delta Z = 0.05$ for $Z = 1$ particles. The TOF is able to differentiate charges up to Zinc, as shown in Fig. 3.8.

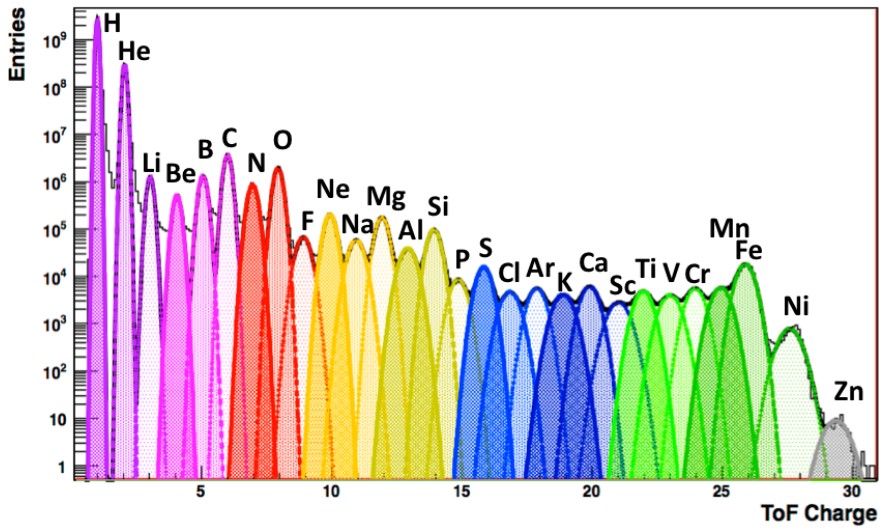

Figure 3.8: The charge distribution measured by the TOF, from $Z = 1$ (protons) up to $Z = 30$ (Zinc). Credit: Ref. [AmsWebsite]

3.4 Transition Radiation Detector (TRD)

The Transition Radiation Detector (TRD) [Kirn2013; Heil2013] is located at the top of the AMS-02 detector. It is designed to discriminate between light and heavy particles, such as positrons and protons, by exploiting the γ dependence of the transition radiation effect.

Transition radiation [Ginzburg1945] is produced by highly relativistic charged particles, with a large Lorentz factor γ, when crossing the boundary of two materials with different dielectric constants. The dipole formed by the charged particle with its mirror charge will change as it passes the interface, and this gives rise to emission of soft x-ray photons.

The TRD has an inverted octagonal pyramid shape, as shown in Fig. 3.9.

Figure 3.9: Picture of the TRD during assembly, showing the inverted octagonal pyramid shape. Credit: Ref. [AmsWebsite]

It is mounted between the first layer of the tracker (Section 3.2) and the first layer of the TOF (Section 3.3). The TRD is 80 cm high and spans 2 m at its top plane and 1.5 m at its bottom plane. The detector is placed in a skeleton made of aluminium honeycomb walls. It is populated with 5248 proportional tubes with a diameter of 6 mm, made from 72 mm thick double-layered kapton-aluminium foils, which functions as the cathode of the proportional tubes. The tubes are grouped into 328 modules, with lengths from 0.8 m to 2 m, depending on the position where the module is mounted in the pyramid shape.

A 30 mm thick gold-plated tungsten wire is mounted in the middle of each straw tube, acting as anode. Each tube is filled with a gas mixture of approximately 90:10 ratio of xenon (Xe) to carbon dioxide (CO_2). When a traversing charged particle ionizes the gas in a tube, a voltage proportional to the number of ionized gas atoms is produced on the output of the wire. This proportionality is called *gas gain*.

Xenon is used to detect the ionization signal of crossing charged particles in addition to the low energy photons of the transition radiation, while carbon dioxide acts as a quenching gas for charge multiplication, ensuring that the gas returns to its initial state for the next measurement, after a particle traversal.

To compensate the gas gain change due to diffusion across tube walls, a daily high voltage adjustment is performed to keep the gas gain at a predefined level, while the total pressure in the TRD decreases, due to the diffusion loss. To keep the total pressure at around 1 bar gas is refilled using a gas supply system approximately once a month. The TRD gas system is equipped with 49 kg xenon and 5 kg CO_2, allowing for a continuous operation in space for 30 years.

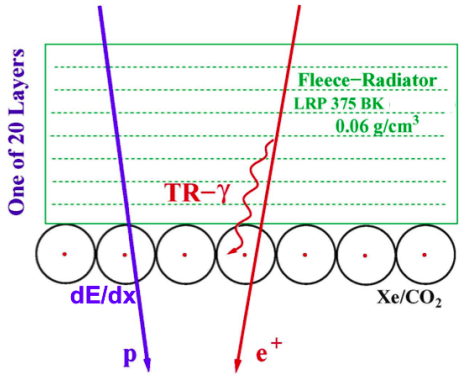

Figure 3.10: Working principle of the TRD. Credit: Ref. [AmsWebsite]

The probability of emitting transition radiation photons increases with the number of boundaries crossed. For that reason the modules are arranged into 20 vertical layers with 22 mm of fleece radiator interleaved between each layer. The fleece radiator is composed of 10 mm polypropylene/polyethylene fibers with a density of 0.06 g cm^{-3}. The proportional tubes in the four highest and lowest layers of the TAS are mounted parallel to the x-axis of the AMS-02 coordinate system (non-bending plane of the magnetic field), while the straw tubes in the middle layers are parallel to the y-axis (bending plane of the magnetic field), to allow for a three-dimensional reconstruction of the particle trajectory.

The working principle of the TRD is illustrated in Fig. 3.10. A proton traversing the straw tube ionizes the gas. A positron at the same energy will additionally emit transition radiation photons

during the passage through the radiator, as the γ factor is $\approx$ 2000 times larger. The low energy photons will be absorbed by the xenon and enhance the signal measured on the tungsten wire.

By combining the dE/dx measurement from all 20 TRD layers a likelihood estimator can be constructed, that separates light from heavy particles, such as electrons or positrons from protons, as illustrated in Fig. 3.11. A detailed description of the TRD estimator Λ_{TRD} is given in Section 4.2.6.

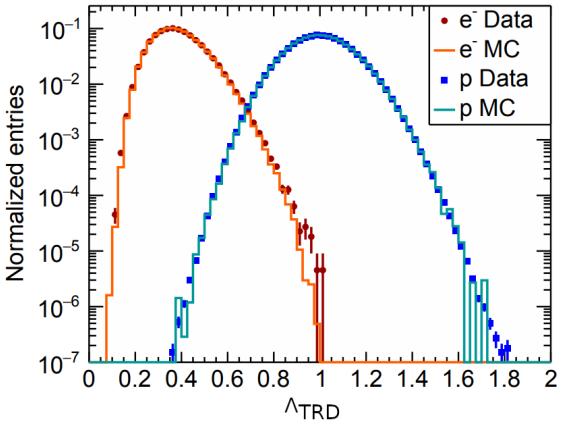

Figure 3.11: Example showing the TRD estimator, which combines the dE/dx measurements from all 20 TRD layers into a single estimator, in the energy range 10 – 100 GeV. Credit: Ref. [Raiha2017]

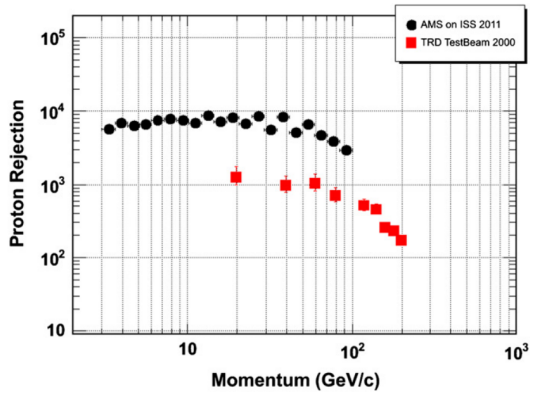

(a) Credit: Ref. [Kirn2013]

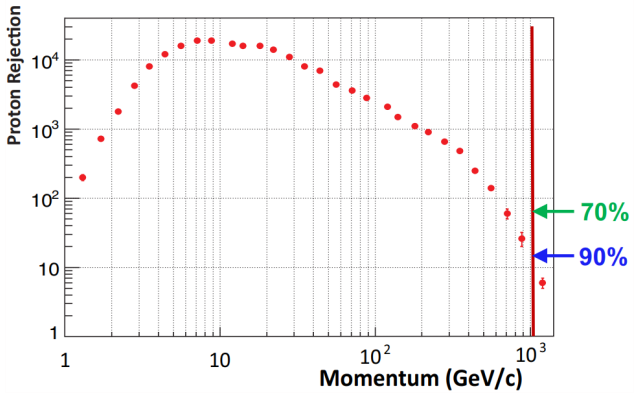

(b) Credit: Ref. [Kounine2017b]

Figure 3.12: Proton rejection of the TRD as function of the $e^{\pm}$ momentum at 90 % $e^{\pm}$ efficiency. The left plot shows the proton rejection determined during testbeam in 2000, in comparison with the proton rejection determined from ISS data in 2011. The right plot shows the most recent measurement of the proton rejection, which greatly improved with more ISS statistics and sophisticated reconstruction algorithms.

The primary purpose of the TRD is to identify positrons from the proton background by transition radiation. The abundance ratio between protons and positrons is about 1000 at 10 GeV and it increases with energy. At an $e^{\pm}$ efficiency of 90 %, the TRD proton rejection exceeds 10^4 above 4 GeV, gradually decreasing to 10^3 at $\approx$ 200 GeV, until it reaches approximately 20 at $\approx$ 1 TeV, as shown in Fig. 3.12.

3.5 Electromagnetic Calorimeter (ECAL)

The AMS-02 ECAL consists of a multilayer sandwich of lead foils and ≈ 50,000 scintillating fibers with an active area of 648 mm × 648 mm and a thickness of 166.5 mm, corresponding to 17 radiation lengths X_0 [RosierLees2012]. The calorimeter is composed of 9 superlayers, each 18.5 mm thick and made of 11 grooved, 1 mm thick lead foils interleaved with 10 layers of 1 mm diameter scintillating fibers. In each superlayer, the fibers are oriented in only one direction. The 3D imaging capability of the detector is obtained by stacking alternating superlayers with fibers parallel to the x-axis and y-axis (five and four superlayers, respectively).

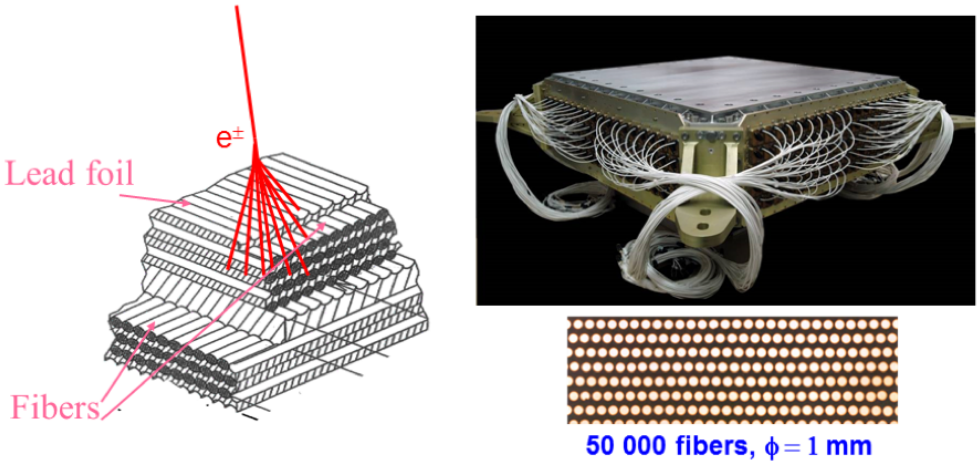

Figure 3.13: Schematic of the electromagnetic shower development in the ECAL. Credit: Ref. [AmsWebsite]

The scintillating fibers are read out on one end by 324 photomultipliers (PMT). Each PMT has four anodes and is surrounded by a magnetic shield which contains light guides, the frontend electronics and the PMT base. An ECAL cell is defined as an area of 9 mm × 9 mm, covering approximately 35 fibers, corresponding to one anode. In total there are 1296 cells segmented into 18 layers longitudinally, with 72 transverse cells in each layer. This design allows a sampling of the shower in three dimensions with a fine granularity. The PMT / electronics are able to process the signals over a wide dynamic range, from minimum ionizing particles (MIPs), which produce ≈ 10 photoelectrons per cell, up to the ≈ 60,000 photoelectrons produced in one cell by the core of an electromagnetic shower of a 1 TeV electron or positron [Kounine2017a].

The primary purpose of the ECAL is to separate electrons and positrons from protons, as well as providing an accurate energy measurement for electron and positrons up to the TeV regime. When an electron or positron traverses the first layer of the ECAL it starts to emit bremsstrahlung photons, which further convert into additional electron and positron pairs through the interaction with the nuclei of the high-density material of the ECAL. The secondary electrons and positrons also emit bremsstrahlung photons and an *electromagnetic shower* cascade develops. The two processes (bremsstrahlung and pair-production) continue until photons fall below the pair production threshold and energy losses of electrons and positrons due to ionization start to dominate over the losses due to bremsstrahlung.

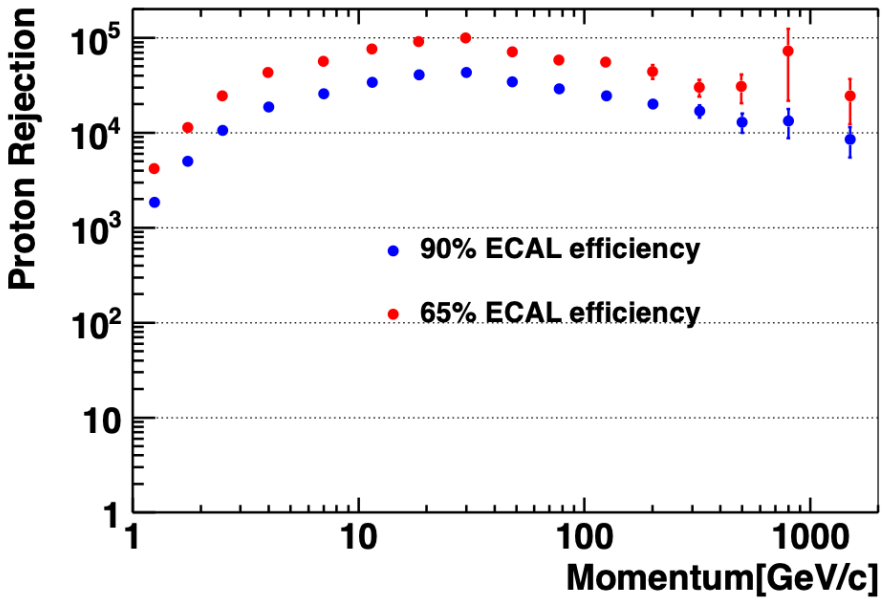

Figure 3.14: Proton rejection of the ECAL as function of the $e^{\pm}$ momentum. Credit: Ref. [AmsWebsite]

The ECAL, combined with the Tracker ($E/|R|$ cut), offers a proton rejection larger than 10^4, at an $e^{\pm}$ efficiency of 90 %, between 3 – 1,000 GeV, as shown in Fig. 3.14. Approximately one order of magnitude of the rejection power stems from the combination of Tracker and ECAL - the $E/|R|$ cut. Another order of magnitude from the proton spectrum[2] and the remaining 2-3 orders of magnitude from the ECAL itself, which is a common magnitude of proton rejection for an ECAL.

In a dedicated testbeam the ECAL energy resolution [Gallucci2015] was measured to be

$$\frac{\sigma_E(E)}{E} = \frac{(10.4 \pm 0.2)\,\%}{\sqrt{E}} \oplus (1.4 \pm 0.1)\,\%.$$

3.6 Anti-Coincidence Counter (ACC)

The ACC counters [Doetinchem2009], shown in Fig. 3.15, form a barrel surrounding the inner tracker, with overlapping coverage along the vertical edges to ensure efficient detection of particles traversing in all directions. Their purpose is to detect events with unwanted particles that enter or leave the inner tracker volume transversely.

[2] When determining the proton rejection as function of ECAL energy, low energetic protons are naturally suppressed, as protons do not deposit all of their energy in an ECAL. On average, the protons in the event sample, categorized as function of ECAL energy, have a three times larger rigidity than measured ECAL energy. Thus the proton spectrum is sampled at higher rigidities, where the spectrum is rapidly falling (power law), leading to a smaller proton background, compared to measuring the proton rejection as function of rigidity.

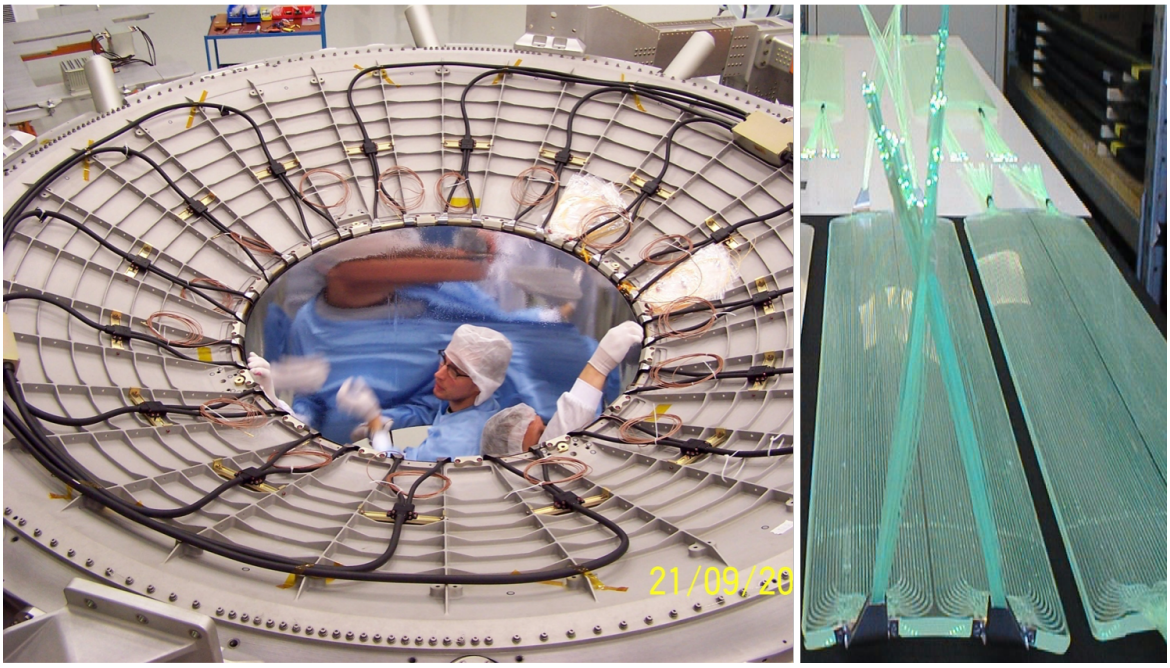

Figure 3.15: Picture of the ACC during construction. Credit: Ref. [AmsWebsite]

The ACC consists of sixteen curved scintillator panels of 0.8 m length, instrumented with wavelength-shifting fibers to collect the scintillation light. The ACC signal is an important part for the trigger logic, as it is used to veto particles coming from the side, as illustrated in Fig. 3.16.

The performance of the ACC was tested extensively using atmospheric muons: the upper limit on the ACC inefficiency are set to be $I < 1.5 \times 10^{-5}$ at 95 % confidence level.

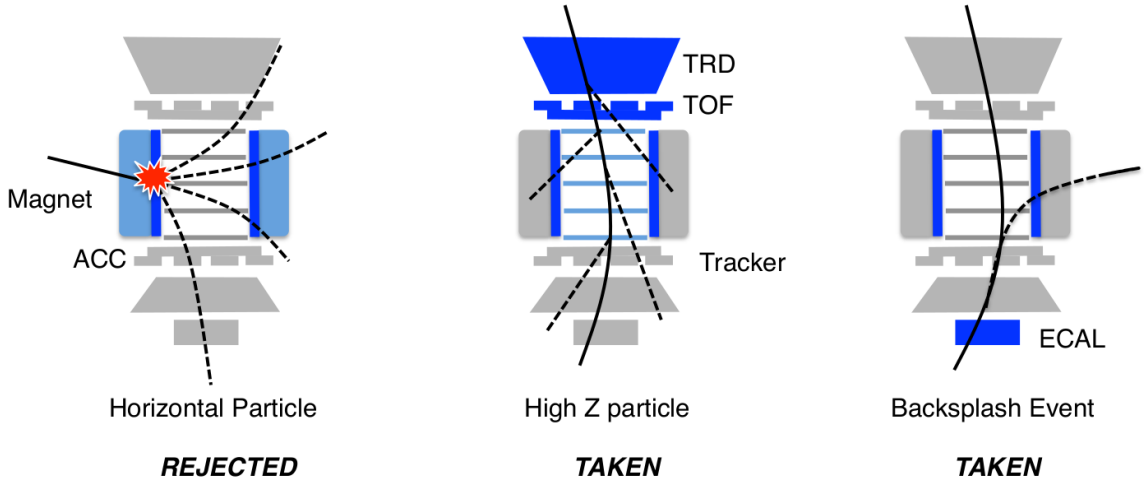

Figure 3.16: Illustration of the operation mode of the ACC. Credit: Ref. [AmsWebsite]

3.7 Ring-Imaging Cherenkov counter (RICH)

The AMS-02 RICH [Giovacchini2014], shown in Fig. 3.17, is mounted between the lower TOF planes and the ECAL. The RICH is designed to measure the absolute charge of relativistic particles and their velocity with a precision of ≈ 0.1 % for protons.

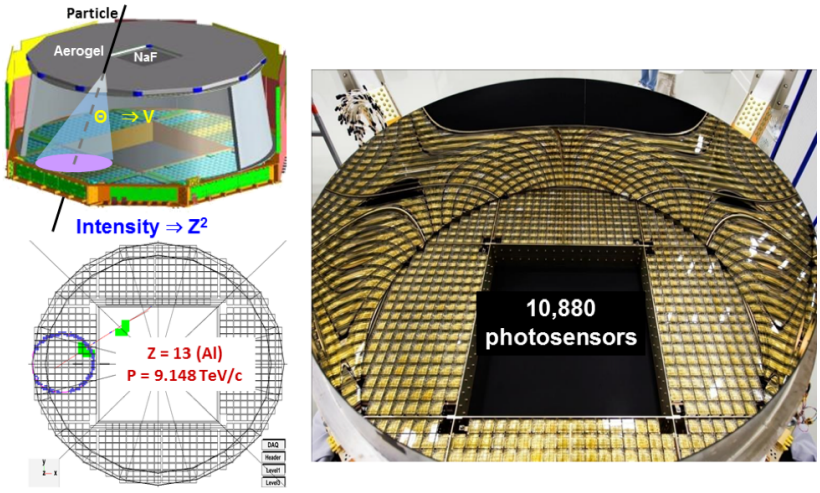

Figure 3.17: Picture of the RICH and its working principle. Credit: Ref. [AmsWebsite]

The detector consists of a layer of radiator material, a conical reflector and a detection plane. The RICH has a truncated conical shape with a 60 cm upper radius, a 67 cm lower radius and a height of 47 cm. The upper plane contains the radiator, which is made of two non-overlapping dielectric materials.

The dielectric radiators induce the emission of a cone of Cherenkov photons when traversed by charged particles with a velocity greater than the velocity of light in the material. The central radiator is formed by 16 sodium fluoride, NaF, tiles, each 8.5 cm $\times$ 8.5 cm $\times$ 0.5 cm, with a refractive index $n = 1.33$. These are surrounded by 92 tiles, each 11.5 cm $\times$ 11.5 cm $\times$ 2.5 cm, of silica aerogel with a refractive index $n = 1.05$. This allows the detection of particles with velocities $\beta > 0.75$, for those which pass through the NaF radiator and $\beta > 0.953$ for those which pass through the aerogel radiator.

The Cherenkov photons are emitted only when velocity of incoming particle exceed the threshold velocity $1/n$. These photons are emitted under an angle θ with respect to the particle direction, where θ is given by $\cos\theta = \beta \cdot n$. The number of generated photons per track length is proportional to Z^2.

An expansion volume with a height of 45 cm between the radiators and the photon detection plane allows the ring of Cherenkov photons to expand. A high reflectivity mirror surrounds the expansion volume to reduce the lateral loss of photons. The Cherenkov photons are detected by an array of 10,880 photosensors with a spatial granularity of 8.5 mm $\times$ 8.5 mm. It is designed such that photons produced by the NaF radiator in the middle have a larger cone size and therefore no photosensors are needed in the middle at the end of the expansion volume to detect them. This is especially important as the ECAL is mounted in the middle block, at the end of the expansion volume, and material above the calorimeter needs to be avoided to avoid pre-showering.

The β resolution was measured to be $\Delta\beta/\beta \approx 0.001$ for $Z = 1$ particles in a dedicated testbeam study.

3.8 Trigger

The AMS-02 trigger logic [Lin2005] utilizes signals from TOF, ACC and ECAL to take a fast decision whether an event should be recorded or not. The trigger logic takes $\approx 1\,\mu s$ to make a decision, which represents a significant contribution to the dead time of the experiment. The detector is in a busy state and cannot detect new particles during the dead time.

AMS-02 uses a complex decision tree architecture with three different stages: the "Fast trigger", the "Level 1 trigger" and the "Level 3 trigger".

Only if the conditions of the first trigger stage are fulfilled, the next is considered, to save processing time. At the time of writing only the first two trigger stages are used - the Level 3 trigger stage is deactivated as there is enough bandwidth available to transfer all events triggered by the Level 1 trigger to the ground.

The fast trigger conditions are designed for different particle types: FTC for charged particles, FTZ for particles with high charge (or strangelets) and FTE for all particles that produce electromagnetic showers (photons / leptons). If any of the three conditions are fulfilled, a fast trigger signal is generated.

If a fast trigger signal is generated, the dedicated JLV1 electronics board [Kounine2009] starts evaluating 15 different Level 1 trigger conditions, which can be grouped into five categories:

(a) **Charged particles**
Events with at least 3 out of 4 TOF panels with a signal over threshold are accepted.

(b) **Big Z particles**
Events with large energy depositions in the TOF panels are accepted.

(c) **ACC**
Provides a veto to reject particles traversing AMS horizontally.

(d) **ECAL-F / ECAL-A**
Events with energy depositions in the ECAL layers are accepted.

(e) **External** (not used on the ISS)
Accepts events if an external trigger condition is fulfilled, e.g. the Cherenkov counters in the beam test that were connected with the AMS-02 JLV1 trigger boards.

From the 15 trigger signals, seven sub-triggers were carefully chosen for data taking onboard the ISS [Kounine2011a]:

1. **Unbiased charged**
Requires 3 out of 4 TOF panels in coincidence – efficiency is close to unity. Only every 100^{th} event fulfilling this condition is recorded, to reduce the trigger rate and save downlink bandwidth.

2. **Single charged**
Requires 4 out of 4 TOF panels in coincidence and no ACC hits.

3. **Normal ions**
Requires 4 out of 4 TOF panels in coincidence with large energy deposition and less than five ACC hits.

4. **Slow ions**
   Equal to "Normal ions", except that the gate width is extended (see [Kounine2011a] for details) to account for the slow strangelet particle.

5. **Electrons**
   Requires 3 out of 4 TOF panels in coincidence plus at least one ECAL shower reconstructed.

6. **Photons**
   Requires energy depositions in the ECAL in both X/Y super-layers.

7. **Unbiased EM**
   Requires only energy depositions in the ECAL. Only every 1000^{th} event fulfilling this condition is recorded, to reduce the trigger rate and save downlink bandwidth.

The **Single charged**, **Normal ions**, **Slow ions**, **Electrons** and **Photons** trigger branches are called **physics triggers**. The remaining trigger branches **Unbiased charge** and **Unbiased EM** are used to measure the physics trigger efficiency directly from ISS data. The assumption - which was verified in dedicated studies - is that these unbiased triggers have an efficiency close to unity, such that no particle can traverse AMS-02 vertically without firing an unbiased trigger signal.

CHAPTER 4

Analysis

In this chapter the electron flux and the positron flux analysis is presented, as well as the dedicated positron/electron ratio and positron fraction analysis.

At first the data analysis framework is introduced (Section 4.1), which is used to analyze the AMS-02 data. It is shown which subdetectors are needed to separate the $e^{\pm}$ signal from the overwhelming proton background in cosmic rays, and how to combine the subdetector measurements in an optimal way (Section 4.2), including a discussion of the *charge-confusion*, the misreconstructing of a positively charged particle as negative, and vice-versa. An overview of the data selection criteria is presented (Section 4.3) and the necessary techniques used to differentiate between signal and background (Section 4.4). Afterwards the time-averaged fluxes and ratios are presented (Sections 4.5 and 4.7) including a discussion of all systematic uncertainties (Sections 4.6 and 4.8). The chapter is concluded with the presentation of the time-dependent fluxes and ratios (Sections 4.9 and 4.11) and a discussion of their uncertainties (Sections 4.10 and 4.12).

The fluxes of cosmic-ray electrons or cosmic-ray positrons for a time interval i in the energy bin E of width ΔE are given by

$$\Phi_{e^{\pm},i}(E) = \frac{N_{e^{\pm},i}(E)}{\Delta E \cdot T_i(E) \cdot A_{e^{\pm},i}(E) \cdot \epsilon_{e^{\pm},i}(E)}, \tag{4.1}$$

where $N_{e^-,i}(E)$ and $N_{e^+,i}(E)$ are the numbers of electrons and positrons, respectively. $A_{e^{\pm},i}(E)$ is the acceptance and $\epsilon_{e^{\pm},i}(E)$ the combined signal selection efficiency. Both quantities potentially differ for electrons and positrons. $T_i(E)$ refers to the energy-dependent measurement time in the given time interval i and is independent of the particle species.

In the following sections detailed descriptions are given how to derive all ingredients necessary for the electron and positron fluxes and which challenges arise.

4.1 Data analysis framework

The AMS-02 detector produces approximately 3.7 Mbit of data for each event, containing information from the ≈ 300,000 readout channels. Events are recorded at rates up to 2 kHz resulting in a data rate of 7 Gbit/s, which is reduced to an average of 10 Mbit/s without loss of physics information. The data is transmitted to the White Sands Ground Terminal in New Mexico via the High Rate Data Link (HRDL) link using the NASA Tracking and Data Relay Satellite (TDRS) satellite system. Afterwards

the data is forwarded to Marshall Space Flight Center (MSFC), buffered and finally transmitted to the AMS-02 Payload Operation Control Center (POCC) at CERN via the Internet.

The incoming raw data is reconstructed using the AMS-02 *gbatch* software package, which was developed by the collaboration during the past decade. The result no longer contains raw data, but high-level reconstructed objects such as tracks, showers, particles, etc. The data files are written to disk as ROOT [Brun1997] trees and are called **AMS ROOT** files. The 6.5 years dataset used in this thesis corresponds to ≈ 890 TB of data. Each AMS ROOT file covers approximately ≈ 22 min of science data and has a size of ≈ 6 GB on average. In total 143,608 files have to be processed, to run once over the dataset. Due to limitations in the *gbatch* software framework, each file has to be processed using a single CPU core. The typical processing time of the full dataset is in the order of weeks when using a few thousand CPU cores. Furthermore when e.g. running 1000 batch jobs at the same time on a supercomputer - each processing a single AMS ROOT file - the I/O access pattern is inefficient. Many random accesses on the storage backends lead to I/O congestion and thus the available bandwidth is dramatically decreasing and the runtime of each job increases.

In order to speed up the turnaround time for analysis I developed a special data format together with Bastian Beischer and Henning Gast to overcome limitations of the AMS ROOT files: the **ACQt files**. An ACQt file can be analyzed in parallel by multiple nodes in a supercomputer, using hundreds of CPU cores at the same time. The *ACsoft* software package produces ACQt files from AMS ROOT files, maintaining a 1:1 correspondence. After a full data production, a certain number of ACQt files are merged together in so-called **Multi-ACQt files**. Each Multi-ACQt file covers a full day of AMS-02 data and has a typical size of ≈ 100 GB. Furthermore the individual ACQt files are much smaller on disk than their AMS ROOT file counterparts, since the information is tightly encoded and optimized as much as possible[1]. This allows us to shrink the analysis turnaround time from weeks to days, which makes an iterative analysis, like the one presented in this thesis, possible.

During the past seven years I developed the whole framework, in collaboration with Bastian Beischer, that automatizes the ACQt file production, ensures their consistency and takes care of the bookkeeping. Each dataset is cataloged in a database: the number of events in each file, the production duration, the disk space consumption etc. The whole AMS analysis group in Aachen uses this analysis framework and significant scientific results were produced using it, such as Refs. [Aguilar2014a; Aguilar2018].

4.2 Event reconstruction

In order to identify electrons or positrons in events recorded by AMS-02, the measurements of the individual subdetectors need to be combined. This is a challenging task, as ambiguities in the event reconstruction need to be resolved. An incoming electron or positron might emit bremsstrahlung photons, which convert into secondary electron and positron pairs. The secondary products as well as the primary particle may leave hits in the silicon tracker and thus multiple tracker tracks might be reconstructed. Furthermore multiple ECAL showers might be reconstructed, if more than one particle propagates towards the ECAL and the displacement between the individual particles (e.g. the primary particle and a secondary electron or positron) is large enough - which frequently happens at low energies.

[1] Each variable is transformed and rounded to fit into the smallest possible bit representation: between 1 – 4 byte.

4.2.1 TOF velocity and charge reconstruction

In the AMS-02 TOF reconstruction all PMTs covering the TOF paddles are read out independently to collect the TOF PMT anode and dynode signal. If a signal is present in any of the TOF paddles, a TOF cluster is formed, associated with a time measurement and a layer/bar index [Bindi2014].

From the reconstructed TOF clusters a pattern recognition algorithm selects TOF clusters in each of the four TOF layers belonging to the same trajectory, by utilizing external information e.g. from the tracker or the TRD, to resolve ambiguities. This might lead to multiple combinations of TOF clusters, each potentially belonging to a different incident particle.

For each of the TOF cluster combinations the charge in the upper and lower TOF bars is computed, as well as the time of flight velocity β of the incident particle. The velocity $\beta = \Delta x/(c \cdot \Delta t)$ is measured using the particle time of flight Δt between the upper and lower planes and the path length Δx - e.g. given by the tracker. The time measurement is performed using the anode signals from the PMT (Section 3.3).

The measurement of the charge from the PMT anode signals allows to determine the charge with high precision[2]. The energy deposited in the TOF bars, dE/dx, by the passage of particles is proportional to Z^2. Furthermore it depends on the velocity of the particle, such that: $\mathrm{dE/dx} \propto f(\beta) \cdot Z^2$.

For the analysis the correct TOF cluster combination needs to be selected, matching the selected tracker track - to ensure the Δx was taken from the correct track, and thus the β is correctly computed.

4.2.2 Tracker track reconstruction

In the AMS-02 tracker track reconstruction [Hass2004; BazoAlba2013] all silicon ladders are read out independently in X and Y direction. For each ladder and each direction, strips with the highest amplitudes - seed strips - are identified. The seed strips define the starting point for the cluster building procedure. The energy depositions in the strips to the left and to the right of the seed strip are merged together with the seed strip energy deposition, as long as their amplitude is higher than a predefined threshold. The silicon strips in the interval [seedStrip - nStripsLeft, seedStrip + nStripsRight] then form a cluster. The first phase of the track reconstruction yields an independent list of X and Y clusters for each ladder which are then matched in the second phase to form reconstructed hits.

A reconstructed tracker hit consists of a Y cluster and eventually a X cluster. In AMS-02 the X-side is read out using much less channels (described in Section 3.2) than the Y-side, leaving an ambiguity of 8 cm in the coordinate along the ladder, that needs to be resolved during the track reconstruction. The multiplicity resolving depends on external information from other subdetectors, such as the TOF or the TRD. If the multiplicity could be resolved the reconstructed hit additionally contains an associated X cluster.

A reconstructed tracker track is formed by applying a pattern recognition algorithm to select possible combinations of reconstructed hits, that may form a track, spanning multiple tracker layers. This potentially leads to a reconstruction of multiple tracker tracks for an event.

[2] The PMT anode signals start to saturate around $Z \approx 4\,e$. The PMT dynode signals are used to extend the measurement range up to heavy nuclei, such as Iron.

4.2.3 TRD track reconstruction

The AMS-02 TRD track reconstruction [Gast2015] identifies segments (straight lines in X-Z / Y-Z projection) for all TRD layers in X-Z orientation and all TRD layers in Y-Z orientation, independently. This procedure might identify multiple segments per projection, depending on the amount of hits in the TRD.

A reconstructed TRD track consists of a segment in X-Z orientation and another segment in Y-Z orientation. If an ECAL shower is present in the event, the TRD segments will be extrapolated to the ECAL shower with the highest energy and the position is compared to the centre-of-gravity of the shower. The segments with the lowest deviation from the shower centre-of-gravity are selected to form a reconstructed TRD track. If no ECAL shower is present in the event, a TRD track is only reconstructed, if exactly one segment in X-Z direction and one segment in Y-Z direction is available.

4.2.4 ECAL shower and energy reconstruction

In the AMS-02 ECAL shower reconstruction [Gallucci2015; Kounine2017a] all cells are considered that recorded an energy deposition exceeding a predefined threshold, corresponding to a few MeV. In each layer the cell with the largest energy deposition is identified, forming the start position of the cluster search. The energy depositions in the cells to the left and to the right of the start cluster are merged together, as long as their amplitude is higher than a predefined threshold – similar to the cluster finding procedure used in the tracker track reconstruction. This yields a number of one-dimensional clusters for each layer. Since the layers are alternating in X-Z and Y-Z direction two-dimensional clusters can be formed, by utilizing external information (e.g. a reconstructed tracker track). One or more two-dimensional clusters form an ECAL shower, depending on the spatial difference between the reconstructed clusters. If the clusters are close, they are associated to the same ECAL shower. If the displacement is large enough, multiple ECAL showers may be identified for an event.

The sum of all energy depositions in all cells of the clusters associated with the ECAL shower is called *deposited energy*. As described in Ref. [Gallucci2015] several corrections are applied on the cell level energy depositions: attenuation correction (correcting the light attenuation along the fiber), equalization (ensure that the response for MIPs is identical in each cell) and anode efficiency (the true energy deposition is underestimated towards the borders of the cell). The energy scale used for the analysis is the *reconstructed energy* which corrects the *deposited energy* for rear leakage: the loss of energy in transversal direction, when the electromagnetic shower cascade is not fully contained anymore in the calorimeter[3]. The effect gains importance with increasing energy. The reconstructed energy scale is derived with the help of the Monte-Carlo simulation and was verified in dedicated testbeam measurements.

4.2.5 Combining subdetector measurements

Custom particle reconstruction algorithms were developed to combine the subdetector information in an optimal way. The particle reconstruction algorithm utilizes all necessary AMS-02 subdetectors to form a **primary particle**. The **primary particle** groups together the individual subdetector measurements belonging to the same particle that entered the instrument. For each event the particle reconstruction algorithm defines exactly one primary particle, by construction, even if certain subdetector information

[3] Only $\approx 75\,\%$ of the energy released by a TeV $e^{\pm}$ is contained in the calorimeter, the rest leaks out.

are missing (e.g. no tracker track reconstructed, no TOF β / charge measurement available, no ECAL shower present, etc.) or multiple combinations could be used to define the primary particle.

As first step in the particle reconstruction, the list of all reconstructed tracker tracks is filtered, to reject those without a corresponding TOF β / charge measurement. Multiple TOF β and charge measurements are available for each event, as the charge is derived from the TOF dE/dx measurements multiple variants are computed, depending on the dx, as described in Section 4.2.1.

As second step in the particle reconstruction, the spatial difference between the centre-of-gravity of each ECAL shower in the event and each tracker track (extrapolated to the Z position of the ECAL shower centre-of-gravity) is computed. The pair (ECAL shower + tracker track with associated TOF β measurement), for which the spatial difference between the track extrapolation and the shower centre-of-gravity is smallest, is selected as **particle candidate** for further analysis.

Thus after running the first two steps of the particle reconstruction algorithm, a TOF β and charge measurement, an ECAL shower and a tracker track is selected, forming a particle candidate. If any of these quantities is missing, a fallback solution is implemented: selecting e.g. the TOF β measurement, with the highest $|\beta|$, or the tracker track with the best goodness-of-fit parameter in bending plane, or the ECAL shower with the largest energy deposition.

As third step in the particle reconstruction, each reconstructed TRD track in the event is extrapolated to the Z position of the ECAL shower centre-of-gravity and the spatial difference between the TRD track extrapolation and the shower centre-of-gravity is computed. The TRD track whose spatial difference is smallest is selected as TRD track for further analysis. The TRD track is reconstructed as a straight line, as no magnetic field is present in the TRD, which might alter the trajectory. To extrapolate the TRD track to the ECAL, the magnetic field, produced by the magnet surrounding the inner tracker, needs to be taken into account. The extrapolation is done using two hypotheses[4]: use $(+p)$, or $(-p)$ as momentum for the extrapolation, where p is proportional to the rigidity of the tracker track belonging to the primary particle candidate.

After the association of a TRD track, the primary particle reconstruction is complete, but does not guarantee that all subdetector measurements refer to the same incident particle. When applying the preselection cuts - Section 4.3.3 - during analysis, events with inconsistent measurements are rejected.

4.2.6 Construction of the TRD estimator Λ_{TRD}

The TRD allows one to separate light from heavy particles, as described in Section 3.4.

The energy depositions in a single straw tube for electrons or positrons are higher than for protons, due to the additional TR photons that are absorbed in the xenon – this allows one to build an estimator which can be used to distinguish electrons or positrons from protons. A particle traversing the TRD may leave traces in all 20 layers and these measurements can be combined into a single estimator: the TRD estimator Λ_{TRD}.

According to the Neyman-Pearson-Lemma [Neyman1933] the best statistical test to decide between two hypothesis is the likelihood ratio, which can be defined as:

$$\Lambda_{\text{TRD}} = -\log\left(\mathcal{L}_{e^-}/(\mathcal{L}_{e^-} + \mathcal{L}_p)\right). \tag{4.2}$$

[4] Both hypotheses need to be checked, otherwise the extrapolation is correlated with the charge-confusion effect. A misreconstructed charge-sign would lead to a decreased TRD matching efficiency, which needs to be avoided.

The determination of the PDFs $\mathcal{L}_{e^-}$ and $\mathcal{L}_p$ in Eq. (4.2) is the key ingredient[5] to build the TRD estimator.

The PDFs depend on the gas composition (the partial pressure of the xenon - p(Xe), the layer number n (relevant for electrons as the amount of transition radiation depends on the number of layers crossed in the TRD), the rigidity R of the particle and the path length dx traversed in the straw tube.

There are two independent ways to compute the path length dx. The first option is to determine the path length purely from the TRD. In each projection X-Z and Y-Z track finding is performed, by combining the hits in the straw tubes into segments (Section 4.2.3). The best matching segments in X-Z and Y-Z are then combined into a 3D trajectory from which the path length in each straw tube can be calculated. The accuracy is limited due to the rather large diameter of the straw tubes of 6 mm.

The second option is to rely on the extrapolation of a track reconstructed in the silicon tracker, which offers a much more precise trajectory reconstruction, but fails at the lowest rigidity where the extrapolation of the tracker track through the TRD is imprecise due to multiple scattering in the material above the silicon tracker. This distorts the trajectory and is relevant for electrons below rigidities of R $\approx$ 8 GV.

Therefore the best option is to combine both approaches using an rigidity dependent weighted mean, and use the path length estimation from the most precise source, depending on the reconstructed rigidity of the particle. This hybrid approach is used to form the TRD estimator Λ_{TRD}, which offers a rejection power of greater than 10^2 between 0.5 – 700 GeV, as shown in Section 3.4.

4.2.7 Construction of the ECAL estimator Λ_{ECAL}

The ECAL allows one to separate electrons or positrons from protons, as described in Section 3.5, by exploiting the differences in the shower development in the electromagnetic calorimeter.

In contrary to electrons or positrons, protons traversing the ECAL do not develop electromagnetic showers. Since the nuclear radiation length λ of the ECAL is 0.6, $\approx$ 50 % of the protons traverse the whole ECAL only losing energy via ionization. The typical energy loss is in the order of a few hundred MeV. These protons are called Minimum Ionizing Particle (MIP).

Proton MIP events can be easily rejected by a minimum energy cut on the order of $\approx$ 0.5 GeV. Protons that develop *hadronic showers* have a different characteristic with respect to *electromagnetic showers*. The hadronic showering process is dominated by inelastic hadronic interactions. High energetic protons may produce multiple particles (mostly charged pions and nucleons) due to the inelastic interactions. Secondary particles are emitted originating from nuclear decay of excited nuclei.

Because of the π^0 creation that decay predominantly into $\gamma\gamma$, there is also an electromagnetic component present in hadronic showers, usually starting deeper in the ECAL than a purely electromagnetic shower.

The differences in the shower development between electrons or positrons and protons were exploited to construct a multi-variate estimator - Λ_{ECAL} - utilizing 22 variables based on the longitudinal shower profile, the lateral shower profile energy fractions (energy released in first layer divided by total energy deposition, etc.) and many more. The ECAL estimator Λ_{ECAL} combined with the Tracker ($E/|R|$ cut) offers a rejection power greater than 10^4 between 3 – 1,000 GeV, as shown in Section 3.5.

[5] The set of PDFs used in this analysis are called "Trd-P" [Gast2015] and were derived in the Aachen group in 2015.

4.2.8 Construction of the charge-confusion estimator Λ_{CC}

A crucial part of the electron and positron analysis is the understanding and treatment of the charge-confusion effect. The charge sign of a particle might be misreconstructed due to interactions in the detector or the finite resolution of the silicon tracker at the highest energies. In this analysis, special attention was given to construct a multi-variate estimator which can be used to compare the charge-confusion prediction from the Monte-Carlo simulation with the ISS data: the CCMVA estimator Λ_{CC}.

It is important to note that the topology of the event is responsible for the amount of charge-confusion: events where only a single tracker track was reconstructed, matching to a single TRD track and a single ECAL shower have the smallest probability to have a misreconstructed charge sign. The probability of misidentification of the charge-sign increases with the track multiplicity: the more tracks are reconstructed, the more probable it is for the track reconstruction to associate wrong hits to a track, eventually resulting in a flipped charge sign or a wrong rigidity value.

In total 21 variables were identified that are sensitive to charge-confusion, 15 are relevant in both single-track and multi-tracks samples, whereas six variables are only relevant in the multi-tracks sample. In the following all CCMVA input quantities are defined and the distributions taken from the electron Monte-Carlo simulation are compared between the correct and wrong reconstructed charge sample. In Appendix A.2 a comparison of all input variables between the electron Monte-Carlo simulation and the ISS negative rigidity data sample is shown, demonstrating that all input variables are consistent between the Monte-Carlo simulation and ISS data.

The six most important input variables for the example energy bin 17.98 – 18.99 GeV - identified by TMVA [TMVA2007] during training - out of the 15 relevant for the single-track sample are presented - the remaining nine variables are described in Appendix A.2.

1. **Lower TOF charge**

   The lower TOF charge is computed by taking the average of the available charge measurements in the lower TOF clusters, as identified in the particle reconstruction, described in Section 4.2.5.

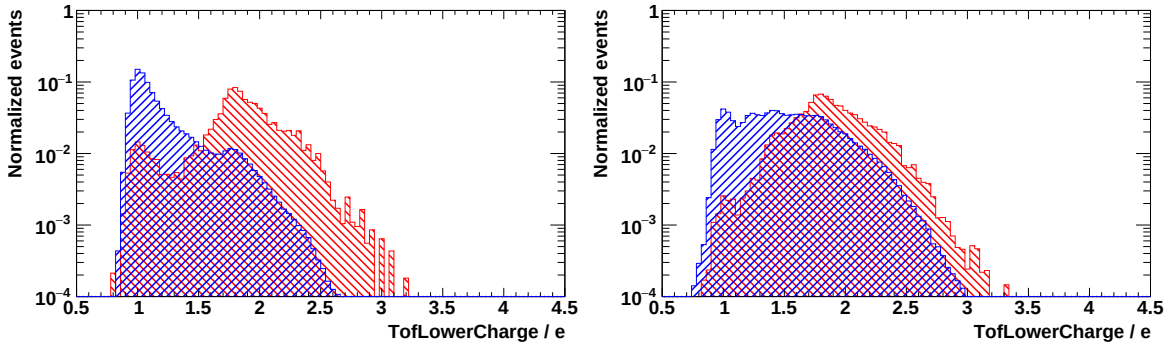

(a) Single-track sample **(b)** Multi-tracks sample

Figure 4.1: Example of TofLowerCharge distribution in the energy bin 17.98 – 18.99 GeV in the electron Monte-Carlo simulation. The red histogram shows the charge-confused sample (R > 0) and the blue histogram the correct reconstructed sample (R < 0), after applying all preselection, selection and $e^{\pm}$ identification cuts.

Figure 4.1 shows the TofLowerCharge distribution in an example energy bin for both the correct and wrong rigidity sample in the electron Monte-Carlo simulation.

The lower TOF charge is usually larger than the upper TOF charge as bremsstrahlung photons might convert in the inner tracker between the upper and lower TOF bars. The difference between the upper and lower TOF charges is an indication for the amount of interactions in the inner tracker and thus a useful quantity for the MVA estimator.

2. **Energy/Rigidity matching**

LogEnergyOverRigidity is defined as the logarithm of the energy deposited in the ECAL divided by the rigidity of the selected primary tracker track:

$$\text{LogEnergyOverRigidity} = \log\left(E_{\text{ECAL}}/\left|R_{\text{primary}}\right|\right)$$

When the primary particle interacted during the passage through AMS, by bremsstrahlung emission and conversions of the emitted photons, the secondary particles/photons usually travel collinear to the primary particle and are contained within the vicinity of the shower of the primary particle in the ECAL.

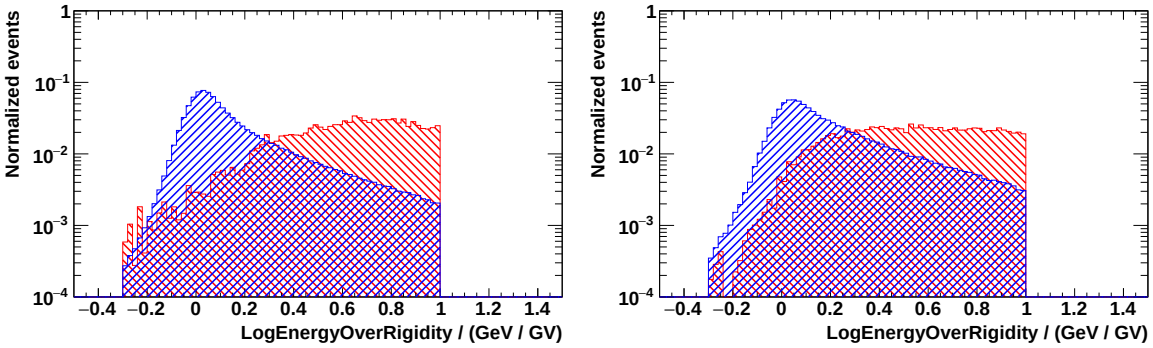

(a) Single-track sample **(b)** Multi-tracks sample

Figure 4.2: Example of LogEnergyOverRigidity distribution in the energy bin 17.98 – 18.99 GeV in the electron Monte-Carlo simulation. Note that LogEnergyOverRigidity is bounded between $-0.3 < \log\left(E_{\text{ECAL}}/\left|R_{\text{primary}}\right|\right) < 1$, due to the $E\,|R|$ cut in the $e^{\pm}$ identification cuts.

The rigidity on the other hand is more difficult to reconstruct, as in the case of multiple reconstructed tracks, a misassociation of individual hits is possible, leading to a distorted rigidity measurement. Correctly reconstructed events usually peak at 0, wrongly reconstructed events at larger or negative values, as shown in Fig. 4.2.

3. **Influence of single tracker hits on rigidity reconstruction**

In order to study the influence of single hits on the reconstructed rigidity, it is necessary to refit the track several times. In each iteration one of the layers is explicitly excluded from the track fit and the rigidity is determined. The difference in sagitta ($\propto$ inverse rigidity) with respect to the

original track fit, which includes all available hits, is calculated for each layer. The maximum difference in sagitta enters the MVA estimator as input quantity:

$$\text{TrkMaxDeltaSagittaFromRemovingHits} = \text{sgn}(R_{\text{primary}}) \max_{l \in [1,9]} \left| \frac{1}{R_{\text{primary}}} - \frac{1}{R_{\text{exclude layer } l}} \right|$$

The $\text{sgn}(R_{\text{primary}})$ factor ensures that the quantity is symmetric between correct reconstructed electrons and positrons. Figure 4.3 shows the TrkMaxDeltaSagittaFromRemovingHits distribution in an example energy bin for both the correct and wrong rigidity sample in the electron Monte-Carlo simulation.

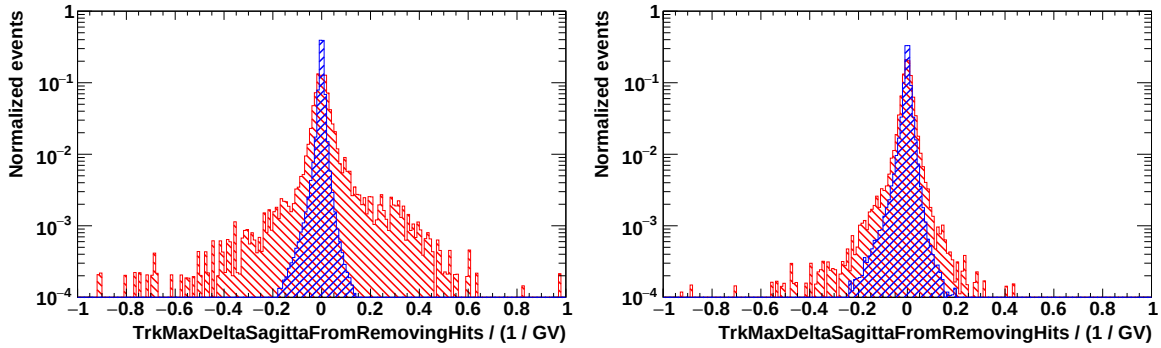

(a) Single-track sample **(b)** Multi-tracks sample

Figure 4.3: Example of TrkMaxDeltaSagittaFromRemovingHits distribution in the energy bin 17.98 – 18.99 GeV in the electron Monte-Carlo simulation. The red histogram shows the charge-confused sample (R > 0) and the blue histogram the correct reconstructed sample (R < 0), after applying all preselection, selection and $e^{\pm}$ identification cuts.

4. **Inner tracker charge**

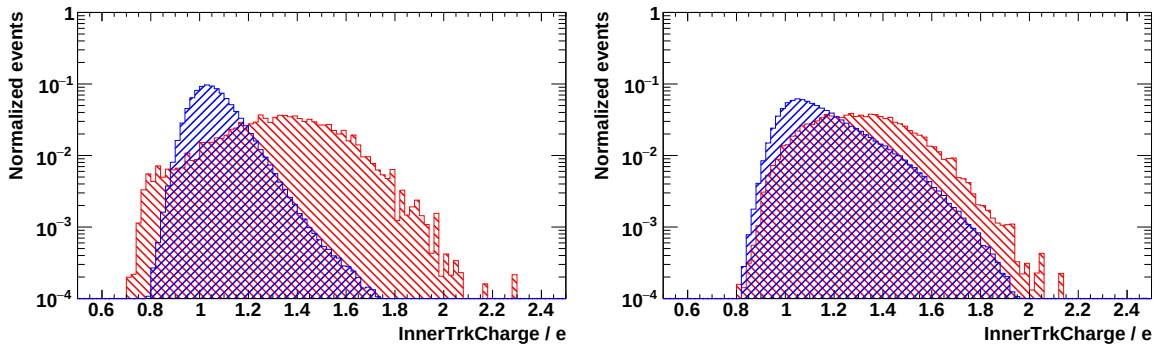

(a) Single-track sample **(b)** Multi-tracks sample

Figure 4.4: Example of InnerTrkCharge distribution in the energy bin 17.98 – 18.99 GeV in the electron Monte-Carlo simulation. The red histogram shows the charge-confused sample (R > 0) and the blue histogram the correct reconstructed sample (R < 0), after applying all preselection, selection and $e^{\pm}$ identification cuts.

The inner tracker charge offers a handle to distinguish interactions within the inner tracker. It is computed based on the Y charges in the inner tracker layers using a truncated mean algorithm, ignoring the highest outliers. The wrong reconstructed sample tends to have a larger inner tracker charge, as shown in Fig. 4.4.

5. **Tracker track goodness-of-fit in X-Z orientation &**
6. **Tracker track goodness-of-fit in Y-Z orientation**

The logarithms of the track fit χ^2 in X-Z and Y-Z projection enter the MVA as input quantities. It is expected that the wrong charge sign sample has a tendency to larger χ^2 values as the correct charge sign sample, which offers separation power for the MVA.

Figure 4.5 shows the LogTrkChi2X and LogTrkChi2Y distribution in an example energy bin for both the correct and wrong rigidity sample in the electron Monte-Carlo simulation.

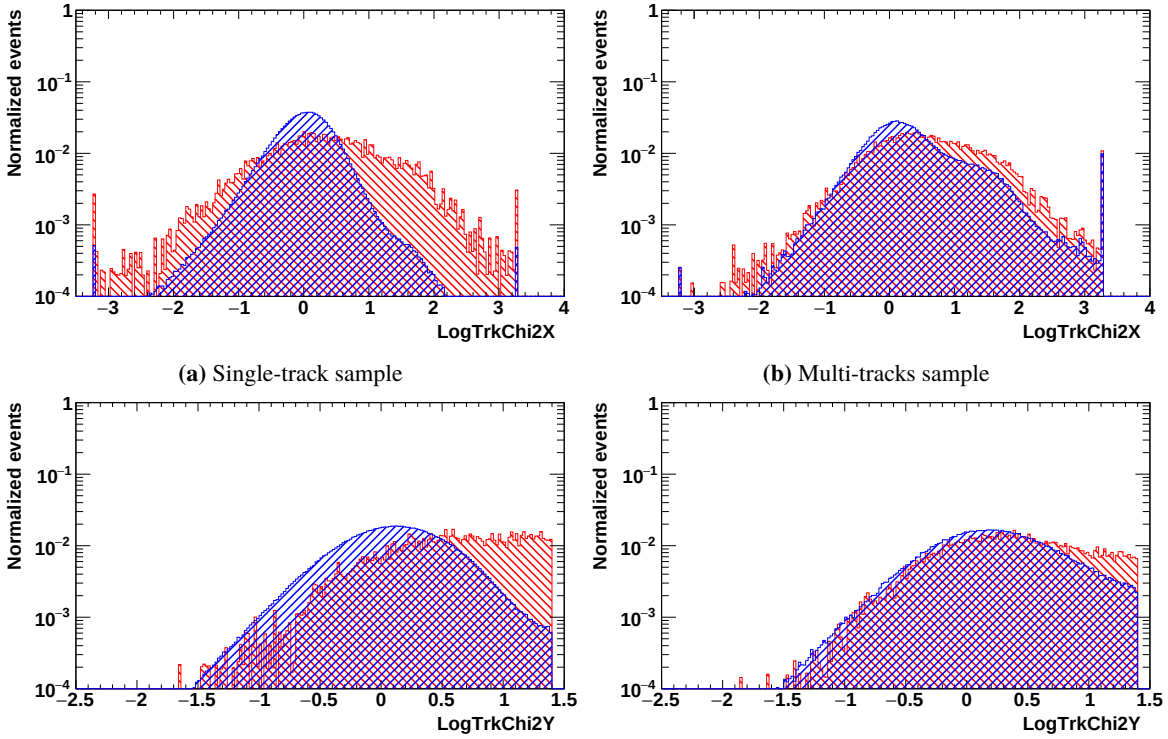

(a) Single-track sample

(b) Multi-tracks sample

(c) Single-track sample

(d) Multi-tracks sample

Figure 4.5: Example of LogTrkChi2X / LogTrkChi2Y distribution in the energy bin 17.98 – 18.99 GeV in the electron Monte-Carlo simulation. The red histogram shows the charge-confused sample (R > 0) and the blue histogram the correct reconstructed sample (R < 0), after applying all preselection, selection and $e^{\pm}$ identification cuts.

The three most important input variables for the example energy bin 17.98 – 18.99 GeV out of the six relevant for the multi-tracks sample are presented in the following - the remaining three variables are described in Appendix A.2.

7. **Primary over sum of other rigidities**

The logarithm of the ratio between the primary rigidity of the selected tracker track R_{primary} and the reconstructed rigidities R_i - associated with the secondary tracker tracks i - is defined as LogPrimaryRigidityOverOtherRigiditiesRatio:

$$\text{LogPrimaryRigidityOverOtherRigiditiesRatio} = \log\left(R_{\text{primary}} \Big/ \sum_{i=2}^{N} R_i\right)$$

Figure 4.6 shows the LogPrimaryRigidityOverOtherRigiditiesRatio distribution in an example energy bin for both the correct and wrong rigidity sample in the electron Monte-Carlo simulation.

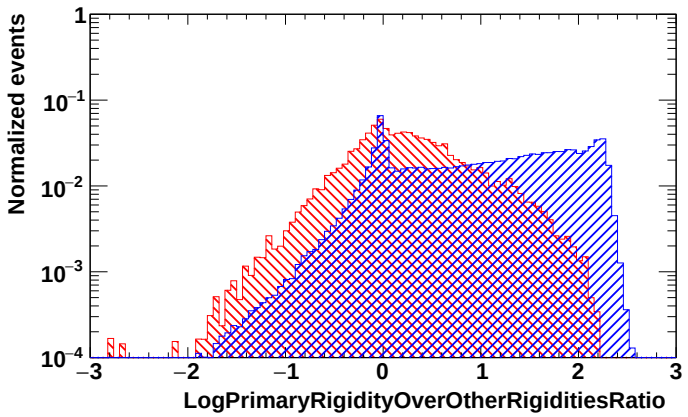

Figure 4.6: Example of LogPrimaryRigidityOverOtherRigiditiesRatio distribution in the energy bin 17.98 – 18.99 GeV in the electron Monte-Carlo simulation. The red histogram shows the charge-confused sample (R > 0) and the blue histogram the correct reconstructed sample (R < 0), after applying all preselection, selection and $e^{\pm}$ identification cuts.

8. **Tracker track bottom distance x-direction &**
9. **Tracker track bottom distance y-direction**

The primary tracker track is extrapolated to tracker layer 9 at $z = 113.55$ cm and the result is denoted as $x_{\text{bottom, primary}}$ / $y_{\text{bottom, primary}}$. The extrapolation is repeated for all other reconstructed tracker tracks in the event.

TrkMinDXBottom is then defined as as the minimum distance in x-direction between the primary tracker track and any of the secondary tracks at the tracker layer 9 position. TrkMinDYBottom refers to the y-coordinate in the bending plane:

$$\text{TrkMinDXTop} = \min_{i\,>\,1} \left|x_i - x_{\text{bottom, primary}}\right|$$
$$\text{TrkMinDYTop} = \min_{i\,>\,1} \left|y_i - y_{\text{bottom, primary}}\right|$$

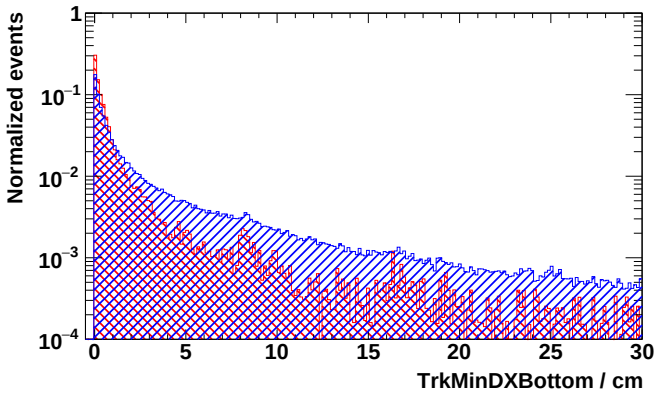

(a) TrkMinDXBottom: Multi-tracks sample

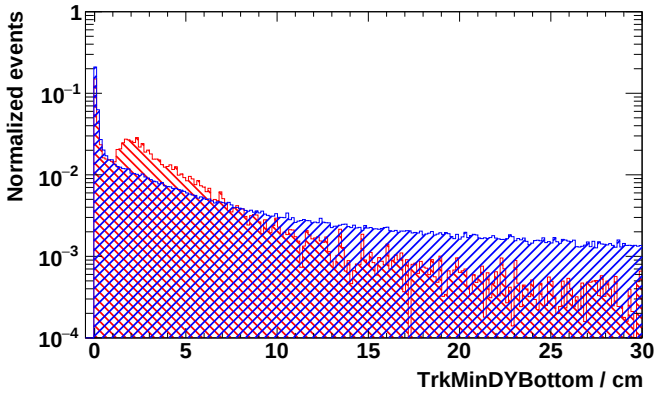

(b) TrkMinDYBottom: Multi-tracks sample

Figure 4.7: Example of TrkMinDXBottom / TrkMinDYBottom distributions in the energy bin 17.98 – 18.99 GeV in the electron Monte-Carlo simulation. The red histogram shows the charge-confused sample (R > 0) and the blue histogram the correct reconstructed sample (R < 0), after applying all preselection, selection and $e^{\pm}$ identification cuts.

Figure 4.7 shows the TrkMinDXBottom / TrkMinDYBottom distributions in an example energy bin for both the correct and wrong rigidity sample in the electron Monte-Carlo simulation.

The shape of the TrkMinDYBottom distribution is clearly different for the correct and wrong rigidity sample and offers a unique way to discriminate the two samples in the MVA. It offers the highest separation power of all observables in the multi-tracks sample.

In Appendix A.2, a comparison of all input variables between the electron and positron Monte-Carlo simulation can be found. There are no charge-sign dependent differences in the input quantities – by construction the same MVA is applicable to electrons and positrons. An electron with negative charge sign appears identical as a positron with positive charge sign, and vice-versa.

The CCMVA estimator Λ_{CC} is trained individually for each energy bin in the analysis using the aforementioned input variables on an electron Monte-Carlo simulation, using the TMVA [TMVA2007] package. Several classifier algorithms (Multi-Layer Perceptron, Fisher-Likelihood, etc.) were tested and the Boosted Decision Tree (BDT) [Roe2005] was selected for this analysis. The output shape is

gaussian like and suitable for a template fit. 300 individual decision trees were trained for each energy bin using an adaptive gradient boosting technique.

All preselection, selection and $e^{\pm}$ identification cuts - Sections 4.3.2 to 4.3.4 are applied on the electron Monte-Carlo simulation to prepare the training data sample.

If the reconstructed rigidity of the primary tracker track is negative it is classified as **"signal event"** otherwise as **"background event"**. This is the only distinction[6] to differentiate between the correct and wrong reconstructed rigidity sample. Furthermore the sample is split in two disjoint categories: the **"single-track sample"** (TrkNumTracks = 1) and the **"multi-tracks sample"** (TrkNumTracks > 1). The training is applied individually for each energy bin and each of the tracker pattern samples. Overtraining checks were performed, to ensure that the MVA is unbiased.

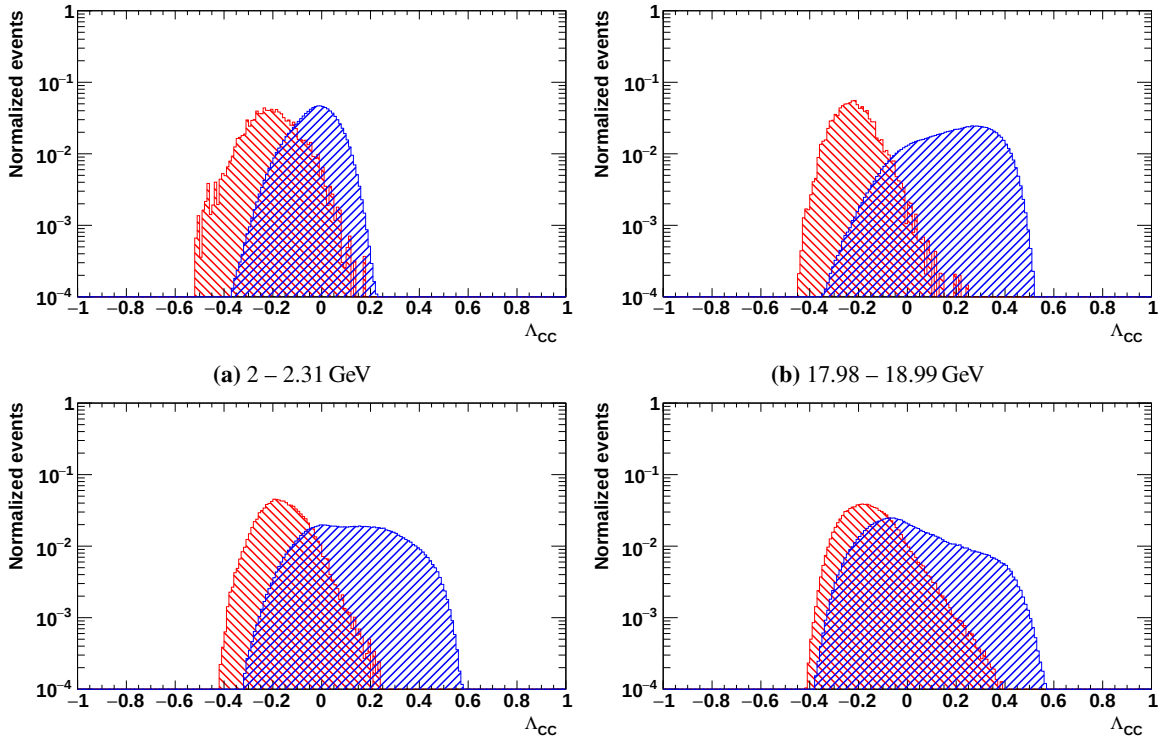

(a) 2 – 2.31 GeV

(b) 17.98 – 18.99 GeV

(c) 197.69 – 237.16 GeV

(d) 700 GeV – 1 TeV

Figure 4.8: Overview of the CCMVA estimator in the single-track sample in four different energy intervals, from low energies to the highest energy in this analysis. The red histogram shows the charge-confused sample (R > 0) and the blue histogram the correct reconstructed sample (R < 0), after applying all preselection, selection and $e^{\pm}$ identification cuts.

[6] Other definitions were tested, such as requiring the reconstructed rigidity to be compatible with the generated energy of the particle within the four times the rigidity resolution. The rejection power of the so-obtained MVA did not improve or change, compared to the simple definition, by only using the rigidity sign to discriminate signal / background events.

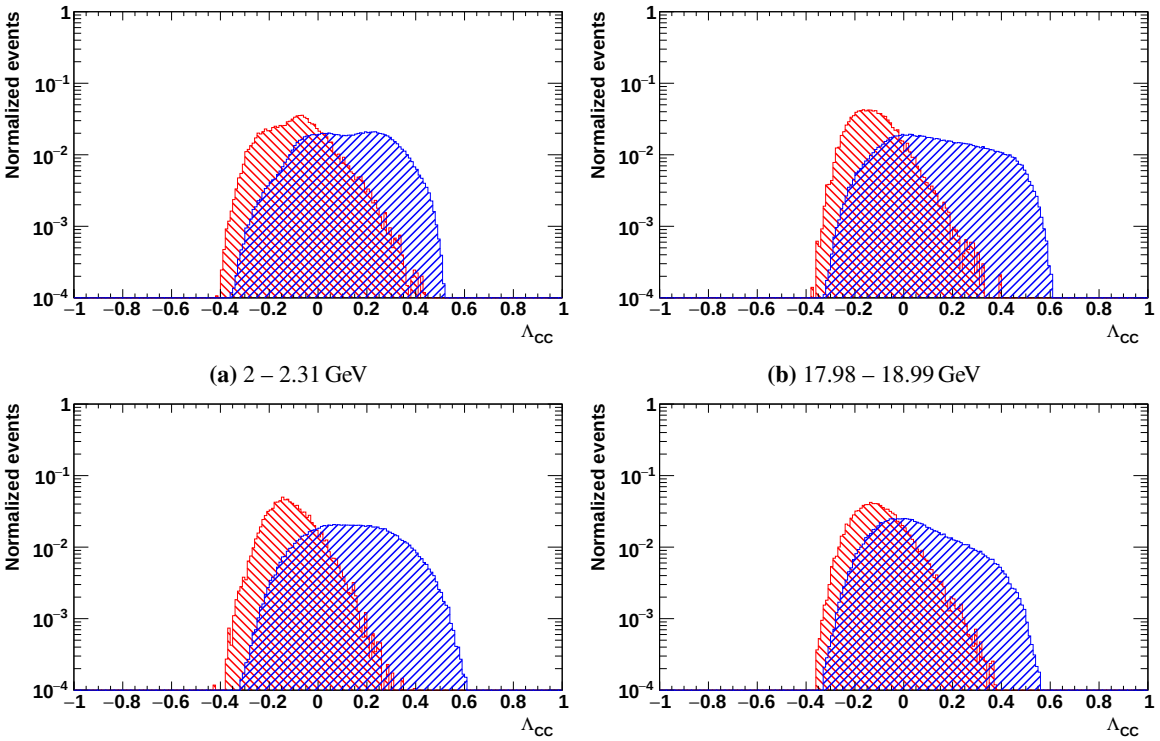

(a) 2 – 2.31 GeV

(b) 17.98 – 18.99 GeV

(c) 197.69 – 237.16 GeV

(d) 700 GeV – 1 TeV

Figure 4.9: Overview of the CCMVA estimator in the multi-tracks sample in four different energy intervals, from low energies to the highest energy in this analysis.

Figure 4.8 shows the CCMVA estimator in four example energy bins for the single-track sample. Figure 4.9 shows the same energy bins for the multi-tracks sample. It is evident that the constructed CCMVA estimator Λ_{CC} can be used to discriminate the correct and wrong charge samples.

The shapes are suitable for template fits, which allows one to extract the magnitude of the charge-confusion effect directly on ISS data, when applying the MVA estimator to an electron sample on ISS data. This will be shown later in Section 4.4.5.

To characterize the performance of the CCMVA estimator, Receiver Operating Characteristic (ROC) curves are computed for all energy bins. A ROC curve is a plot of the background rejection as function of the signal efficiency. On the electron Monte-Carlo simulation two histograms are filled for each energy bin, separately for the single-track and the multi-tracks sample with the MVA estimator output for the positive rigidity sample ("background sample") and the negative rigidity sample ("signal sample"), respectively.

The signal efficiency ϵ_{signal} is scanned from 0 – 100 % to produce the ROC curve. A cut value x_{cut}, is chosen corresponding to the given signal efficiency ϵ_{signal}. The number of signal/background events for a given cut value x_{cut} can be computed by integrating the signal/background histograms:

$$N_{\text{sig}} = \int_{x_{\text{cut}}}^{\infty} H_{\text{sig}}(x)\,\mathrm{d}x = \epsilon_{\text{signal}} \int_{-\infty}^{\infty} H_{\text{sig}}(x)\,\mathrm{d}x; \qquad N_{\text{bkg}} = \int_{x_{\text{cut}}}^{\infty} H_{\text{bkg}}(x)\,\mathrm{d}x. \tag{4.3}$$

The signal/background efficiency is defined as N_{sig} / N_{bkg} divided by all events in the signal/background histogram.

After repeating the procedure for all possible values of ϵ_{signal} the ROC curve can be computed, as shown in Fig. 4.10 for an example energy bin. The rejection power for the single-track MVA is intrinsically higher than for the multi-tracks MVA estimator.

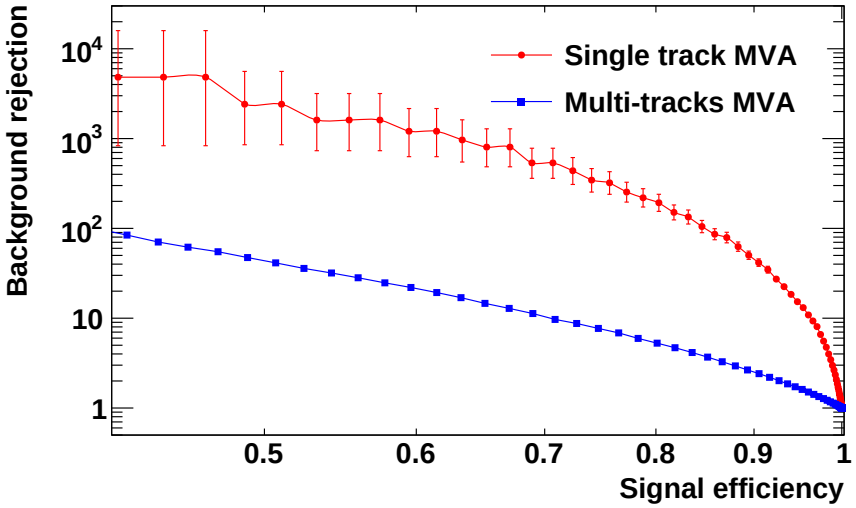

Figure 4.10: ROC curve of the CCMVA estimator in the energy bin 17.98 – 18.99 GeV. The red curve represents the ROC curve for the single-track sample and the blue curve represents the multi-tracks sample.

The ROC curves for all energy bins are evaluated at a fixed signal efficiency of 70 % and the result is aggregated in a graph (Fig. 4.11). For both the single-track sample and the multi-tracks sample the CCMVA estimator offers a good background rejection power.

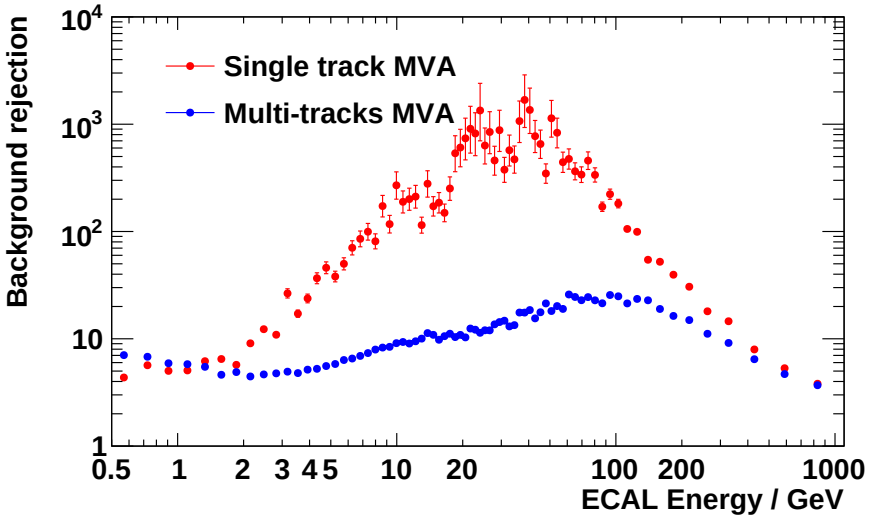

Figure 4.11: Rejection of the CCMVA estimator as function of energy. The background rejection exceeds 10^2 in the energy range 10 – 100 GeV, when choosing a fixed signal efficiency of 70 %.

The CCMVA estimator performs best at intermediate energies between 10 – 100 GeV. At high energies, when approaching Maximum Detectable Rigidity (MDR), the intrinsic charge-confusion due to the finite resolution of the silicon tracker is unavoidable. Thus the rejection power decreases towards high energies. At low energies multiple scattering leads to an unavoidable amount of charge-confusion, also reducing the rejection power. The shape of the CCMVA rejection curve follows the expectation from first principles.

4.3 Data selection criteria

For the electron and positron analysis, the overwhelming proton background in cosmic rays has to be suppressed as much as possible. AMS-02 is equipped with several subdetectors to fulfill the task, most importantly the TRD (Section 3.4), the ECAL (Section 3.5) and the tracker (Section 3.2).

As first step in the analysis flow, the **detector quality cuts** are applied, ensuring that only seconds are analyzed, in which the detector is in nominal data-taking condition, as discussed in Section 4.3.1. Afterwards the **preselection cuts** and **selection cuts** are applied, presented in Sections 4.3.2 and 4.3.3 This leaves a data sample where all events are guaranteed to be primary cosmic rays: events, whose reconstructed energy is above the geomagnetic cut-off. As last step the $\boldsymbol{e^{\pm}}$ **identification cuts** - discussed in Section 4.3.4 - are applied, which reduce the proton background and select a sample enhanced by $e^{\pm}$.

4.3.1 Detector quality cuts

All time intervals are excluded in which the detector is in a known, non-nominal condition, e.g. during TRD gas refills or when certain detectors are not calibrated. The **detector quality cuts** are evaluated for each second of ISS data. Only if all cuts pass for a given second, events recorded within that second are analyzed and contribute to the measuring time $T_i(E)$. The list of all cuts and their description is given in Appendix A.1.

In total 93.78 % of all seconds within the data taking period between **May 20$^{\text{th}}$, 2011** and **November 12$^{\text{th}}$, 2017** pass the detector quality cuts.

4.3.2 Preselection cuts

As next step in the analysis flow, the **preselection cuts** are applied. These cuts ensure that a signal is present in all subdetectors required for the electron and positron analysis and that all measurements referring to the primary particle, as defined in Section 4.2.5, are consistent. The cuts are not $e^{\pm}$ specific and must have a signal selection efficiency close to unity. An example of the signal[7] efficiency ϵ_{sig} determined from the electron Monte-Carlo simulation at a fixed energy of 20 GeV is given for each cut, and an example of the background efficiency ϵ_{bkg} determined from the proton Monte-Carlo simulation.

1. **At least one ECAL shower, within fiducial volume** (ϵ_{sig} = 99.39 %; ϵ_{bkg} = 69.67 %)
   As the ECAL provides the energy scale for the $e^{\pm}$ flux measurement, it is required that at least one shower is present in the calorimeter. The efficiency for this requirement is close to unity, if

[7] The trajectory of the particle is required to pass through the TRD, the TOF, the inner tracker and the ECAL.

the particle traversing AMS-02 is leptonic, passes within the ECAL acceptance and has at least 500 MeV of energy. Furthermore it is required that the centre-of-gravity of the reconstructed shower is at least 1.3 Molière radii away from the borders of the ECAL, to ensure that only a small amount of energy may leak out of the fiducial volume of the ECAL.

2. **At least one useful TRD track** ($\epsilon_{\text{sig}} = 98.01\,\%$; $\epsilon_{\text{bkg}} = 88.87\,\%$)
   In order to discriminate light from heavy particles such as protons and ions the TRD is a necessary subdetector for the $e^{\pm}$ flux analysis. Thus it is required that each event in the analysis, contains a reconstructed TRD track, whose direction is compatible with the reconstructed ECAL shower axis. This refines the selection criteria, described in the TRD track reconstruction (Section 4.2.3), to take into account not only the spatial difference between the ECAL shower centre-of-gravity and the extrapolated TRD track, but also the direction, with respect to the ECAL shower axis.

3. **At least one useful TOF cluster combination** ($\epsilon_{\text{sig}} = 99.36\,\%$; $\epsilon_{\text{bkg}} = 97.86\,\%$)
   The TOF serves as trigger for all charged-particles within AMS-02. It is a crucial subdetector for the $e^{\pm}$ flux analysis, providing the direction of the trajectory of the incident particle (up- or down-going). For the $e^{\pm}$ flux measurement only particles coming from the top are considered and all others are rejected.

   Thus it is required that at least three out of the four TOF bars recorded a signal and the reconstructed incident direction is down-going. The time difference between the traversal of the upper and lower TOF bars has to be compatible with a relativistic electron or positron.

   Furthermore the previously selected TRD track is matched with all reconstructed TOF clusters (Section 4.2.1), to ensure that the correct TOF cluster combination was selected in the particle reconstruction (Section 4.2.5).

4. **Highest energetic ECAL shower was selected** ($\epsilon_{\text{sig}} = 99.98\,\%$; $\epsilon_{\text{bkg}} = 91.93\,\%$)
   Ensure that the particle reconstruction algorithm (Section 4.2.5) selected the ECAL shower containing the highest energy. If not, the primary particle definition is inconsistent and the event needs to be rejected.

5. **Not in ISS solar array shadow**
   If a tracker track was reconstructed in the event, it must not point to the ISS solar arrays. When solar arrays are in the field of view of AMS, primary particles entering the solar arrays might produce secondary particles, which have to be rejected for the $e^{\pm}$ flux analysis.

In total 96.84 %[8] of all signal events in the electron Monte-Carlo simulation survive the preselection cuts and only 70.62 % of all background events in the proton Monte-Carlo simulation.

4.3.3 Selection cuts

Only events which contain an ECAL shower, a compatible TRD track, matched with the TOF clusters survive the preselection. The next step is to apply selection cuts, which specifically target a leptonic $Z = 1$ selection, reducing the background as much as possible, while keeping a high signal efficiency.

[8] This is not the product of all individual signal efficiencies, as that would neglect correlations. Instead the number of passed events is determined after all preselection cuts passed.

1. **TOF velocity measurement** (ϵ_{sig} = 99.85 %; ϵ_{bkg} = 99.66 %)
   The measured velocity needs to be larger than 0.8 c, to reject slow protons/ions. For the energies considered in this analysis, all leptonic particles have a velocity close to 1 c, as shown in Fig. 4.12. The reconstructed TOF β measurement does not exhibit an energy dependence, thus the cut value distribution is shown for the whole energy range of the analysis: 0.5 – 1,000 GeV.

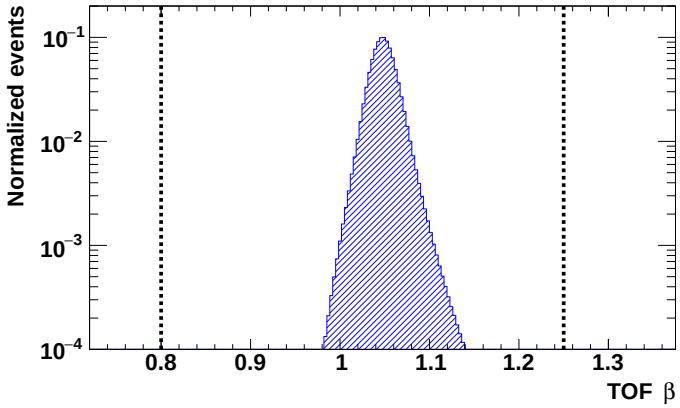

Figure 4.12: Plot of the TOF velocity β in the energy range 0.5 – 1,000 GeV for the electron Monte-Carlo simulation. The applied lower and upper cut values are shown as black dashed lines. The chosen cut values are loose: all signal events are kept and only a few slow protons/ions at low energies are rejected.

2. **Upper TOF charge** (ϵ_{sig} = 93.73 %; ϵ_{bkg} = 97.42 %)
   The charge reconstructed in the upper TOF bars must not exceed 2 e. The loose charge requirement is connected to the nature of electrons and positrons which lose energy when traversing AMS-02 by emission of bremsstrahlung photons along the trajectory due to the magnetic field. These photons can convert into additional e^- / e^+ pairs in the detector material, for example in the upper TOF bars. When three particles - the primary electron or positron and an additional electron and positron pair - traverse a single TOF bar, the charge measurement will yield Z ≈ 1.7 e, as shown in Fig. 4.13.

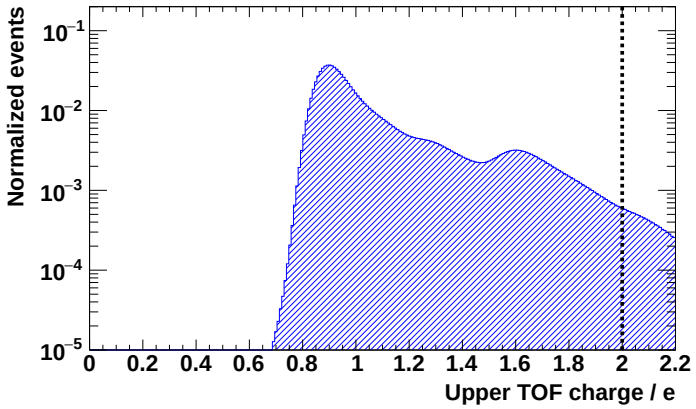

Figure 4.13: Plot of the charge measurement in the upper TOF in the energy range 0.5 – 1,000 GeV for the electron Monte-Carlo simulation. The applied upper cut value is shown as black dashed line.

The reconstructed upper TOF charge measurement does not exhibit an energy dependence, thus the cut value distribution is shown for the whole energy range of the analysis: 0.5 – 1,000 GeV.

3. **Enough active layers in TRD** (ϵ_{sig} = 89.82 %; ϵ_{bkg} = 87.58 %)
   When a non-interacting particle traverses the TRD, a large number of TRD layers (on average > 18 out of 20) have recorded an energy deposition in the straw tubes. A cut requiring at least 16 active TRD layers is applied[9], as shown in Fig. 4.14.

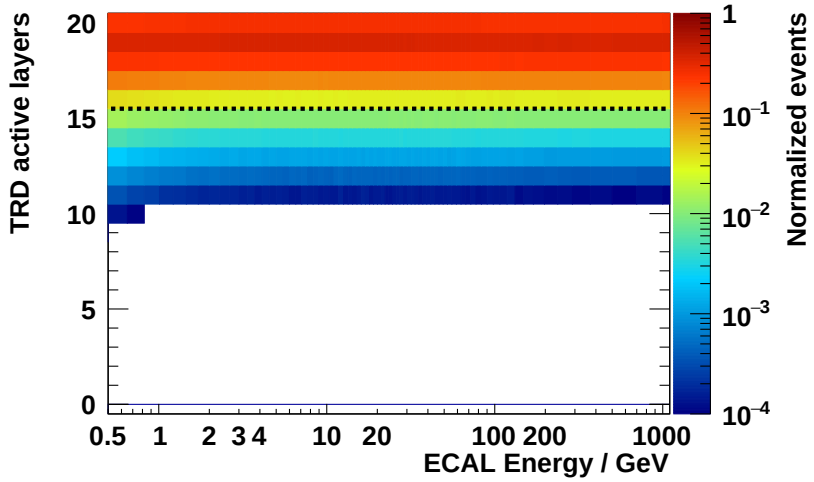

Figure 4.14: Plot of the active layers in the TRD as function of energy for the electron Monte-Carlo simulation. The applied lower cut value is shown as black dashed line.

4. **TRD helium rejection** (ϵ_{sig} = 96.64 %; ϵ_{bkg} = 70.96 %)
   The dE/dx measurements from all active straw tubes are combined into a single likelihood estimator $\mathcal{L}_{e^-/\text{He}}$, which can be used to check the hypothesis whether the particle traversing the TRD is helium like or $e^{\pm}$ like.

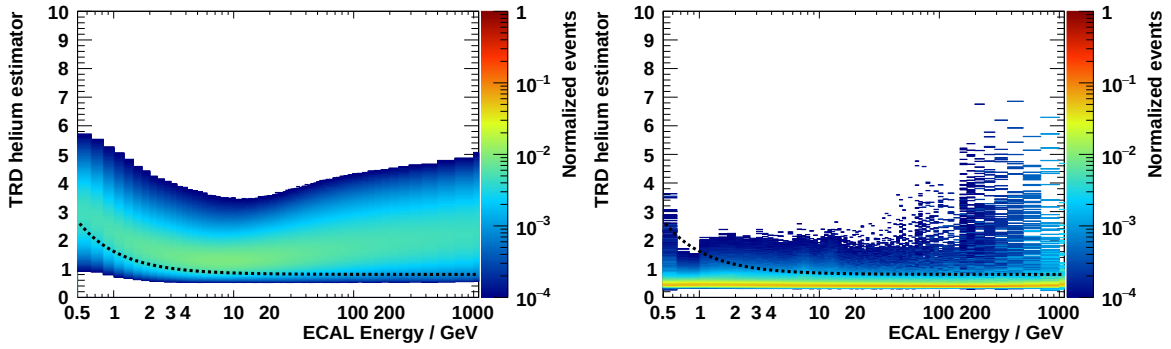

(a) Electron Monte-Carlo

(b) ISS Helium sample

Figure 4.15: Plot of the TRD likelihood estimator $\mathcal{L}_{e^-/\text{He}}$ as function of energy for the electron Monte-Carlo simulation (left) and the ISS Helium sample (right). The applied lower cut value is shown as black dashed line.

[9] The energy-dependence of the TRD active layers cut is flat because of the use of **hybrid hits**, as explained in Section 4.2.6. When using only the tracker to determine the path length, the efficiency for this cut would decrease to lower energies.

Figure 4.15(b) shows that the energy dependent lower cut value removes most of the helium background events, while keeping the majority of all signal events, as shown in Fig. 4.15(a).

The chosen cut value rejects a non-negligible amount of signal events below ≈ 10 GeV. A tight cut is necessary to reach a sufficient helium rejection, which was determined in a dedicated study.

5. **Tracker hit pattern** (ϵ_{sig} = 86.80 %; ϵ_{bkg} = 85.70 %)
   This analysis requires the tracker track to be well reconstructed in order to have a reliable charge-sign measurement, allowing to separate electrons from positrons. It is requested that at least one tracker track is reconstructed within the cone defined by the TRD track and the ECAL shower axis, with a certain number of tracker layers that have a signal. Besides the inner tracker (layer 3 or 4, layer 5 or 6, layer 7 or 8), there must be at least a hit in the layer 1, layer 9 or layer 2 in order to accept the event for further analysis.

   The maximum detectable rigidity for a so-called full-span event (layer 1 + 2 + 9 + inner tracker) is ≈ 1.2 TeV for $e^{\pm}$. All other classes have a smaller MDR and a higher probability of misreconstructing the charge-sign. The allowed classes for this analysis, were chosen in order to maximize the signal efficiency, while keeping the misidentification probability under a tolerable level - which will be discussed in detail in later sections of this thesis (Section 4.4.5).

6. **Inner tracker charge** (ϵ_{sig} = 99.99 %; ϵ_{bkg} = 99.99 %)
   The charge measurements from all inner tracker layers are combined into a single charge measurement, by using a truncated mean, in order to remove outliers. A loose cut 0.5 e < Z <1.8 e is applied, to keep the three particle events (Z ≈ 1.7 e), as shown in Fig. 4.16(a), while removing the majority of the helium background events, as shown in Fig. 4.16(b).

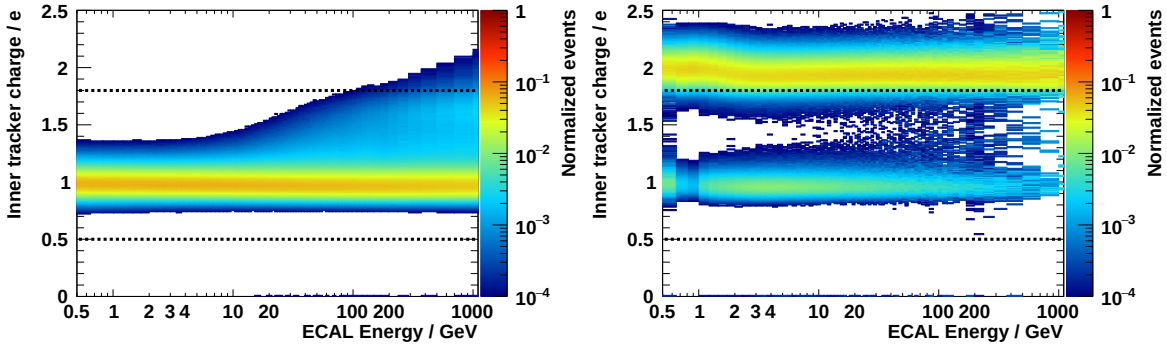

(a) Electron Monte-Carlo

(b) ISS R > 0 sample

Figure 4.16: Plot of the charge measurement in the inner tracker as function of energy for the electron Monte-Carlo simulation (left) and the ISS R > 0 sample (right). The applied lower and upper cut values are shown as black dashed lines.

7. **Tracker track goodness-of-fit in Y-projection** (ϵ_{sig} = 95.98 %; ϵ_{bkg} = 98.10 %)
   A cut is applied on the tracker track goodness-of-fit χ^2_y estimator. From the track fit procedure a χ^2 can be computed, describing the goodness-of-fit in the bending plane. This quantity is connected with charge-confusion. The higher the χ^2 value, the more likely a misreconstructed charge sign.

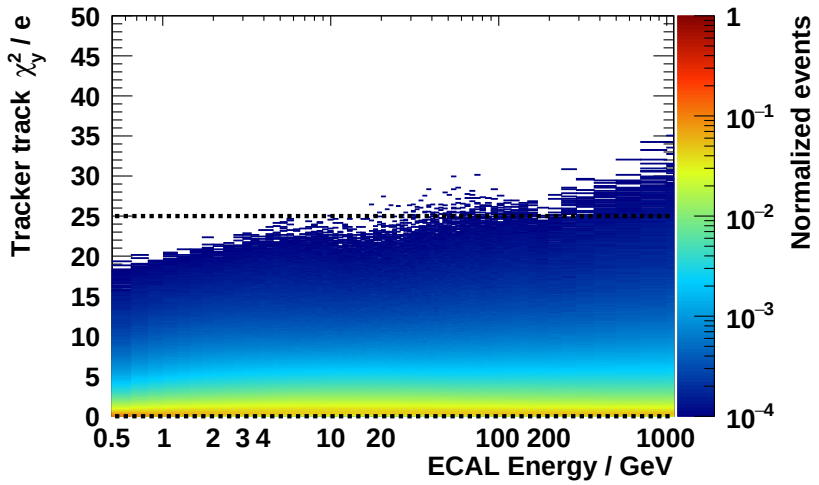

Figure 4.17: Plot of the tracker track goodness-of-fit χ^2_y as function of energy for the electron Monte-Carlo simulation. The applied lower and upper cut values are shown as black dashed lines.

As compromise between high signal efficiency and a tolerable charge-confusion a cut value of $\chi^2_y < 20$ was chosen, as shown in Fig. 4.17.

8. **Energy above geomagnetic cut-off**
   As last step in the selection, the energy reconstructed by the ECAL is required to be larger than 1.2 times the geomagnetic cut-off rigidity, computed in the current geomagnetic location AMS-02. The procedure is described in detail in Section 4.5.3.

In total 67.78 % of all signal events in the electron Monte-Carlo simulation survive the selection cuts and only 71.53 % of all background events in the proton Monte-Carlo simulation.

4.3.4 Electron and positron identification cuts

All events passing the selection contain measurements in all subdetectors relevant for the $e^{\pm}$ flux analysis. No cuts have been applied to reduce the proton background, except the presence of an ECAL shower, which remove protons that pass the ECAL as MIPs (Section 4.2.7). As next step specific cuts can be applied that further suppress the proton background.

1. **Energy ↔ rigidity matching** (ϵ_{sig} = 94.27 %; ϵ_{bkg} = 13.94 %)
   The ratio of the measured energy in the calorimeter and the momentum measured by the tracker is required to fulfill: $0.5 < E/|R| < 10$. Leptons up to the TeV regime release all their kinetic energy in the calorimeter. When the tracker rigidity is correctly reconstructed, $e^{\pm}$ peak at E/R values of ≈ 1, or larger, when the rigidity is underestimated, due to bremsstrahlung loss or interactions in the detector.

   The lower cut value of 0.5 thus removes proton events, which deposited only parts of their energy in the calorimeter, as shown in Fig. 4.18(b), while keeping as much signal events as possible (Fig. 4.18(a)).

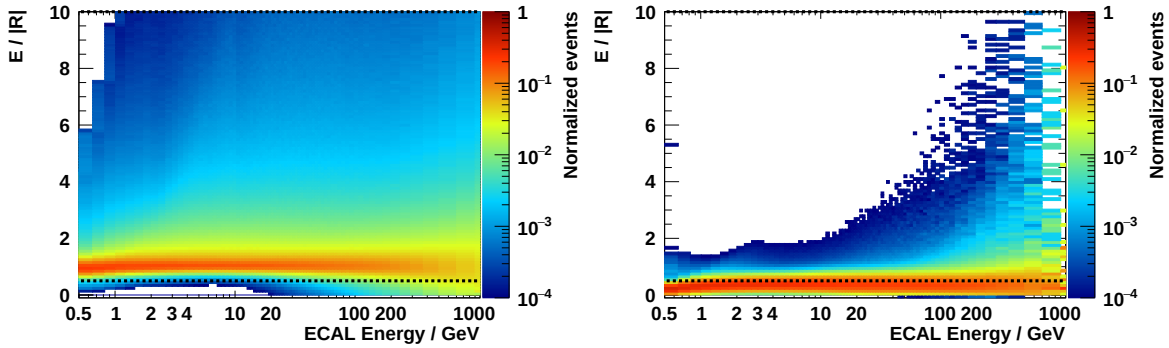

(a) Electron Monte-Carlo **(b)** ISS R > 0 sample

Figure 4.18: Plot of the $E/|R|$ distribution as function of energy for the electron Monte-Carlo simulation (left) and the ISS R > 0 sample (right). The applied lower and upper cut values are shown as black dashed lines.

Protons need to create π^0 in the ECAL which further decay into photons, in order to release a large amount of energy in the electromagnetic calorimeter. Most protons traverse the calorimeter losing only a small fraction of their energy via ionization losses.

The upper cut value of 10 was chosen to maximize statistics, while keeping the charge-confusion under a tolerable level. The higher the E/R value for $e^{\pm}$, the more probable it becomes that the rigidity sign is misreconstructed.

2. **ECAL lateral shower shape** ($\epsilon_{\text{sig/bkg}} = 100.00\,\%$)
   The lateral shower shape is a powerful tool to discriminate between hadronic and leptonic showers. Hadronic showers are wider and less concentrated than electromagnetic showers in the calorimeter and exhibit a more irregular shape.

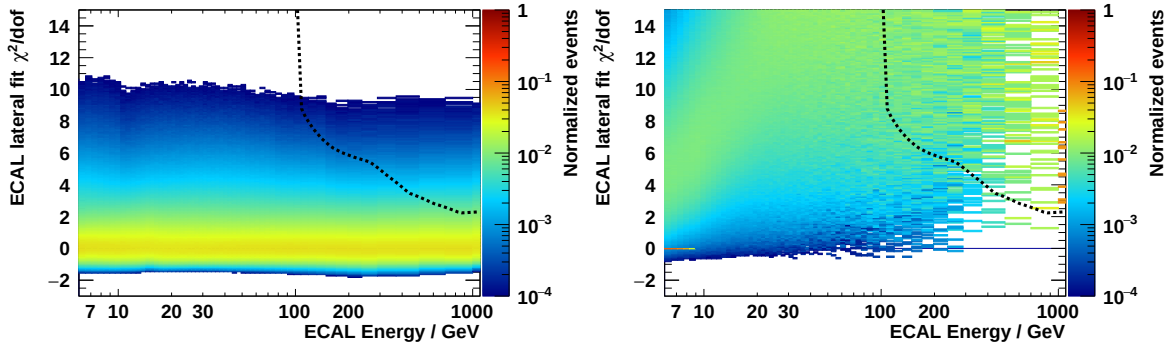

(a) Electron Monte-Carlo **(b)** ISS R > 0 sample

Figure 4.19: Plot of the ECAL lateral goodness-of-fit distribution as function of energy for the electron Monte-Carlo simulation (left) and the ISS R > 0 sample (right). The applied upper cut value is shown as black dashed line.

A lateral shower fit is performed on the ECAL shower profile and an energy dependent cut is applied to reject proton events above $\approx 100\,\text{GeV}$, as shown in Fig. 4.19(a). The shape of the cut value was optimized to keep all signal events below 100 GeV and to reject as many

charge-confused protons as possible from the high-energy R < 0 sample. The R < 0 sample is used later on to define an optimal cut on the ECAL estimator to precisely control the proton and charge-confused proton background in the R > 0 and R < 0 sample, respectively. A soft cut on the lateral shower shape already removes many protons at high energy, as shown in Fig. 4.19(b).

3. **Tracker ↔ ECAL matching in X-projection** (ϵ_{sig} = 97.46 %; ϵ_{bkg} = 85.00 %) &
4. **Tracker ↔ ECAL matching in Y-projection** (ϵ_{sig} = 99.99 %; ϵ_{bkg} = 90.64 %)

   The tracker track is extrapolated to the Z position of the centre of gravity of the ECAL shower. Energy dependent cuts are applied on the ΔX/ΔY to ensure a good match between both detectors. While this is strictly not related to electron or positron identification, it is applied here to be able to define sensible cut values for a sample consisting of mostly $e^{\pm}$.

   The bands at |ΔX| = 8 cm are due to ambiguities in the tracker track reconstruction, as the X position is not precisely known due to the readout of the K side ladders (Section 3.2). For the ΔY sample only an upper cut is applied, as the tail towards large negative ΔY values is unavoidable, due to bremsstrahlung emission, which distorts the tracker track extrapolation. Note that for the positive rigidity sample the same cut is applied, but on −ΔY instead of ΔY.

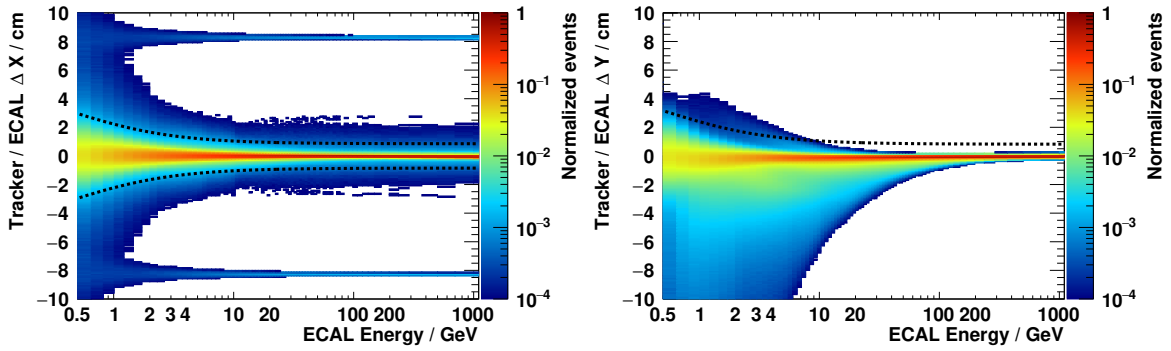

(a) Tracker ↔ ECAL - ΔX **(b)** Tracker ↔ ECAL - ΔY

Figure 4.20: Plot of the ΔX (left) and ΔY (right) between the tracker track extrapolation and the ECAL shower centre of gravity as function of energy for the electron Monte-Carlo simulation. The applied lower and upper cut values are shown as black dashed lines.

In total 91.92 % of all signal events in the electron Monte-Carlo simulation survive the $e^{\pm}$ identification cuts and only 10.29 % of all background events in the proton Monte-Carlo simulation.

After applying all aforementioned cuts a sample is left, which is enhanced by electrons and positrons and where many protons are removed. The last cut that is applied is the requirement of a **"physics trigger"**. The purpose of this cut and its implications will be discussed in Section 4.5.2.

The selection cuts already provide a factor ≈ 30 proton rejection - only every 30$^{\text{th}}$ proton passes the selection cuts. The proton background will be further reduced due to cuts on the ECAL shower shape, which will be described later in Section 4.5.1, since the ECAL shower shape cut is not part of the $e^{\pm}$ identification cuts, but treated separately.

In the following sections it will be shown how to extract the electron and positron counts as a function of kinetic energy and how the remaining proton background is treated.

4.4 Electron and positron counts

The main ingredient of a flux measurement is the number of particles in a given energy and time interval. After applying all cuts described in the last chapter an electron and positron enhanced sample is left, as illustrated in Fig. 4.21 for the energy range 20 – 50 GeV.

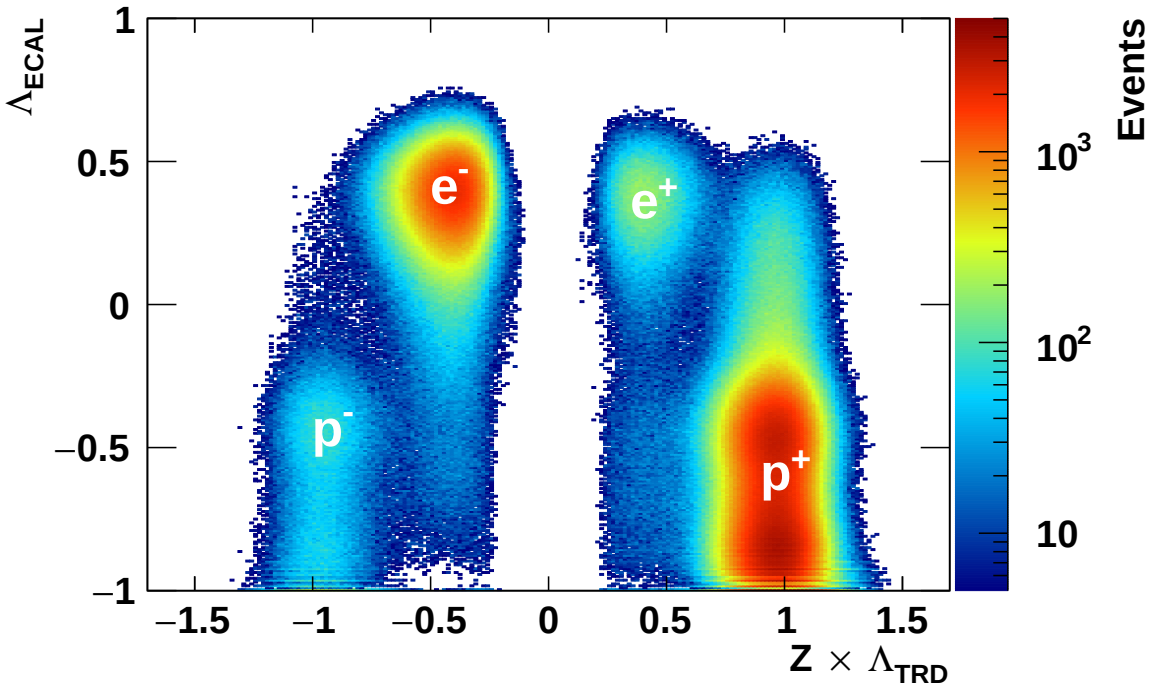

Figure 4.21: Overview of the ISS data sample after applying all selection cuts in the energy range 20 – 50 GeV. The ECAL estimator Λ_{ECAL} is drawn on the y-axis and the TRD estimator Λ_{TRD} multiplied by the charge sign Z of the primary tracker track on the x-axis. Clearly these two estimators allow to separate the different species: electrons, positrons, protons and charge-confused protons or antiprotons.

The data sample presented in Fig. 4.21 contains many background events that can be removed by imposing a cut on the ECAL estimator Λ_{ECAL}. A suitable cut value is chosen for each energy interval, as discussed in detail in Section 4.5.1.

The leftover data sample contains electrons, positrons and a reduced amount of protons and antiprotons. Depending on the energy, a non-negligible amount of charge-confused electrons, charge-confused positrons and charge-confused protons is also present in the data sample, which cannot be disentangled using neither the ECAL estimator, nor the TRD estimator. To separate charge-confused electrons and charge-confused positrons from nominal electrons and positrons, a multi-variate estimator - the CCMVA estimator Λ_{CC} was constructed, which was described in detail in Section 4.2.8.

Figure 4.22 shows the ($Z \times \Lambda_{TRD}$ - Λ_{CC}) plane for the same data sample as Fig. 4.21, after imposing a cut on the ECAL estimator Λ_{ECAL}. In this representation six components can be identified: electrons (e^-), charge-confused electrons ($e^- \rightarrow e^+$), positrons (e^+), charge-confused positrons ($e^+ \rightarrow e^-$), protons (p^+), antiprotons and charge-confused protons (p^-). Antiprotons and charge-confused protons are not differentiated, because the CCMVA estimator was not trained or designed to resolve the difference between antiprotons and charge-confused protons. For the electron and positron analysis

there is no need to resolve them, since both are background events. Furthermore the amount of charge-confused protons exceeds the amount of antiprotons, whose abundance is suppressed by a factor of $\approx 10^4$ in cosmic rays, compared to protons. Thus the amount of charge-confused protons is expected to be larger than the amount of antiprotons in the whole energy range in this analysis.

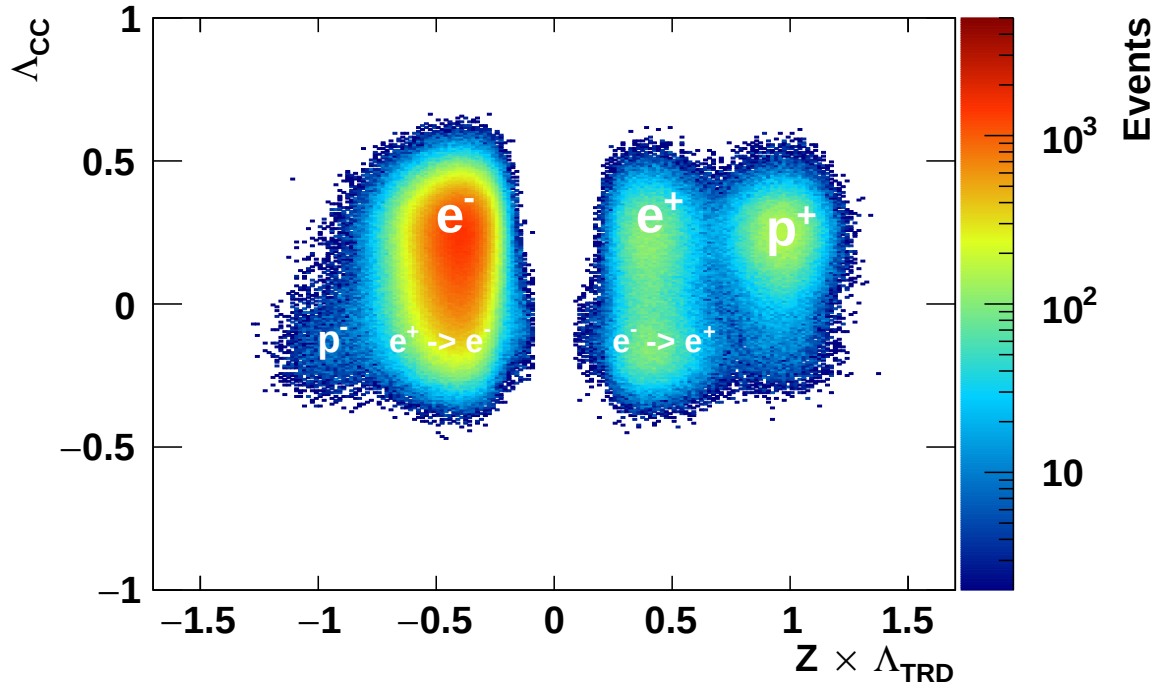

Figure 4.22: Overview of the ISS data sample after applying all selection cuts and an additional cut on the ECAL estimator Λ_{ECAL} to reduce the proton background in the energy range 20 – 50 GeV. The CCMVA estimator Λ_{CC} is drawn on the y-axis and the TRD estimator Λ_{TRD} multiplied by the charge sign Z of the primary tracker track on the x-axis. Clearly these two estimators allow to separate the different species: electrons, positrons, protons and their charge-confused counterparts.

The true number of electrons is equal to the number of electrons that were correctly reconstructed with a negative charge sign plus the electrons misreconstructed with positive charge sign (charge-confused electrons). Analogous, the true number of positrons is equal to the number of positrons that were correctly reconstructed with a positive charge sign plus the positrons misreconstructed with a negative charge sign (charge-confused positrons).

To extract the true number of electrons or positrons a two-dimensional template fit is performed in the ($Z \times \Lambda_{TRD}$ - Λ_{CC}) plane for a given energy and time interval, which will be described in detail in Section 4.4.5. To perform the template fit, reference distributions for all components (electrons, positrons, protons, and their charge-confused counterparts) need to be obtained for both the TRD estimator Λ_{TRD} and the CCMVA estimator Λ_{CC}.

In the following sections it will be presented how the TRD and CCMVA templates are obtained and how the two-dimensional template fit works in detail.

4.4.1 Binning

The electron and positron flux, as well as the positron fraction and the positron/electron ratio will be determined in 74 energy bins, from 0.5 GeV up to 1 TeV using the same binning as used in previous AMS-02 electron and positron flux publications [Aguilar2014a; Aguilar2019a; Aguilar2019b].

The binning is chosen according to the energy resolution σ_{ECAL} (Section 3.5): the bin width exceeds $3 \cdot \sigma_{\mathrm{ECAL}}$, to minimize migration effects. Above ≈ 100 GeV the criteria is relaxed and the bin width enlarged in order to have sufficient statistics in each high-energy analysis bin.

4.4.2 TRD templates

As shown in Fig. 4.21 the ECAL estimator, the TRD estimator and the charge sign of the reconstructed tracker track can be used to separate electrons, positrons, protons, charge-confused protons. To obtain reference distributions for the TRD estimator, pure data samples need to be selected using only the ECAL estimator and the charge sign of the reconstructed tracker track. The purity of these data samples decrease with increasing energy – the higher the energy, the more difficult it becomes to obtain a pure sample with decent statistics.

For example, the negative rigidity sample contains mostly electrons, but also a non-negligible amount of charge-confused protons. In order to extract a pure reference distribution for electrons one needs to take the charge-confused proton background into account and properly subtract it.

Three ISS data samples are prepared, in order to extract the reference distributions for the TRD estimator. All detector quality, preselection and selection cuts - Sections 4.3.1 to 4.3.3 - are applied when selecting the ISS data samples. Furthermore the same $0.5 < E/|R| < 1$ cut as for the signal event selection is applied. The following enumeration lists the sample specific cuts used to select the data samples, from which the TRD templates are extracted:

1. **Electron sample**
   - ISS data: negative rigidity sample (R < 0)
   - Electron like ECAL shower ($\Lambda_{\mathrm{ECAL}} > 0$)
   - Energy dependent cut on the lateral shape (defined in Section 4.3.4 - Item 2)
2. **Charge-confused proton sample**
   - ISS data: negative rigidity sample (R < 0)
   - Hadron-like ECAL shower ($\Lambda_{\mathrm{ECAL}} < 0$)
3. **Proton sample**
   - ISS data: positive rigidity sample (R > 0)
   - Hadron-like ECAL shower ($\Lambda_{\mathrm{ECAL}} < 0$)

It is important to note that the shape of the TRD estimator depends on the topology of the event. Events where only a single tracker track is reconstructed ("single-track sample") and events with multiple reconstructed tracker tracks ("multi-tracks sample") differ in the shape[10] of the TRD estimator. Therefore all template extraction procedures are executed separately for both orthogonal event samples.

[10] In multi-track events, the path length in the TRD tubes (dx) is defined less precisely than in the single-track sample, which alters the TRD estimator shape.

For both track samples, all reference distributions can be parameterized by a sum of analytical functions: a gaussian function $G(x;\mu,\sigma)$ and the Novosibirsk function $N(x;\mu,\sigma,\tau)$:

$$G(x;\mu,\sigma) = \frac{1}{\sqrt{2\pi\sigma^2}} \exp\left(-\frac{(x-\mu)^2}{2\sigma^2}\right), \tag{4.4}$$

$$\begin{aligned} N(x;\mu,\sigma,\tau) &= \exp\left(-\frac{1}{2}\left(\frac{(\ln(\lambda(x;\mu,\sigma,\tau)))^2}{\tau^2} + \tau^2\right)\right), \text{where} \\ \lambda(x;\mu,\sigma,\tau) &= 1 + \tau(x-\mu)\frac{\sinh\left(\tau\sqrt{\ln 4}\right)}{\sigma\tau\sqrt{\ln 4}}. \end{aligned} \tag{4.5}$$

The following enumeration shows the parameterizations that are used to describe the TRD templates analytically for each energy bin in the analysis:

1. **Electron template**

$$\begin{aligned} f_{\text{elec}}(x = \Lambda_{\text{TRD}}) = \alpha_{\text{elec, novo}} &\cdot N(x;\mu_{\text{elec, novo}},\sigma_{\text{elec, novo}},\tau_{\text{elec, novo}}) \\ + (1-\alpha_{\text{elec, novo}}) &\cdot G(x;\mu_{\text{elec, gaus}},\sigma_{\text{elec, gaus}}) \end{aligned} \tag{4.6}$$

2. **Charge-confused proton template**

$$f_{\text{ccprot}}(x = \Lambda_{\text{TRD}}) = N(x;\mu_{\text{ccprot, novo}},\sigma_{\text{ccprot, novo}},\tau_{\text{ccprot, novo}}) \tag{4.7}$$

3. **Proton template**

$$\begin{aligned} f_{\text{prot}}(x = \Lambda_{\text{TRD}}) = \alpha_{\text{prot, novo}} &\cdot N(x;\mu_{\text{prot, novo}},\sigma_{\text{prot, novo}},\tau_{\text{prot, novo}}) \\ + (1-\alpha_{\text{prot, novo}}) &\cdot G(x;\mu_{\text{prot, gaus}},\sigma_{\text{prot, gaus}}), \text{where} \\ \sigma_{\text{prot, gaus}} = \sigma_{\text{prot, novo}} + \delta_{\sigma\,\text{prot, gaus}}&\cdot \end{aligned} \tag{4.8}$$

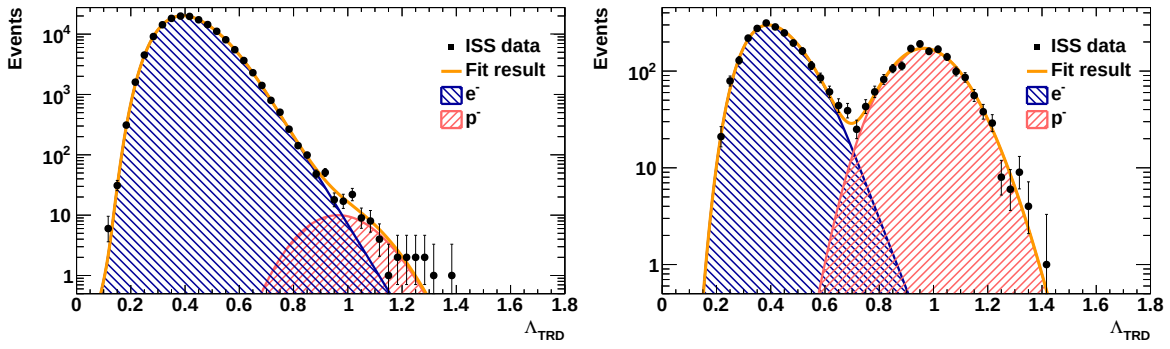

(a) Electron sample - single-track

(b) Charge-confused proton sample - single-track

Figure 4.23: Simultaneous fit of the electron template Eq. (4.6) and the charge-confused proton template Eq. (4.7) in the energy bin 17.98 – 18.99 GeV for the single-track sample. The dark blue area corresponds to the electron template, the light red area to the charge-confused proton template and the orange line to the sum of all templates.

For each energy bin a maximum likelihood fit is performed, simultaneously on the "Electron sample" and the "Charge-confused proton sample", to determine the parameters that describe the electron template - Eq. (4.6) - and the charge-confused proton template - Eq. (4.7).

Figures 4.23 and 4.24 show an example of the fit procedure for the single-track sample and the multi-tracks sample, respectively, for an example energy bin. It is evident that the charge-confused proton component is enlarged in the multi-tracks sample and thus it is important to extract the TRD templates separately for the single-track and multi-tracks sample.

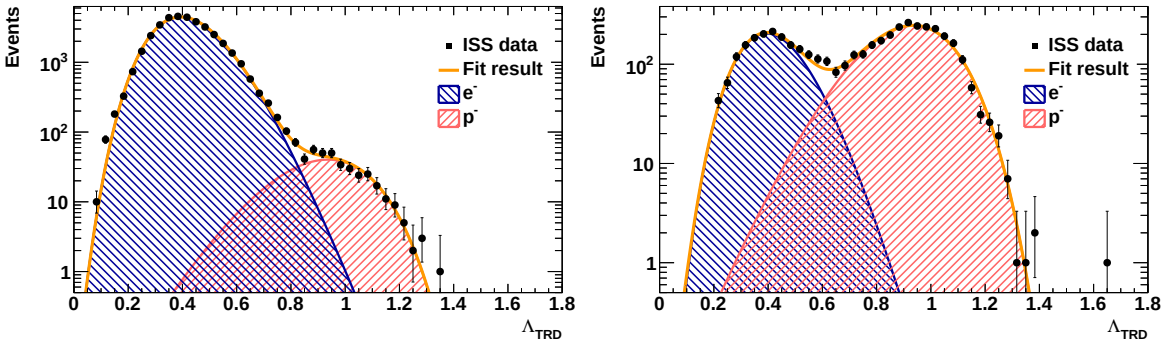

(a) Electron sample - multi-tracks

(b) Charge-confused proton sample - multi-tracks

Figure 4.24: Simultaneous fit of the electron template Eq. (4.6) and the charge-confused proton template Eq. (4.7) in the energy bin 17.98 – 18.99 GeV for the multi-tracks sample. The dark blue area corresponds to the electron template, the light red area to the charge-confused proton template and the orange line to the sum of all templates.

Once the electron template is known, the positron template necessary to describe the positrons in the positive rigidity sample, is known as well, since they are indistinguishable by the TRD and share the same template. Therefore the proton template - Eq. (4.8), can be extracted, using a maximum likelihood fit on the "Proton sample", as shown in Fig. 4.25(a) for the single-track sample and in Fig. 4.25(b) for the multi-tracks sample for an example energy bin.

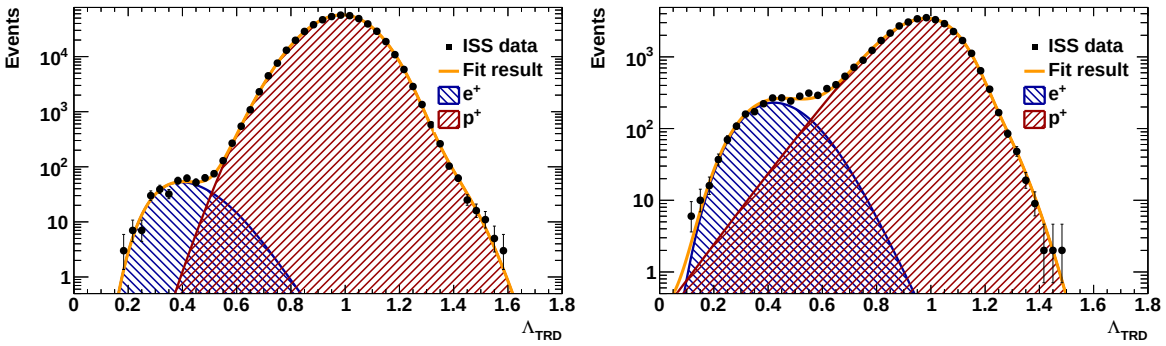

(a) Single-track sample

(b) Multi-tracks sample

Figure 4.25: Fit of the proton template Eq. (4.8) in the energy bin 17.98 – 18.99 GeV for the single-track sample and the multi-tracks sample. The dark blue area corresponds to the electron template, the light red area to the charge-confused proton template and the orange line to the sum of all templates.

The template extraction procedure is repeated independently for all energy bins in the analysis, yielding a list of parameters for each energy bin and each template component. The energy dependence of each of the parameters can be parameterized by a smooth function: a spline [Birkhoff1960].

Figure 4.26 shows the charge-confused proton template parameters as function of energy for the single-track sample and Fig. A.17 for the multi-tracks sample.

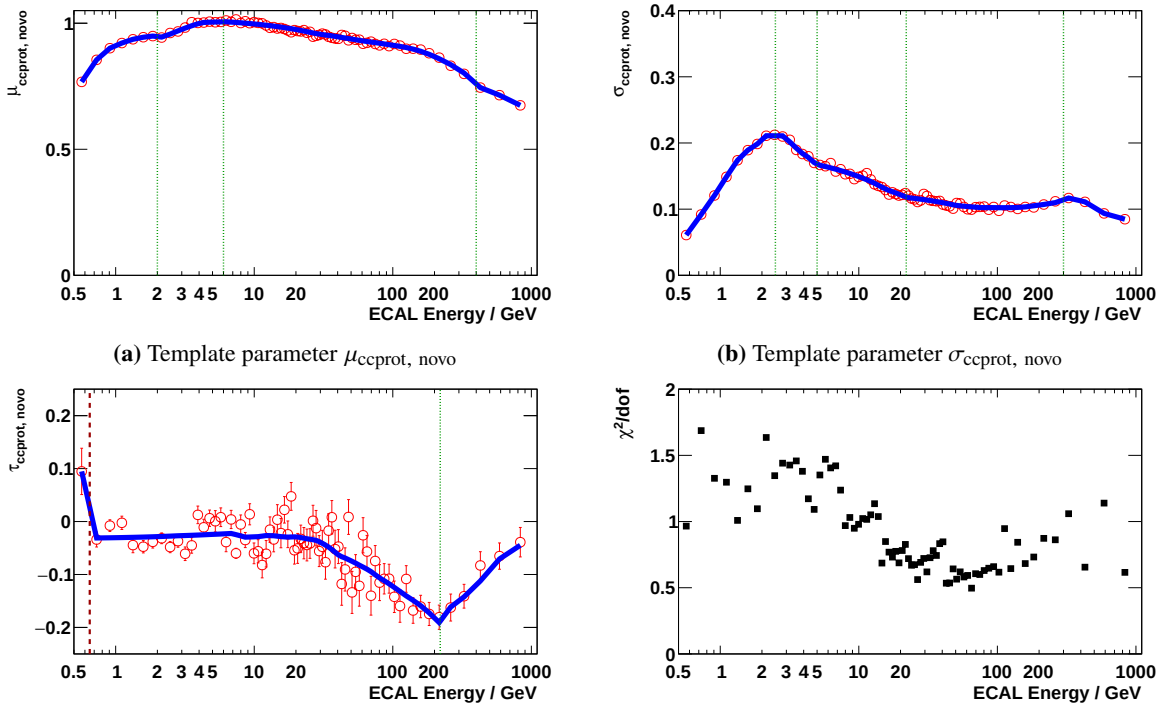

(a) Template parameter $\mu_{\text{ccprot, novo}}$

(b) Template parameter $\sigma_{\text{ccprot, novo}}$

(c) Template parameter $\tau_{\text{ccprot, novo}}$

(d) Goodness-of-fit

Figure 4.26: Analytical TRD template parameters describing the evolution of the charge-confused proton template as function of energy for the single-track sample. In each energy bin the analytical function - Eq. (4.7) - is fit to the template data sample, yielding the red points. A smoothing procedure yields the blue curves, which are used as template parameters for the analysis. The vertical dashed green lines mark areas where different isolated smoothing procedures are applied. The goodness-of-fit is indicated by the black points in the lower right plot.

Only three parameters are necessary to describe the template analytically for all energies: the peak position $\mu_{\text{ccprot, novo}}$, the width $\sigma_{\text{ccprot, novo}}$ and the tail parameter $\tau_{\text{ccprot, novo}}$.

The χ^2/dof of the fit is shown in Fig. 4.26(d) for the single-track sample. The goodness-of-fit of the single-track sample exhibits a $\chi^2/\text{dof} > 1$ towards low energies, which can be cured by introducing another degree of freedom: an additional Novosibirsk component below 10 GeV.

While this improves the χ^2, it has no impact on the template fits that will be executed using these templates – for that reason the additional Novosibirsk component was omitted, to stabilize the minimization procedure.

The results for the multi-tracks sample are presented in Appendix A.3. The conclusions are identical as for the single-track sample.

A similar smoothing procedure is applied for the electron template, as shown in Fig. 4.27 for the single-track sample and in Fig. A.18 for the multi-tracks sample. In total six parameters are relevant to describe the template analytically for all energies: three parameters corresponding to the Novosibirsk function in the electron model (peak position $\mu_{\text{elec, novo}}$, width $\sigma_{\text{elec, novo}}$ and tail parameter $\tau_{\text{elec, novo}}$), two for the gaussian part (peak position $\mu_{\text{elec, gaus}}$, width $\sigma_{\text{elec, gaus}}$) and a ratio describing the relative contribution of the Novosibirsk needed to fit the template (fraction $\alpha_{\text{elec, novo}}$).

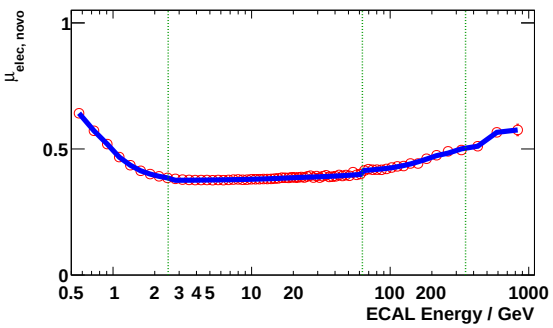

(a) Template parameter $\mu_{\text{elec, novo}}$

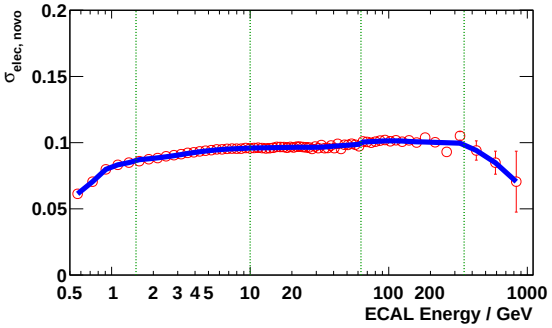

(b) Template parameter $\sigma_{\text{elec, novo}}$

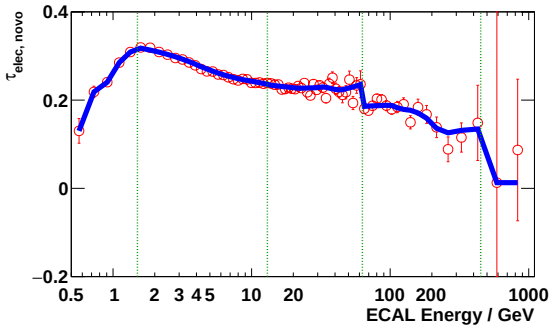

(c) Template parameter $\tau_{\text{elec, novo}}$

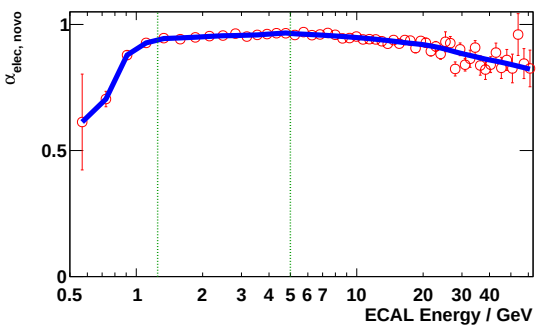

(d) Template parameter $\alpha_{\text{elec, novo}}$

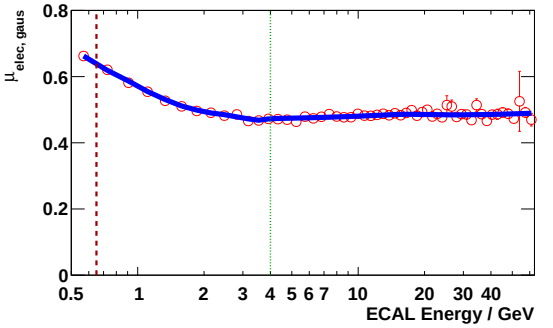

(e) Template parameter $\mu_{\text{elec, gaus}}$

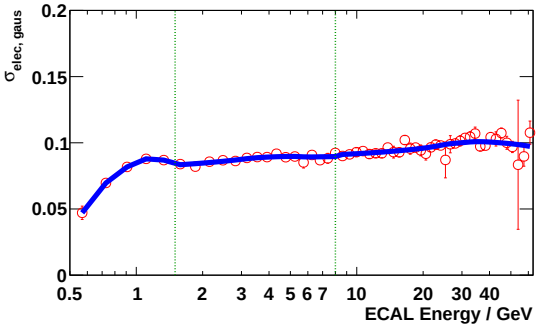

(f) Template parameter $\sigma_{\text{elec, gaus}}$

Figure 4.27: Analytical TRD template parameters describing the evolution of the electron template as function of energy for the single-track sample. In each energy bin the analytical function - Eq. (4.6) - is fit to the template data sample, yielding the red points. A smoothing procedure yields the blue curves, which are used as template parameters for the analysis. The vertical dashed green lines mark areas where different isolated smoothing procedures are applied. The vertical dashed red lines mark energies where the smoothing procedure starts – points before this border are preserved.

The three template parameters $\alpha_{\text{elec, novo}}$, $\mu_{\text{elec, gaus}}$ and $\sigma_{\text{elec, gaus}}$ presented in Figs. 4.27(d) to 4.27(f) are only relevant below 65 GeV. Above this energy threshold the electron template can be described with a single Novosibirsk, without a gaussian component.

The χ^2/dof of the fit for the single-track sample, as shown in Fig. 4.28, is consistent with 1 over the whole energy range.

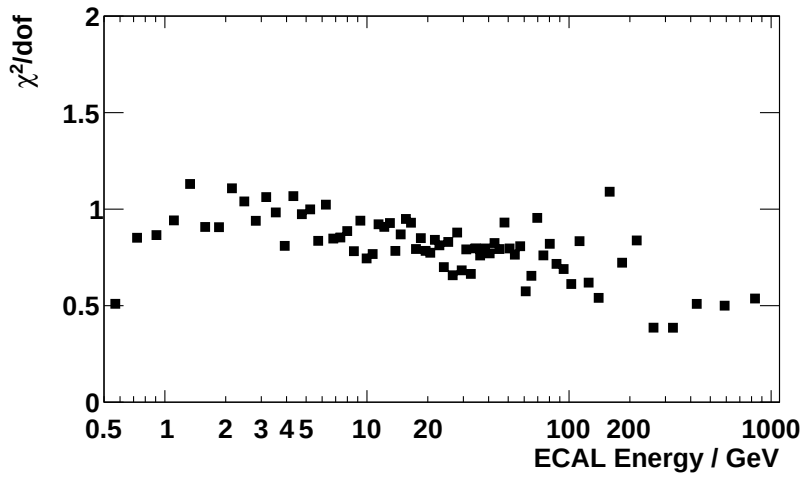

Figure 4.28: Goodness of fit of the model Eq. (4.6) with respect to the template data in the single-track sample. The black points show the χ^2/dof as function of energy. The result is consistent with 1 for all energies for the single-track sample.

The results for the multi-tracks sample are presented in Appendix A.3. The conclusions are identical as for the single-track sample.

An analogous smoothing procedure is applied for the proton template, as shown in Fig. 4.29 for the single-track sample. In total six parameters are relevant to describe the template analytically for all energies: three parameters corresponding to the Novosibirsk function in the proton model (peak position $\mu_{\text{prot, novo}}$, width $\sigma_{\text{prot, novo}}$ and tail parameter $\tau_{\text{prot, novo}}$), two for the gaussian part (peak position $\mu_{\text{prot, gaus}}$, width delta $\delta_{\sigma\,\text{prot, gaus}}$) and a ratio describing the relative contribution of the Novosibirsk needed to fit the template (fraction $\alpha_{\text{prot, novo}}$), corresponding to Eq. (4.8).

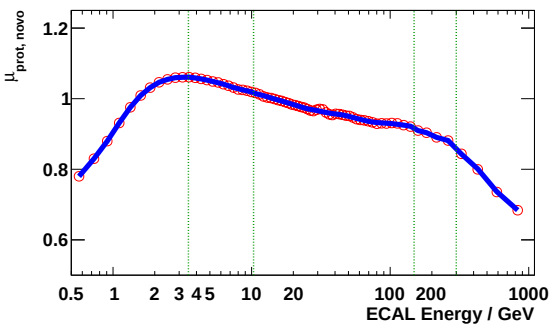

(a) Template parameter $\mu_{\text{prot, novo}}$

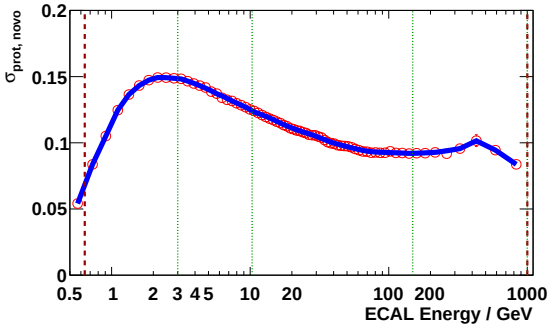

(b) Template parameter $\sigma_{\text{prot, novo}}$

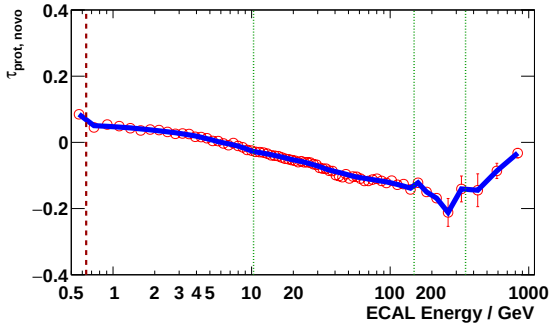

(c) Template parameter $\tau_{\text{prot, novo}}$

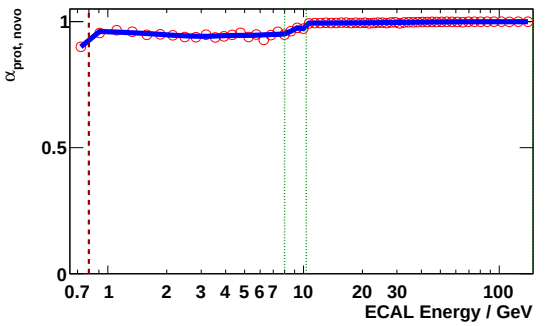

(d) Template parameter $\alpha_{\text{prot, novo}}$

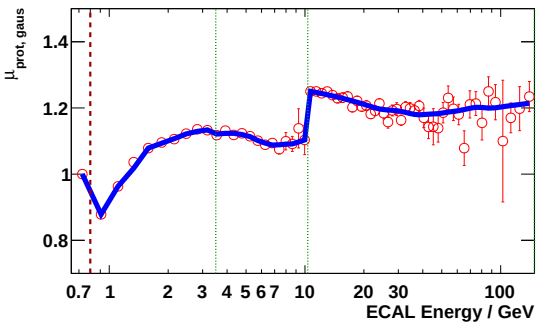

(e) Template parameter $\mu_{\text{prot, gaus}}$

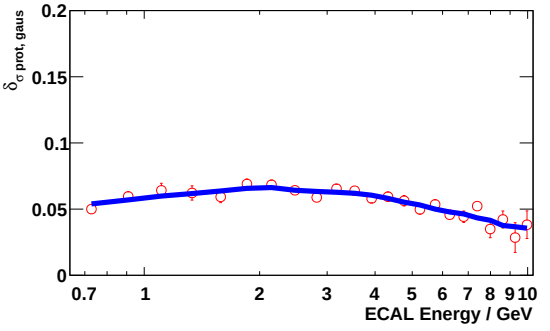

(f) Template parameter $\delta_{\sigma\,\text{prot, gaus}}$

Figure 4.29: Analytical TRD template parameters describing the evolution of the proton template as function of energy for the single-track sample. In each energy bin the analytical function - Eq. (4.8) - is fit to the template data sample, yielding the red points. A smoothing procedure yields the blue curves, which are used as template parameters for the analysis. The vertical dashed green lines mark areas where different isolated smoothing procedures are applied. The vertical dashed red lines mark energies where the smoothing procedure starts/ends – points before/after this border are preserved.

The two template parameters $\alpha_{\text{prot, novo}}$ and $\mu_{\text{prot, gaus}}$ presented in Figs. 4.29(d) and 4.29(e) are only relevant below 110 GeV. Above this energy threshold the proton template can be described with a single Novosibirsk, without a gaussian component.

The template parameter $\delta_{\sigma\,\text{prot, gaus}}$ shown in Fig. 4.29(f) mainly improves the goodness-of-fit of the fit procedure at low energies and remains constant zero above 10 GeV for the single-track sample. For the multi-tracks sample the parameter is absent because its introduction lead to numerical instabilities in the fit procedure.

The χ^2/dof of the fit, Fig. 4.30, is consistent with 1 over the whole energy range.

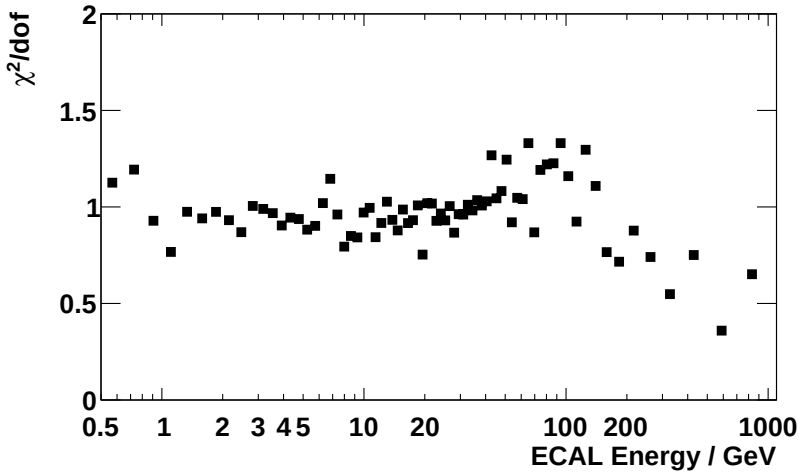

Figure 4.30: Goodness of fit of the model Eq. (4.8) with respect to the template data in the single-track sample. The black points show the χ^2/dof as function of energy. The result is consistent with 1 for all energies for the single-track sample.

The results for the multi-tracks sample are presented in Appendix A.3. The conclusions are identical as for the single-track sample.

The set of parameters presented in Fig. 4.26 for the charge-confused protons, Fig. 4.27 for the electrons and Fig. 4.29 for the protons for the single-track sample and for the multi-tracks sample (Figs. A.17 to A.19) form a fully analytical description of the TRD templates as function of energy. This is a major building block in the electron and positron analysis.

4.4.3 Charge-confusion templates

The CCMVA estimator Λ_{CC}, described in Section 4.2.8, will be used together with the TRD estimator Λ_{TRD} to perform two-dimensional template fits on ISS data to extract the number of electrons and positrons in different energy intervals on ISS data, taking the charge-confusion effect into account.

To perform the two-dimensional template fit, templates for protons, charge-confused protons, electrons, positrons, charge-confused electrons and charge-confused positrons need to be known in two variants: for the single-track sample and for the multi-tracks sample. The distinction between the two different track topologies is equally important as for the TRD estimator, as the amount of charge-confusion in both samples is vastly different. Another important difference with respect to the

TRD estimator is that the CCMVA estimator shape cannot be derived from first principles, thus no physically motivated analytical description of the shape is available. In order to construct templates either histograms containing the output of the CCMVA distribution will be used, if the statistics are sufficient, or analytical approximations, by utilizing methods such as Kernel Density Estimation (KDE) [Rosenblatt1956; Parzen1962].

The electron, positron, proton and charge-confused proton templates can be extracted from ISS data. The charge-confused electron and positron template can only be derived from the Monte-Carlo simulation, as there is no way to select a pure sample of charge-confused electrons or charge-confused positrons on ISS data. Charge-confused protons are selectable on ISS data, as the amount of antiprotons that could be misreconstructed as charge-confused protons is negligible. The charge-confused electron sample on ISS data would be dominated by correctly reconstructed positrons plus an additional contribution from charge-confused electrons. This ambiguity forces one to use the Monte-Carlo simulation to extract the charge-confused electron and charge-confused positron templates. The positron and charge-confused positron templates are identical to their electron counterparts as both particles behave in the same way with respect to the CCMVA estimator, which was verified using dedicated electron and positron Monte-Carlo simulations.

The cuts to prepare the template samples are similar as for the TRD estimator, presented in Section 4.4.2. All detector quality, preselection and selection cuts - Sections 4.3.1 to 4.3.3 - are applied when selecting the data samples. Furthermore the same $0.5 < E/|R| < 1$ cut as for the signal event selection is applied. The following enumeration lists the sample specific cuts:

1. **Proton sample**
   - ISS data, positive rigidity sample (R > 0)
   - Hadron-like ECAL shower ($\Lambda_{\mathrm{ECAL}} < 0$)
   - TRD electron/proton likelihood ratio $\Lambda_{\mathrm{TRD}} > 0.8$
2. **Charge-confused proton sample**
   - ISS data, negative rigidity sample (R < 0)
   - Hadron-like ECAL shower ($\Lambda_{\mathrm{ECAL}} < 0$)
   - TRD electron/proton likelihood ratio $\Lambda_{\mathrm{TRD}} > 0.8$
3. **Electron sample**
   - ISS data, negative rigidity sample (R < 0)
   - Energy dependent cut on the lateral shape (defined in Section 4.3.4 - Item 2)
   - Electron like ECAL shower ($\Lambda_{\mathrm{ECAL}} > 0$)
   - TRD electron/proton likelihood ratio $\Lambda_{\mathrm{TRD}} < 0.75$
4. **Charge-confused electron sample**
   - Electron Monte-Carlo simulation, positive rigidity sample (R > 0)
   - Energy dependent cut on the lateral shape (defined in Section 4.3.4 - Item 2)
   - Electron like ECAL shower ($\Lambda_{\mathrm{ECAL}} > 0$)
   - TRD electron/proton likelihood ratio $\Lambda_{\mathrm{TRD}} < 0.75$

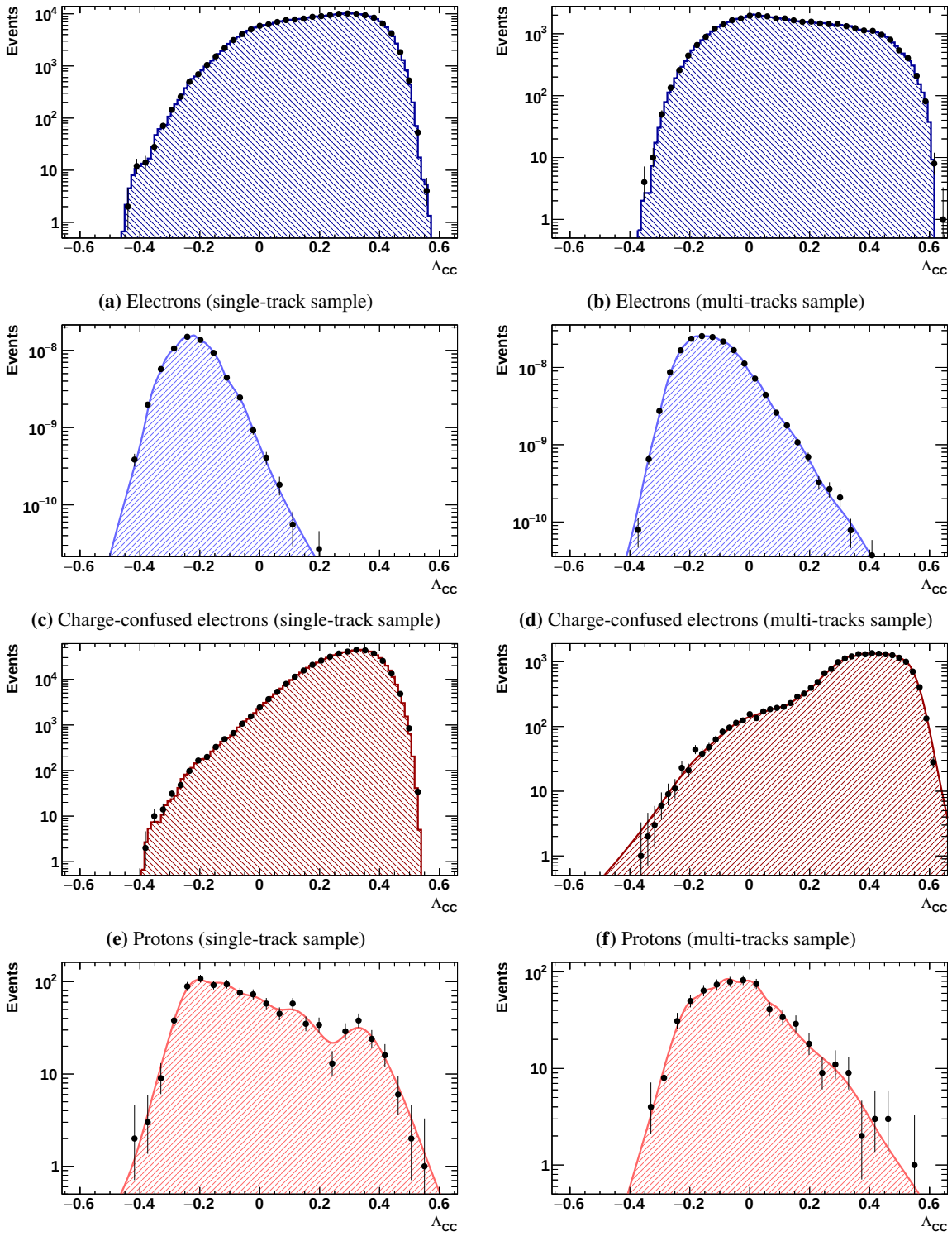

(a) Electrons (single-track sample)

(b) Electrons (multi-tracks sample)

(c) Charge-confused electrons (single-track sample)

(d) Charge-confused electrons (multi-tracks sample)

(e) Protons (single-track sample)

(f) Protons (multi-tracks sample)

(g) Charge-confused protons (single-track sample)

(h) Charge-confused protons (multi-tracks sample)

Figure 4.31: Overview of the CCMVA templates in the energy bin 17.98 – 18.99 GeV: electrons (dark blue area), charge-confused electrons (light blue area), protons (dark red area) and charge-confused protons (light red area). The black points show the CCMVA estimator output, either obtained from electron Monte-Carlo simulation or ISS data - depending on the data sample.

Figure 4.31 shows the electron template, the charge-confused electron template, the proton template and the charge-confused proton template in an example energy bin. Depending on the statistics in the examined data sample, either a histogram is used as template PDF, or if the statistics are too low, a KDE technique is applied to extract an analytical approximation as template PDF. This is necessary to avoid the propagation of statistical fluctuations from the template data samples to the template PDF.

The procedure to extract the charge-confusion templates is repeated for all energy bins in the analysis.

The positron and charge-confused positron templates are exactly identical to the electron and charge-confused electron templates by construction. This was verified on ISS data up to the highest energies for the electron template and using positron Monte-Carlo simulation for the charge-confused electron and charge-confused positron template.

4.4.4 Construction of two-dimensional TRD / CCMVA templates

The previously constructed one-dimensional TRD and CCMVA templates can be combined into two-dimensional templates according to Eq. (4.9), as they are assumed to be uncorrelated - which was verified in dedicated Monte-Carlo simulations. The correlation is negligible, as the TRD estimator Λ_{TRD} is computed using the ECAL energy as input, not the tracker rigidity.

$$\mathcal{P}_{\mathrm{2D}}(x, y) = \mathcal{P}_{\mathrm{TRD}}(x) \cdot \mathcal{P}_{\mathrm{CC}}(y) \tag{4.9}$$

Figures 4.32 to 4.34 shows the two-dimensional templates in an example energy bin for the single-track sample. The same overview is presented in Fig. A.20 for the multi-tracks sample. The TRD component is only slightly different compared to the single-track sample, whereas the CCMVA distribution is vastly different, as the response of the CCMVA is different for the multi-tracks sample.

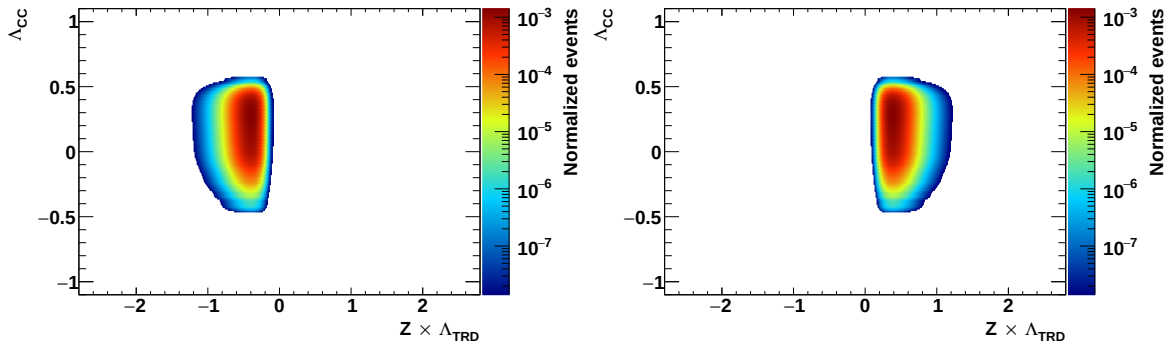

(a) Electrons **(b)** Positrons

Figure 4.32: Two-dimensional TRD / CCMVA templates in the energy bin 17.98 – 18.99 GeV for the electrons and positrons in the single-track sample. The color encodes the amount of normalized entries in the histogram, a red color corresponds to a large number of events, a blue color to a small number of events.

The two-dimensional positron template (Fig. 4.32(b)) is constructed by mirroring the two-dimensional electron template (Fig. 4.32(a)) around the y-axis.

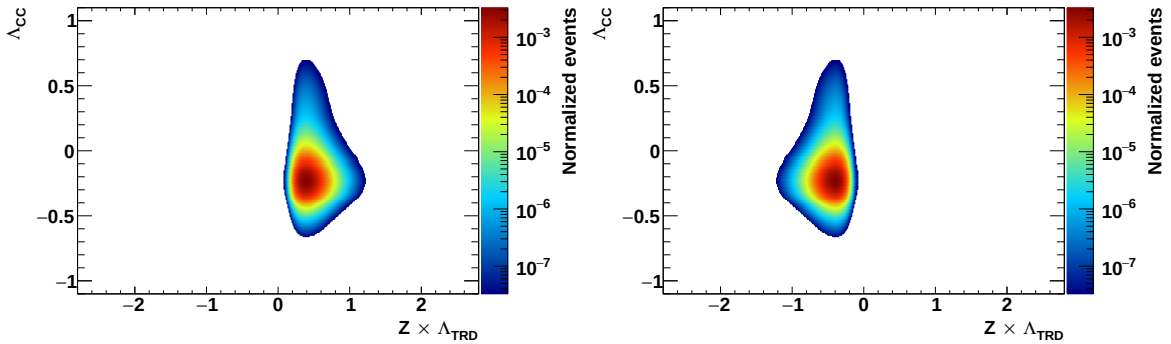

(a) Charge-confused electrons **(b)** Charge-confused positrons

Figure 4.33: Two-dimensional TRD / CCMVA templates in the energy bin 17.98 – 18.99 GeV for the charge-confused electrons and charge-confused positrons in the single-track sample. The color encodes the amount of normalized entries in the histogram, a red color corresponds to a large number of events, a blue color to a small number of events.

Analogous the charge-confused positron template (Fig. 4.33(b)) is constructed by mirroring the charge-confused electron template (Fig. 4.33(a)).

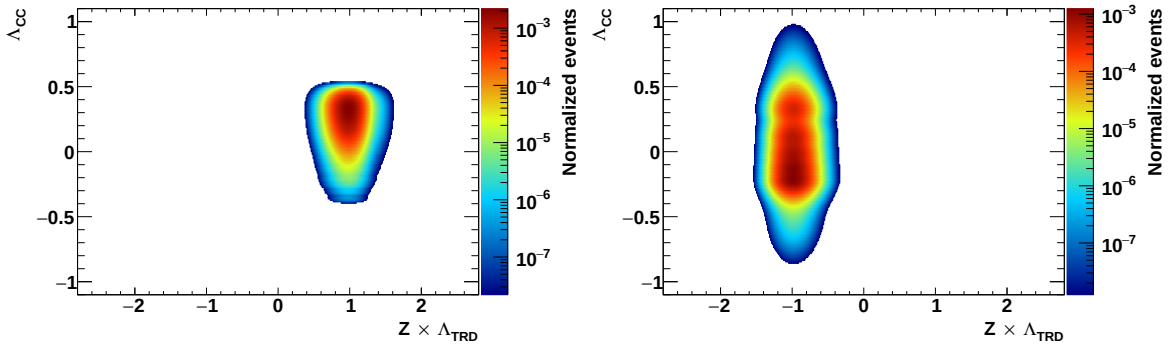

(a) Protons **(b)** Charge-confused protons

Figure 4.34: Two-dimensional TRD / CCMVA templates in the energy bin 17.98 – 18.99 GeV for the protons and charge-confused protons in the single-track sample. The color encodes the amount of normalized entries in the histogram, a red color corresponds to a large number of events, a blue color to a small number of events.

The construction of the two-dimensional templates is repeated for each energy interval in the analysis. These templates will be used in a fit procedure to extract the number of electrons and positrons in each energy interval, which will be shown in the next section.

4.4.5 Two-dimensional template fit

Figure 4.35(a) shows a typical ISS data distribution in an example energy bin, 17.98 – 18.99 GeV, after applying all data quality, preselection, selection and $e^{\pm}$ identification cuts (Section 4.3). Figure 4.35(b) shows the same data sample, after applying a cut on the ECAL estimator Λ_{ECAL} to reduce the proton background. The choice of the ECAL estimator cut value will be discussed separately in Section 4.5.1.

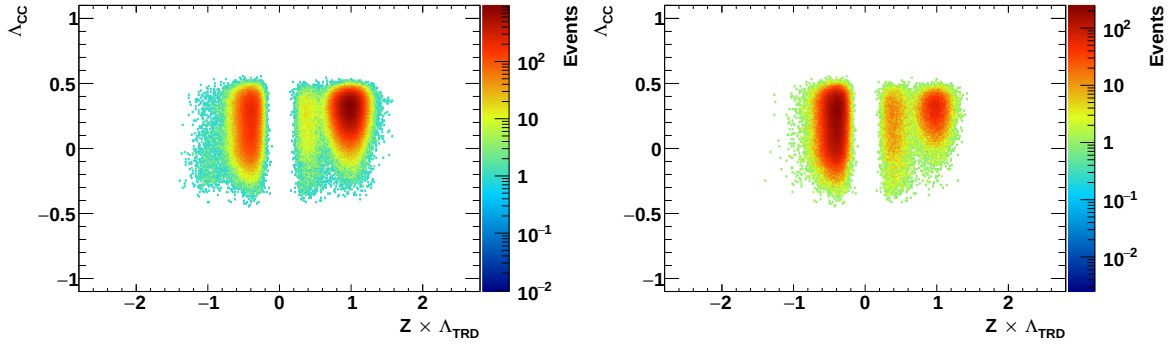

(a) Before cut on ECAL estimator

(b) After cut on ECAL estimator

Figure 4.35: ISS data distribution in the energy bin 17.98 – 18.99 GeV for the single-track sample, as example, before and after applying a cut on the ECAL estimator to reduce the proton background.

To extract the number of electrons and positrons an extended binned maximum likelihood fit [Cowan1998] is performed on the data sample in each energy interval. The binned two-dimensional distribution of the data sample is denoted as $\mathcal{D}(x, y)$, where x refers to the charge sign multiplied with the TRD estimator - $Z \times \Lambda_{\mathrm{TRD}}$ - and y to the charge-confusion estimator Λ_{CC}. The fit is performed, by minimizing the negative log-likelihood function, Eq. (4.10), denoted as $\mathcal{L}(x, y)$.

The goal is to extract five parameters for each energy interval: the number of electrons N_{e^-}, the number of positrons N_{e^+}, the number of protons N_{p^+}, the number of charge-confused protons N_{p^-} and the amount of charge-confusion f_{cc} in the leptonic sample.

In the fit procedure all particle counts are represented as fractions of the total number of events, e.g. $N_{e^-} = f_{\mathrm{elec}} \cdot N_{\mathrm{events}}$, where $N_{\mathrm{events}} = \sum_x \sum_y D(x, y)$. The negative log-likelihood function - Eq. (4.10) - is minimized using the Minuit [James1975] minimizer and the best-fit parameters are extracted. The last additive term in the likelihood functions differs from the standard maximum likelihood function: the normalisation of the probability distribution function is allowed to vary. The number of events N_{events} follows a Poissonian distribution and the last additive term in the likelihood function takes this into account.

$$\begin{aligned}\mathcal{L}(x, y) = &-\left(\sum_x \sum_y \mathcal{D}(x, y) \cdot \log(\mathcal{P}(x, y))\right) \\ &+ \underbrace{(f_{\mathrm{prot}} + f_{\mathrm{ccprot}} + f_{\mathrm{elec}} + f_{\mathrm{posi}}) \cdot N_{\mathrm{events}}}_{\text{extended likelihood term}}\end{aligned} \tag{4.10}$$

The normalized likelihood value $\mathcal{P}(x, y)$ is defined in Eq. (4.11) as sum of the products of the particle fraction f_k with the template $\mathcal{P}_k(x, y)$, for each template component k.

The definition of the normalized likelihood value is the crucial part of the two-dimensional fit procedure. By the introduction of the amount of charge-confusion f_{cc}, four out of the six PDFs $\mathcal{P}_{elec}(x,y)$, $\mathcal{P}_{ccelec}(x,y)$, $\mathcal{P}_{posi}(x,y)$, $\mathcal{P}_{ccposi}(x,y)$ are no longer independent in the fit procedure but connected via f_{cc}, reducing the free parameters of the fit.

$$\begin{aligned}\mathcal{P}(x,y) = {} & f_{prot} \cdot \mathcal{P}_{prot}(x,y) + f_{ccprot} \cdot \mathcal{P}_{ccprot}(x,y) + \\ & (1-f_{cc}) \cdot f_{elec} \cdot \mathcal{P}_{elec}(x,y) + f_{cc} \cdot f_{elec} \cdot \mathcal{P}_{ccelec}(x,y) + \\ & (1-f_{cc}) \cdot f_{posi} \cdot \mathcal{P}_{posi}(x,y) + f_{cc} \cdot f_{posi} \cdot \mathcal{P}_{ccposi}(x,y)\end{aligned} \tag{4.11}$$

The ISS data distribution for the single-track sample (Fig. 4.35(b)), is fit using the single-track templates shown in Figs. 4.32 to 4.34, for an example energy bin 17.98 – 18.99 GeV. The ISS data distribution is presented in a three-dimensional plot in Fig. 4.36 along with the fit results, split in the negative rigidity sample (Fig. 4.36(b)) and the positive rigidity sample (Fig. 4.36(c)).

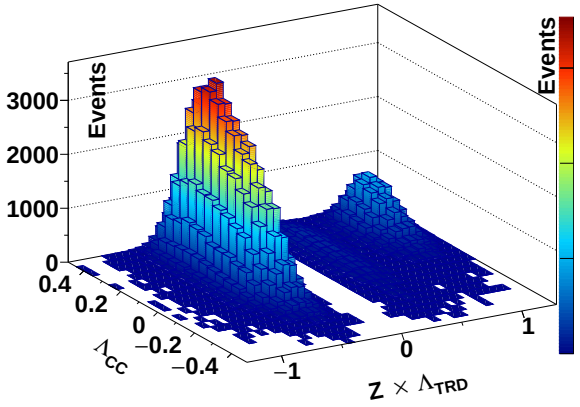

(a) ($Z \times \Lambda_{TRD}$ - Λ_{CC}) data distribution

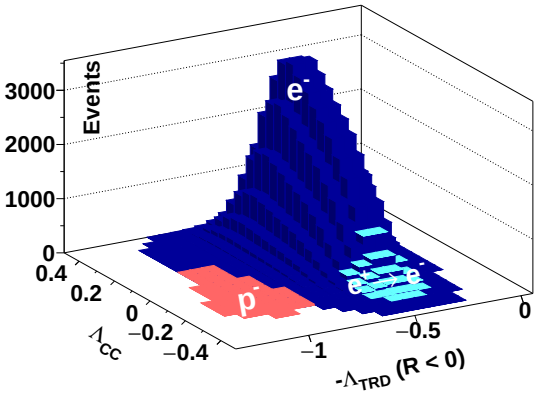

(b) Fit results for R < 0 sample

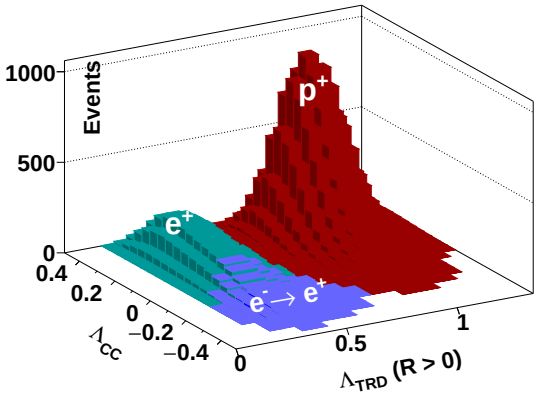

(c) Fit results for R > 0 sample

Figure 4.36: ISS data distribution in the energy bin 17.98 – 18.99 GeV for the single-track sample as three-dimensional plot (top) along with the results of the fit procedure, split in two parts: one plot showing the fit results in the negative rigidity sample (lower left) and another plot showing the fit results in the positive rigidity sample (lower right).

Figure 4.37 shows a projection of the three-dimensional fit result representation to the x-axis ("$Z \times \Lambda_{\mathrm{TRD}}$") and the y-axis ("$\Lambda_{\mathrm{CC}}$"), separately. The $Z \times \Lambda_{\mathrm{TRD}}$ projection (Fig. 4.37(a)) is suitable to identify the different particle species: electrons, positrons, protons, and charge-confused protons, whereas the Λ_{CC} projection is helpful to visualize the amount of charge-confusion in the electron or positron component. Therefore the Λ_{CC} projection was obtained twice, once for the negative rigidity sample (to identify electrons and charge-confused positrons - see Fig. 4.37(b)) and once for the positive rigidity sample (to identify the positrons, and charge-confused electrons - see Fig. 4.37(c)). Furthermore an additional cut on the TRD estimator was applied when obtaining the Λ_{CC} projection, to reduce the proton background, which is not helpful to disentangle electrons or positrons from their charge-confused counterparts.

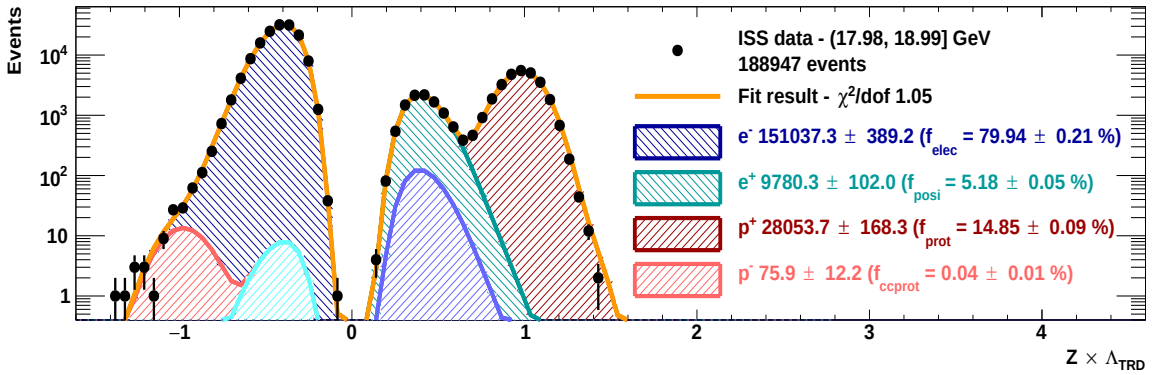

(a) $Z \times \Lambda_{\mathrm{TRD}}$ projection

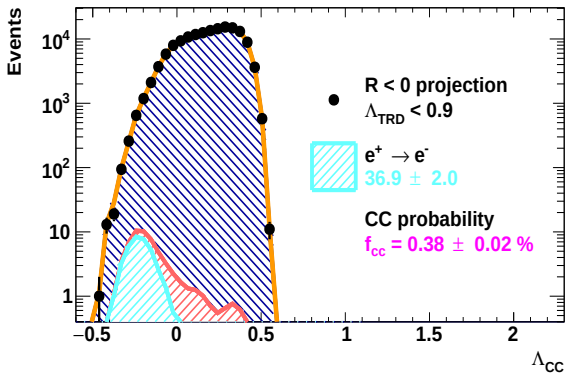

(b) Λ_{CC} projection - R < 0

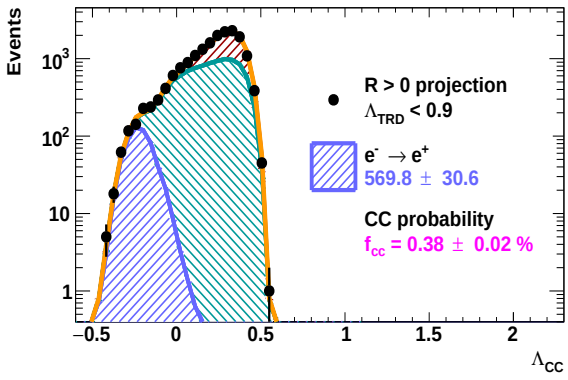

(c) Λ_{CC} projection - R > 0

Figure 4.37: Results of the two-dimensional TRD / CCMVA template fit in the energy bin 17.98 – 18.99 GeV for the single-track sample drawn as stacked histograms. The upper panel shows the projection of the two-dimensional fit to the x-axis. The lower left panel shows the projection to the y-axis, containing only events with R < 0. In this plot **electrons**, **charge-confused positrons** and **charge-confused protons** are visible. The lower right panel shows the projection to the y-axis, containing only events with R > 0. In this plot **positrons**, **charge-confused electrons** and **protons** are visible.

It is immediately apparent that the amount of charge-confusion in the leptonic sample is mostly determined by the amount of charge-confused electrons in the positive rigidity sample, as shown in Fig. 4.37(c). When studying the "$Z \times \Lambda_{\mathrm{TRD}}$" projection it is obvious that the charge-confusion

effect is significant and needs to be taken into account for this analysis. Without a proper treatment of the charge-confusion effect, all positron-like events in the region around x ≈ 0.4 would be identified as positrons, but in fact a significant fraction are electrons that are misreconstructed with positive rigidity: charge-confused electrons. The same argument holds for the region around x ≈ -0.4, however less pronounced. Most events are electrons but a non-negligible amount are positrons that are charge-confused.

It is important to understand that the charge-confusion does not affect the energy measurement in the ECAL, but only the reconstructed rigidity - otherwise the analysis strategy would be completely different, since the charge-confused events from a true energy E would not be contained in the data distribution for the same bin, but elsewhere. Therefore the CCMVA estimator plays the key role in this analysis allowing to separate the charge-confused from the correctly reconstructed $e^{\pm}$.

The $\chi^2/\mathrm{dof} = 1.05$ is computed using the full two-dimensional model and shows that a good description of the data is available. Empty bins are skipped and do not contribute to the χ^2 computation.

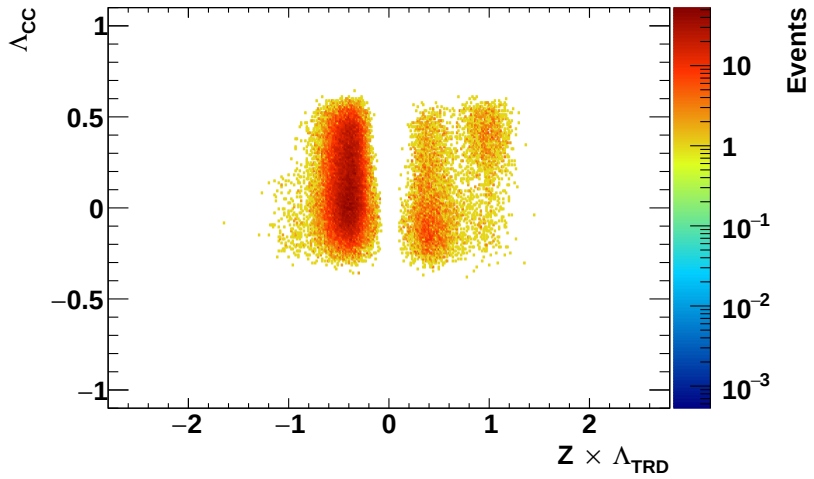

Figure 4.38: ISS data distribution in the energy bin 17.98 – 18.99 GeV for the multi-tracks sample, after applying a cut on the ECAL estimator to reduce the proton background.

As next step the multi-tracks sample, Fig. 4.38 is fit using the multi-tracks templates shown in Fig. A.20. The fit results are presented in Fig. 4.39 for an example energy bin.

As in the single-track sample case the $\chi^2/\mathrm{dof} = 1.02$ proofs that a good description of the multi-tracks data sample is available.

It is important to note that the number of charge-confused electrons - 2226.3 - is comparable to the number of correctly reconstructed positrons - 2188.1 - in this energy bin. This is a general feature of the multi-tracks sample: the charge-confusion is an order of magnitude larger than in the single-track sample (6.01 % in the multi-tracks sample vs. 0.38 % in the single-track sample).

For the flux analysis, the gain in statistics by adding the multi-tracks sample, outweighs the increase of systematic uncertainties. For the determination of the positron fraction, or the positron over electron ratio, this is not the case, as important uncertainties of the flux analysis cancel in the ratios. This topic will be revisited and discussed in detail in Section 4.6.

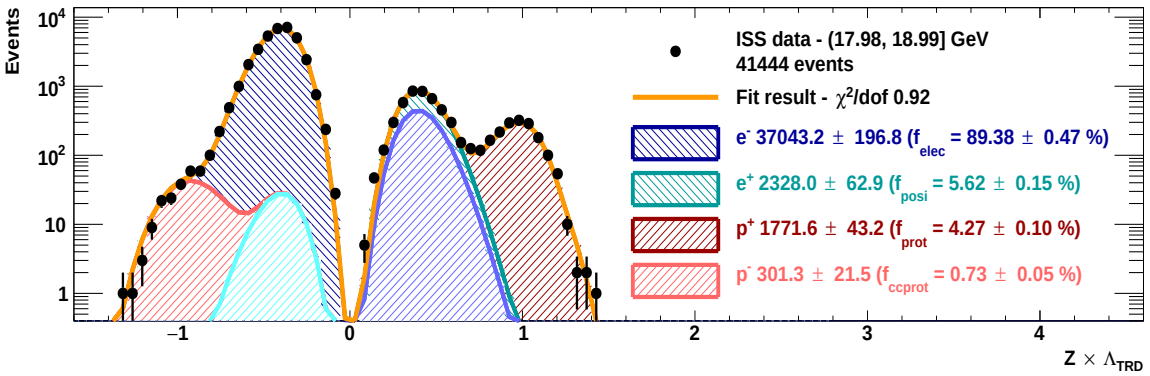

(a) $Z \times \Lambda_{\mathrm{TRD}}$ projection

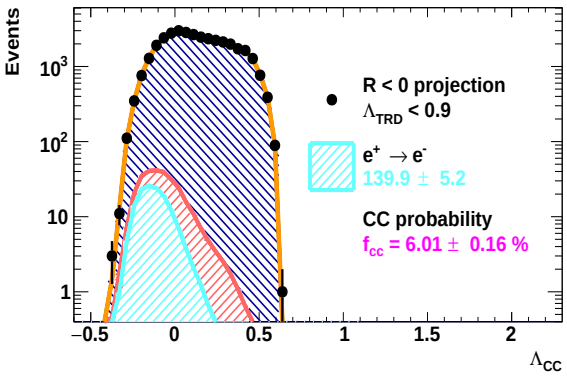

(b) Λ_{CC} projection - R < 0

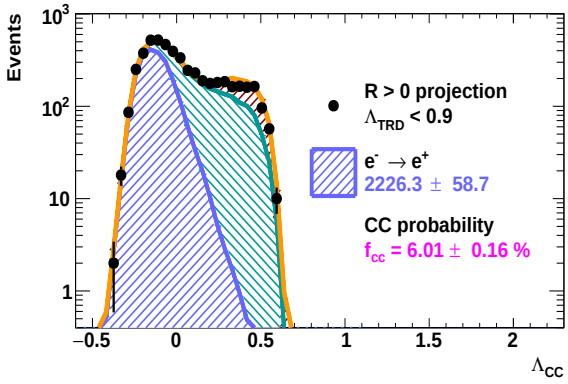

(c) Λ_{CC} projection - R > 0

Figure 4.39: Results of the two-dimensional TRD / CCMVA template fit in the energy bin 17.98 – 18.99 GeV for the multi-tracks sample drawn as stacked histograms. The upper panel shows the projection of the two-dimensional fit to the x-axis. The lower left panel shows the projection to the y-axis, containing only events with R < 0. In this plot **electrons**, **charge-confused positrons** and **charge-confused protons** are visible. The lower right panel shows the projection to the y-axis, containing only events with R > 0. In this plot **positrons**, **charge-confused electrons** and **protons** are visible.

The results of the single-track sample and the multi-tracks sample can be added to compute the results for the all-tracks sample. For historical[11] reasons a separate template fit on the all-tracks sample is performed and the results of that fit will be used to derive the electron flux and the positron flux.

In order to describe the data in the all-tracks sample, templates for the all-tracks sample have to be constructed from the single-track templates and the multi-tracks templates. For each template component k the fraction of single-track events α_k in the all-tracks sample needs to be determined, by counting. Using this information all-tracks templates $\mathcal{P}_{k,\ \text{all-tracks}}(x, y)$, can be derived:

$$\mathcal{P}_{k,\ \text{all-tracks}}(x, y) = \alpha_k \cdot \mathcal{P}_{k,\ \text{single-track}}(x, y) + (1 - \alpha_k) \cdot \mathcal{P}_{k,\ \text{multi-tracks}}(x, y). \tag{4.12}$$

[11] It is sufficient to combine the results of the single-track and the multi-tracks fit to extract the number of electrons and positrons in the all-tracks data sample. To extract the correlation coefficient ρ, denoting the correlation between the fitted number of electrons and positrons, it is more convenient to execute a separate template fit for the all-tracks data sample and directly extract the parameter ρ. ρ is needed when computing e.g. the uncertainty of the positron fraction or the positron/electron ratio from the fit results, by error propagation.

After performing the single-track sample fit and the multi-tracks sample fit the number of events n_k in each template component k is known. Thus the fraction of single-track events α_k in each template component k can be derived: $\alpha_k = n_{k,\text{ single-track}}/(n_{k,\text{ single-track}} + n_{k,\text{ multi-tracks}})$. Table 4.1 shows the so-obtained fractions of single-track events per template component. Using these α_k values, templates for the all-tracks sample can be constructed from the single-track templates and the multi-tracks templates, following the prescription in Eq. (4.12).

Component	Fraction of single-track events α_k
Electrons	0.81
Charge-confused electrons	0.20
Positrons	0.81
Charge-confused positrons	0.21
Protons	0.94
Charge-confused protons	0.20

Table 4.1: Single-track event fractions for all template components in the two-dimensional fit of the all-tracks sample in the energy bin 17.98 – 18.99 GeV. For comparison, the overall fraction of single-track events in this energy bin is 0.82.

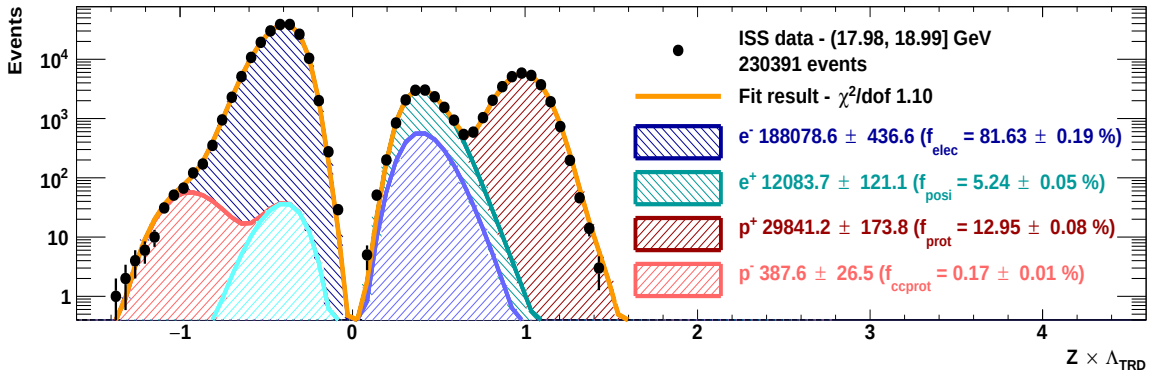

(a) $Z \times \Lambda_{\text{TRD}}$ projection

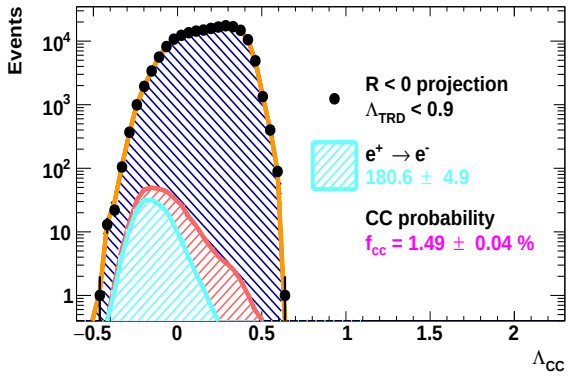

(b) Λ_{CC} projection - R < 0

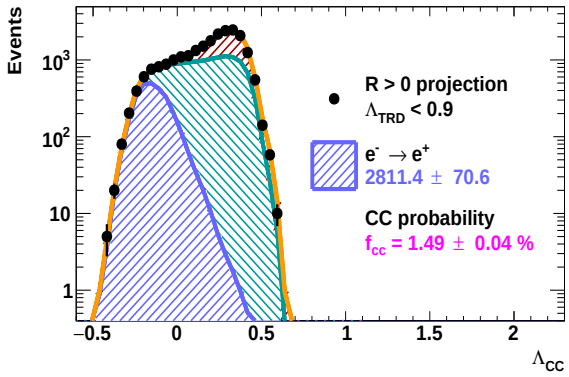

(c) Λ_{CC} projection - R > 0

Figure 4.40: Results of the two-dimensional TRD / CCMVA template fit in the energy bin 17.98 – 18.99 GeV for the all-tracks sample drawn as stacked histograms.

It is important to note that the global fraction of single-track events in the all-tracks sample cannot be used to derive the templates for the all-tracks sample, as the amount of charge-confusion for the single-track and multi-tracks sample is different. Instead the single-track fraction in each component must be determined separately.

The fit result of the all-tracks sample is presented in Fig. 4.40. The $\chi^2/\text{dof} = 1.10$ shows that the model is in very good agreement with the data and with the single-track / multi-tracks fit results - as expected. The overall amount of charge-confusion in the all-tracks sample is approximately four times larger than in the single-track sample (1.49 % in the all-tracks sample vs. 0.38 % in the single-track sample).

The whole fit procedure is repeated for all energy bins in the analysis, for the single-track sample, the multi-tracks sample and the all-tracks sample. Afterwards the amount of charge-confusion for the different samples can be compared with the Monte-Carlo prediction, as presented in Fig. 4.41. All samples show excellent agreement with the prediction from the Monte-Carlo simulation.

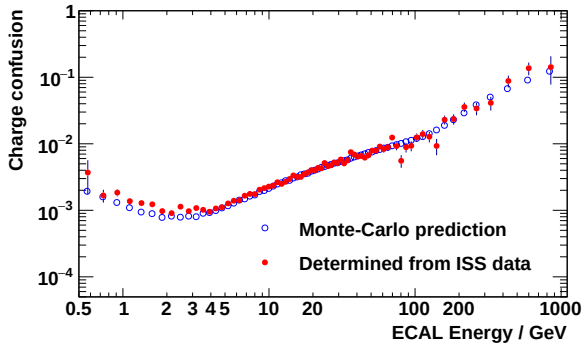

(a) Single-track sample

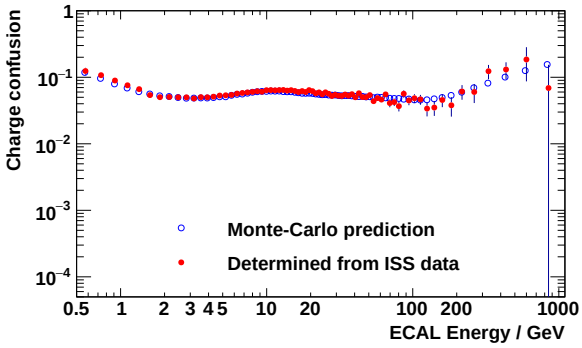

(b) Multi-tracks sample

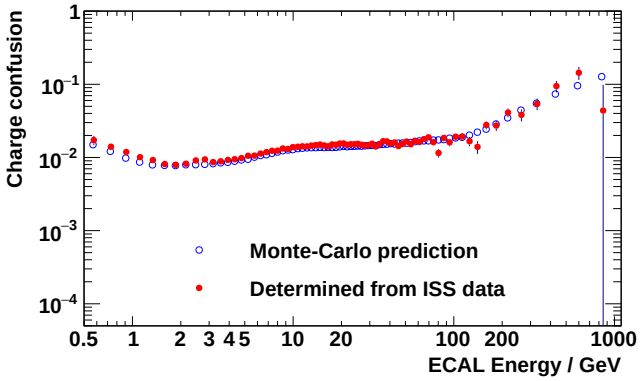

(c) All-tracks sample

Figure 4.41: Comparison of the amount of charge-confusion determined from ISS data with the prediction from the Monte-Carlo simulation for the single-track sample, the multi-tracks sample and the all-tracks sample.

Most importantly the shapes of the charge-confusion curves match the expectation: at low energies the charge-confusion rises, due to multiple scattering. At high energies - around $\approx 150\,\text{GeV}$ - an additional component contributing to the charge-confusion is emerging: the finite resolution of the silicon tracker, when approaching MDR. Furthermore the charge-confusion curves are all smooth, without distinct structures. The transitions at low and high energies are smooth.

The additional degree of freedom in the fit procedure to determine the charge-confusion leads to an increase of the uncertainties on the number of electrons and positrons, which should be minimized for the flux analysis. Since the charge-confusion fitted from ISS data is in agreement with the Monte-Carlo simulation it opens the possibility to fix the amount of charge-confused from the Monte-Carlo prediction and repeat the fit procedure. The fit results are presented in Fig. 4.42 for the all-tracks sample.

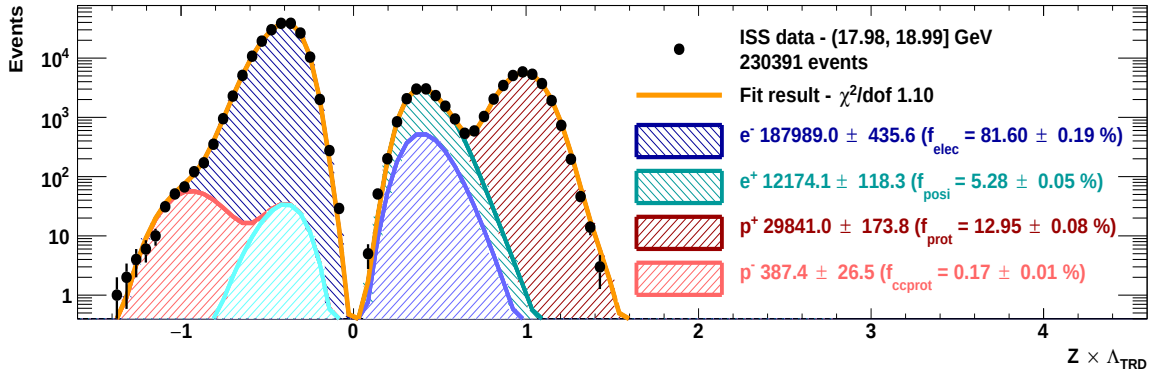

(a) $Z \times \Lambda_{\mathrm{TRD}}$ projection

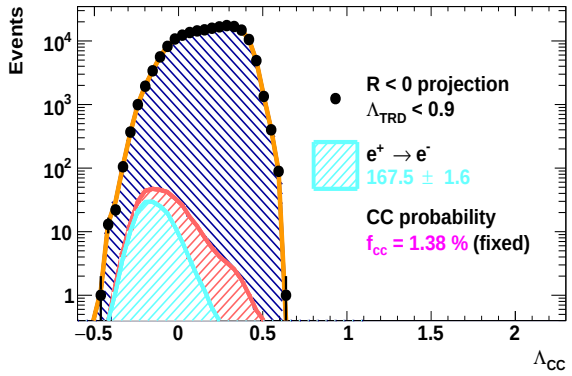

(b) Λ_{CC} projection - R < 0

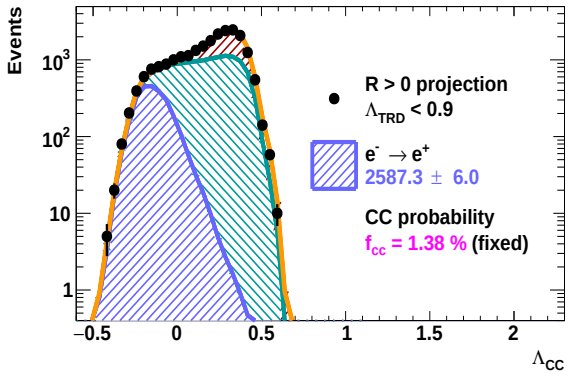

(c) Λ_{CC} projection - R > 0

Figure 4.42: Results of the two-dimensional TRD / CCMVA template fit in the energy bin 17.98 – 18.99 GeV for the all-tracks sample drawn as stacked histograms with the amount of charge-confusion fixed by the prediction from the Monte-Carlo simulation.

The number of positrons is equal to **12083.7 ± 121.1** when the amount of charge-confusion is a free fit parameter. The smallest uncertainty, if the separation between all components would be perfect, is $\sqrt{N}$, corresponding to an expected Poissonian uncertainty in the limit of sufficiently high statistics. The reported uncertainty of **121.1** is $\approx 10.2\,\%$ larger than the ideal uncertainty of $\sqrt{12083.7} \approx 109.9$.

However, if the amount of charge-confusion is fixed to the prediction from the Monte-Carlo simulation the number of positrons is equal to **12174.1 ± 118.3**, which is only $\approx 7.6\,\%$ larger than the smallest uncertainty and shows the gain of fixing the amount of charge-confusion from the Monte-Carlo prediction. The absolute difference in the number of positrons is smaller than one sigma, not only in this energy bin but for the whole energy range of the analysis.

Therefore the charge-confusion value f_{cc} will be fixed to the prediction from the Monte-Carlo simulation, when extracting the number of electrons and positrons for the flux and ratio analysis

Therefore the event counts from the all-tracks analysis will be used, with the charge-confused fixed to the Monte-Carlo prediction, to derive the electron and positron flux. The systematic uncertainty due to the fixing of the charge-confusion will be discussed in detail in Section 4.6.2.

The final event counts are presented in Fig. 4.43. The electron and positron signal events follow smooth curves, even though no corrections for the selection efficiency nor the geomagnetic cut-off is applied at this stage of the analysis.

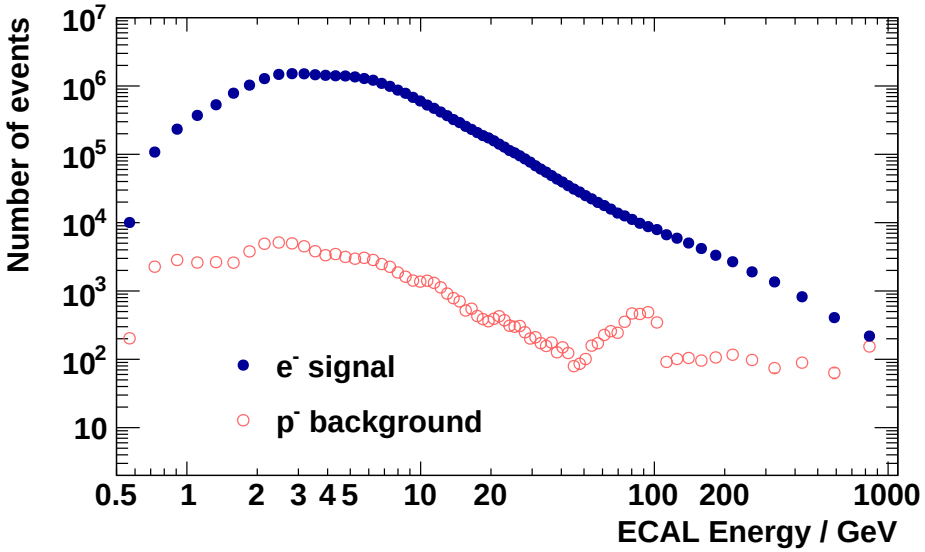

(a) Electrons and charge-confused protons

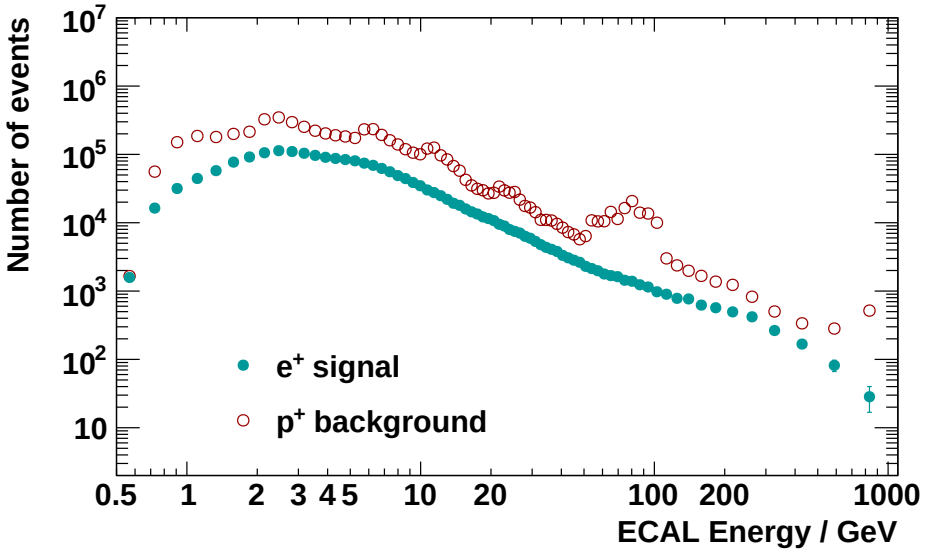

(b) Positrons and protons

Figure 4.43: Number of signal and background events for the all-tracks sample, extracted from the two-dimensional fit procedure.

The number of background events for the negative rigidity sample is always below the number of signal events in each energy bin. The negative rigidity sample is naturally enhanced by electrons and the number of charge-confused protons is much smaller up to the highest energies.

The situation is different for the positive rigidity sample, where the number of background events is always larger than the number of signal events. It is possible to keep the number of background events smaller than the signal events, but this costs signal efficiency and causes an increase of statistical uncertainties. The presented event counts are the result of an iterative optimization procedure. The goal of the optimization procedure is to minimize the statistical uncertainties of the positrons, by increasing the signal efficiency as much as possible. The consequence is a larger background, which is acceptable if the separation of the signal / background components in the template fit is sufficient, which is the case for this analysis. The increase of background events between 50 – 100 GeV is a consequence of only applying a loose cut on the ECAL estimator to reject background events. Above 100 GeV the cut on the ECAL estimator has to be gradually hardened to keep the separation power large enough that a minimal statistical uncertainty for the positrons is reached. The details of choosing the cut on the ECAL estimator will be discussed in detail in Section 4.5.1.

4.5 Time-averaged flux calculation

In this section time-averaged fluxes will be derived, which means that there is only a single time interval i to consider. The time interval starts at the beginning of the data taking period - **May 20$^{\text{th}}$, 2011**, including all data up to **November 12$^{\text{th}}$, 2017** - corresponding to the last day of ISS data that is analyzed in this work.

In total 74 energy bins will be analyzed, from 0.5 GeV up to 1 TeV, as described in Section 4.4.1. The 74 flux data points will be combined into a single energy-dependent flux. $\Phi_{e^\pm}(E)$ describes the electron or positron flux in the energy bin E of width ΔE:

$$\Phi_{e^\pm}(E) = \frac{N_{e^\pm}(E)}{\Delta E \cdot T(E) \cdot A_{e^\pm}(E) \cdot \epsilon_{e^\pm}(E)}. \tag{4.13}$$

$N_{e^\pm}(E)$ are the numbers of electrons or positrons, respectively, as determined in Section 4.4.5 using the two-dimensional fit procedure. $A_{e^\pm}(E)$ is the acceptance, $\epsilon_{e^\pm}(E)$ the signal selection efficiency and $T(E)$ the measurement time.

The efficiency $\epsilon_{e^\pm}(E) = \epsilon(E)$ was found to be independent of the particle species[12] and is defined as the product of the trigger efficiency and the ECAL estimator efficiency:

$$\epsilon(E) = \epsilon_{\text{trigger}}(E) \cdot \epsilon_{\text{ecal}}(E) \tag{4.14}$$

Both efficiencies will be derived directly from ISS data, without involving any Monte-Carlo simulations. The acceptance $A_{e^\pm}(E)$ is defined as the product of the acceptance derived from the electron or positron Monte-Carlo simulation $A^{\text{MC}}_{e^\pm}(E)$ and a correction factor $(1 + \delta_{e^\pm}(E))$, which is used to correct for minor differences between the prediction of the acceptance from the Monte-Carlo simulation and the ISS data:

$$A_{e^\pm}(E) = A^{\text{MC}}_{e^\pm}(E) \cdot (1 + \delta_{e^\pm}(E)). \tag{4.15}$$

The derivation of the correction factor $(1 + \delta_{e^\pm}(E))$ is explained in detail in Section 4.5.4. The acceptance $A^{\text{MC}}_{e^\pm}(E)$ is slightly different for electrons and positrons at low energies, due to differences in the cross-sections, which will be explained in Section 4.5.5.

The correction factor $(1 + \delta_{e^\pm}(E)) = (1 + \delta(E))$ is identical for electrons and positrons at least up to 100 GeV, where the positron ISS statistics is sufficient to perform the cross-check precisely. Since no deviation is exhibited and no differences between electrons and positrons is expected at higher energies from first principles the correction factor is assumed to be identical for $e^\pm$ for all energies.

Thus the resulting acceptance $A_{e^\pm}(E)$ is given by:

$$A_{e^\pm}(E) = A^{\text{MC}}_{e^\pm}(E) \cdot (1 + \delta(E)). \tag{4.16}$$

In the following sections it will be shown how $T(E)$, $A_{e^\pm}(E)$, $\epsilon(E)$ are derived in order to compute electron and positron fluxes and why an unfolding procedure is necessary.

[12] This was tested in dedicated studies up to 200 GeV where the positron ISS statistics is sufficient to perform the cross-check.

4.5.1 ECAL estimator efficiency

The ECAL estimator is the main handle to control the proton background in the ISS data samples. A hard cut on the ECAL estimator significantly reduces the proton background in the positive rigidity sample, but at the same time positrons are lost. A compromise needs to be found to keep the electron and positron signal efficiency as high as possible while rejecting as many proton background events as necessary to keep the template fits stable.

Therefore, as already mentioned in Section 4.4.5, an iterative procedure was developed to optimize the cut on the ECAL estimator. The procedure is illustrated in Fig. 4.44. It requires an initial guess of the ECAL estimator efficiency $\epsilon_{\text{ecal}}(E) = \epsilon_{\text{desired}}(E)$ as starting point. During the procedure the desired efficiency gets refined until the proton rejection is sufficient in each energy bin.

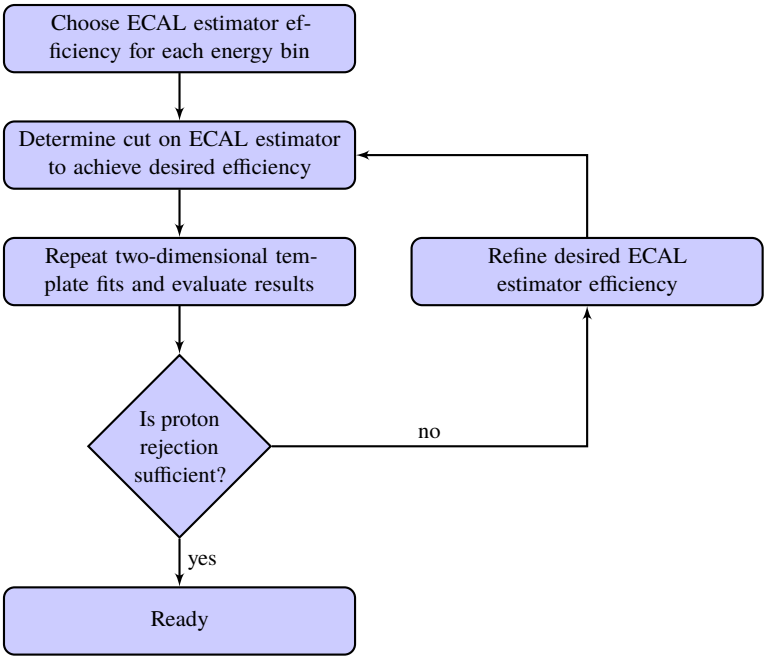

Figure 4.44: Illustration of the iterative procedure used to determine the ECAL estimator cut value / efficiency.

The initial guess for all energies is $\epsilon_{\text{desired}}(E) = 0.99$. If 1.0 was chosen no cut on the ECAL estimator would be applied. Thus a value smaller than 1.0 has to be used, corresponding to a soft cut on the ECAL estimator, which already rejects the majority of the proton background events in the positive rigidity sample. After selecting an initial guess, multiple one-dimensional template fits in the TRD estimator are executed on the negative rigidity sample. At first a fit is executed without imposing a cut on the ECAL estimator, to extract the number of electrons with 100 % signal efficiency: $N^0_{e^-}$. As the negative rigidity sample does not contain protons but only charge-confused protons, which are far less frequent than protons, it is possible to extract the number of electrons with 100 % signal efficiency in all energy bins without imposing a cut on the ECAL estimator. For the positive rigidity sample the amount of protons is orders of magnitudes higher than the amount of positrons, if no ECAL estimator cut is imposed. Thus it is not possible to extract a reliable estimate of the true number of positrons at 100 % signal efficiency. This is the reason why the procedure to determine the ECAL estimator cut value is performed only on the negative rigidity sample.

After determining the number of electrons with 100 % signal efficiency - $N^0_{e^-}$ - the template fit will be repeated multiple times, gradually hardening the cut on the ECAL estimator. For each iteration m the number of electrons is extracted as $N^m_{e^-}$. The ratio of $N^m_{e^-}/N^0_{e^-}$ yields the ECAL estimator efficiency $\epsilon^m_{\text{ecal}}(E)$ for a given ECAL estimator cut value η^m_{ecal}.

This allows to choose the cut value which corresponds to the desired efficiency $\epsilon_{\text{desired}}(E)$. Figure 4.45 presents the result of the optimization procedure: the chosen ECAL estimator cut value η_{ecal} and its associated efficiency $\epsilon_{\text{ecal}}(E)$.

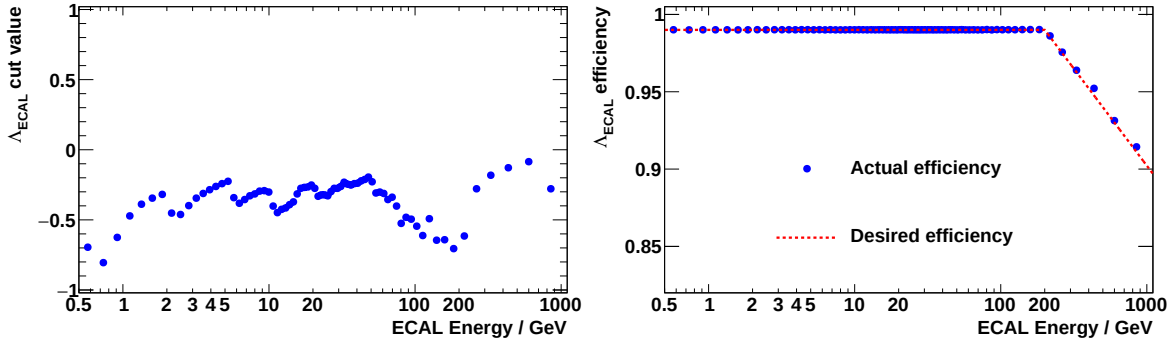

(a) ECAL estimator cut value

(b) ECAL estimator cut efficiency

Figure 4.45: Chosen ECAL estimator efficiency for the analysis of the all-tracks sample. The left plot shows the ECAL estimator cut value that is used in the analysis. The visible structures originate in different training intervals used to train the ECAL estimator. The right plot shows the ECAL estimator efficiency $\epsilon_{\text{ecal}}(E)$ as function of energy. The dashed red line in the right plot represents the desired ECAL estimator efficiency and the blue symbols the actual efficiency in each energy bin, determined by a one-dimensional TRD template fit on the negative rigidity sample on ISS data.

Figure 4.45(b) shows that the efficiency in the highest energy bin in the analysis is $\approx 70\,\%$. The event counts extracted from the two-dimensional fit procedure must be increased by approximately $\approx 30\,\%$ to account for the loss of statistics due to the imposed cut on the ECAL estimator. Likewise all other energy bins need a correction, which decreases with decreasing energy.

It is important to note that the procedure to extract this efficiency from ISS data is necessary as the Monte-Carlo simulation cannot reproduce the ECAL estimator efficiency in the current generation of the simulation software (B1092), as the lateral shower shape is not correctly described, above $\approx 200\,\text{GeV}$. Therefore the ISS data needs to be used to extract the efficiency of the ECAL estimator.

The presented optimization procedure is very useful to determine the cut value η_{ecal} for the ECAL estimator. However there is no uncertainty associated with the efficiency $N_{e^-}/N^0_{e^-}$ that stem from the two independent template fits. This explains the absence of errors bars on the blue symbols in Fig. 4.45(b). The number of events after applying the ECAL estimator cut is a subset of the number of events without imposing a cut on the ECAL estimator.

Therefore there is no straight-forward solution to extract the efficiency with an associated uncertainty using this technique.

A statistically sound method to extract the ECAL estimator efficiency with uncertainty is to carry out *one* template fit simultaneously on two disjoint samples: those events that pass the ECAL estimator cut ("passed sample") and those events that do not pass the cut ("failed sample").

$$\begin{aligned} N_{e^-,\,\text{passed}} &= N_{e^-} \cdot \epsilon_{\text{sig}}; \quad N_{e^-,\,\text{failed}} = N_{e^-} \cdot (1 - \epsilon_{\text{sig}}), \\ N_{p^-,\,\text{passed}} &= N_{p^-} \cdot \epsilon_{\text{bkg}}; \quad N_{p^-,\,\text{failed}} = N_{p^-} \cdot (1 - \epsilon_{\text{bkg}}). \end{aligned} \tag{4.17}$$

Four fit parameters are used to describe both data samples: two event counts N_{e^-}, N_{p^-} and two efficiencies ϵ_{sig}, ϵ_{bkg} - coupling the disjoint data samples (Eq. (4.17)). The cut value of the ECAL estimator - η_{ecal} - for which the signal efficiency and uncertainty is determined by the simultaneous fit is given by the aforementioned optimization procedure. The goal of the simultaneous fit method is to confirm the signal efficiency as determined by the optimization procedure and to additionally quote an uncertainty on the efficiency value.

Figure 4.46 shows the fit results in an example energy bin. Both samples are described accurately, confirmed by good χ^2/dof values in both cases. The simultaneous fit procedure directly yields the number of electrons / charge-confused protons without imposing a cut on the ECAL estimator as well as the efficiency on the signal / background simple, if the cut is applied.

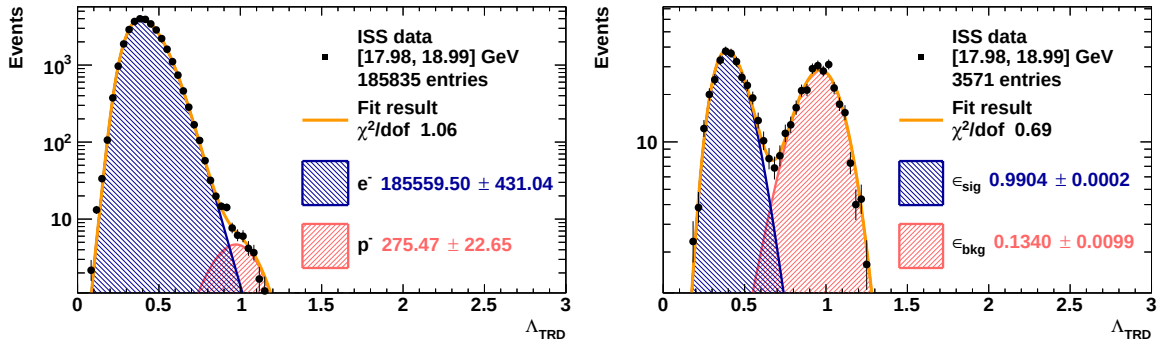

(a) Events that pass the ECAL estimator cut

(b) Events that do not pass the ECAL estimator cut

Figure 4.46: Results of the simultaneous fit to extract the ECAL estimator efficiency in the energy bin 17.98 – 18.99 GeV for the all-tracks sample. The dark blue area corresponds to the electron template, the light red area to the charge-confused proton template and the orange line to the sum of all templates.

To verify the absence of a bias in the simultaneous fit method, a bootstrap [Efron1979] method is used: The idea of bootstrapping is to repeat the fit procedure M times on sub-samples of the original data sample - which contains N_{all} events. The number of events N in each sub-sample is generated by a random number generator following a Poisson distribution, such that $\text{Prob}(N) = 1/N! \cdot \exp(-N_{\text{all}}) \cdot N_{\text{all}}^N$. N events are randomly selected out of the $[1, N_{\text{all}}]$ in the original data sample. These N events form the sub-sample, specific for the m^{th} iteration of the bootstrap procedure.

The fit procedure is now executed $M \approx O(100)$ times. In each iteration the signal efficiency is recorded. The RMS of the signal efficiency distribution is an estimate of the true uncertainty of the signal efficiency. If the original uncertainty estimation, performed on the full data sample, is unbiased, it should be approximately equal to the RMS of the signal efficiency distribution. Furthermore the mean value of the signal efficiency distribution should be approximately equal to the results of a single fit, obtained on the full data sample, within the quoted uncertainties.

Figure 4.47 shows a comparison between the desired efficiency, the efficiency from the simultaneous fit method and the efficiency from the bootstrap method. All results are in excellent agreement. The efficiency and uncertainty presented here is unbiased and a correct measure of the ECAL estimator efficiency on ISS data.

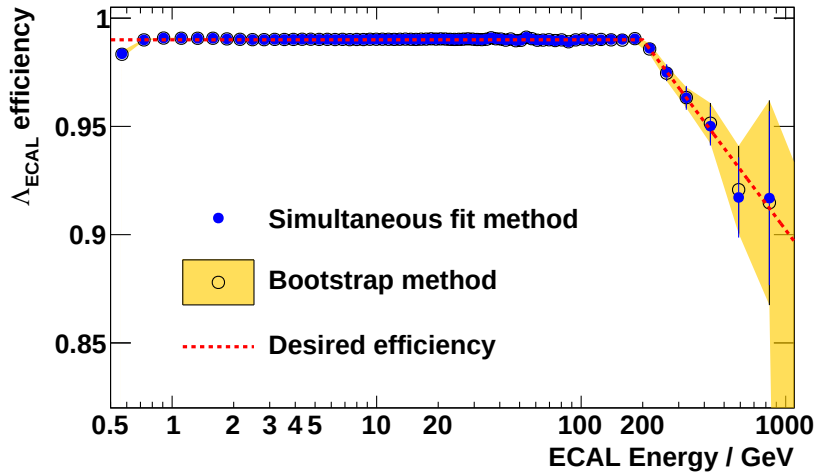

Figure 4.47: Final result showing the ECAL estimator efficiency $\epsilon_{\text{ecal}}(E)$ as function of energy derived using two different methods. The dashed red line represents the desired ECAL estimator efficiency and the blue symbols the actual efficiency in each energy bin, determined by a simultaneous fit on the passed/failed data sample. The black open symbols belong to the efficiency determined by the bootstrap method and the orange band represents the associated uncertainty.

4.5.2 Trigger efficiency

In Section 3.8 the AMS-02 logic was described in detail. In the electron and positron analysis the data sample is mainly triggered by the **Single charged** and the **Electrons** trigger, as shown in Fig. 4.48.

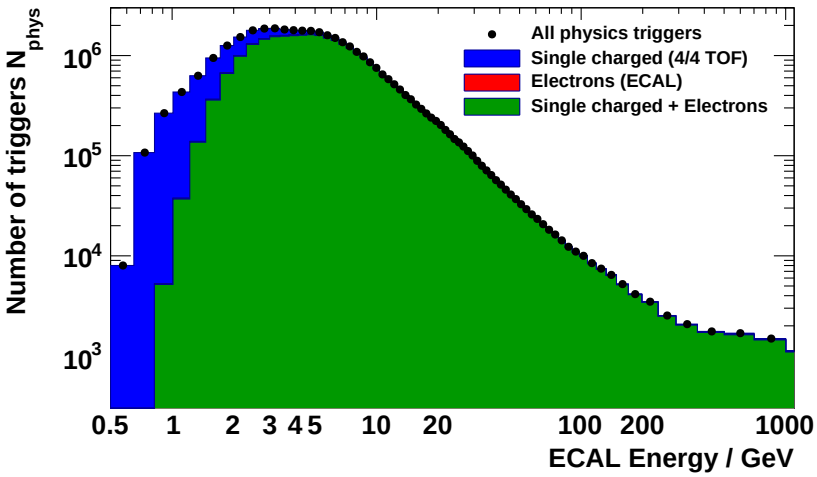

Figure 4.48: Decomposition of the physics triggers as stacked histograms. Two main trigger branches form the physics trigger for the $e^{\pm}$ analysis: the **Single charged** trigger and the **Electrons** trigger.

The efficiency for the **Electrons** trigger rapidly decreases below 2 GeV, thus $e^{\pm}$ at these energies are only triggered by the **Single charged** trigger. For all energies above 2 GeV the **Electrons** trigger is not visible on a logarithmic scale since most events are triggered using both trigger branches: the combined **Single charged + Electrons** trigger (dark green).

The trigger efficiency $\epsilon_{\text{trigger}}(E)$ is approximated by the ratio between all events triggered by any of the physics triggers and all available triggers, including the unbiased triggers.

By intention an unbiased event should only be triggered either via the **Unbiased charge** trigger or via the **Unbiased EM** trigger, otherwise the prescaling factor to use is undefined. The analysis shows that in the final data sample for the electron and positron analysis there are N_{phys} events with physics trigger, N_{tof} events with an **Unbiased charge** trigger (prescaled by $f_{\text{tof}} = 100$) and N_{ecal} events with an **Unbiased EM** trigger (prescaled by $f_{\text{ecal}} = 1000$). Due to a bug in the trigger hardware there is a non-negligible amount of events that have both trigger bits set: $N_{\text{tof+ecal}}$. The prescaling factor $f_{\text{tof+ecal}}$ for these events can be calculated via probability theory:

$$\begin{aligned} p(\text{tof} \cup \text{ecal}) &= p(\text{tof}) + p(\text{ecal}) - p(\text{tof} \cap \text{ecal}) = \frac{1}{f_{\text{tof}}} + \frac{1}{f_{\text{ecal}}} - \frac{1}{f_{\text{tof}} \cdot f_{\text{ecal}}}, \\ f_{\text{tof+ecal}} &= 1/p(\text{tof} \cup \text{ecal}) \approx 90.99 \end{aligned} \tag{4.18}$$

Figure 4.49 shows the distribution of the unbiased triggers as function of energy.

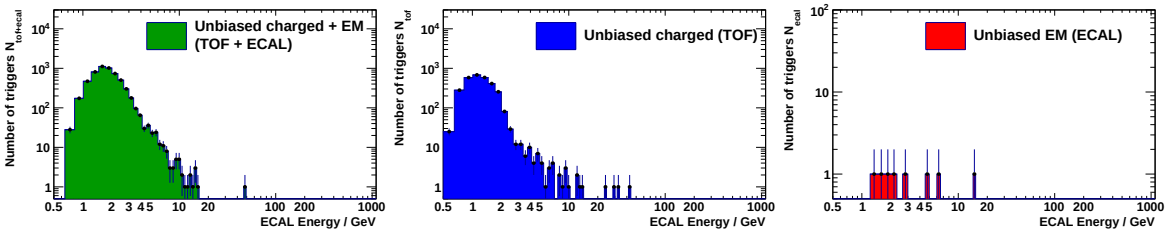

(a) Unbiased charged + EM triggers **(b) Unbiased charged** triggers **(c) Unbiased EM** triggers

Figure 4.49: Distribution of the unbiased triggers as function of energy. The most abundant unbiased triggers are the **Unbiased charged + Unbiased EM** triggers, followed by the **Unbiased charged** triggers. The least abundant triggers are the **Unbiased EM** triggers.

After knowing the prescaling factors and the number of unbiased and physics triggers as function of energy, the trigger efficiency can be approximated from ISS data:

$$\epsilon_{\text{trigger}}(E) = \frac{N_{\text{phys}}}{N_{\text{phys}} + f_{\text{tof}} \cdot N_{\text{tof}} + f_{\text{ecal}} \cdot N_{\text{ecal}} + f_{\text{tof+ecal}} \cdot N_{\text{tof+ecal}}}. \tag{4.19}$$

The results are shown in Fig. 4.50 including a comparison with the Monte-Carlo simulation. There are discrepancies below 2 GeV, where the Monte-Carlo simulation predicts a higher efficiency compared to ISS data, due to an imperfect simulation of the **Unbiased EM** trigger. Overall the results are in good agreement.

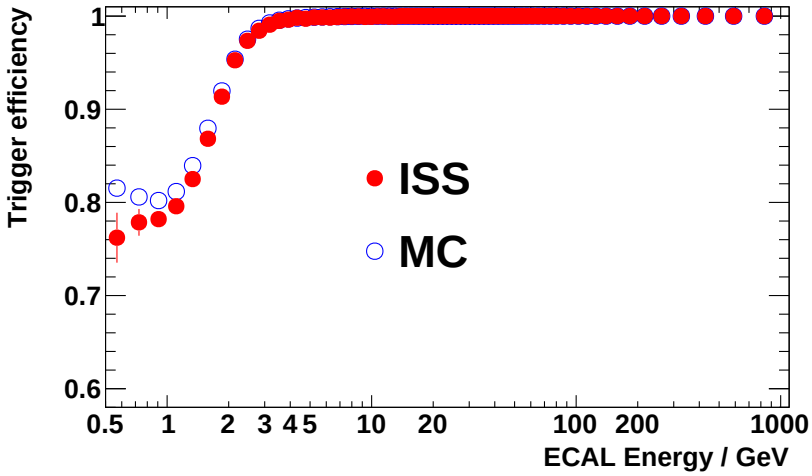

Figure 4.50: Comparison of the trigger efficiency $\epsilon_{\text{trigger}}(E)$ as function of energy between ISS data and Monte-Carlo simulation. The red symbols represent the trigger efficiency determined from ISS data according to Eq. (4.19). The blue symbols show the trigger efficiency determined by the Monte-Carlo simulation, by counting the number of unbiased and physics triggers.

4.5.3 Measuring time

To determine the measuring time the amount of seconds between the first event of the data taking period T_0 and the last event of the data taking period T_1 is counted. This defines the "exposure time", where AMS-02 was operational and could record events. Afterwards each second will be tested if it is usable for physics analysis, by applying the detector quality cuts (Section 4.3.1). The amount of seconds that pass the detector quality cuts define the time period for which the "measuring time" $T(E)$ will be computed.

The live-time fraction $f_{\text{live-time}}(t)$, defined in Section 3.8, needs to be taken into account for each of the seconds. Figure 4.51 shows the trigger rate and live-time as function of the ISS position, projected to geographic longitude/latitude.

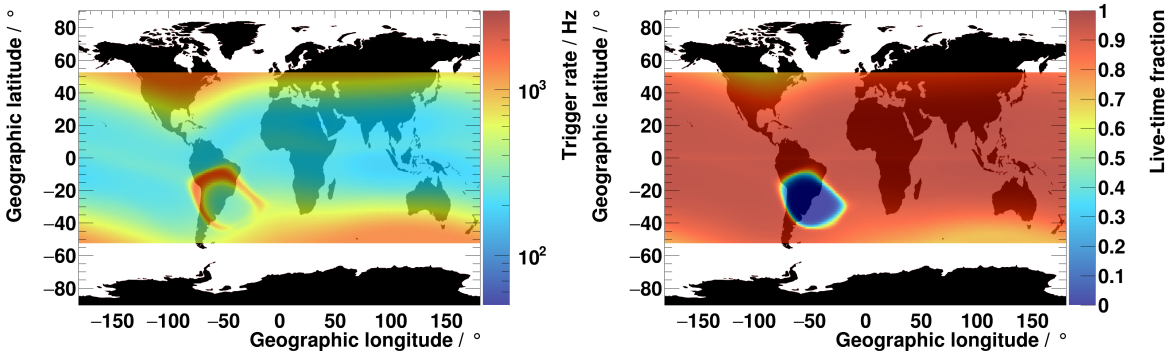

(a) Trigger rate vs. ISS position

(b) Live-time fraction vs. ISS position

Figure 4.51: The left plot shows the trigger rate of the experiment vs. ISS position and the right plot shows the live-time fraction of the experiment vs. ISS position. The live-time fraction is exceptionally low at the South Atlantic Anomaly (SAA) [Kurnosova1962] due to an intense flux of low-energy particles, filling the detector.

In certain geographic locations - like the SAA [Kurnosova1962] - the live-time fraction can become exceptionally low and the trigger rate increases. The live-time fraction is correlated with the geomagnetic cut-off rigidity R_c: if R_c is low (e.g. near the poles) many more low energetic particles can reach AMS-02 and thus the live-time fraction decreases, due to an increase in the trigger rate. The detector quality cuts reject periods where the live-time fraction is below 50 %, which effectively masks out the SAA for analysis, where the flux of low-energy particles is intense.

The energy-independent measuring time is equal to the sum of the live-time fraction of all seconds in the measuring time period:

$$T = \sum_{t=T_0}^{T_1} f_{\text{live-time}}(t). \tag{4.20}$$

Figure 4.52 shows the live-time fraction distribution of all seconds that form the measuring time. For the period **May 20$^{\text{th}}$, 2011 - November 12$^{\text{th}}$, 2017** the measuring time - weighted by the live-time fraction - is **1883.61 days**.

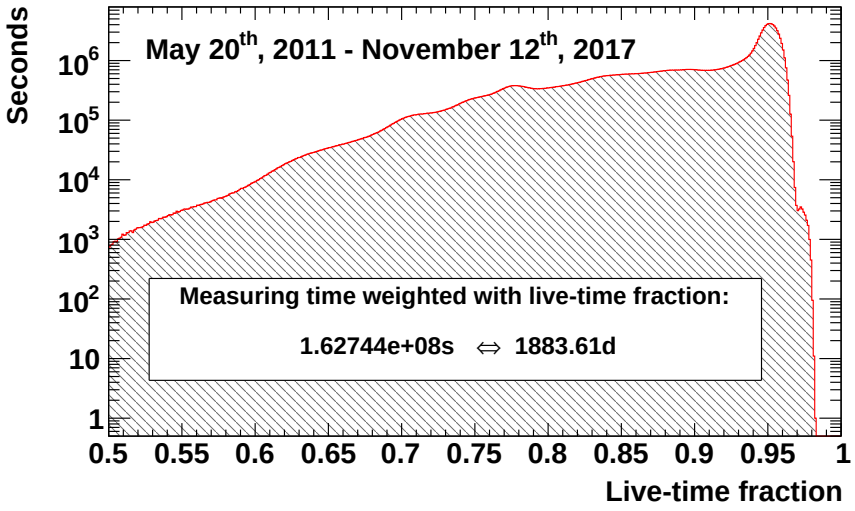

Figure 4.52: The plot shows the distribution of the live-time fraction of the experiment for all seconds that form the measuring time period. The distribution peaks at 95 % with a long tail towards smaller live-time fractions. Live-time fractions below 50 % are excluded for analysis by the detector quality cuts.

The energy dependence of the measuring time $T(E)$ arises from the geomagnetic cut-off, as presented in Section 2.5. It was shown that the geomagnetic cut-off rigidity R_c changes as function of the geomagnetic longitude/latitude.

Particles below a certain rigidity - R_c - cannot penetrate the magnetosphere which surrounds the earth and thus cannot be measured with AMS-02. The geomagnetic cut-off rigidity R_c changes as function of longitude and latitude. At the pole regions the cut-off rigidity is minimal, due to the direction of the magnetic fields lines, which are directed towards earth. This means that low-rigidity particles can be detected effectively only at the pole regions, not in equatorial regions. This leads to an energy dependence of the measuring time $T(E)$. Since the maximum value of the geomagnetic cut-off rigidity R_c is ≈ 25 GV, the energy dependence of the measuring time vanishes above this energy.

For the $e^{\pm}$ analysis, only events are allowed where the measured ECAL energy E_{measured} exceeds the maximum geomagnetic cut-off rigidity R_c times a safety factor f_{safety} in a 25° field-of-view. The requirement imposed for the analysis is: $E_{j,\,\text{low}} > f_{\text{safety}} \cdot R_c$, where $E_{j,\,\text{low}}$ denotes the minimum bin energy of bin j, in which the energy E_{measured} was classified. In this work the cut-off rigidity is calculated using the Størmer formula[13] (Section 2.5).

For each energy bin j of the analysis the energy-dependent measuring time T_j can be calculated:

$$T_j = \sum_{t=T_0}^{T_1} \begin{cases} f_{\text{live-time}}(t) & E_{j,\,\text{low}} > f_{\text{safety}} \cdot R_c \\ 0 & \text{otherwise} \end{cases} \tag{4.21}$$

The measuring time T_j for each energy bin j can be combined into a single histogram $T(E)$, which is shown in Fig. 4.53. The detector quality cuts, the live-time fraction of the experiment and most importantly the geomagnetic cut-off, which is the reason for the energy dependence, are all taken into account.

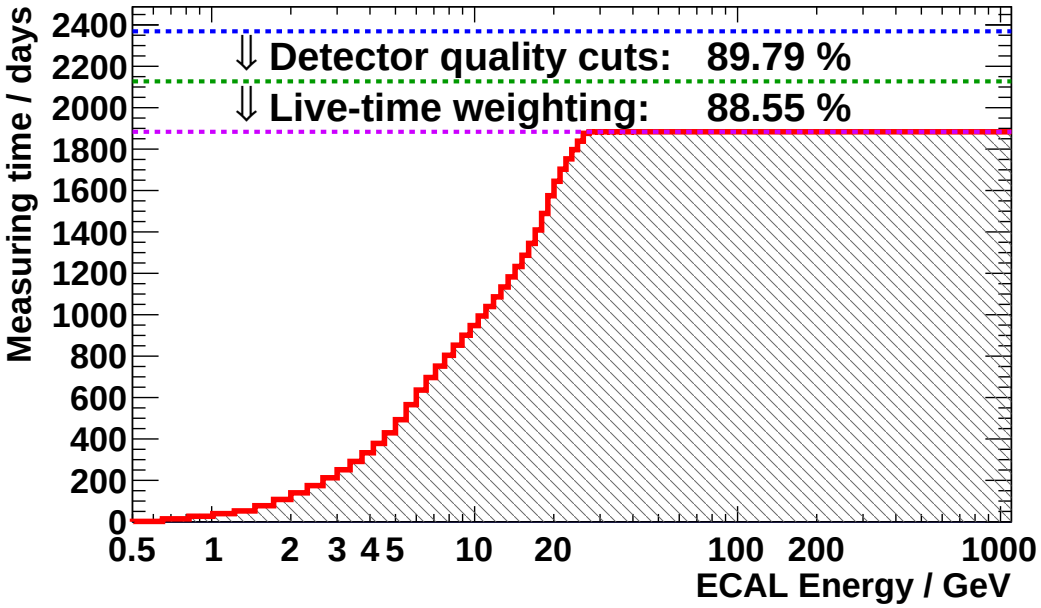

Figure 4.53: Visualization of the measurement time $T(E)$ as function of energy. The dashed blue line marks the nominal exposure time for the period **May 20th, 2011 - November 11th, 2017**. The dashed green line denotes the measuring time after applying the detector quality cuts. The dashed violet line marks the energy-independent measuring time, after accounting for the live-time fraction. Finally the **red line** represents the measuring time $T(E)$ after taking the geomagnetic cut-off into account.

The exposure time for the period **May 20th, 2011 - November 11th, 2017** equals to **2368.94 days**. After applying the detector quality cuts the remaining measuring time equals to **2127.17 days**. When taking the live-time into account a total of **1883.61 days** remain. This number remains constant above ≈ 25 GeV.

[13] Several methods were tested to calculate the geomagnetic cut-off rigidity, such as the IGRF [Thebault2015] cut-off evaluated using a backtracing technique, as described in Ref. [Fiandrini2015]. All results are compatible and the Størmer approach was chosen, which is easy to compute.

4.5.4 Acceptance

The acceptance is one of the most important ingredients in the $e^{\pm}$ flux analysis: a large acceptance corresponds to a large number of events that can be collected. Thus the effective acceptance - including all selection efficiencies - should be as high as possible. The choice of subdetectors that participate in the data analysis impose a limit on the maximum acceptance that can be achieved: the geometrical acceptance A_{geom}. The geometrical acceptance can be calculated either using a standalone simulation that accurately models the geometry of all subdetectors, or by using the AMS-02 Monte-Carlo simulation, based on GEANT4 [Agostinelli2003; Allison2006; Allison2016].

The full AMS-02 model is placed inside a hypothetical cube with an edge length of 3.9 m. Above the top surface $S_{\text{generator}}$ an isotropic flux is generated of so-called **"charged geantinos"**. Charged geantinos are artificial particles that can be used as geometrical probe. They are only transported through the AMS-02 model, but do not interact. The direction and rigidity is chosen randomly above the top surface to simulate an isotropic flux.

According to Sullivan [Sullivan1971] the only ingredients needed to compute the geometrical acceptance are the number of events that triggered the experiment $N_{\text{triggered}}$ and the number of generated events $N_{\text{generated}}$ above the top surface $S_{\text{generator}} = 3.9 \cdot 3.9\,\text{m}^2$. Using these numbers the geometrical acceptance can be computed according to:

$$A_{\text{geom}} = \pi \cdot S_{\text{generator}} \cdot \frac{N_{\text{triggered}}}{N_{\text{generated}}}.$$

No selection cuts are applied in order to extract $N_{\text{triggered}}$ from the Monte-Carlo simulation for this study, but it is required that the geantino can geometrically reach the TRD, the TOF, the tracker and the ECAL. The resulting geometrical acceptance is $A_{\text{geom}} \approx 735\,\text{cm}^2\,\text{sr}$. Thus the acceptance $A_{e^{\pm}}^{\text{MC}}(E)$ is strictly smaller than or equal to A_{geom}, since $A_{e^{\pm}}^{\text{MC}}(E)$ includes the efficiency of several selection cuts that further reduce the acceptance.

$A_{e^{\pm}}^{\text{MC}}(E)$ is derived in the same way as the geometrical acceptance, but using electrons or positrons instead of charged geantinos. The main difference is that interactions are allowed and all selection cuts are applied, except the **"physics trigger"** requirement and the final ECAL estimator cut (derived using the iterative procedure described in Section 4.5.1). The physics trigger requirement is not part of the acceptance as its efficiency $\epsilon_{\text{trigger}}(E)$ is determined directly from ISS data and thus should not enter the acceptance, to avoid double-counting. The ECAL estimator cut is not applied in the Monte-Carlo simulation, since its sole purpose is to reduce proton background, which is not present in the electron Monte-Carlo simulation. Furthermore its efficiency ϵ_{ecal}(E) is determined directly from the ISS data and thus its efficiency is not part of the acceptance.

Figure 4.54 shows the acceptance $A_{e^-}^{\text{MC}}(E)$ from the electron Monte-Carlo simulation as function of the generated energy of the simulated particles. The positron acceptance $A_{e^+}^{\text{MC}}(E)$ is slightly higher than the electron acceptance at low energies, due to differences in the scattering cross-sections, which will be explained in Section 4.5.5.

To ensure the validity of the acceptance $A_{e^-}^{\text{MC}}(E)$ from the electron Monte-Carlo simulation every cut efficiency needs to be verified using ISS data. The goal is to derive a correction factor $(1 + \delta(E))$, which absorbs any differences between the ISS data and the Monte-Carlo simulation, to ensure that the acceptance describes the ISS data properly.

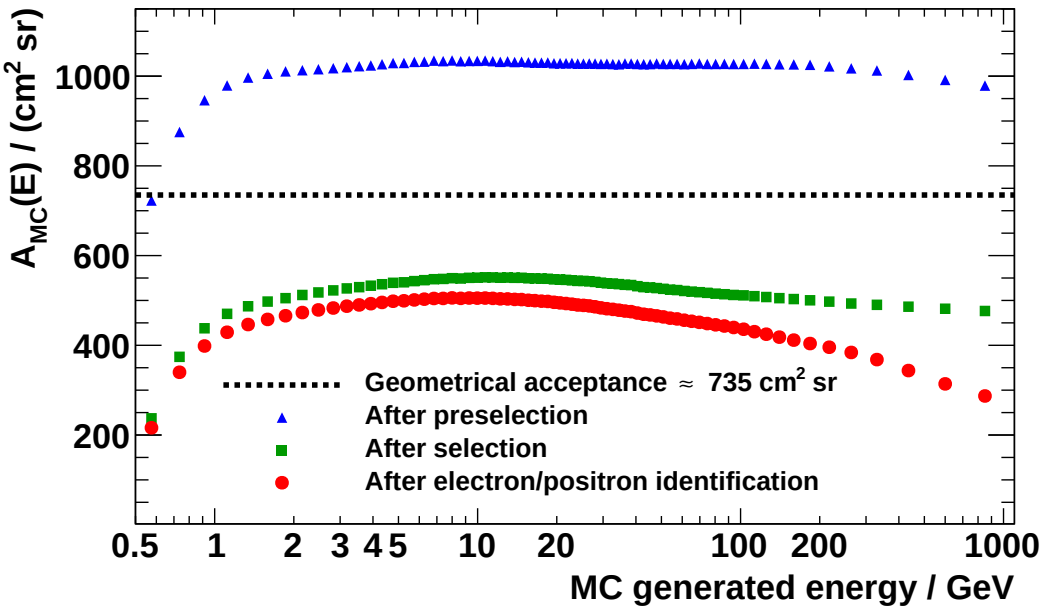

Figure 4.54: Determination of the acceptance $A_{e^-}^{\mathrm{MC}}(E)$ from the electron Monte-Carlo simulation as function of the generated energy of the simulated particles. The black dashed line shows the geometrical acceptance A_{geom}. The other symbols show the acceptance after applying the preselection, selection and $e^{\pm}$ identification cuts. The acceptance after applying only the preselection cuts is higher than the geometrical acceptance, since in the preselection tracker requirements are not imposed yet, unlike in the definition of the geometrical acceptance. After applying the selection cuts, the acceptance curve is smaller than the geometrical acceptance.

In order to determine the correction $(1 + \delta^c(E))$, a negative rigidity sample (**"tag sample"**) is selected for every cut c using information from the detectors unrelated to that cut. The efficiency of each cut c is compared between ISS data and electron Monte-Carlo simulation, by taking the ratio ISS efficiency over MC efficiency. If the ratio differs from unity, it is parameterized using a simple model, e.g. a constant or a straight line. The best matching model is fit to the ratio. Afterwards it will be tested if the deviation from unity is significant, according to the uncertainty of the fit parameters.

Since all correction factors $(1 + \delta^c(E))$ are uncorrelated by a careful construction of the tag samples, the final correction $(1 + \delta(E))$ is the product of all individual significant correction factors $(1 + \delta^c(E))$:

$$1 + \delta(E) = \prod_c (1 + \delta^c(E)). \tag{4.22}$$

All tag cuts used to prepare the tag samples, for each cut c, are listed in Appendix A.5. Seven cuts exhibit a significant ISS/Monte-Carlo deviation and in all cases two simple models were sufficient to parameterize the ISS over Monte-Carlo cut efficiency ratio:

(a) **Straight line in logarithmic scale**
Parameters: p_0 = Offset, p_1 = Slope

The correction is significant, if $|1 - p_0| \geq 2 \cdot \sigma_{p_0}$ or $|1 - p_0| \geq 0.005$.

$$m_1(E; p_0, p_1) = p_0 + p_1 \cdot \log_{10}(E) \tag{4.23}$$

(b) **Two straight lines with a break in logarithmic scale**
Parameters: p_0 = Offset of 1st line, p_1 = Slope of 1st line, p_2 = Slope of 2nd line, p_3 = Break
The correction is always considered significant

$$m_2(E; p_0, p_1, p_2, p_3) = \begin{cases} p_0 + p_1 \cdot \log_{10}(E) & E \leq p_3 \\ \left(m_2(p_3) - p_2 \cdot \log_{10}(p_3)\right) + p_2 \cdot \log_{10}(E) & E > p_3 \end{cases} \tag{4.24}$$

The seven cuts with a significant ISS/Monte-Carlo correction will be presented in the following:

1. Preselection cut: **"At least one useful TRD track"** &
2. Preselection cut: **"At least one useful TOF cluster combination"**

Figure 4.55 shows the summary of the tag & probe method for both cuts. The tag sample selection cuts are given in Appendices A.6.1 and A.6.2. The cut efficiency is compared between ISS data and Monte-Carlo simulation up to 250 GeV - above that energy a cut-based identification of electrons is not pure enough anymore.

At 0.5 GeV a deviation of ≈ 1.5 % between the ISS and Monte-Carlo efficiency is exhibited for the TRD track requirement, which gradually decreases until 5 GeV. The TOF track requirement shows a similar shape, albeit with a smaller deviation of below ≈ 1 % at 0.5 GeV.

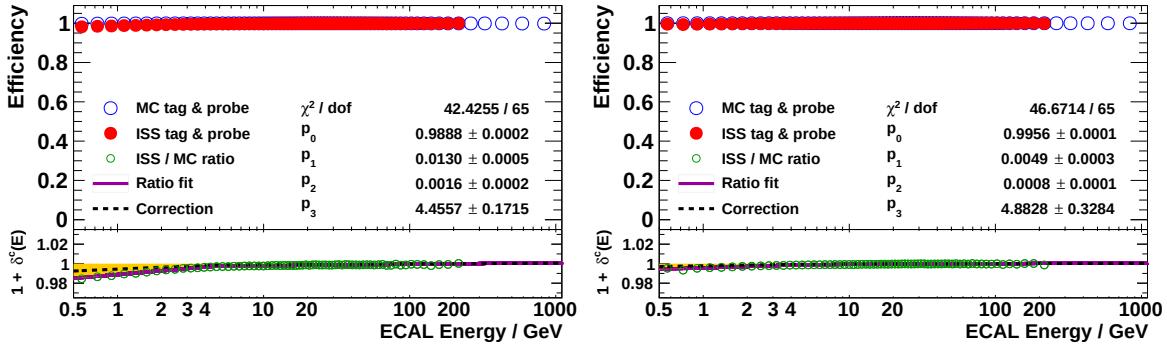

(a) "At least one useful TRD track" **(b) "At least one useful TOF cluster combination"**

Figure 4.55: Determination of the Data/Monte-Carlo correction factors $(1+\delta^c(E))$ for the preselection cuts: **"At least one useful TRD track"** (left) and **"At least one useful TOF cluster combination"** (right) (Section 4.3.2 - Items 2 and 3). The open blue symbols in the upper plots show the cut efficiency determined on the electron Monte-Carlo simulation on a dedicated sample: the tag sample. The filled red symbols in the upper plots show the cut efficiency determined from ISS data using the same tag cuts. The lower plots show the ratio ISS efficiency over MC efficiency as open green symbols. Equation (4.24) is fit to the ratios, represented as magenta lines. The dashed black lines show that half of the deviation from unity is taken as correction to the Monte-Carlo acceptance $A_{e^-}^{\mathrm{MC}}(E)$. The associated systematic uncertainty is visualized by the orange bands.

The Monte-Carlo efficiency is higher than the observed efficiency on ISS data for both cuts. Since it is not known whether the description of the efficiency in the Monte-Carlo simulation is correct or whether the ISS data efficiency is correct, a conservative approach is chosen: use half of the deviation as correction to the Monte-Carlo acceptance. The uncertainty on the correction due to the fit parameter uncertainty is added in quadrature with the deviation from unity and treated as systematic uncertainty.

3. Selection cut: **“Upper TOF charge”** &
4. Selection cut: **“Enough active layers in TRD”**

Figure 4.56 shows the summary of the tag & probe method for both cuts. The tag sample selection cuts are given in Appendices A.6.3 and A.6.4. The cut efficiency is compared between ISS data and Monte-Carlo simulation up to 250 GeV - above that energy a cut-based identification of electrons is not pure enough anymore.

Both cuts exhibit only a small deviation from the predicted efficiency by the Monte-Carlo simulation. The upper TOF charge measurement ISS/MC ratio is best parameterized with a straight line in logarithmic scale. The TRD active layers requirement shows a deviation of $\approx 1\,\%$ at 0.5 GeV, which vanishes above 5 GeV and thus the associated ISS/MC ratio is best described with two connected straight lines including a break.

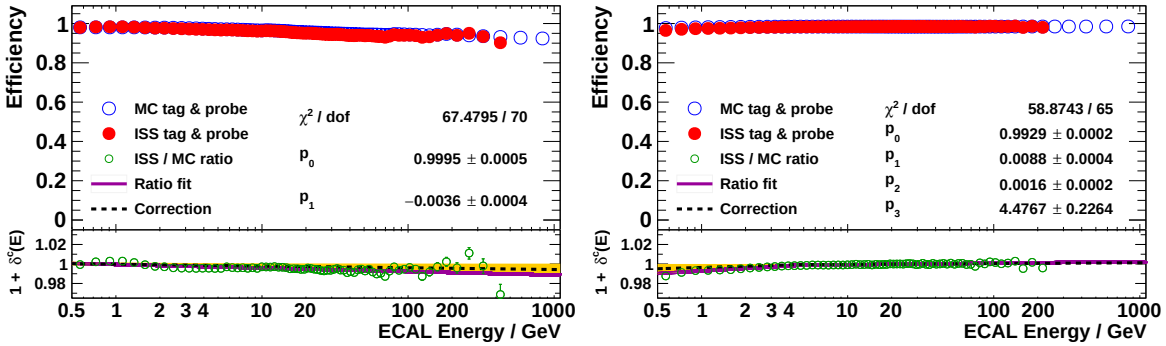

(a) “Upper TOF charge” **(b) “Enough active layers in TRD”**

Figure 4.56: Determination of the Data/Monte-Carlo correction factors $(1 + \delta^c(E))$ for the selection cuts: **“Upper TOF charge”** (left) and **“Enough active layers in TRD”** (right) (Section 4.3.3 - Items 2 and 3). The open blue symbols in the upper plots show the cut efficiency determined on the electron Monte-Carlo simulation on a dedicated sample: the tag sample. The filled red symbols in the upper plots show the cut efficiency determined from ISS data using the same tag cuts. The lower plots show the ratio ISS efficiency over MC efficiency as open green symbols. Equation (4.23) is fit to the left ratio, Eq. (4.24) is fit to the right ratio, represented as magenta lines. The dashed black lines show that half of the deviation from unity is taken as correction to the Monte-Carlo acceptance $A_{e^-}^{\mathrm{MC}}(E)$. The associated systematic uncertainty is visualized by the orange bands.

Since it is not known whether the description of the efficiency in the Monte-Carlo simulation is correct or whether the ISS data sample is pure, a conservative approach is chosen: use half of the deviation as correction to the Monte-Carlo acceptance. The uncertainty on the correction due to the fit parameter uncertainty is added in quadrature with the deviation from unity and treated as systematic uncertainty.

5. Selection cut: **“Tracker track goodness-of-fit in Y-projection”**

Figure 4.57 shows the summary of the tag & probe method for this cut. The tag sample selection cuts are given in Appendix A.6.5. The remaining three cuts to be tested (including this one) will yield the largest Data/Monte-Carlo correction factors $(1 + \delta^c(E))$. It is crucial to ensure that they are valid up to the highest energies and the associated systematic uncertainties are as small as possible.

At this stage of the analysis all subdetector information to select e^- enhanced samples are available - most noticeable: two out of three tracker quality cuts were applied (charge measurement and tracker hit pattern requirements). This gives the opportunity to avoid cut based tag & probe methods, but instead perform template fits in the TRD estimator to determine the efficiencies. The benefit is that one no longer has to ensure a minimum contamination of charge-confused protons in the negative rigidity sample, since the template fit is able to discriminate between electrons and charge-confused protons.

Squares as markers instead of circles for the efficiencies in the tag & probe method summary plot - Fig. 4.57 - indicate that the method to determine them has changed from a cut-based approach to a template-fit approach. Furthermore the energy range that is tested could be doubled from 250 GeV to 500 GeV.

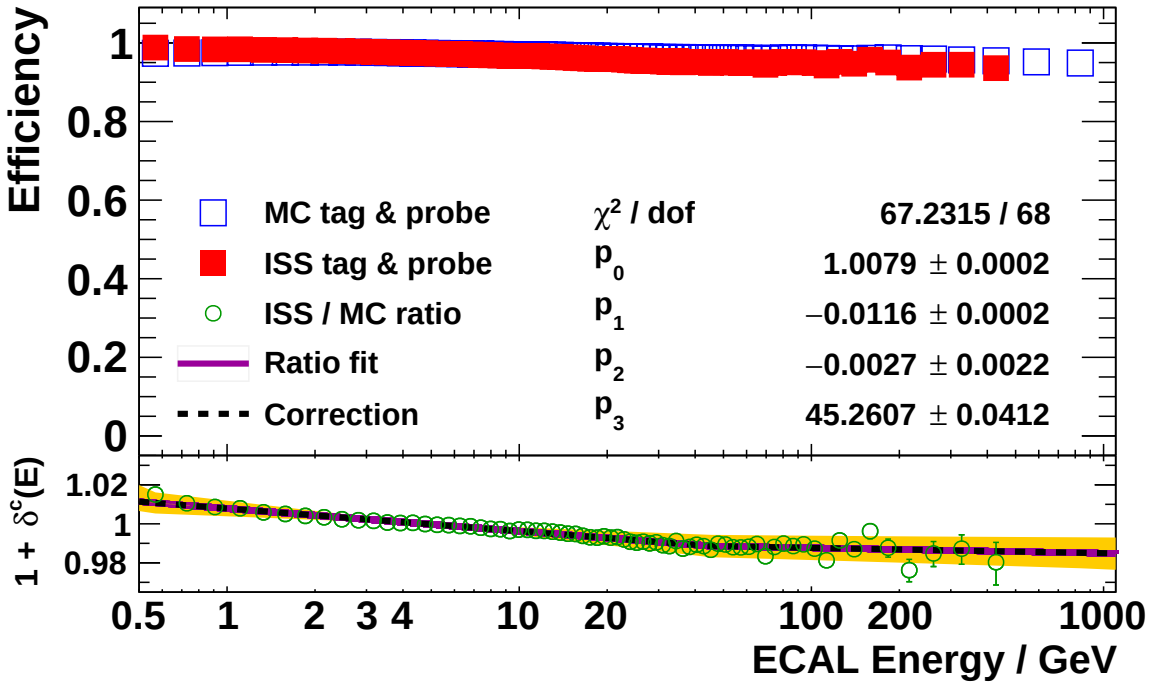

Figure 4.57: Determination of the Data/Monte-Carlo correction factor $(1 + \delta^c(E))$ for the selection cut: **"Tracker track goodness-of-fit in Y-projection"** (Section 4.3.3 - Item 7). The open blue symbols in the upper plots show the cut efficiency determined on the electron Monte-Carlo simulation on a dedicated sample: the tag sample. The filled red symbols in the upper plots show the cut efficiency determined from ISS data using the same tag cuts. The lower plots show the ratio ISS efficiency over MC efficiency as open green symbols. Equation (4.24) is fit to the ratio, represented as magenta line. The dashed black line shows that half of the deviation from unity is taken as correction to the Monte-Carlo acceptance $A_{e^-}^{\mathrm{MC}}(E)$. The associated systematic uncertainty is visualized by the orange band.

Due to the introduction of the template-fit method to extract the efficiencies it is no longer necessary to question the purity of the ISS tag sample. The full deviation of the ISS efficiency with respect to the Monte-Carlo efficiency is used as correction factor for the Monte-Carlo acceptance. The systematic uncertainty no longer includes the deviation from unity, but only represents the uncertainty of the correction due to the uncertainty of the model fit parameters.

6. $e^{\pm}$ identification cut: **"Energy ↔ rigidity matching"** &
7. $e^{\pm}$ identification cut: **"Tracker ↔ ECAL matching in X-projection"**

Figure 4.58 shows the summary of the tag & probe method for both cuts. The tag sample selection cuts are given in Appendices A.6.6 and A.6.7.

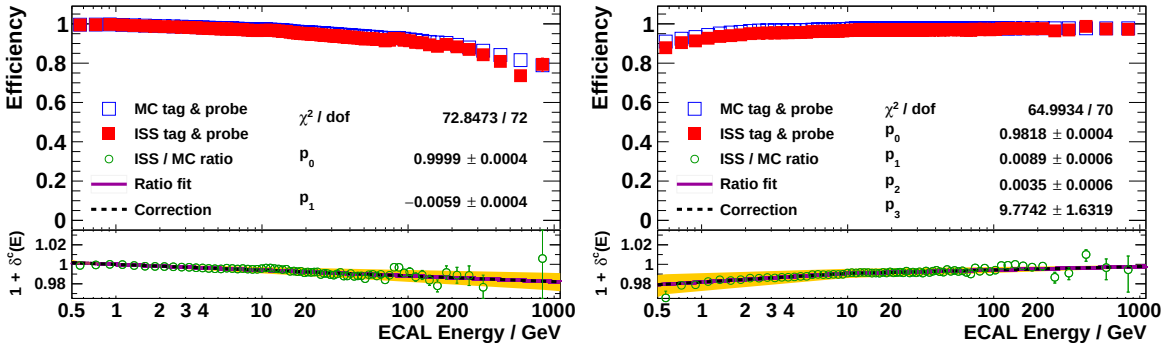

(a) "Energy ↔ rigidity matching" **(b) "Tracker ↔ ECAL matching in X-projection"**

Figure 4.58: Determination of the Data/Monte-Carlo correction factors $(1 + \delta^c(E))$ for the $e^{\pm}$ identification cuts: **"Energy ↔ rigidity matching"** (left) and **"Tracker ↔ ECAL matching in X-projection"** (right) (Section 4.3.4 - Items 1 and 3). The open blue symbols in the upper plots show the cut efficiency determined on the electron Monte-Carlo simulation on a dedicated sample: the tag sample. The filled red symbols in the upper plots show the cut efficiency determined from ISS data using the same tag cuts. The lower plots show the ratio ISS efficiency over MC efficiency as open green symbols. Equation (4.23) is fit to the left ratio, Eq. (4.24) is fit to the right ratio, represented as magenta lines. The dashed black lines show that half of the deviation from unity is taken as correction to the Monte-Carlo acceptance $A_{e^-}^{\mathrm{MC}}(E)$. The associated systematic uncertainty is visualized by the orange bands.

Both ISS/Monte-Carlo efficiency ratios are well parameterized by the chosen models. The ISS efficiency was extracted using the template-fit method and the full deviation of the ISS efficiency with respect to the Monte-Carlo efficiency is used as correction factor for the Monte-Carlo acceptance.

Since all correction factors $(1 + \delta^c(E))$ were determined, the final correction to the acceptance $A(E)$ can be computed, according to Eq. (4.22). The uncertainty on the combined Data/Monte-Carlo correction factor $(1 + \delta(E))$ is obtained by adding all the uncertainty of all individual correction factors $(1 + \delta^c(E))$ in quadrature. The resulting acceptance $A(E)$ is shown in Fig. 4.59 and the correction factor in Fig. 4.60.

Note that the x-axis title no longer states "MC generated energy", as in Fig. 4.54, but "ECAL Energy". The reason for this is that the Data/Monte-Carlo correction factor $(1 + \delta(E))$ was determined as function of the ECAL energy, since it involves ISS data where a generated energy is not available. The ECAL energy must be used as best estimator of the true particle energy on ISS data. If the correction factor $(1 + \delta(E))$, Fig. 4.60, would be large and/or a steeply falling or rising curve as function of energy, this could possibly introduce a bias. To avoid a possible bias the number of passed events and the number of total events as function of ECAL energy need to be unfolded to the "Top-Of-Instrument energy", before taking the ratio passed over total events to determine the efficiency for each cut. This was tested for the "Energy ↔ rigidity matching" cut: the effect is small and thus can be neglected.

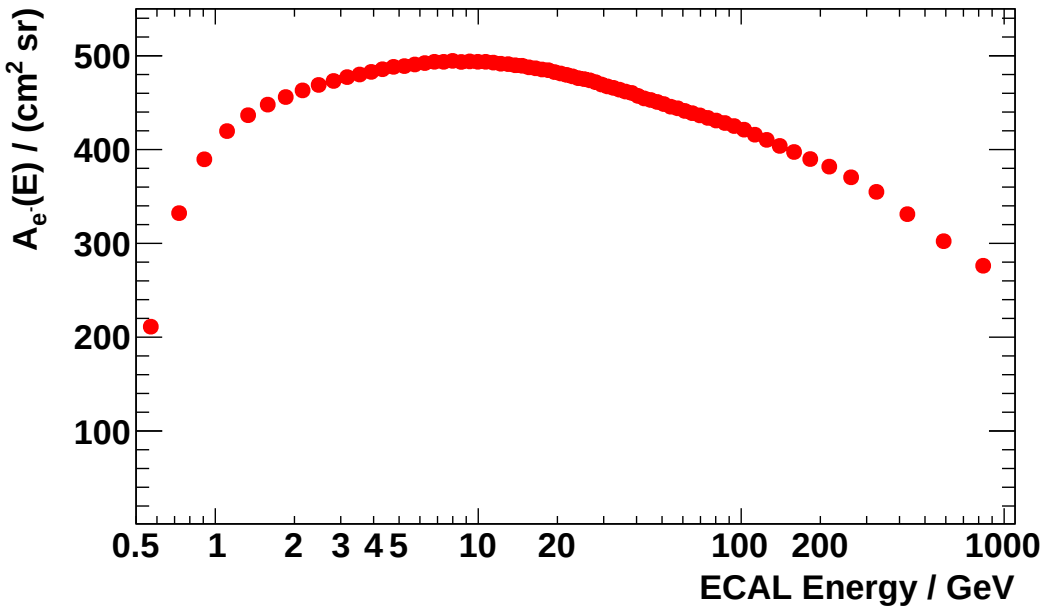

Figure 4.59: Final result of the acceptance $A_{e^-}(E)$ as function of energy, including all Data/Monte-Carlo corrections $(1 + \delta(E))$. The red symbols show that the acceptance is a smooth function with a well-behaving energy dependence.

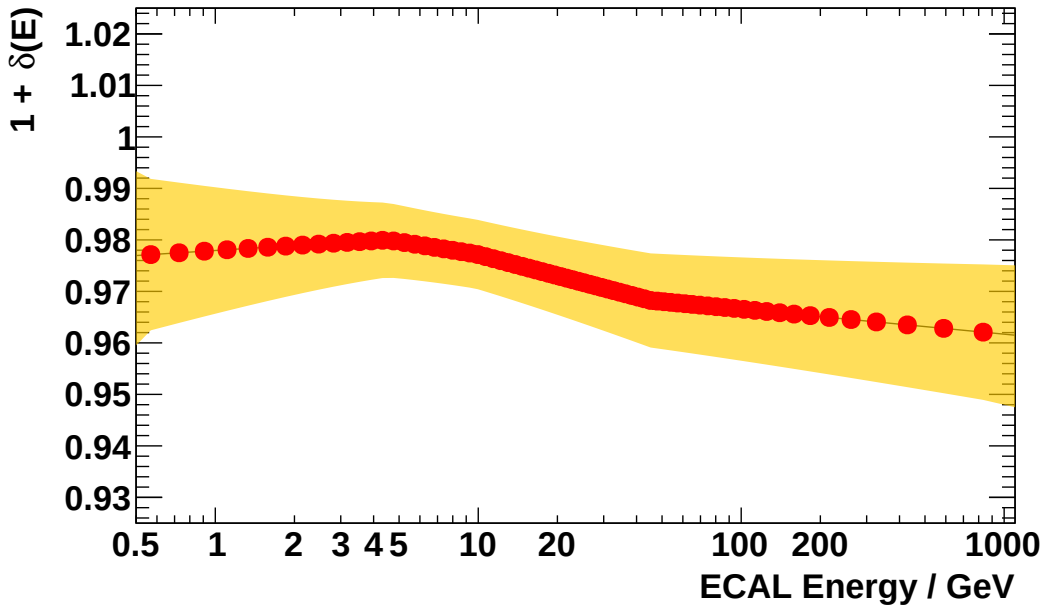

Figure 4.60: The magnitude of the combined Data/Monte-Carlo correction factor $(1 + \delta(E))$ is shown as red symbols. The correction applied to the Monte-Carlo acceptance varies from 2 % at low energies up to 4 % at high energies and is known for all energies better than 1.5 %, indicated by the orange band.

4.5.5 Acceptance asymmetry

The acceptance derived from the electron Monte-Carlo simulation is suitable for electrons but slightly differs for positrons. The scattering cross-section of positrons differs from electrons for scattering by a nuclear coulomb field. The penetration depth in various materials, e.g. C or Si, as well as the multiple scattering is different [Rohrlich1954]. Thus the acceptance determination was repeated using a positron Monte-Carlo simulation, up to 200 GeV.

Figure 4.61 shows the positron over electron acceptance ratio $A_{e^+}(E)/A_{e^-}(E)$. The acceptances differ at most by 0.6 % over all energies. At energies below $\approx$ 8 GeV the acceptances are no longer indistinguishable, but show a small difference in the energy dependence.

To derive the electron flux the acceptance $A_{e^-}(E)$ is used and $A_{e^+}(E)$ to derive the positron flux. For the positron over electron ratio and the positron fraction analysis, the acceptance asymmetry ratio $A_{e^+}(E)/A_{e^-}(E)$ is used as correction factor.

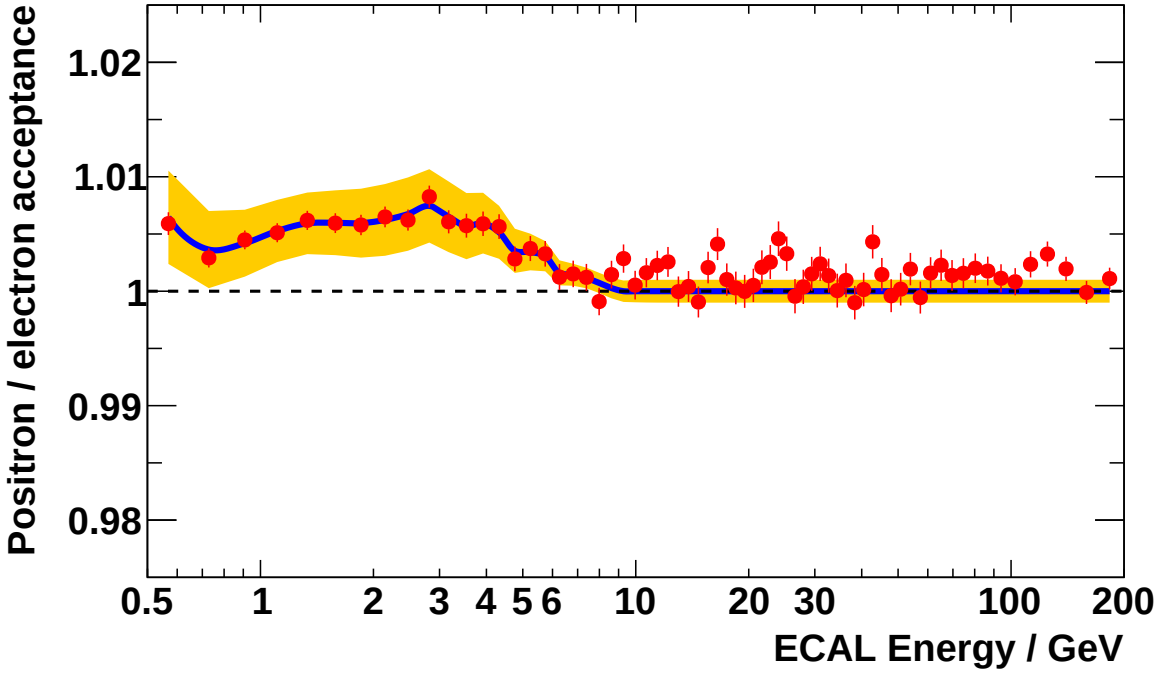

Figure 4.61: Visualization of the positron over electron acceptance ratio $A_{e^+}(E)/A_{e^-}(E)$, shown as red symbols. The difference is around 1 % at 3 GeV where the difference between the electron and the positron acceptance is largest. The blue curve multiplied to the electron acceptance yields the positron acceptance.

The uncertainty indicated by the orange band in Fig. 4.61 is propagated to the uncertainty of the positron acceptance $A_{e^+}(E)$ - the electron acceptance $A_{e^-}(E)$ is not affected. When computing flux ratios, such as the positron/electron ratio or the positron fraction the systematic uncertainty of the acceptance cancels. In those cases the systematic uncertainty of the acceptance asymmetry will be included as extra systematic uncertainty on the positron/electron ratio and the positron fraction. This topic will be revisited once the positron/electron ratio and the positron fraction - Section 4.7 - is derived.

4.5.6 Unfolding

In Section 4.4.5 a two-dimensional template fit was used to extract the electron and positron event counts as function of the measured ECAL energy. For the flux measurement the event counts need to be obtained as function of the Top-Of-Instrument (TOI) energy, to correct for the remaining difference between the measured ECAL energy and the true energy.

The applied rear/side leakage correction may overestimate the energy of the incident particle and thus an energy higher than the true energy might be reconstructed. At low energies, emitted bremsstrahlung photons of the primary particle often convert into additional electron and positron pairs, where the momentum distribution is asymmetric: one particle has a higher kinetic energy, than the other. The secondary with the lower energy might leave the detector, due to the bending of the magnetic field. If that happens, the reconstructed energy underestimates the true energy of the primary particle. These kind of effects need to be corrected using the unfolding procedure[14].

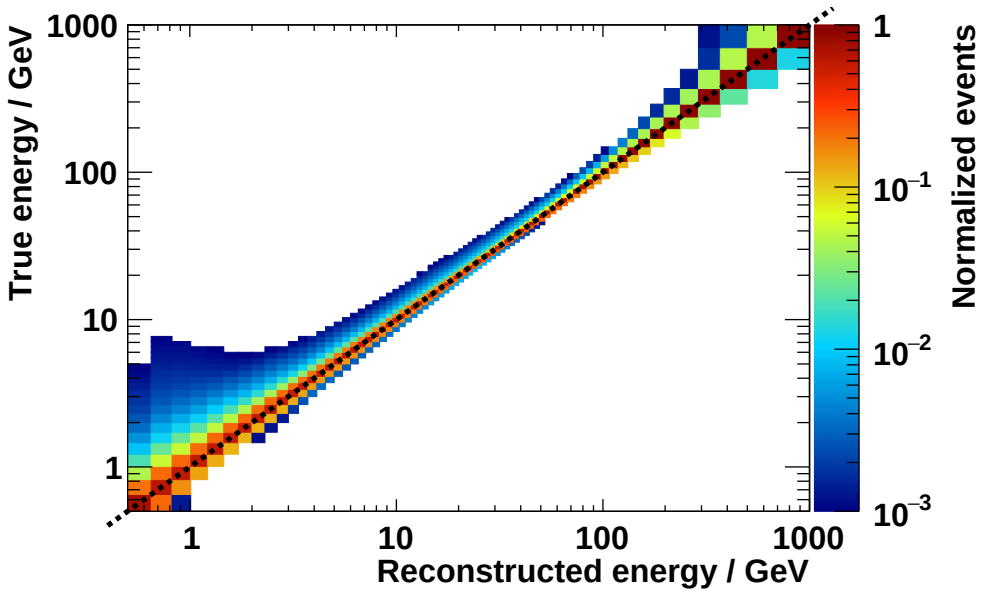

Figure 4.62: Migration matrix **M** obtained from the electron Monte-Carlo simulation, using the same binning as the flux analysis.

Figure 4.62 shows the normalized migration matrix **M**, which shows the measured ECAL energy ("Reconstructed energy") vs. the Monte-Carlo generated energy ("True energy"). The plot shows that for each slice in true energy an interval of possible energies can be reconstructed. The most probable reconstructed energy matches the true energy (diagonal elements of the matrix). It is evident that at low true energies, the reconstructed energy often underestimates the true energy. The probability to underestimate the true energy is generally higher than to overestimate the energy, over the whole energy range.

Mathematically the unfolding process can be written as matrix multiplication:

$$\hat{\mathbf{n}} = \mathbf{U} \cdot \mathbf{n},$$

[14] The unfolding procedure is based on work from Henning Gast and was finalized in close collaboration with him.

where $\mathbf{n}$ denotes the observed distribution in data and $\hat{\mathbf{n}}$ the unfolded, true distribution.

A matrix inversion is enough to solve the equation, but is numerically unstable. In the literature several stable unfolding methods were proposed, such as the Bayesian unfolding (described in Appendix A.7).

The goal for the unfolding is to reconstruct the true energy distribution of the events $\hat{\mathbf{n}}$ from the measured energy distribution $\mathbf{n}$. In total 76 energy bins are available both for the true and measured energy distributions. The actual analysis only uses 74 energy bins (Section 4.4.1), but the event counts are determined in two more bins: one extra low energy bin (0.25 – 0.5 GeV) and one extra high energy bin (1 – 1.5 TeV), to account for migration from/to these "overflow bins"[15]

The probability of measuring a particle with energy n_j given the particle had the true energy $\hat{n}_i$ is already provided by the elements of the migration matrix $\mathbf{M}_{ij}$ (Fig. 4.62). The input for the unfolding procedure in *RooUnfold* is thus the migration matrix $\mathbf{M}$ as two-dimensional histogram and the distribution of the measured events $\mathbf{n}$ as one-dimensional histogram.

The distribution of the measured events $\mathbf{n}$ is affected by the geomagnetic cut-off, since only particles above the cut-off rigidity are analyzed: $E_{j,\,\mathrm{low}} > f_{\mathrm{safety}} \cdot R_c$ (Section 4.5.3).

Figure 4.63 shows the event counts for electrons and positrons $\mathbf{n}$ extracted from the two-dimensional template fit (Section 4.4.5) as red symbols. To visualize the effect of the geomagnetic cut-off the event counts $\mathbf{n}$ are divided by the cut-off weight: $w_{\text{cut-off}}(E) = T(E) \,/\, T(> 25\,\mathrm{GeV})$. The event counts $\mathbf{n}_{\text{no cut-off}} = \mathbf{n}/w_{\text{cut-off}}(E)$, so-obtained, are shown as blue symbols.

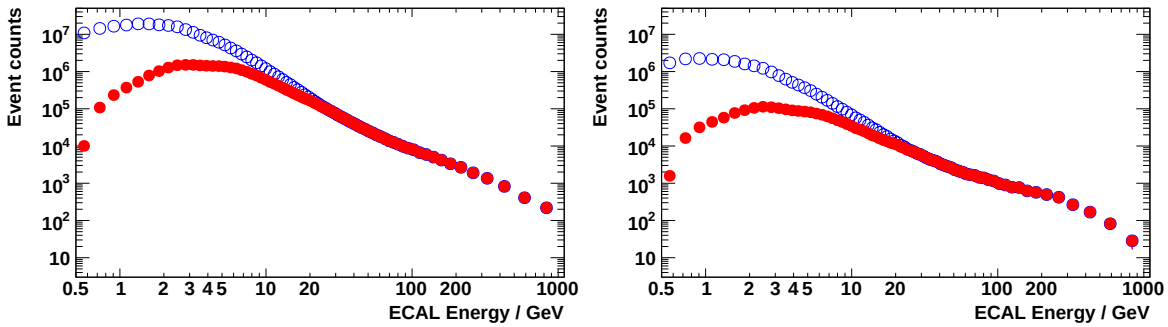

(a) Electron event counts

(b) Positron event counts

Figure 4.63: Comparison of the event counts $\mathbf{n}$ determined from the two-dimensional template fit (red symbols) with the artificial event counts $\mathbf{n}_{\text{no cut-off}}$ that AMS-02 would measure if there was no geomagnetic cut-off effect (blue symbols). The left plot shows the electron event counts, the right plot the positron event counts.

The migration matrix is obtained from the Monte-Carlo simulation and does not contain any information about the loss of events as function of the ***measured*** energy due to the geomagnetic cut-off. To take the geomagnetic cut-off into account the migration matrix needs to be modified. For each bin in x-direction every slice in y-direction needs to be weighted using $w_{\text{cut-off}}(E)$. The resulting migration matrix $\tilde{\mathbf{M}}$ is shown in Fig. 4.64.

[15] In a toy Monte-Carlo simulation it was shown that without using the extra overflow bins the unfolded event counts deviate from the true input flux by more than 50 %. Thus it is important to perform the unfolding process including the overflow bins, to reduce the bias in the first quoted analysis bins.

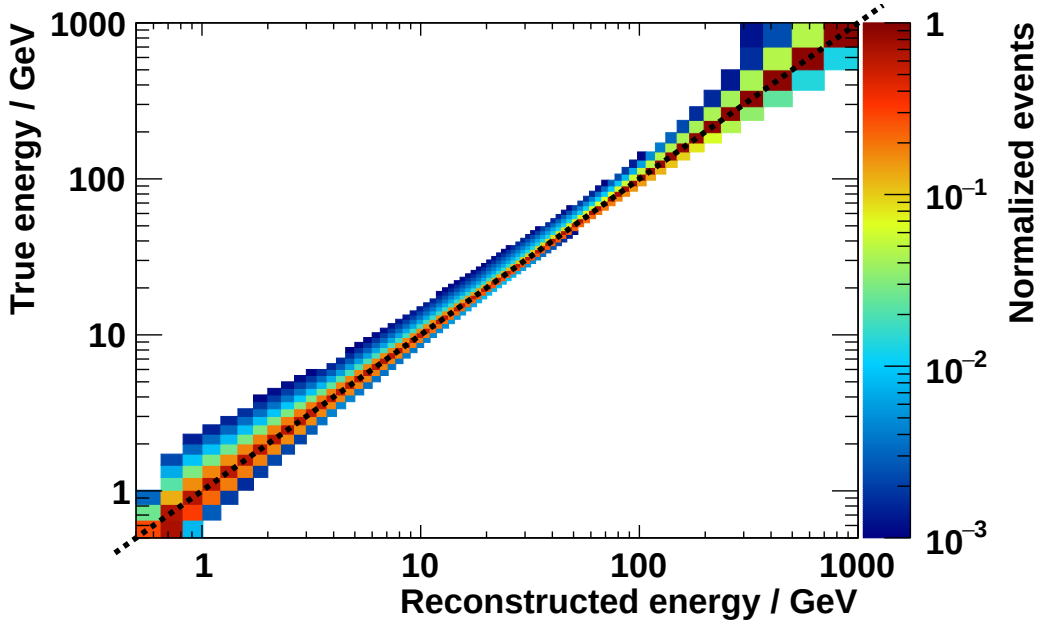

Figure 4.64: Plot of the migration matrix, additionally weighted using the geomagnetic cut-off weight $w_{\text{cut-off}}(E)$ determined from ISS data.

After performing the iterative Bayesian unfolding procedure with four iterations[16] using the measured event counts $\mathbf{n}$ and the migration matrix $\tilde{\mathbf{M}}$ the true event count distribution $\hat{\mathbf{n}}$ is available and can be compared to the measured $\mathbf{n}$ event count distribution to quantify the magnitude of the unfolding.

Figure 4.65 shows the ratios of the unfolded event counts $\hat{\mathbf{n}}$ divided by the measured event counts $\mathbf{n}$ as function of energy for electrons and positrons, respectively.

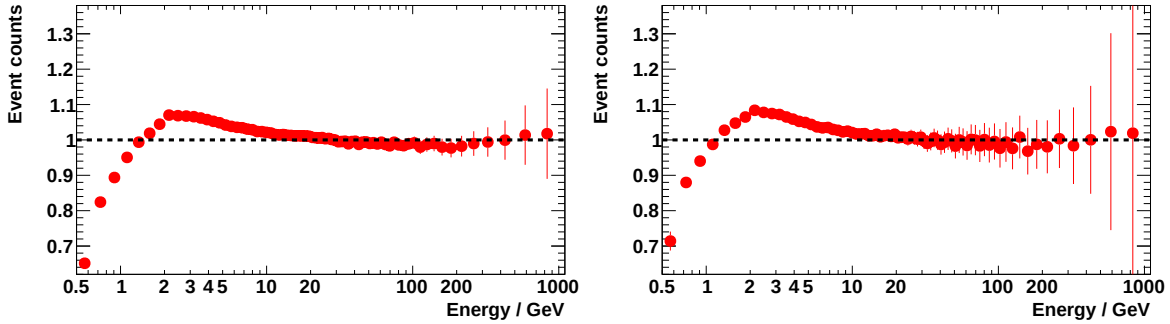

(a) Unfolded / measured electron event counts

(b) Unfolded / measured positron event counts

Figure 4.65: Plot of the ratio of unfolded event counts over measured event counts to quantity the magnitude of unfolding. Above 100 GeV the effect of the unfolding becomes negligible. At low energies the effect is large with corrections up to 60 % in the first energy bin: 0.5 – 0.65 GeV. With increasing energy the magnitude of the unfolding decreases, but it is still a sizeable effect over the whole energy range.

[16] Dedicated studies revealed that $N_{\text{iter}} = 4$ is an optimal choice of the parameter.

Below 10 GeV the effect of the unfolding is most pronounced and it gradually decreases towards high energies. The reason is a combination of two effects: the shape of the event counts as function of energy (flat steeply rising/falling) and the bin width affect the amount of migration. The large bin width at high energies, which exceeds the ECAL energy resolution (Section 3.5) leads to a minimum amount of migration. The smaller the bin width, the larger is the unfolding effect.

Finally an important detail has to be mentioned: the migration matrix $\tilde{\mathbf{M}}$ is derived in two variants, one for unfolding the electron event counts and another variant for unfolding the positron event counts. The difference is the Monte-Carlo event weight that is used when filling the matrix. The Monte-Carlo $e^{\pm}$ datasets used in this work are simulated with a flat energy spectrum in $\log(E)$, which does not represent the energy distribution observed in ISS data. The Monte-Carlo simulation needs to be re-weighted to ensure that the energy distribution follows the one observed in ISS data. To achieve that goal the electron matrix $\tilde{\mathbf{M}}_{\text{elec}}$ is weighted using the final electron flux and the positron matrix $\tilde{\mathbf{M}}_{\text{posi}}$ using the final positron flux. Obviously this is an iterative procedure since the final flux is not known a-priori. As starting point the electron and positron flux from previous publications was used and then refined using the fluxes derived in this work.

The unfolding procedure was repeated using another method: the "folded acceptance method" (bin-by-bin unfolding) which gives consistent results with the Bayesian unfolding, but wrongly estimates the statistical uncertainties of the event counts after unfolding. Further checks are presented in Section 4.6.7.

4.6 Time-averaged systematic uncertainties for flux analysis

In this section all systematic uncertainties that contribute to the time-averaged fluxes are summarized. The most important systematic uncertainty for the flux analysis is the acceptance uncertainty, described in Section 4.6.6, followed by the unfolding uncertainty, described in Section 4.6.7. Above 500 GeV the knowledge of the TRD estimator and the associated uncertainty is the dominant systematic uncertainty, which is presented in the next section.

4.6.1 TRD estimator

In this section the contribution to the overall systematic uncertainty on the fluxes, induced by the choice of the TRD templates, will be quantified. The idea is to randomize the TRD template parameters e.g. $M = 100$ times and repeat the two-dimensional fit procedure with the "smeared" templates. At each iteration m the number of electrons and the number of protons is recorded. When the fit procedure is repeated, a distribution of these numbers emerges. The RMS of the electron and proton distributions is a measure of the systematic uncertainty induced by the limited knowledge of the shape of TRD estimator.

All TRD templates are described analytically as a function of energy with a set of parameters for each energy bin, as described in Section 4.4.2. These parameters have associated uncertainties extracted from the fit procedures. Furthermore the fit procedure not only yields the best-fit parameters with their uncertainties but also the correlations between them, encoded in the covariance matrix $\mathbf{V}$.

The covariance matrix in energy bin j of the fit result for negative rigidities (the fit result of the sample where the electron and charge-confused proton template was determined) is denoted as $\mathbf{V}_{j,\,\mathrm{neg}}$. The values of the N_{neg} electron/charge-confused proton template parameters are denoted as $\mathbf{p}_{\mathrm{neg}}$. The covariance matrix of the fit result for positive rigidities is denoted as $\mathbf{V}_{j,\,\mathrm{pos}}$ and the values of the N_{pos} proton template parameters as $\mathbf{p}_{\mathrm{pos}}$, respectively.

Smeared TRD template parameters for the electron template and charge-confused proton template, for the m^{th} iteration in energy bin j are obtained by:

$$\tilde{\mathbf{p}}_{\mathrm{neg}} = \mathbf{p}_{\mathrm{neg}} + (\mathbf{v}_{m,\,\mathrm{neg}} \cdot \mathbf{L}^{\intercal}_{j,\,\mathrm{neg}}).$$

$\mathbf{v}_{m,\,\mathrm{neg}}$ is a vector of N_{neg} random variables, following a normal distribution:

$$\mathbf{v} = \begin{pmatrix} v_0 \\ \vdots \\ v_N \end{pmatrix} = \begin{pmatrix} \mathcal{N}(\mu = 0,\, \sigma^2 = 1) \\ \vdots \\ \mathcal{N}(\mu = 0,\, \sigma^2 = 1) \end{pmatrix}.$$

In the same way new TRD proton template parameters can be generated:

$$\tilde{\mathbf{p}}_{\mathrm{pos}} = \mathbf{p}_{\mathrm{pos}} + (\mathbf{v}_{m,\,\mathrm{pos}} \cdot \mathbf{L}^{\intercal}_{j,\,\mathrm{pos}}). \tag{4.25}$$

The matrices $\mathbf{L}_{j,\,\mathrm{neg}}$ and $\mathbf{L}_{j,\,\mathrm{pos}}$ can be derived from the covariance matrices $\mathbf{V}_{j,\,\mathrm{neg}}$ and $\mathbf{V}_{j,\,\mathrm{pos}}$, respectively. The covariance matrix $\mathbf{V}$ can be factored uniquely into a product - "Cholesky decomposition" [Golub1996] - such that::

$$\mathbf{L}^{\intercal} \cdot \mathbf{L} = \mathbf{V}.$$

For each energy bin j the two-dimensional fit procedure is repeated $M = 100$ times and at each iteration m all three TRD templates - electron template, charge-confused proton template and proton template - are varied. From these "smeared" one-dimensional TRD templates two-dimensional templates are constructed, by taking the product of the "smeared" one-dimensional TRD templates with the regular one-dimensional CCMVA templates. The two-dimensional positron template is built by mirroring the electron template around the y-axis, identical to the construction of the regular two-dimensional positron template from the regular electron template. By varying only the TRD part of the two-dimensional templates, the limited knowledge of the TRD templates can be quantified in isolation from the CCMVA estimator. Thus a systematic uncertainty can be extracted, quantifying the knowledge of the shapes of the TRD estimator. Note that the amount of charge-confusion is fixed from the Monte-Carlo simulation (Section 4.4.5), when repeating the two-dimensional template fits.

Figure 4.66 shows the resulting relative systematic uncertainty $\sigma_{\text{trd}}(E)/\Phi_{e^{\pm}}(E)$ for the electron flux and the positron flux. The uncertainty associated with the positron flux is larger than the one associated with the electron flux. The variation of the charge-confused proton template is almost negligible, since the amount of charge-confused protons is small, compared to the number of electrons. The consequence is that when determining the number of electrons at each iteration k, the RMS is dominated by the knowledge of the electron template. On the other hand, when determining the number of positrons, the positron template and the proton template are equally important, as the number of protons and positrons are comparable in each energy bin. This difference is the main reason why the uncertainty from the TRD estimator for the positron flux is larger than for the electron flux.

The shape of the relative systematic uncertainty follows the statistical uncertainty of the data sample, from which the templates are extracted. It is evident that this is the limiting factor on the knowledge of the TRD templates at high energies and thus reflected in this uncertainty, which goes up to $\approx 10\,\%$ in the highest energy bin.

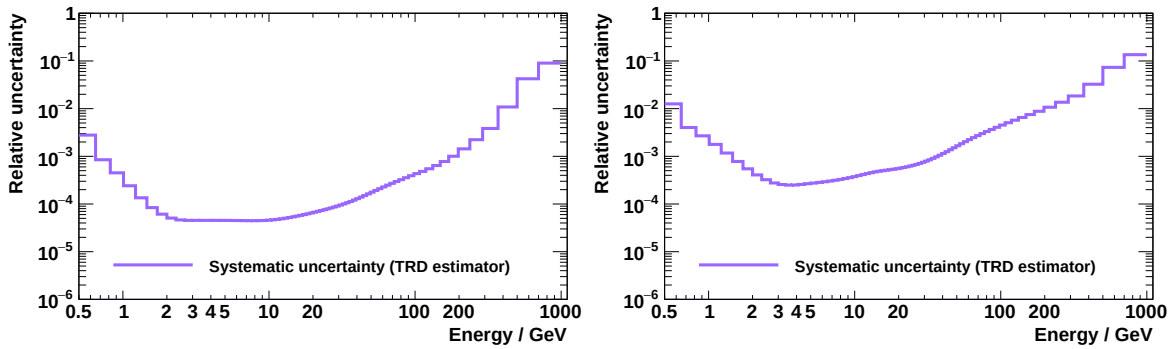

(a) For electron flux

(b) For positron flux

Figure 4.66: Visualization of the relative systematic uncertainty associated with the electron flux (left plot) and associated with the positron flux (right plot) due to the knowledge of the TRD estimator.

4.6.2 CCMVA estimator

The two-dimensional template fit presented in Section 4.4.5 is executed twice for each of the single-track / multi-tracks / all-tracks samples. In the first iteration the charge-confused is a free fit parameter. In the second iteration the charge-confusion is fixed to the Monte-Carlo prediction, as good agreement was found between ISS data and the Monte-Carlo simulation (Fig. 4.41).

From the difference in the magnitude of charge-confusion a systematic uncertainty can be derived. Figure 4.67 shows the ratio: ISS charge-confusion over Monte-Carlo prediction for the three different track samples. The uncertainty was chosen by hand to ensure that at least ≈ 67 % of all data points are covered by the uncertainty band. Since the charge-confusion curves (Fig. 4.41) are smooth as function of energy and show no prominent structures, statistical fluctuations were minimized, by averaging over three analysis energy bins.

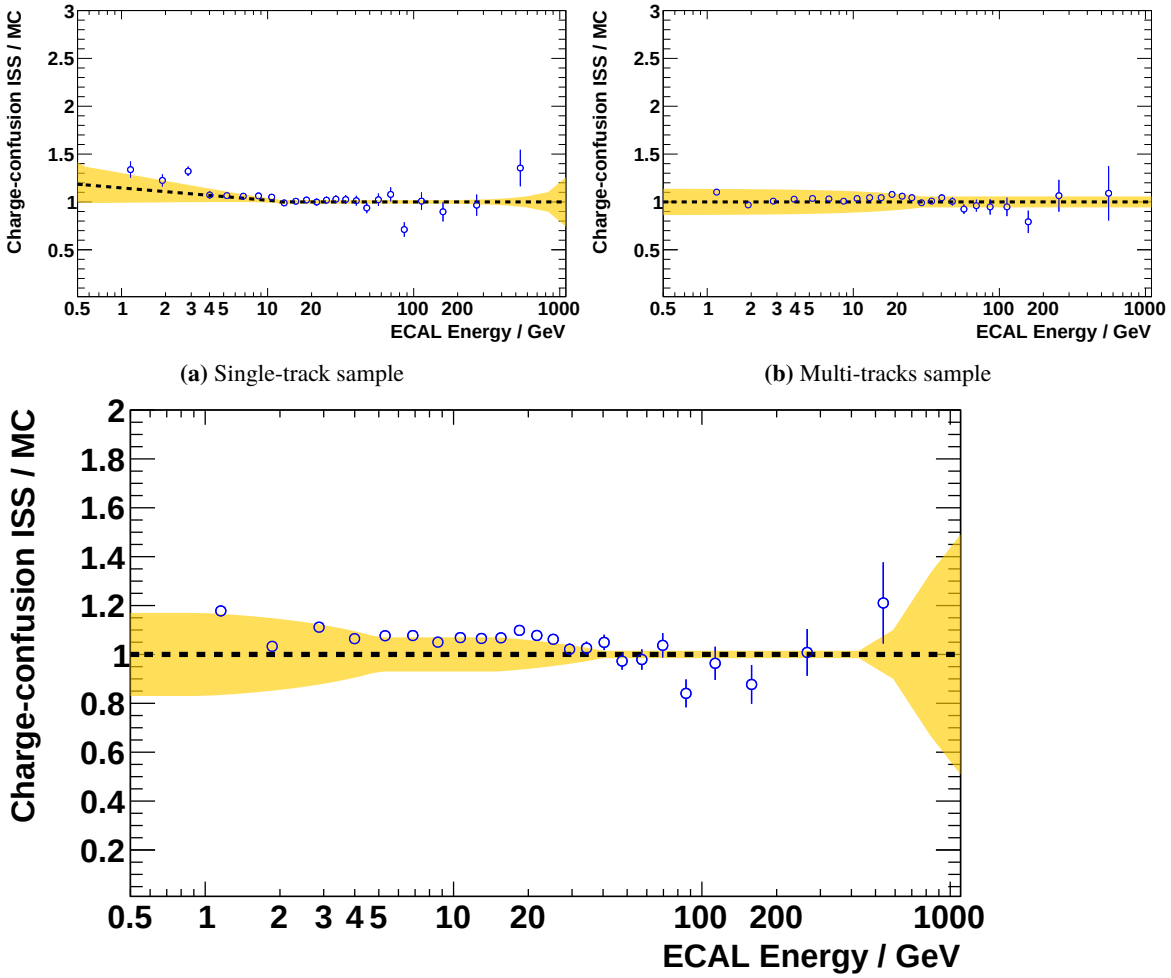

(a) Single-track sample

(b) Multi-tracks sample

(c) All-tracks sample

Figure 4.67: Comparison of the ratio of charge-confusion determined from ISS data divided by the prediction from the Monte-Carlo simulation (blue symbols) for the single-track sample, the multi-tracks sample and the all-tracks sample. The orange band represents the chosen systematic uncertainty to cover the differences between the ISS data and the Monte-Carlo simulation.

For the flux analysis the all-tracks samples is used and thus the systematic uncertainty from the lower plot in Fig. 4.67 needs to be examined. The uncertainty is 17 % at 0.5 GeV and decreases to 7 % at 5 GeV. Between 15 – 40 GeV it gradually decreases to 1.5 % and stays constant until 500 GeV, where it increases again up to to 35 % at 1 TeV.

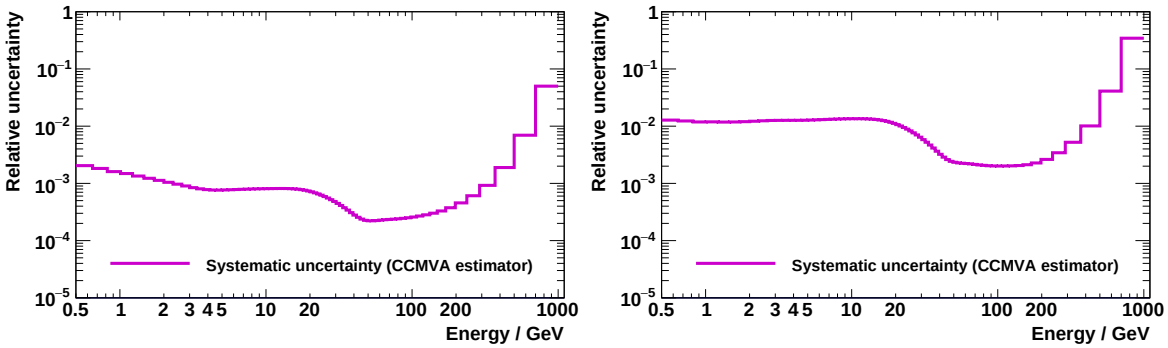

(a) For electron flux

(b) For positron flux

Figure 4.68: Visualization of the relative systematic uncertainty associated with the electron flux (left plot) and associated with the positron flux (right plot) due to the knowledge of the charge-confusion.

Since the systematic uncertainty of the charge-confusion determination - $\sigma_{\mathrm{cc}}(E)$ - is known, the effect on the fluxes can be quantified, by error propagation. Figure 4.68 shows the resulting relative systematic uncertainty $\sigma_{\mathrm{cc},\, e^{\pm}}(E)/\Phi_{e^{\pm}}(E)$ as function of energy.

The systematic uncertainty due to the knowledge of the charge-confusion affects the positron flux stronger than the electron flux. For the electron flux the systematic uncertainty gradually increases from the permille level up to $\approx 5\,\%$ at 1 TeV. For the positron flux the situation is different: the charge-confusion systematic uncertainty starts at $\approx 1\,\%$, slowly decreasing to $0.25\,\%$ at $\approx 150\,\mathrm{GeV}$ and then gradually increases up to to $35\,\%$ at 1 TeV.

This behaviour matches the expectation since there are many more charge-confused electrons that can be misreconstructed as positrons, than charge-confused positrons that can be be misreconstructed as electrons. Due to the larger abundance of electrons compared to positrons in cosmic rays the electrons are less affected by the charge-confusion, which is reflected in the systematic uncertainty.

4.6.3 ECAL estimator efficiency

The derivation of the ECAL estimator efficiency including its uncertainty was already discussed in Section 4.5.1. The uncertainty determined using the "Simultaneous fit method" (Fig. 4.47) is used as systematic uncertainty of the ECAL estimator efficiency.

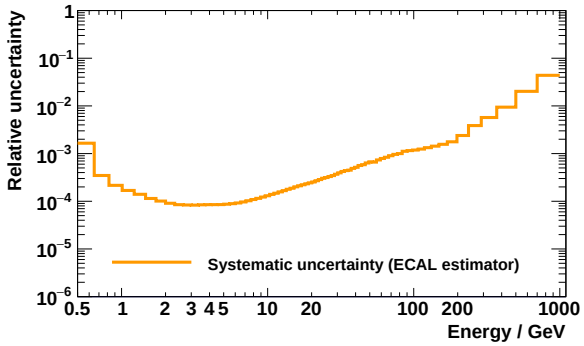

Figure 4.69: Visualization of the relative systematic uncertainty associated with the electron flux and the positron flux due to the knowledge of the ECAL estimator efficiency.

Figure 4.69 shows the resulting relative systematic uncertainty $\sigma_{\text{ecal}}(E)/\Phi_{e^{\pm}}(E)$ as function of energy. The uncertainty associated with the electron flux is identical to the uncertainty associated with the positron flux.

4.6.4 Trigger efficiency

The uncertainty of the trigger efficiency stems from the number of unbiased triggers, which rapidly decreases with increasing energy. The physics trigger histogram as function of energy (all physics triggers sample) is divided by the total trigger histogram as function of energy (all physics and unbiased triggers after prescaling is applied) to deduce the trigger efficiency. The associated uncertainty is computed according to Clopper-Pearson [ClopperPearson1934].

Above $\approx 15\,\text{GeV}$ only six unbiased events remain in the ISS data sample. The lower limit on the trigger efficiency above 15 GeV is 0.9999 at 95 % confidence level. The systematic uncertainty on the trigger efficiency above 15 GeV is extrapolated from the data below 15 GeV, by hand. This does not impose any bias for the flux analysis, since the contribution to the overall systematic uncertainty is below the permille level at energies above 15 GeV.

Figure 4.70 shows the resulting relative systematic uncertainty $\sigma_{\text{trigger}}(E)/\Phi_{e^{\pm}}(E)$ as function of energy. The uncertainty associated with the electron flux is identical to the uncertainty associated with the positron flux.

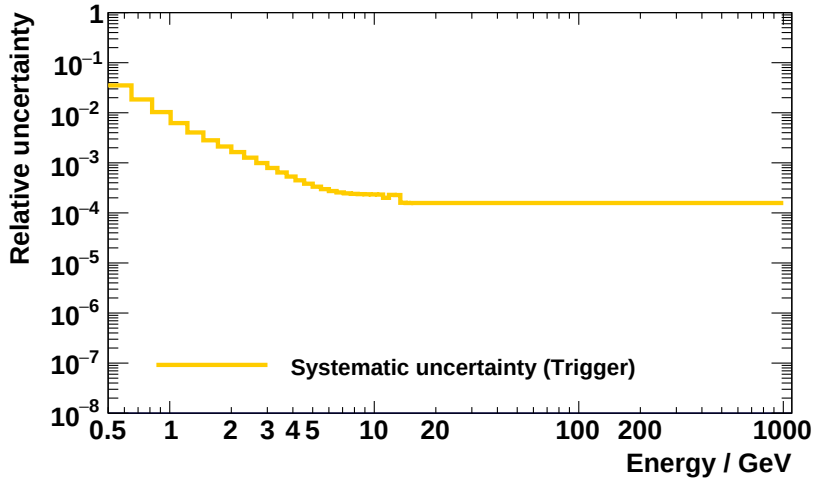

Figure 4.70: Visualization of the relative systematic uncertainty associated with the electron flux and the positron flux due to the knowledge of the trigger efficiency.

4.6.5 Measuring time

The measuring time $T(E)$ was derived in Section 4.5.3. The energy-independent part of the measuring time is free of any systematic uncertainty since all ingredients are known accurately: the seconds between the start and the end of data taking and the live-time of the experiment in each second. A possible source of a systematic uncertainty arises in the energy-dependence: the geomagnetic cut-off calculation.

Different geomagnetic cut-off modes were tested: Størmer [Stoermer1956] cut-off in 25°, 30°, 35° and 40° field of view. With an increased field of view the geomagnetic cut-off in each second is enlarged. Therefore the measured event counts at low energies decrease since less particles at a given energy fulfill the requirement of having a measured energy above the geomagnetic cut-off, which is the necessary requirement to classify them as primary cosmic rays. With the chosen safety factor $f_{\text{safety}} = 1.2$ the fluxes in each field of view were identical, except for an increased statistical error, as expected from the decreased event counts.

Furthermore the Størmer cut-off was exchanged for the more sophisticated IGRF cut-off while scanning the safety factor from $0.9 - 1.4$. With the chosen nominal safety factor $f_{\text{safety}} = 1.2$ all fluxes were identical to those obtained using the Størmer cut-off, except for the first energy bin $0.5 - 0.7$ GeV which has zero events when using the IGRF cut-off. Since AMS already published electron and positron fluxes starting at 0.5 GeV and since the remaining flux data points are consistent between IGRF / Størmer, the Størmer cut-off was chosen for this work.

The aforementioned cross-checks all yield consistent results, therefore no additional systematic uncertainty for the measuring time $T(E)$ is needed.

4.6.6 Acceptance

The acceptance was derived in Section 4.5.4. Two possible sources of systematic uncertainties arise: the finite Monte-Carlo statistics used to derived the acceptance from the Monte-Carlo simulation and the Data/Monte-Carlo correction factor $(1 + \delta(E))$. The Monte-Carlo statistics exceeds the ISS statistics over all energies, as shown in Fig. 4.71. Especially at high energies the Monte-Carlo contains orders of magnitudes more events than the ISS data. The uncertainty from the Monte-Carlo statistics is negligible over all energies.

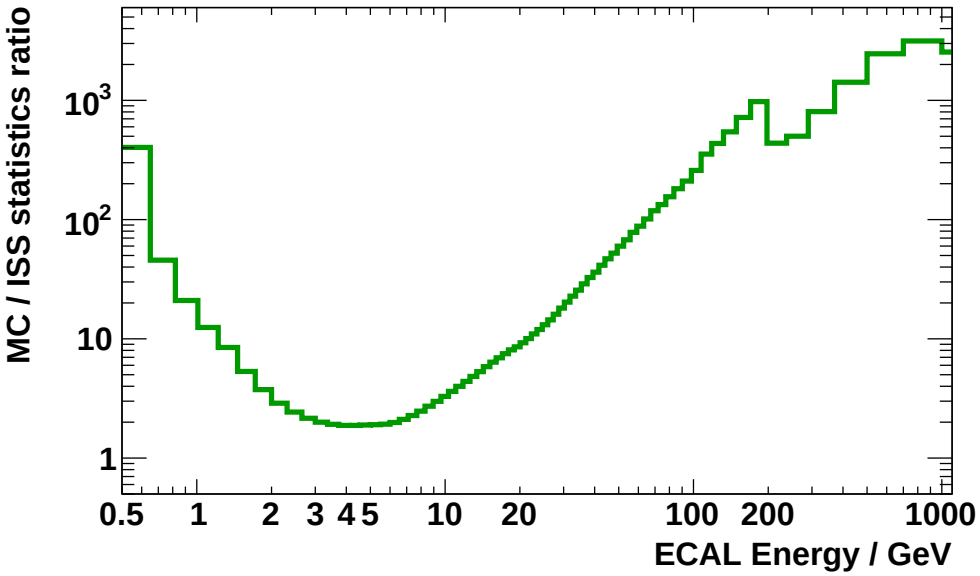

Figure 4.71: Comparison of the available Monte-Carlo statistics to the ISS statistics after applying all data quality, preselection, selection and identification cuts. The green line shows the ratio of negative rigidity Monte-Carlo event counts divided by ISS event counts.

Thus the only relevant systematic uncertainty for the acceptance stems from the uncertainty on the correction factor $(1 + \delta(E))$. The uncertainty on the correction factor was described in detail in Section 4.5.4. The magnitude of the combined Data/Monte-Carlo correction factor $(1 + \delta(E))$ was presented in Fig. 4.60. The correction applied to the Monte-Carlo acceptance varies from 2 % at low energies up to 4 % at high energies and is known for all energies better than 1.5 %, indicated by the orange band in the plot. This directly translates into the systematic uncertainty used for the $e^{\pm}$ fluxes.

Figure 4.72 shows the resulting relative systematic uncertainty $\sigma_{\text{acc}}(E)/\Phi_{e^{\pm}}(E)$ as function of energy. The uncertainties associated with the electron flux and the positron flux is identical.

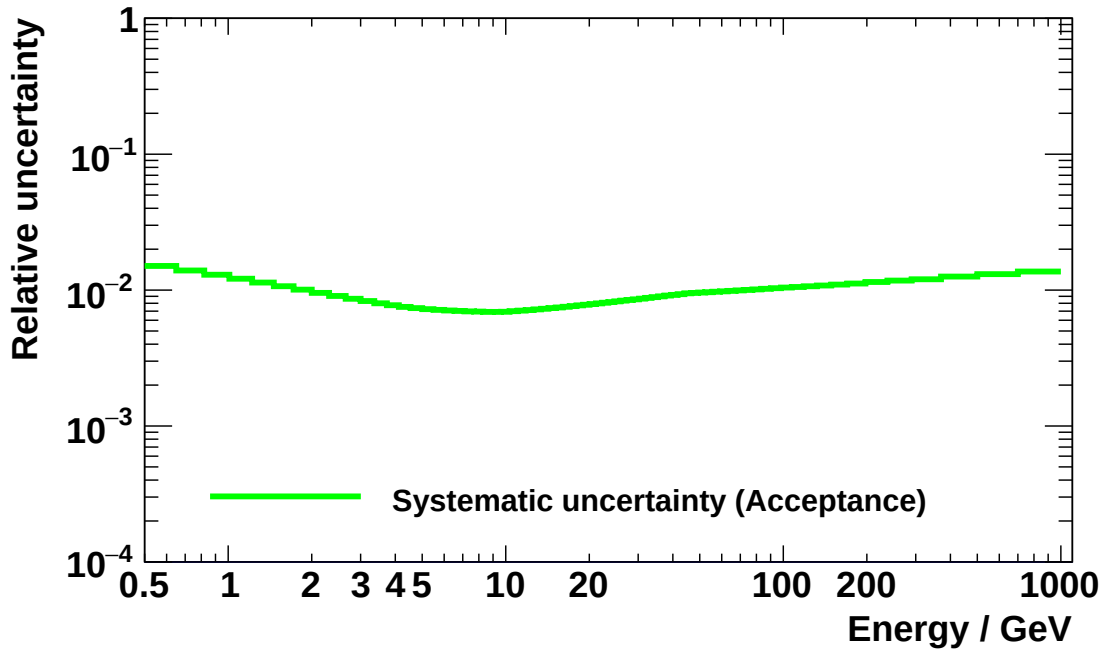

Figure 4.72: Visualization of the relative systematic uncertainty associated with the electron flux and the positron flux due to the knowledge of the acceptance.

4.6.7 Unfolding

The unfolding procedure was described in detail in Section 4.5.6. Two possible sources of systematic uncertainties arise: the degree to which the migration matrix is known and the stability of the unfolding procedure.

Knowledge of the migration matrix

To obtain the migration matrix one has to rely on the Monte-Carlo simulation. As AMS-02 was extensively tested in a beam test, the migration matrix can be cross-checked at different energies and compared with the Monte-Carlo simulation, for both electrons and positrons. This allows to asses the uncertainty of the unfolding method, due to the knowledge of the migration matrix.

To ease the comparison between the Monte-Carlo simulation and the test beam data, the migration matrix will be parameterized using an analytical model. The migration matrix, shown in Fig. 4.62, is

projected to the x-axis (reconstructed energy axis) for each bin in y-direction (true energy axis). In each of the projections an analytical model of the reconstructed energy migration is derived, to create a full model of the reconstructed energy as function of the true energy.

A sum of a *Landau* distribution and a *Crystal Ball* function forms the analytical model:

$$f_{\text{model}}(E) = \xi \cdot p_{\text{landau}}(E) + \nu \cdot f_{\text{cb}}(E), \tag{4.26}$$

where ξ and ν denote the relative contributions of both functions to the model. The analytical model depends on seven parameters, two of them describing the shape of the *Landau* distribution, four associated with the *Crystal Ball* function and one additional parameter n_{lf}, which controls how much the landau distribution contributes to the sum ($\xi \propto n_{\text{lf}}$).

The *Landau* distribution [Landau1944] is characterized by the Most Probable Value (MPV) μ and the width σ. The *Crystal Ball* function [Skwarnicki1986] consists of a gaussian core and a power law tail below a certain threshold. It depends on four parameters: $f_{\text{cb}}(E; \alpha, n, \bar{x}, \sigma)$.

Figure 4.73 shows the analytical model of the migration matrix in an example energy bin. The analytical model is a PDF – the integral over the curve yields 1.

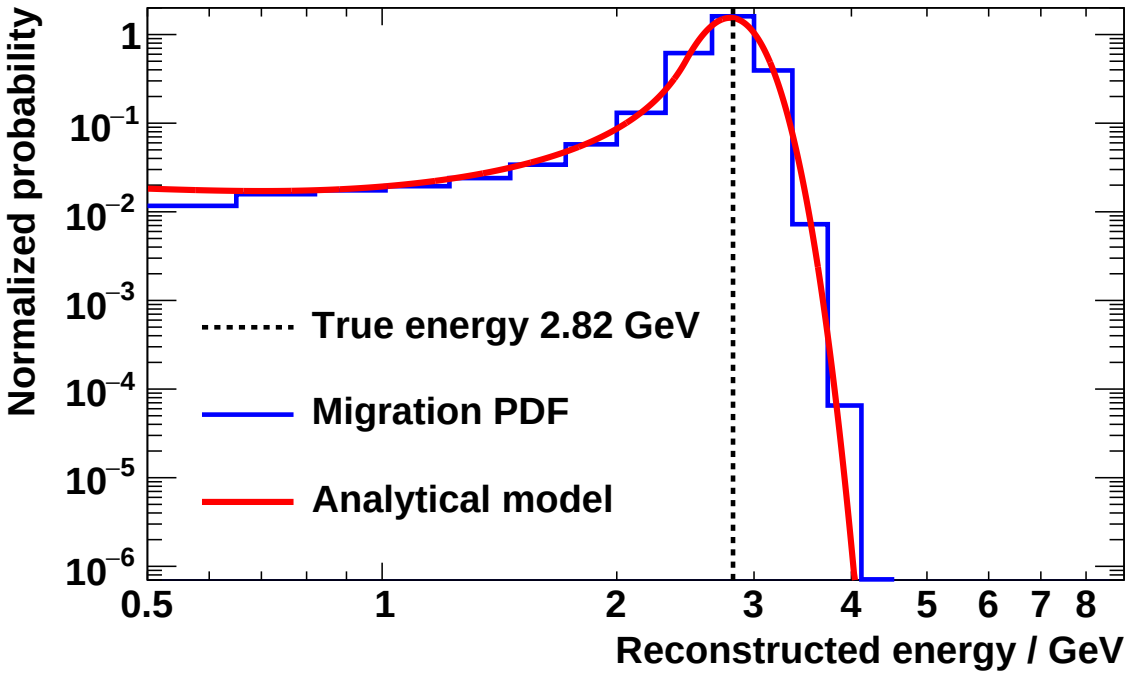

Figure 4.73: Projection of the migration matrix, Fig. 4.62, to the x-axis (reconstructed energy) for a given true energy. The projection is shown as blue histogram and the red line shows the analytical model - Eq. (4.26) - fit to the blue histogram. The black dashed line shows the true energy (y = 2.82 GeV) for comparison.

The analytical model - Eq. (4.26) - is fitted to all bins in y-direction (true energy) of the migration matrix.

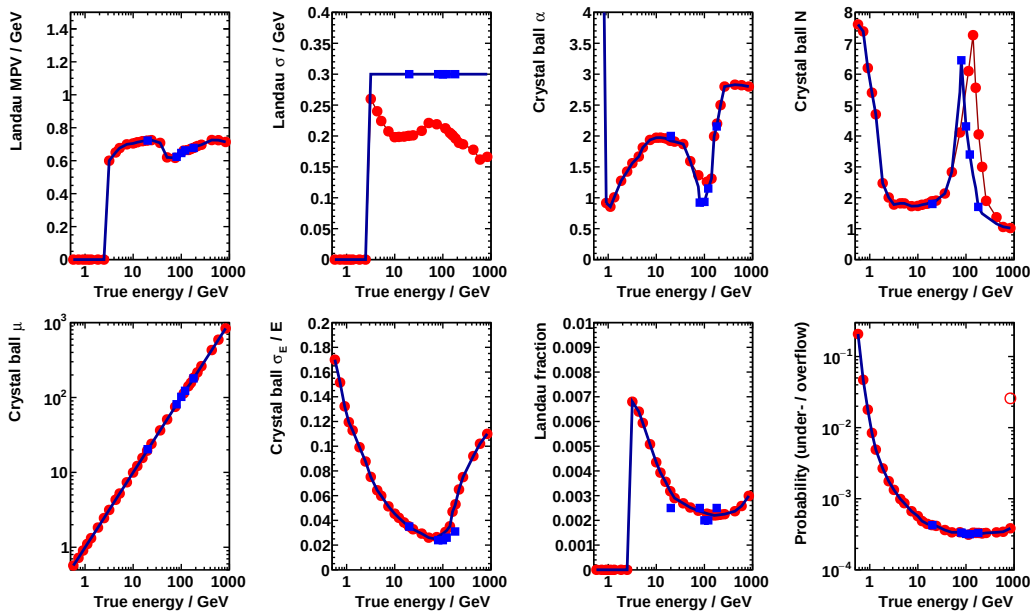

Figure 4.74: Results of the fit of the analytical model - Eq. (4.26) - to all bins in y-direction (true energy) of the migration matrix obtained from the Monte-Carlo simulation (red symbols), compared to the analytical model fit to the migration matrices obtained from the mono-energetic testbeam data sets (blue symbols). The testbeam data sets that were analyzed are e^+ at 20 and 80 GeV, e^- at 100, 120 and 180 GeV, yielding five different migration matrices. The analytical model is fit to all five migration matrices and the parameters are extracted, shown as blue symbols. The testbeam results can be compared to the prediction from the Monte-Carlo simulation: Three parameters show a significant deviation: the Landau σ, the Crystal Ball α and N parameters. The dark blue line marks the extrapolation of the parameters obtained from the discrete test beam data points towards the whole energy range.

Figure 4.74 shows a comparison of the analytical model parameters for the migration matrix obtained from the Monte-Carlo simulation with the parameters obtained for the migration matrices from the testbeam data. All except three parameters show a good agreement with the Monte-Carlo simulation. The Landau σ differs by more than 50 % from the Monte-Carlo prediction and the energy dependence appears flat. The origin of this difference has to be clarified in a dedicated study. The Crystal Ball α parameter shows a deviation from the Monte-Carlo simulation at 100 GeV, whereas the other data points agree with the Monte-Carlo simulation. The Crystal Ball N parameter shows a similar magnitude and energy dependence but is slightly shifted towards smaller energies, with respect to the parameters obtained from the Monte-Carlo simulation. Note that the α and N parameters are highly correlated, leading to a degeneracy in the fit procedure. The dark blue line represents the extrapolation of the test beam parameters to the whole energy range.

After finishing the fit procedure two distinctive set of parameters - describing the migration matrix analytically - are available: the parameters obtained from the Monte-Carlo simulation and the parameters obtained with the help of the testbeam data. The next step is to generate toy fluxes according to a predefined model of the electron or positron flux and fold them once with the migration matrix from the Monte-Carlo simulation and once with the analytical migration matrix from the test beam. The ratio of the two fluxes shows the impact of the choice of the parameterization on the resulting fluxes and thus is a measure of the systematic uncertainty induced by the migration matrix.

Figure 4.75 shows the ratio of the toy e^- flux forward folded with the migration matrix obtained from the Monte-Carlo parameterization over the toy e^- flux forward-folded with the migration matrix obtained from the testbeam parameterization. Figure 4.76 shows the same ratio for the e^+ toy fluxes. From the data points that are incompatible with unity a systematic uncertainty can be derived, due to the limited knowledge of the migration matrix. This is shown as orange band and is equal for $e^\pm$.

All data points above ≈ 5 GeV are consistent with unity, except for a few outliers around ≈ 100 GeV. In this energy range the simple analytical model - Eq. (4.26) - does not fully describe the true migration PDF. Using a better parameterization these outliers can be avoided. Therefore this does not represent a real effect, but only reveals a deficiency in the choice of the parameterization.

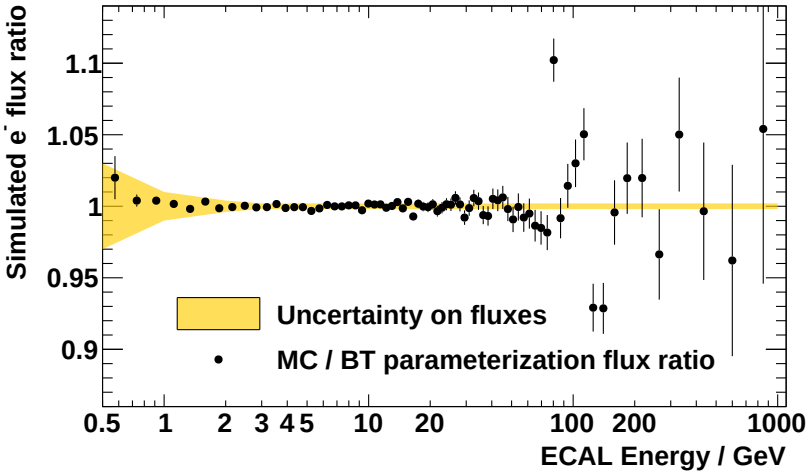

Figure 4.75: Ratio of the toy e^- flux forward folded with the Monte-Carlo parameterization over the toy e^- flux forward-folded with the testbeam parameterization - shown as black symbols. The orange band represents the systematic uncertainty on the fluxes due to the knowledge of the migration matrix.

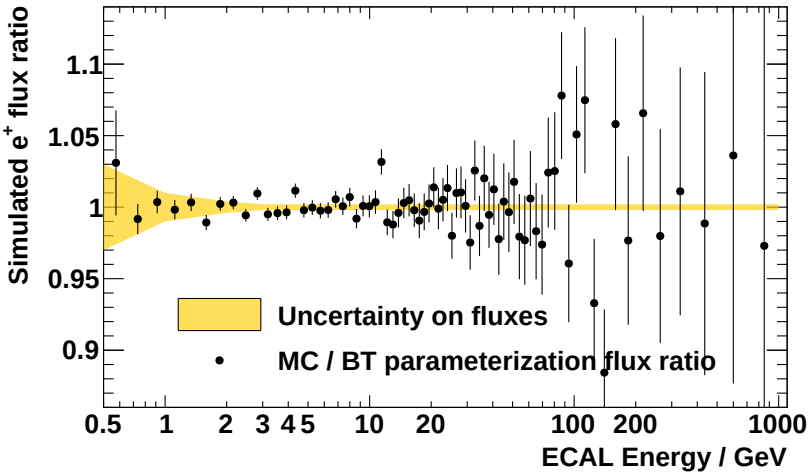

Figure 4.76: Ratio of the toy e^+ flux forward folded with the Monte-Carlo parameterization over the toy e^+ flux forward-folded with the testbeam parameterization - shown as black symbols. The orange band represents the systematic uncertainty on the fluxes due to the knowledge of the migration matrix.

Stability of unfolding procedure

Figure 4.77 shows an overview of the procedure that was developed to assess the stability of the unfolding. The idea is to generate a toy flux many times, according to a predefined model of the true $e^{\pm}$ flux. This toy flux is then forward folded using the migration matrix and unfolded afterwards using the Bayesian unfolding method. This yields O unfolded fluxes which can be compared with the single true input flux model. Any deviation from the true flux has to be attributed to a systematic uncertainty in the unfolding procedure.

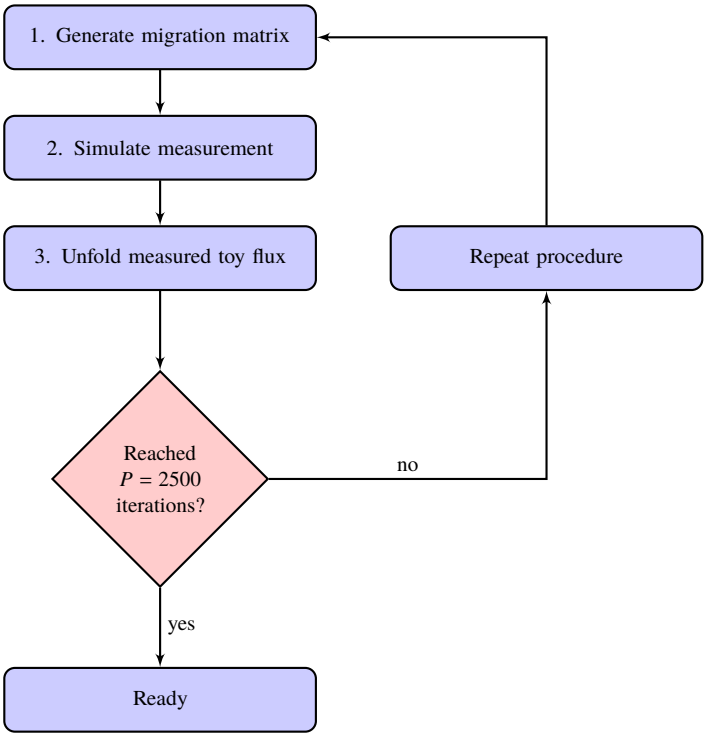

Figure 4.77: Illustration of the procedure to assess the stability of the unfolding procedure.

The procedure outlined in Fig. 4.77 is repeated $P = 2500$ times. At each iteration p the following steps are executed:

1. **Generate migration matrix**
   A new migration matrix $\mathbf{M}$ is filled with $M \approx 10^9$ entries. For each entry m a true energy E^m_{true} is drawn from a random number generator, following a power law of E^{-1} between 0.25 GeV and 1.5 TeV. The reconstructed energy is derived by smearing the true energy according to the analytical model from Eq. (4.26): $E^m_{\text{reconstructed}} = f_{\text{model}}(E^m_{\text{true}})$ and the migration matrix is filled.

   A predefined flux $\Phi_{\text{true}}(E_{\text{true}})$ is used as weight, to correctly model the true energy distribution of the cosmic-ray $e^{\pm}$ fluxes. The predefined $e^{\pm}$ fluxes are modelled as broken power laws with different breaks and spectral indices, closely matching the final $e^{\pm}$ fluxes derived in this work.

   This recipe leads to a unique toy migration matrix $\mathbf{M}^p$ for each iteration p of the procedure illustrated in Fig. 4.77.

2. **Simulate measurement**
   The toy flux $\Phi_{\text{true}}(E_{\text{true}})$ is multiplied with the acceptance, the trigger efficiency and scaled by the measuring time over cut-off (which is an energy-independent scalar above $\approx 25\,\text{GeV}$) to compute the number of true event counts as function of the true energy: $N_{\text{true}}(E_{\text{true}})$, explicitly ignoring the geomagnetic cut-off. The geomagnetic cut-off must be factored out at this point, since it is only known as function of the reconstructed energy. In each energy bin the true event counts $N_{\text{true}}(E_{\text{true}})$ are then smeared according to a Poisson distribution to obtain $\hat{N}_{\text{true}}(E_{\text{true}})$, to simulate an actual measurement.

   As next step the number of measured event counts as function of the reconstructed energy $\hat{N}_{\text{rec}}(E_{\text{rec}})$ can be computed. For each true energy bin k the energy E^k_{true} and the number of true event counts $\hat{N}^k_{\text{true}}$ are known.

   The reconstructed energy is now computed $\hat{N}^k_{\text{true}}$ times by smearing the true energy according to the analytical model from Eq. (4.26): $E^k_{\text{rec}} = f_{\text{model}}(E^k_{\text{true}})$.

   This yields $\hat{N}^k_{\text{true}}$ reconstructed energies E^k_{rec}, corresponding to the $\hat{N}^k_{\text{true}}$ number of true event counts before smearing. The so-obtained reconstructed energies are filled into a one-dimensional histogram storing the reconstructed event counts $N_{\text{rec}}(E_{\text{rec}})$, if the reconstructed energy is above the geomagnetic cut-off. The geomagnetic cut-off is simulated by drawing a random number between 0 and 1 and comparing if the random number is smaller than the cut-off probability $w_{\text{cut-off}}(E) = T(E) \,/\, T(> 25\,\text{GeV})$ (defined in Section 4.5.6). Only if that condition is fulfilled, the reconstructed energy is filled into the aforementioned histogram $N_{\text{rec}}(E_{\text{rec}})$.

   This procedure is repeated for all true energy bins $\forall k \in [1, 76]$ in the analysis. Afterwards the simulation of a measurement is completed: both the true event counts $\hat{N}_{\text{true}}(E_{\text{true}})$ and the reconstructed event counts $N_{\text{rec}}(E_{\text{rec}})$, including the simulation of the geomagnetic cut-off are available.

   The reconstructed event counts are then divided by the bin widths, the trigger efficiency, the acceptance and the energy-dependent measuring time to obtain the reconstructed toy flux $\Phi^p_{\text{rec}}(E_{\text{rec}})$ for iteration p, as for a real measurement.

3. **Unfold measured toy flux**
   The standard unfolding procedure, described in Section 4.5.6, is executed using the migration matrix $\mathbf{M}^p$ from step 1, and the reconstructed flux $\Phi^p_{\text{rec}}(E_{\text{rec}})$ from step 2. This yields the unfolded flux: $\tilde{\Phi}^p_{\text{unfolded}}(E_{\text{true}})$.

   The deviation of the unfolded flux $\tilde{\Phi}^p_{\text{unfolded}}(E_{\text{true}})$ from the true flux $\Phi_{\text{true}}(E_{\text{true}})$ divided by the true flux is calculated and recorded for each iteration p.

After repeating the aforementioned procedure P times a distribution of the deviation of the unfolded flux $\tilde{\Phi}_{\text{unfolded}}$ from the true flux Φ_{true} divided by the true flux can be obtained (Fig. 4.78). The ratio is compatible with unity above $\approx 1\,\text{GeV}$ indicating that the unfolding procedure is free of a bias. Below that energy threshold a large deviation is exposed, which gets larger with decreasing energy.

Note that the plot starts at 0.5 GeV even though the unfolding procedure operates on one more bin on the left side - 0.25 – 0.5 GeV - and one more bin on the right side of the analysis binning: 1 – 1.5 TeV. Without the extra bin on the left side the bias in the first analysis bin 0.5 – 0.65 GeV is even larger than the $\approx 25\,\%$ that is visible in the plot. This shows the limits of the unfolding procedure:

not all energy bins that are unfolded are free of a bias. Especially the border regions are problematic and need to be excluded for further analysis. This is the main reason why the unfolding procedure uses 76 energy bins, out of which 74 are used to produce the fluxes. The problem is less severe at high energies, simply due to the spectral index of the fluxes. There are much less events at high energies that could migrate to lower energy bins and thus the problem is less pronounced than at low energies.

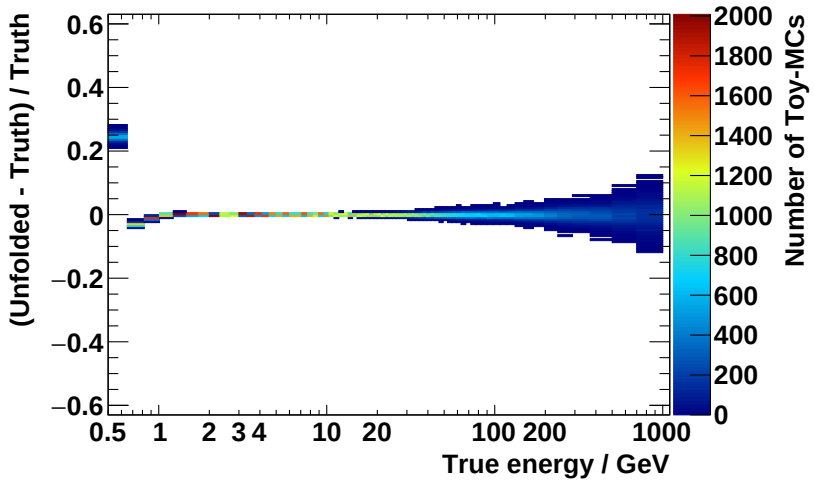

Figure 4.78: Distribution of the deviation of the unfolded e^- flux $\tilde{\Phi}_{\text{unfolded}}$ from the true flux Φ_{true} divided by the true flux for P Toy-MCs as function of the true energy.

To quantify the bias, projections to the y-axis are generated for each true energy bin. Figure 4.79 shows several example projections, from which the bias and the width can be deduced.

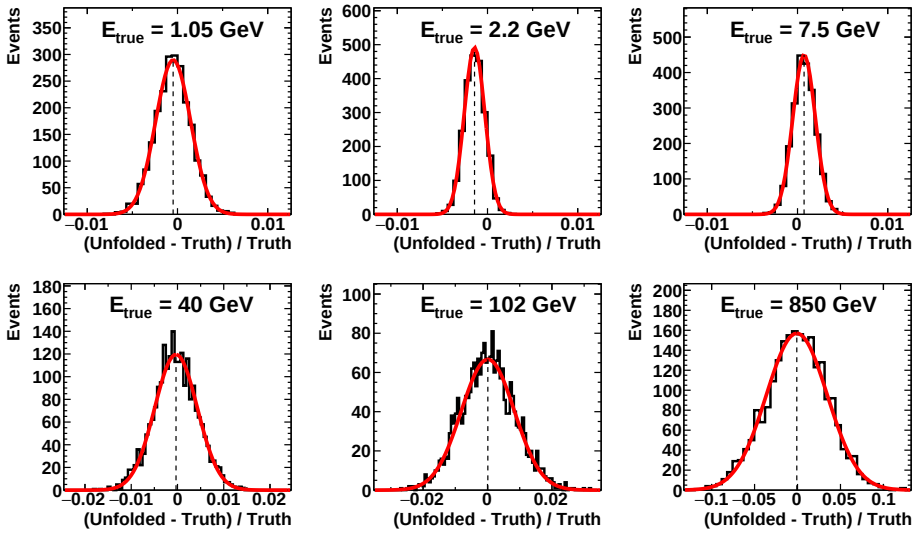

Figure 4.79: Example projections in several energy bins from Fig. 4.78 to the y-axis for the e^- fluxes. The black histogram shows the projection and the red line a gaussian fit to the histogram. The black dashed line indicates the mean of the gaussian, which is a measure of the bias.

After performing gaussian fits to the projections in all true energy bins the bias as function of the true energy can be quantified, as shown in Fig. 4.80 for the e^- flux.

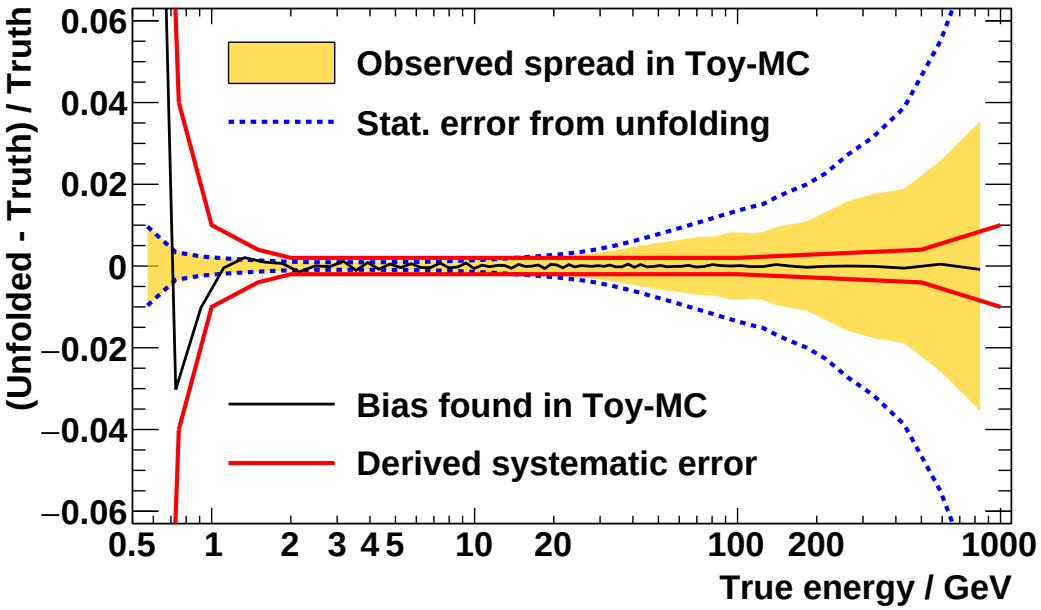

Figure 4.80: Visualization of the bias of the unfolding procedure for the e^- flux, extracted from the gaussian fits of Fig. 4.79, as function of the true energy. The black line shows the bias of the unfolded flux with respect to the true flux. The red line shows the associated systematic error, which by construction encloses the black line. The blue line shows the statistical uncertainty of the unfolded flux and the orange band the observed spread from the toy Monte-Carlo simulation - corresponding to the width of the gaussians in Fig. 4.79.

The same study can be performed for the e^+ flux: Fig. 4.81 shows the deviation of the unfolded flux $\tilde{\Phi}_{\text{unfolded}}$ from the true flux Φ_{true} divided by the true flux.

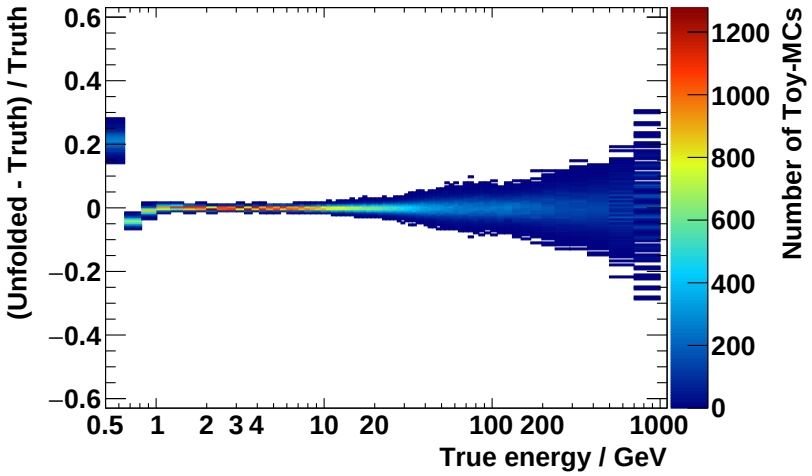

Figure 4.81: Distribution of the deviation of the unfolded e^+ flux $\tilde{\Phi}_{\text{unfolded}}$ from the true flux Φ_{true} divided by the true flux for P Toy-MCs as function of the true energy.

The ratio is compatible with unity above ≈ 1 GeV indicating that the unfolding procedure is free of a bias. Below that energy threshold a large deviation is exposed, which gets larger with decreasing energy. This behaviour is identical as for the electrons.

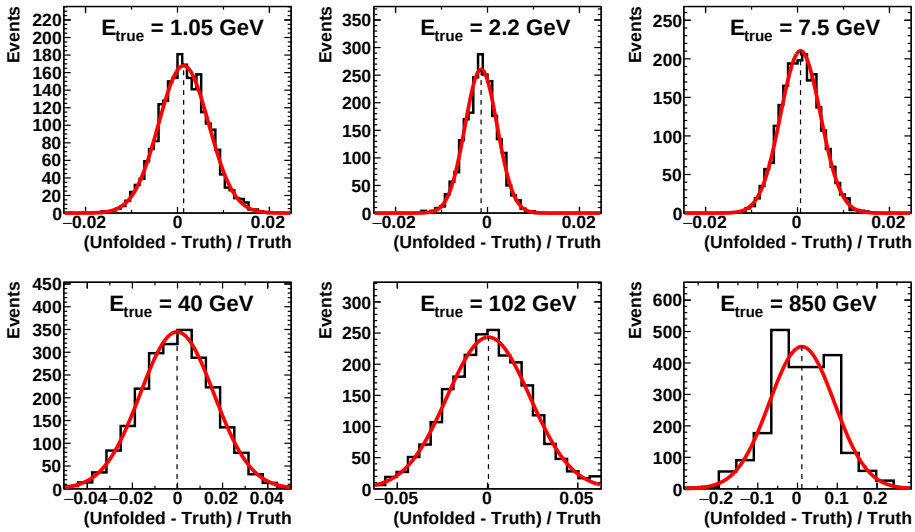

Figure 4.82: Example projections in several energy bins from Fig. 4.81 to the y-axis for the e^+ fluxes.

To quantify the bias, projections to the y-axis are performed for each true energy bin. Figure 4.82 shows several example projections, from which the bias can be deduced. After performing gaussian fits to the projections in all true energy bins the bias as function of the true energy can be quantified, as shown in Fig. 4.83 for the e^+ flux.

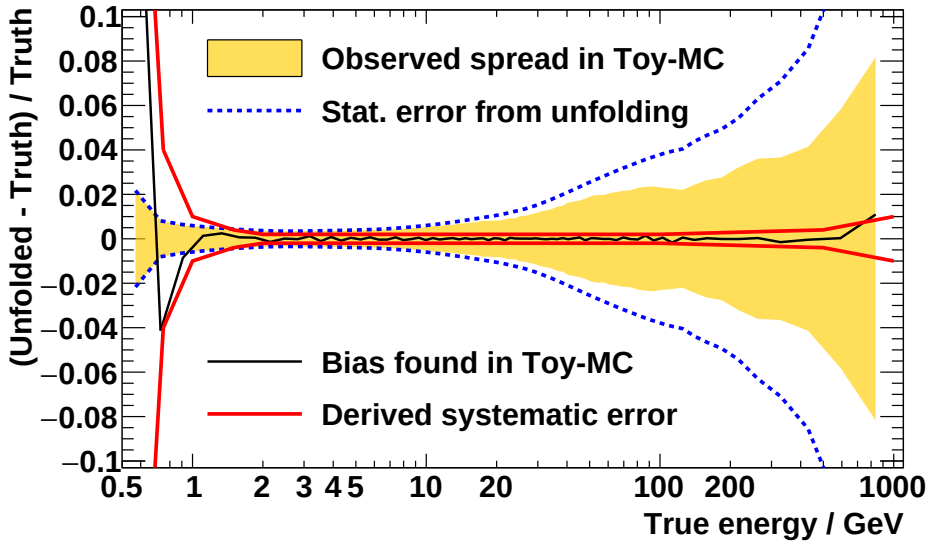

Figure 4.83: Visualization of the bias of the unfolding procedure for the e^+ flux, extracted from the gaussian fits of Fig. 4.82, as function of the true energy.

Note that the observed spread from the toy Monte-Carlo simulation (orange band) should match the statistical uncertainty from the unfolding procedure (blue line). Up to ≈ 10 GeV both methods yield the same results, at higher energies the spread in the Toy-MC is smaller than the expectation, which is in indication that the unfolding procedure slightly overestimates the true statistical uncertainty.

Derivation of the final unfolding uncertainty

Both components that contribute to the unfolding systematic uncertainty were determined: the limited knowledge of the migration matrix and the bias in the unfolding procedure. Figure 4.84 shows the resulting relative systematic uncertainty $\sigma_{\text{unf}}(E)/\Phi_{e^{\pm}}(E)$ as function of energy. The uncertainty associated with the electron flux is identical to the uncertainty associated with the positron flux.

From 3 – 100 GeV the uncertainty is constant at the permille level and thus negligible. It slightly increases towards high energies, due to the bias in the unfolding procedure and reaches less than 1 % at 1 TeV. At low energies the systematic uncertainty increases up to ≈ 20 % at 0.5 GeV.

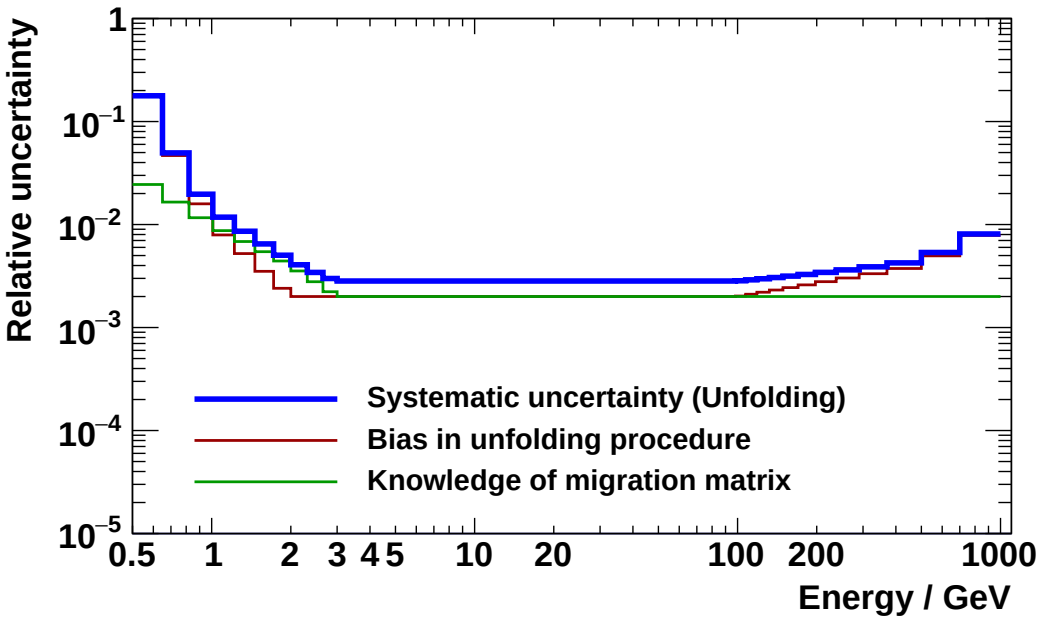

Figure 4.84: Visualization of the relative systematic uncertainty associated with the electron flux and the positron flux due to the unfolding procedure.

4.6.8 Summary

Figure 4.85 shows the composition of the relative systematic uncertainty $\sigma(E)/\Phi_{e^-}(E)$ as function of energy for the e^- flux.

Above ≈ 70 GeV the statistical uncertainty dominates the uncertainty of the e^- flux measurement. Below this energy, the systematic uncertainty always exceeds the statistical uncertainty. The acceptance uncertainty $\sigma_{\text{acc}}(E)$, described in Section 4.6.6, is the largest contribution to the overall systematic uncertainty between 1 – 600 GeV. Between 0.5 – 1 GeV the unfolding uncertainty $\sigma_{\text{unf}}(E)$, described in Section 4.6.7, dominates the systematic uncertainty.

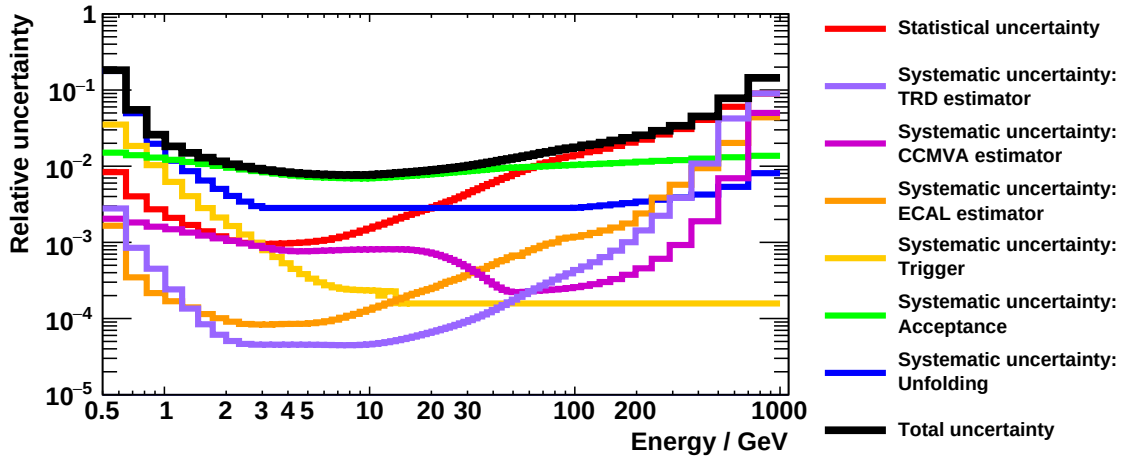

Figure 4.85: Composition of the relative systematic uncertainty associated with the electron flux.

Figure 4.86 shows the composition of the relative systematic uncertainty $\sigma(E)/\Phi_{e^+}(E)$ as function of energy for the e^+ flux. The statistical uncertainty dominates the uncertainty of the e^+ flux measurement, above 20 GeV. This observation is identical as for the e^- flux, with the difference that statistical limitations are already exposed at lower energies, as there a significantly less positrons in cosmic rays than electrons. Between 0.5 – 1 GeV the unfolding uncertainty $\sigma_{\text{unf}}(E)$, described in Section 4.6.7, dominates the systematic uncertainty - identical as for the electrons. The charge-confusion uncertainty $\sigma_{\text{cc}}(E)$, described in Section 4.6.2, and the acceptance uncertainty $\sigma_{\text{acc}}(E)$, described in Section 4.6.6, are the largest contributions to the overall systematic uncertainty at energies between 1 – 200 GeV. Above $\approx$ 200 GeV the uncertainty $\sigma_{\text{trd}}(E)$, associated with the knowledge of the shape of the TRD estimator (Section 4.6.1), dominates the systematic uncertainty.

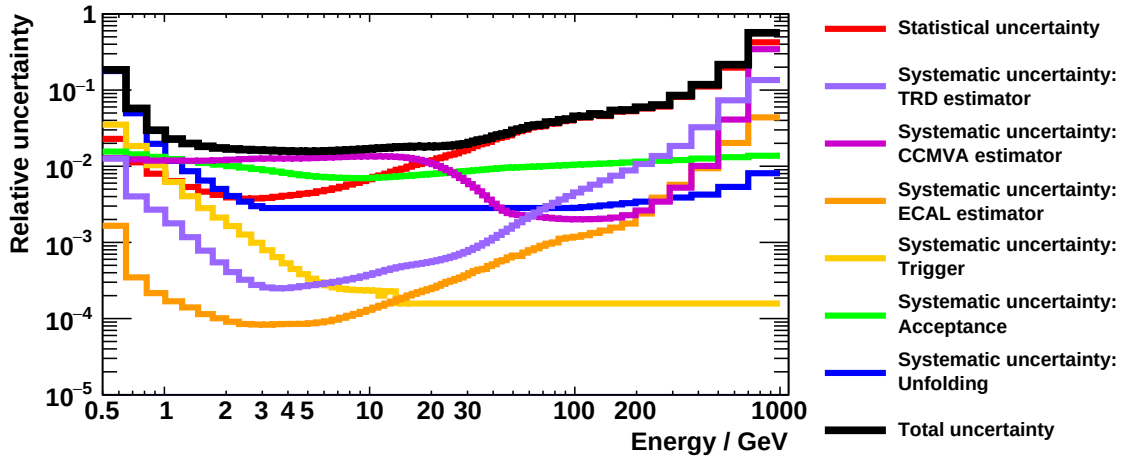

Figure 4.86: Composition of the relative systematic uncertainty associated with the positron flux.

4.7 Time-averaged positron/electron ratio and positron fraction calculation

The time-averaged positron/electron ratio in the energy bin E of width ΔE is given by

$$R_e(E) = \frac{\Phi_{e^+}(E)}{\Phi_{e^-}(E)}, \tag{4.27}$$

and the positron fraction by

$$p(E) = \frac{\Phi_{e^+}(E)}{\Phi_{e^+}(E) + \Phi_{e^-}(E)}. \tag{4.28}$$

When inserting the $e^\pm$ fluxes $\Phi_{e^\pm,i}(E)$ from Eq. (4.1) into the equations for the positron/electron ratio Eq. (4.27) and the positron fraction Eq. (4.28) it is obvious that the bin width ΔE and the measuring time $T(E)$ as well as the efficiencies $\epsilon(E)$ cancel. The acceptance does not cancel strictly, since it slightly differs for positrons/electrons at low energies:

$$\begin{aligned} R_e(E) &= \frac{N_{e^+}(E)}{N_{e^-}(E)} \cdot \frac{\mathbf{A_{e^-}(E)}}{\mathbf{A_{e^+}(E)}}, \\ p(E) &= \frac{N_{e^+}(E)}{N_{e^+}(E) + N_{e^-}(E) \cdot \frac{\mathbf{A_{e^+}}}{\mathbf{A_{e^-}}}}. \end{aligned} \tag{4.29}$$

The positron over electron acceptance ratio

$$\frac{A_{e^+}(E)}{A_{e^-}(E)} = \frac{A^{\mathrm{MC}}_{e^+}(E)}{A^{\mathrm{MC}}_{e^-}(E)} \cdot \frac{1+\delta_{e^+}(E)}{1+\delta_{e^-}(E)} = \frac{A^{\mathrm{MC}}_{e^+}(E)}{A^{\mathrm{MC}}_{e^-}(E)} \tag{4.30}$$

was determined from the electron and positron Monte-Carlo simulation, as described in Section 4.5.5, and is used to correct the positron/electron ratio and the positron fraction results. Since in the positron/electron ratio and the positron fraction the uncertainty on the absolute acceptance is not present, the acceptance asymmetry uncertainty $\sigma_{\mathrm{asymm}}(E)$ must be taken into account.

The number of electrons and positrons $N_{e^\pm}(E)$ can be extracted from the two-dimensional template fit procedure, with the charge-confusion value fixed to the Monte-Carlo prediction, as described in Section 4.4.5. However there are important differences in the data samples that are analyzed between the flux and the ratio analysis. A summary is given in Table 4.2 and will be explained in the following.

Component	Single-track analysis	All-tracks analysis
Statistics	nominal	increased by $\approx 20\,\%$
Acceptance	$(1+\delta(E)) \approx 5\,\%$ larger	$(1+\delta(E))$ nominal
Charge-confusion	$f_{\mathrm{CC}} = 0.38\,\%$ at $\approx 20\,\mathrm{GeV}$	$f_{\mathrm{CC}} = 1.49\,\%$ at $\approx 20\,\mathrm{GeV}$
Suitable for	$R_e(E)$, $p(E)$ analysis	$\Phi_{e^+}(E)$, $\Phi_{e^-}(E)$ analysis

Table 4.2: Comparison of the analysis strategies for the electron and positron flux analysis with respect to the positron/electron ratio and positron fraction analysis. The single-track analysis is chosen for the positron/electron ratio and positron fraction analysis and the all-tracks analysis for the electron and positron flux analysis.

For the flux analysis the "all-tracks sample", a union of the "single-track sample" and the "multi-tracks sample", is used to determine the number of electrons and the number of positrons. Using the all-tracks sample the smallest possible acceptance systematic uncertainty can be achieved, since imposing a single tracker track cut leads to a large deviation between the ISS selection efficiency and the Monte-Carlo prediction. This enlarges the Data/Monte-Carlo correction factor $(1 + \delta(E))$ by $\approx 5\,\%$ and increases the systematic uncertainty by almost 3 %. As side-effect the statistics can be increased by almost $\approx 20\,\%$. The drawback of the all-tracks sample is the enlarged charge-confusion and its associated uncertainty. However the overall uncertainty of the flux analysis based on the all-tracks sample is smaller compared to using the single-track sample. As consequence the all-tracks sample is used for the $\Phi_{e^\pm}(E)$ flux analysis.

For the positron/electron ratio $R_e(E)$ and the positron fraction $p(E)$ this argument does not hold, since the acceptance uncertainty cancels in the ratios. The charge-confusion in the single-track sample is considerable smaller and the magnitude of the unfolding is smaller, since the single-track sample is less affected by migration effects, due to a better energy reconstruction in these events. For these reasons the ratio analysis will be performed using the event counts $N_{e^\pm}(E)$ from the single-track sample.

4.8 Time-averaged systematic uncertainties for positron/electron ratio and positron fraction

In this section all systematic uncertainties that contribute to the time-averaged positron/electron ratio and positron fraction are summarized.

The most important systematic uncertainty for the ratio analysis is the unfolding uncertainty, described in Section 4.8.1, dominating the overall systematic uncertainty up to 50 GeV. Between 2 – 4 GeV the acceptance asymmetry uncertainty is the largest contribution, described in Section 4.8.2. Above 50 GeV the knowledge of the TRD estimator and the associated uncertainty is the dominant systematic uncertainty, presented in Section 4.8.4.

4.8.1 Unfolding

The number of electrons or positrons as function of energy, are unfolded as described in Section 4.5.6 and the uncertainty was redetermined using the single-track sample and is slightly smaller as for the flux analysis presented in Section 4.6.7.

Figure 4.87 shows the resulting relative systematic uncertainty $\sigma_{\text{unf}}(E)/R_e(E)$ as function of energy for the positron/electron ratio. The uncertainty is identical for the positron fraction.

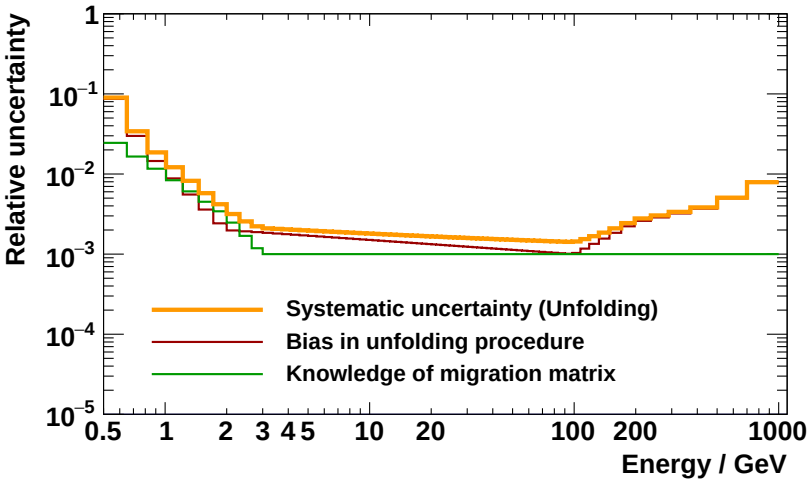

Figure 4.87: Visualization of the relative systematic uncertainty associated with the positron/electron ratio and the positron fraction due to unfolding.

4.8.2 Acceptance asymmetry

The uncertainty was derived for the $e^{\pm}$ fluxes in Section 4.5.5. For the flux analysis the small uncertainty due to the acceptance asymmetry was neglected, since the acceptance uncertainty $\sigma_{\text{acc}}(E)$ is considerable larger. For the positron/electron ratio and the positron fraction the acceptance uncertainty cancels by definition, such that the acceptance asymmetry uncertainty $\sigma_{\text{asymm}}(E)$ becomes important.

Figure 4.88 shows the resulting relative systematic uncertainty $\sigma_{\text{asymm}}(E)/R_e(E)$ as function of energy for the positron/electron ratio and the relative systematic uncertainty $\sigma_{\text{asymm}}(E)/p(E)$ as function of energy for the positron fraction.

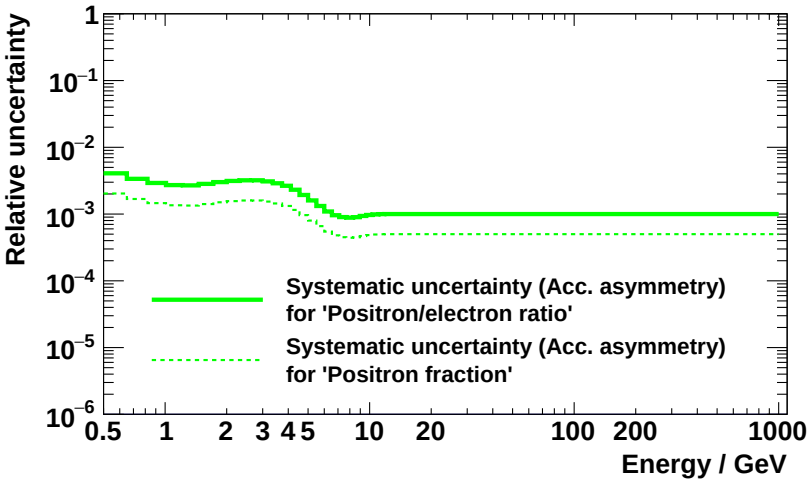

Figure 4.88: Visualization of the relative systematic uncertainty associated with the positron/electron ratio and the positron fraction due to the acceptance asymmetry between e^- / e^+.

4.8.3 CCMVA estimator

The charge-confusion uncertainty was derived for the $e^{\pm}$ fluxes in Section 4.6.2. To study the influence of the amount of charge-confusion on the positron/electron ratio $R_e(E)$ and the positron fraction $p(E)$ the same procedure as for the flux analysis (Section 4.6.2) will be repeated.

Figure 4.89 shows the resulting relative systematic uncertainty $\sigma_{\mathrm{cc}}(E)/R_e(E)$ as function of energy for the positron/electron ratio and the relative systematic uncertainty $\sigma_{\mathrm{cc}}(E)/p(E)$ as function of energy for the positron fraction.

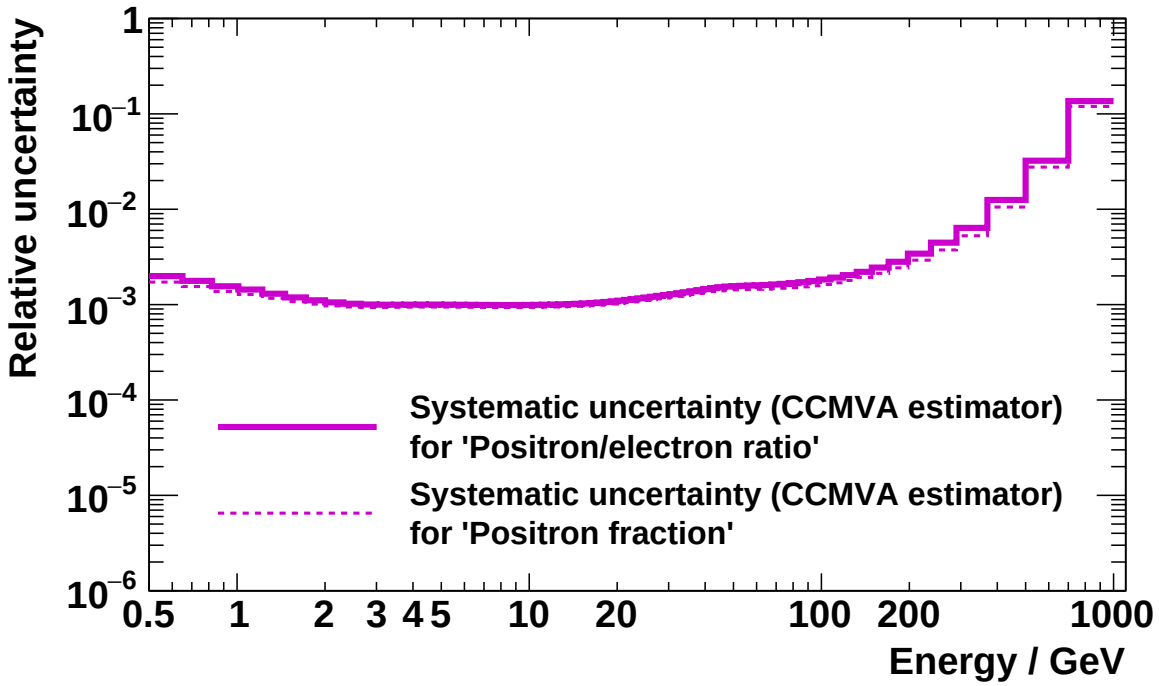

Figure 4.89: Visualization of the relative systematic uncertainty associated with the positron/electron ratio and the positron fraction due to the knowledge of the charge-confusion.

4.8.4 TRD estimator

The TRD estimator uncertainty was derived for the $e^{\pm}$ fluxes in Section 4.6.1. The same procedure is repeated for the positron/electron ratio and the positron fraction, with the only difference that the multi-tracks sample does not need to be considered: only the TRD templates for the single-track sample are varied.

Figure 4.90 shows the resulting relative systematic uncertainty $\sigma_{\mathrm{trd}}(E)/R_e(E)$ as function of energy for the positron/electron ratio and the relative systematic uncertainty $\sigma_{\mathrm{trd}}(E)/p(E)$ as function of energy for the positron fraction.

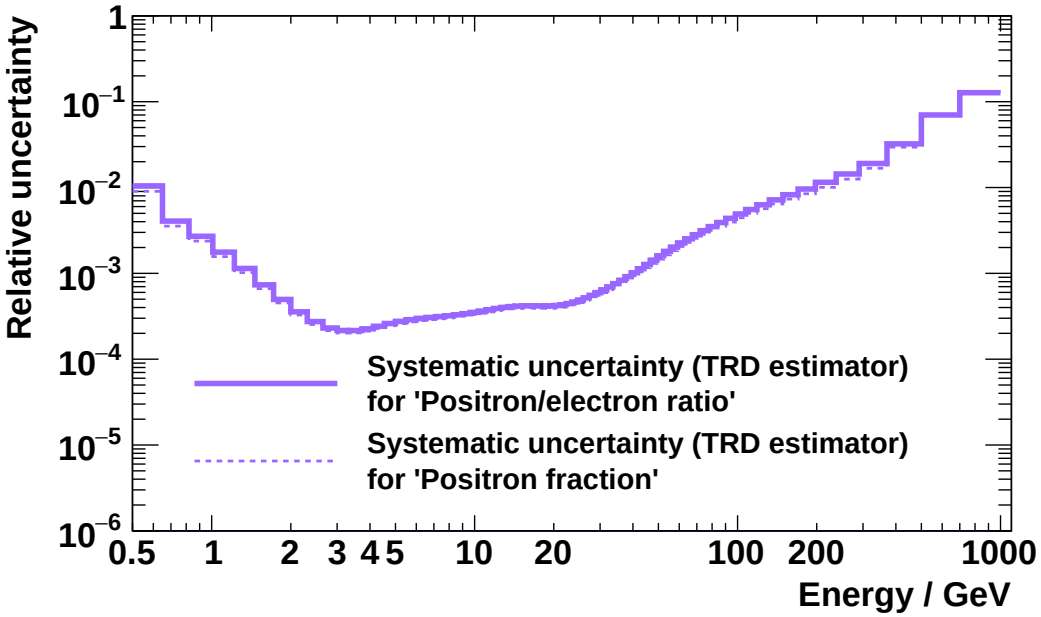

Figure 4.90: Visualization of the relative systematic uncertainty associated with the positron/electron ratio and the positron fraction due to the knowledge of the TRD estimator.

4.8.5 Summary

Figure 4.91 shows the composition of the relative systematic uncertainty $\sigma(E)/R_e(E)$ as function of energy for the positron/electron ratio. The composition of the relative systematic uncertainty $\sigma(E)/p(E)$ as function of energy for the positron fraction is almost identical and thus was omitted.

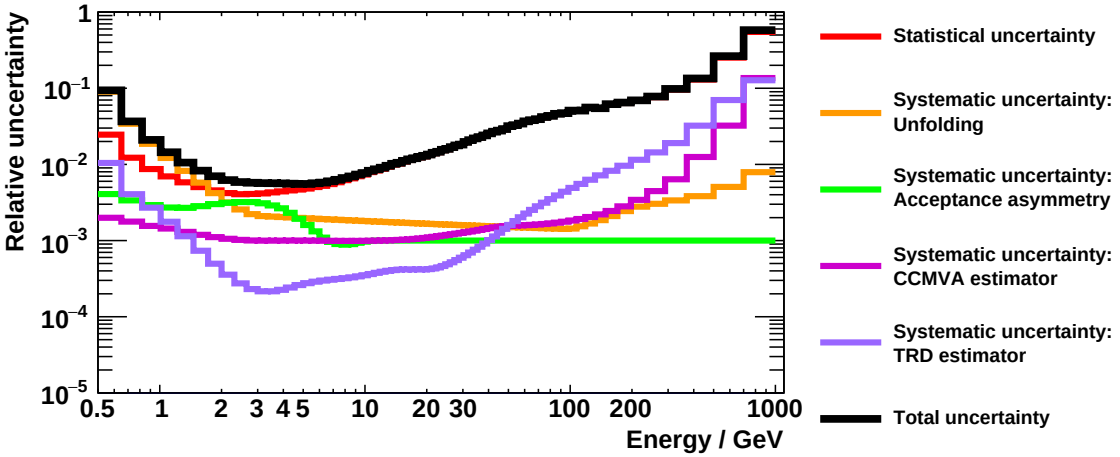

Figure 4.91: Composition of the relative systematic uncertainty associated with the positron/electron ratio.

For both the positron/electron ratio and the positron fraction the unfolding uncertainty dominates at low energies, below ≈ 2 GeV where the migration effect is strong. Above ≈ 2 GeV the statistical uncertainty dominates the overall uncertainty.

4.9 Time-dependent flux calculation

The equation for the flux in time bin i is given by

$$\Phi_{e^{\pm},i}(E) = \frac{N_{e^{\pm},i}(E)}{\Delta E \cdot T_i(E) \cdot A_{e^{\pm},i}(E) \cdot \epsilon_i(E)}. \tag{4.31}$$

The efficiency $\epsilon_i(E)$ is defined in Eq. (4.32) as the product of the trigger efficiency and the ECAL estimator efficiency. Both efficiencies will be derived directly from ISS data, without involving any Monte-Carlo simulations - just like for the time-averaged flux analysis.

$$\epsilon_i(E) = \epsilon_{\text{trigger},i}(E) \cdot \epsilon_{\text{ecal},i}(E) \tag{4.32}$$

For the time-dependent analysis the whole time interval - **May 20$^{\text{th}}$, 2011** until **November 12$^{\text{th}}$, 2017** - is divided into 88 periods that last exactly 27 days - corresponding to one "Bartels rotation" [Bartels1934]. The Bartels rotation number is a monotonically increasing number that marks the apparent rotations of the Sun as viewed from Earth. The first Bartels rotation starts on **February, 8$^{\text{th}}$ 1832** - an arbitrary assignment proposed by Julius Bartels.

In total 49 energy intervals are analyzed spanning the range 1.01 – 49.33 GeV. The same energy intervals are used as for the time-averaged analysis, just in a reduced range, to account for the reduced statistics with respect to the full time range.

To derive time-dependent fluxes the question arises, which components of the flux Eq. (4.31) are time-dependent and which ones can be taken from the time-averaged analysis. Clearly the measuring time $T_i(E)$ and the number of electrons or positrons $N_{e^{\pm},i}(E)$ have to be computed for each Bartels rotation i separately.

4.9.1 ECAL estimator efficiency

The ECAL estimator efficiency $\epsilon_{\text{ecal},i}(E)$ is determined individually in each Bartels rotation i, following the recipe given in the time-averaged flux analysis, described in Section 4.5.1.

The results of the bootstrap method are compared between the time-averaged flux analysis and the time-dependent flux analysis for all energy bins and Bartels rotations. For all energy bins the average of the time-dependent ECAL estimator efficiency is compatible with the time-averaged ECAL estimator efficiency and thus $\epsilon_{\text{ecal},i}(E) = \epsilon_{\text{ecal}}(E)$.

4.9.2 Trigger efficiency

The trigger efficiency $\epsilon_{\text{trigger},i}(E)$ is determined individually in each Bartels rotation i, following the recipe given in the time-averaged flux analysis, described in Section 4.5.2.

Figure 4.92 show the trigger efficiency as function of time for the first energy bin of the time-dependent analysis. For all energy bins the average of the time-dependent trigger efficiency is compatible with the time-averaged trigger efficiency and thus $\epsilon_{\text{trigger},i}(E) = \epsilon_{\text{trigger}}(E)$.

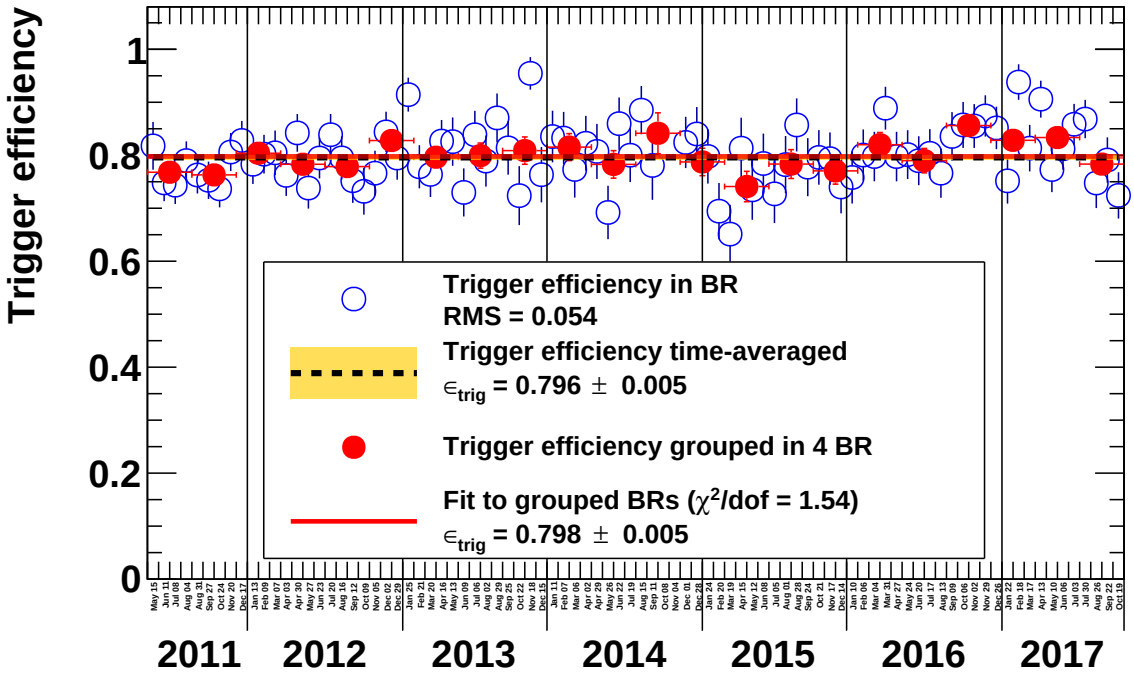

Figure 4.92: Time-dependent trigger efficiency for the energy bin 1.01 – 1.22 GeV. The x-axis spans 88 Bartels rotations and each bin label denotes the date when the Bartels rotation started (in UTC). The blue symbols show the trigger efficiency in the specific energy bin as function of time. The red symbols group four Bartels rotation into one point in time to reduce the statistical fluctuations. The black dashed line shows the time-averaged efficiency for comparison. The red line shows a fit of a constant to the red symbols, yielding an acceptable χ^2/dof = 1.37 value. Within the uncertainties the trigger efficiency is independent of time.

Since both the trigger efficiency and the ECAL estimator efficiency are independent of time the whole efficiency is identical to the time-averaged case (Eq. (4.14) in Section 4.5):

$$\epsilon(E) = \epsilon_{\text{trigger}}(E) \cdot \epsilon_{\text{ecal}}(E).$$

4.9.3 Acceptance

The time-dependent acceptance $A_{e^\pm,i}(E)$ entering the flux Eq. (4.31) is given by

$$A_{e^\pm,i}(E) = A^{\text{MC}}_{e^\pm}(E) \cdot (1 + \delta_i(E)), \tag{4.33}$$

where $\delta_i(E)$ denotes a time-dependent Data/Monte-Carlo correction factor for Bartels rotation i.

For each cut in the preselection category (defined in Section 4.3.2), the selection category (defined in Section 4.3.3) and the $e^\pm$ identification category (defined in Section 4.3.4) and each Bartels rotation i the tag & probe method - described in Section 4.5.4 for the time-averaged flux analysis - is performed.

A negative rigidity sample (**"tag sample"**) is selected for every cut c using information from detectors unrelated to that cut. The efficiency of each cut c is compared between ISS data in Bartels rotation i and the electron Monte-Carlo simulation. The ratio ISS efficiency divided by Monte-Carlo efficiency - as function of energy - is computed. If the ratio differs from unity, it is parameterized

using a simple model, e.g. a constant or a straight line. The best matching model is fit to the ratio. Afterwards it will be tested if the deviation from unity is significant, according to the uncertainty of the fit parameters.

It turns out that the energy dependence of each cut c in each Bartels rotation i is identical to the time-averaged energy dependence. Therefore it is not necessary to compare the ISS data in each Bartels rotation i with the electron Monte-Carlo simulation and parameterize the ISS efficiency over Monte-Carlo efficiency ratio in order to extract the correction factor $(1 + \delta_i^c(E))$. Instead the cut efficiency of each cut c in each Bartels rotation i can be directly compared to the ISS time-averaged cut efficiency, by computing the ratio: efficiency in Bartels rotation i divided by time-averaged ISS cut efficiency.

Figure 4.93 shows the comparison between the time-averaged cut efficiency and the time-dependent cut efficiency in a single Bartels rotation, as example, for the "Tracker hit pattern" cut. The structure in the ratio plot around ≈ 25 GeV is a statistical fluctuation and is not present in other Bartels Rotations.

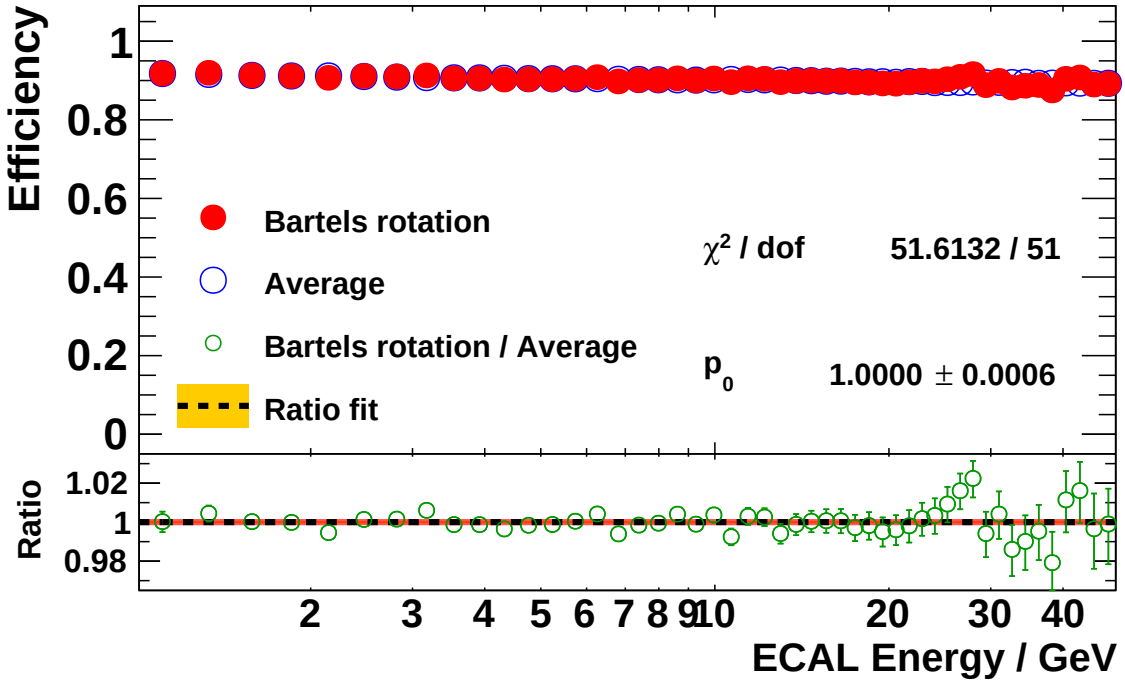

Figure 4.93: Determination of the ratio: time-averaged cut efficiency $(1 + \delta^c(E))$ over time-dependent cut efficiency $(1 + \delta_i^c(E))$ in Bartels rotation $i = 26$ (Apr 16$^{\text{th}}$, 2013 - May 13$^{\text{th}}$, 2013) for the selection cut: **"Tracker hit pattern"** (Section 4.3.3 - Item 5). The blue symbols in the upper plot show the cut efficiency determined from ISS data for the time-averaged analysis on a dedicated sample: the tag sample. The red symbols in the upper plot show the cut efficiency determined from ISS data in Bartels rotation $i = 26$ using the same tag cuts. The lower plot shows the ratio time-averaged efficiency over efficiency in Bartels rotation $i = 26$ as green symbols. A constant is fit to the ratio, shown as dashed black line including the orange uncertainty band.

Figure 4.94 shows the same comparison for the "TRD helium rejection" cut in a single Bartels rotation. These are the only cuts that exhibit a significant time dependence, that needs to be corrected for.

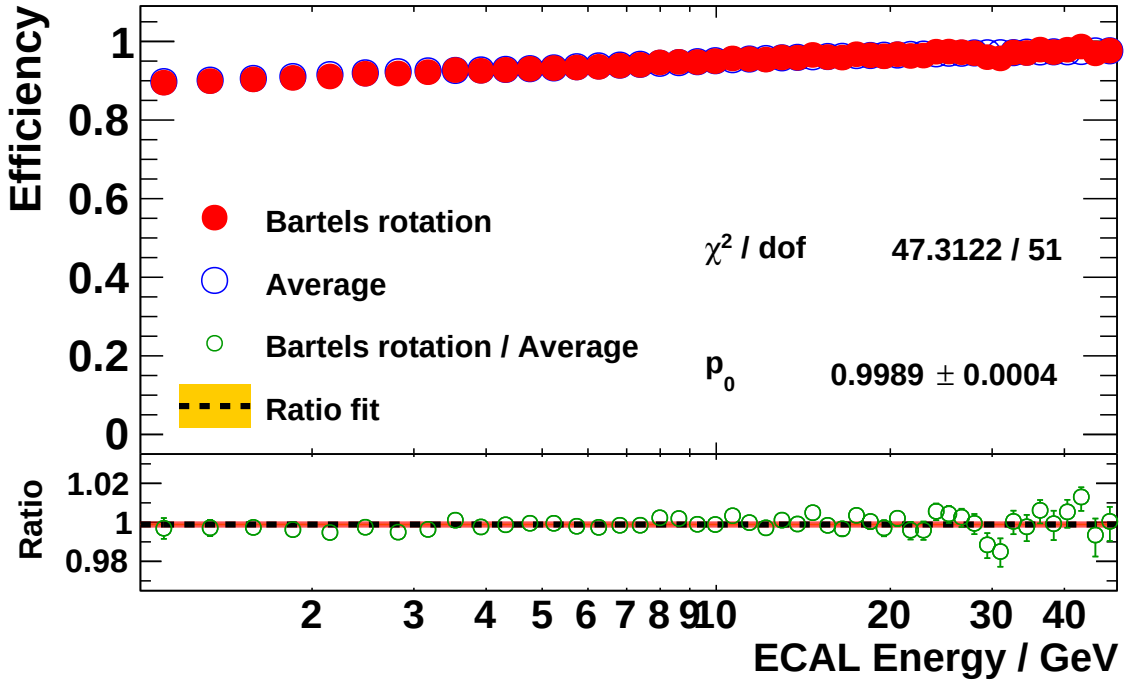

Figure 4.94: Determination of the ratio: time-averaged cut efficiency $(1 + \delta^c(E))$ over time-dependent cut efficiency $(1 + \delta_i^c(E))$ in Bartels rotation $i = 26$ (Apr 16$^{\text{th}}$, 2013 - May 13$^{\text{th}}$, 2013) for the selection cut: **"TRD helium rejection"** (Section 4.3.3 - Item 4). The blue symbols in the upper plot show the cut efficiency determined from ISS data for the time-averaged analysis on a dedicated sample: the tag sample. The red symbols in the upper plot show the cut efficiency determined from ISS data in Bartels rotation $i = 26$ using the same tag cuts. The lower plot shows the ratio time-averaged efficiency over efficiency in Bartels rotation $i = 26$ as green symbols. A constant is fit to the ratio, shown as dashed black line including the orange uncertainty band.

Since the energy dependence of each cut c in each Bartels rotation i is identical to the time-averaged energy dependence, the correction factor $(1 + \delta_i^c(E))$ can be factored into the time-averaged part $(1 + \delta^c(E))$ and an additional time-dependent correction factor $(1 + \hat{\delta}(t))$:

$$1 + \delta_i^c(E) = (1 + \delta^c(E)) \cdot (1 + \hat{\delta}^c(t)).$$

The time-averaged part $(1 + \delta^c(E))$ stems from the time-averaged flux analysis and is derived by comparing the predicted cut efficiency from the electron Monte-Carlo simulation to the time-averaged ISS data for each cut c. The time-dependent part $(1 + \hat{\delta}^c(t))$ is the ratio of the time-dependent ISS cut efficiency in each Bartels rotation i to the time-averaged ISS cut efficiency.

Since all correction factors $(1 + \delta_i^c(E))$ are uncorrelated by a careful construction of the tag samples, the correction $(1 + \delta_i(E))$ is a product of all individual correction factors $(1 + \delta_i^c(E))$:

$$1 + \delta_i(E) = \prod_c (1 + \delta_i^c(E)) = \prod_c (1 + \delta^c(E)) \cdot (1 + \hat{\delta}^c(t)) = (1 + \delta(E)) \cdot (1 + \hat{\delta}(t)).$$

Figure 4.95 shows the time-dependent correction factor $(1 + \hat{\delta}^c(t))$ for the "Tracker hit pattern" cut and Fig. 4.96 shows the same comparison for the "TRD helium rejection" cut.

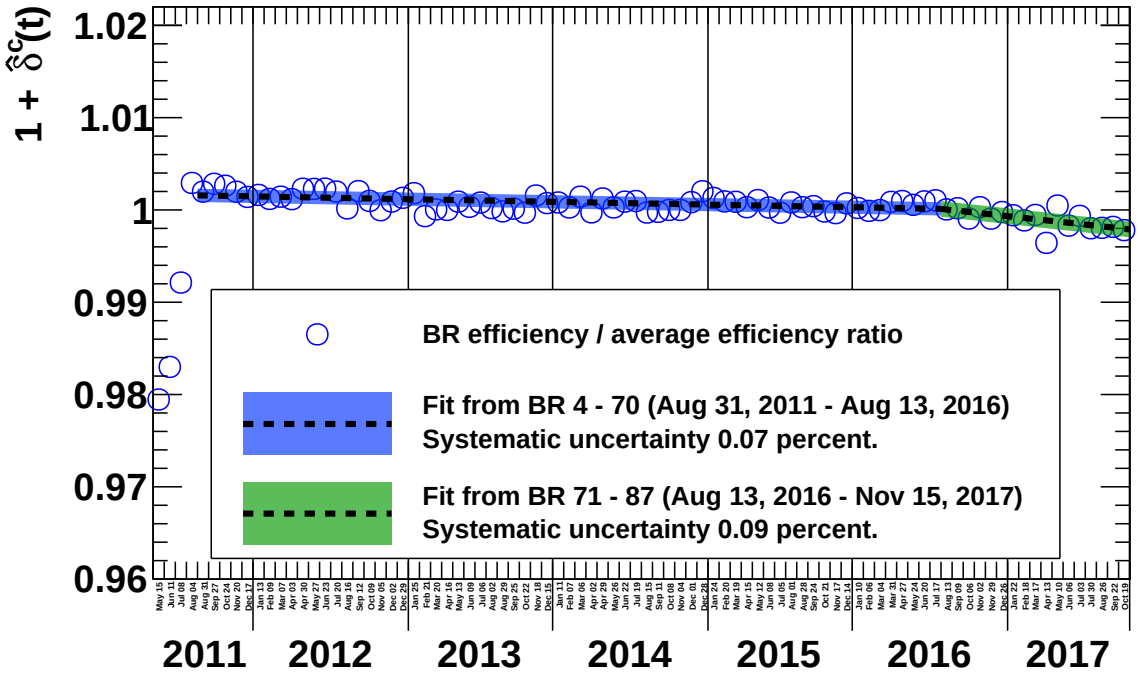

Figure 4.95: Determination of the time-dependent correction factor $(1 + \hat{\delta}^c(t))$ for the selection cut: **"Tracker hit pattern"** (Section 4.3.3 - Item 5). The open blue symbols show the ratio: time-dependent cut efficiency over time-averaged cut efficiency for all Bartels rotations (an example of the ratio determined in a single Bartels rotation is shown in Fig. 4.93). The black dashed lines show regions parameterized using straight lines. When the efficiency remains stable over an extended period of time, following a simple trend (e.g. slowly decreasing or constant) a parameterization of the time period is used instead of the individual data points to describe the time dependency. The colored bands indicate the systematic uncertainty on the time-dependent correction factor $(1 + \hat{\delta}^c(t))$. For individual data points, the uncertainty on the data point - from the previous ratio fit procedure - is taken.

The "Tracker hit pattern" cut is sensitive to the overall tracking efficiency of the tracker. During the first three Bartels rotations the tracker reconstruction efficiency was lower than the average efficiency.

From the beginning of data taking up to July 24$^{\text{th}}$, 2011 the tracker calibration was improved (new second step calibration [BazoAlba2013]) and the reconstruction efficiency was improved by $\approx 2\,\%$.

On December 1$^{\text{st}}$, 2011 six ladders were lost from DAQ because of a power supply malfunction in one crate, leading to a loss of $\approx 1.2\,\%$ of all channels in the readout. This resulted in a slightly reduced overall reconstruction efficiency, which is partly recovered by changes in the offline reconstruction software. From this date onwards the tracking efficiency remained stable. Since the beginning of 2017 a slight degradation is observed - however it is on the permille level and does not significantly affect the reconstruction efficiency.

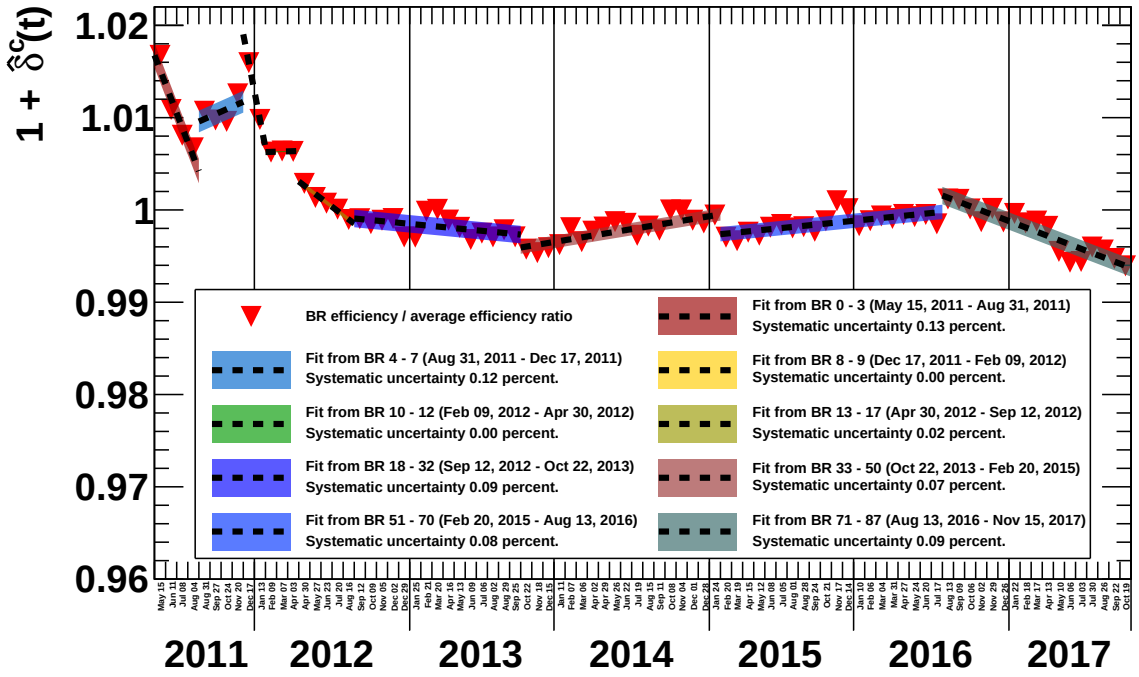

Figure 4.96: Determination of the time-dependent correction factor $(1 + \hat{\delta}^c(t))$ for the selection cut: **"TRD helium rejection"** (Section 4.3.3 - Item 4). The red triangle symbols show the ratio: time-dependent cut efficiency over time-averaged cut efficiency for all Bartels rotations (an example of the ratio determined in a single Bartels rotation is shown in Fig. 4.94). The black dashed lines show regions parameterized using straight lines. When the efficiency remains stable over an extended period of time, following a simple trend (e.g. slowly decreasing or constant) a parameterization of the time period is used instead of the individual data points to describe the time dependency. The colored bands indicate the systematic uncertainty on the time-dependent correction factor $(1 + \hat{\delta}^c(t))$. For individual data points, the uncertainty on the data point - from the previous ratio fit procedure - is taken.

The "TRD helium rejection" cut has a complex time structure, due to recurring changes in the TRD operation (such as gas refills, high-voltage changes, etc.), described in Section 3.4. In the beginning of the data taking period the cut efficiency was higher than the average efficiency, because the TRD was operated with a lower xenon partial pressure [Kirn2019]. This leads to a worse rejection and thus the separation power is smaller.

Since June 2012 the TRD operation is stable and the procedure to keep the rejection at a constant level is established. This is reflected in an extended period of time where the cut efficiency is stable and only varies at the permille level. In 2017 the overall pressure and thus the xenon partial pressure were reduced to lower the diffusion losses. This is reflected as a slight decrease in the cut efficiency.

Since the individual correction factors $(1 + \hat{\delta}^c(t))$ for both cuts are determined, the combined correction factor $(1 + \hat{\delta}(t))$ can be computed, as shown in Fig. 4.97.

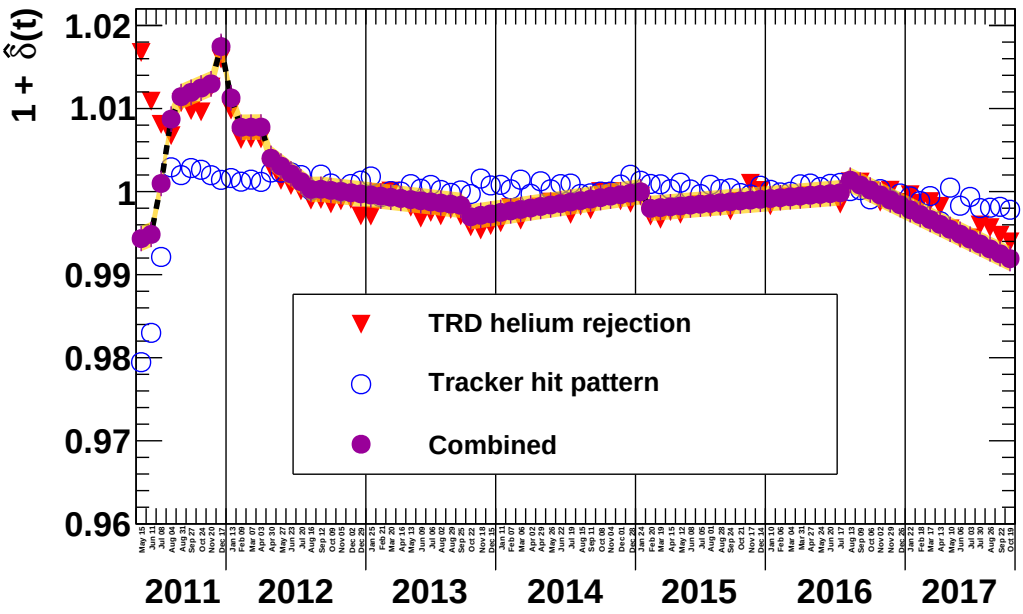

Figure 4.97: Determination of the time-dependent correction factor $(1 + \hat{\delta}(t))$. The red triangle symbols show the correction factor for the **"TRD helium rejection"** cut and the blue circle symbols show the correction factor for the **"Tracker hit pattern"** cut. The combined correction factor is shown as magenta symbols. The uncertainty is shown as orange band on top of the magenta symbols.

The overall time-dependent correction factor $(1 + \hat{\delta}(t))$ varies from 0.5 % to ≈ 2 % for a few Bartels rotations in the beginning of the data taking period. Since the beginning of 2012 the correction is almost flat and varies at the permille level around unity. In late 2016 the correction becomes important again as it rises up to ≈ 1 % in the end of 2017.

4.9.4 Charge-confusion

The charge-confusion $f_{\mathrm{cc},i}(E)$ is determined individually in each Bartels rotation i, following the recipe given in the time-averaged flux analysis, described in Section 4.4.5. The two-dimensional template fit procedure is executed with the charge-confusion as free fit parameter. The so-obtained charge-confusion value for each energy bin j and each Bartels rotation j is then compared to the time-averaged charge-confusion value $f_{\mathrm{cc}}(E)$.

For all energy bins the average of the charge-confusion value is compatible with the time-averaged charge-confusion and thus $f_{\mathrm{cc},i}(E) = f_{\mathrm{cc}}(E)$ (Appendix A.8). As consequence the charge-confusion in the time-dependent two-dimensional templates fits can be fixed to the Monte-Carlo prediction, as for the time-averaged flux analysis.

4.9.5 TRD templates

The procedure to extract the TRD templates from ISS data was described in Section 4.4.2 for the time-averaged analysis. These TRD templates are not applicable for each Bartels rotation, individually, due to recurring changes in the TRD operation. The TRD operation changes are the same reason for the complex time dependence in the "TRD helium rejection" cut.

Five TRD template parameters were identified, having a non-negligible time dependence. One parameter describing the charge-confused protons: peak position $\mu_{\text{ccprot, novo}}$, two parameters for the electron template: peak position $\mu_{\text{elec, novo}}$, width $\sigma_{\text{elec, novo}}$ and two parameters concerning the proton templates: peak position $\mu_{\text{prot, novo}}$ and width $\sigma_{\text{prot, novo}}$.

The time-dependence of each of the TRD template parameter c is examined, by repeating the TRD template extraction procedure in each Bartels rotation i for each energy bin j. For each TRD template parameter c, all energy bins that show a similar time-dependence are grouped together. The time-dependence of all energy bins for the $\mu_{\text{elec, novo}}$ and the $\mu_{\text{prot, novo}}$ parameters is identical. Figures 4.98 and 4.99 show the time-dependence of the $\mu_{\text{elec, novo}}$ and $\mu_{\text{prot, novo}}$ parameters for all energy bins in the time-dependent analysis for the single-track sample. Each energy j bin is represented by a different color. The filled red points represent the average time-dependence of the parameters. It was determined by executing a simultaneous fit of a spline curve to all data points of each TRD template parameter c.

The results for the multi-tracks samples are shown in Appendix A.9.

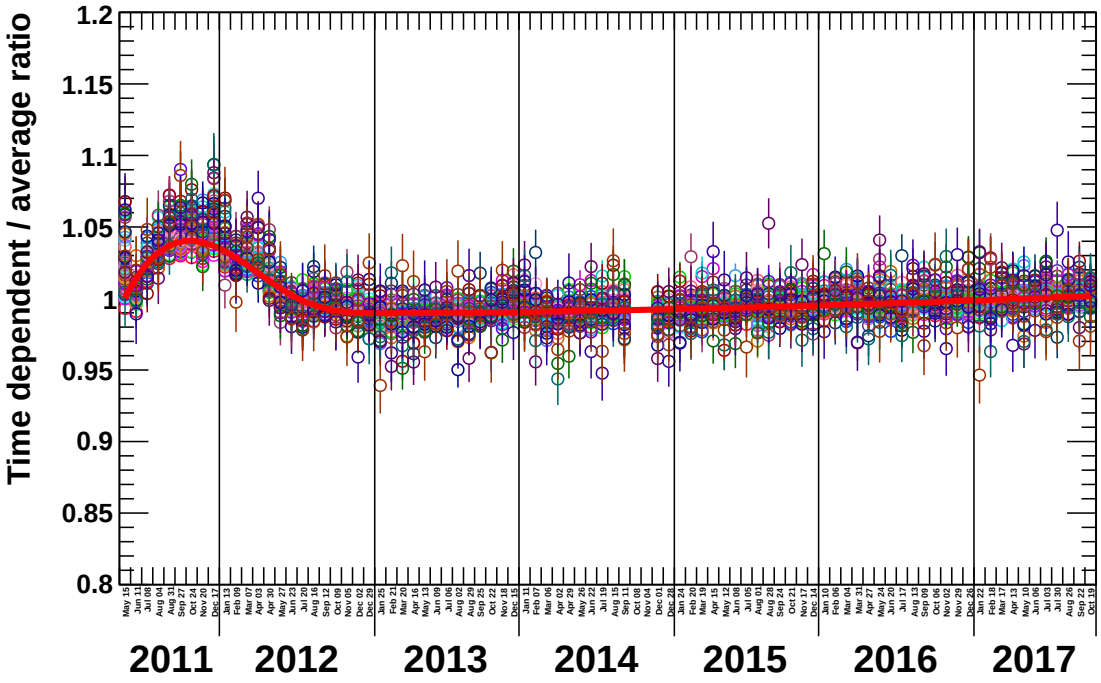

Figure 4.98: Time-dependence of the $\mu_{\text{elec, novo}}$ parameter for all energy bins - 0.65 – 52.33 GeV - in the time-dependent analysis for the single-track sample. Each energy bin is represented by a different color. The filled red line denote the result of a spline fit, simultaneously to all data points, describing the average time-dependence of the $\mu_{\text{elec, novo}}$ parameter.

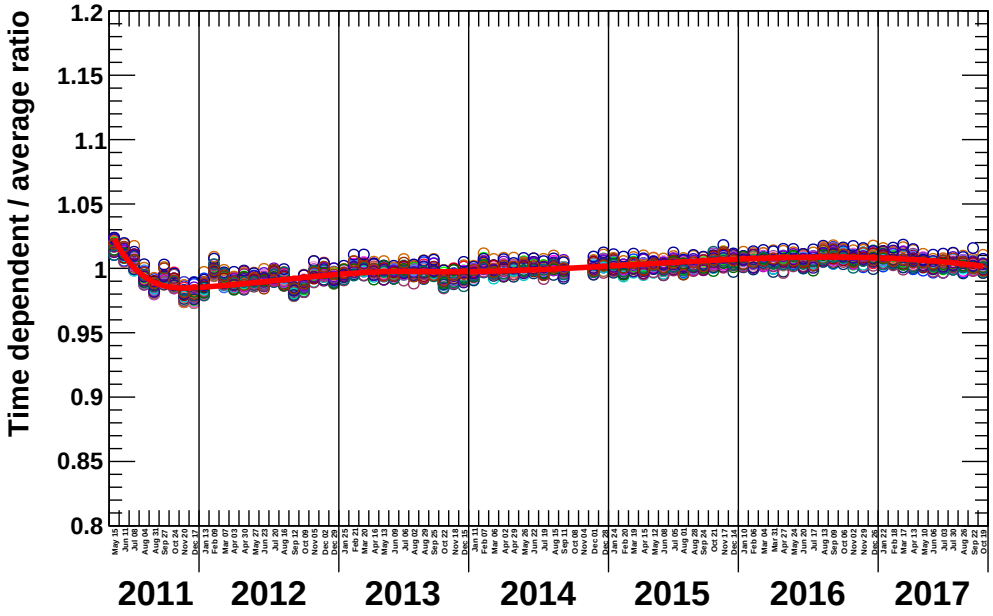

Figure 4.99: Time-dependence of the $\mu_{\text{prot, novo}}$ parameter for all energy bins - 0.65 – 52.33 GeV - in the time-dependent analysis.

The time-dependence of the three remaining parameters - $\mu_{\text{ccprot, novo}}$, $\sigma_{\text{elec, novo}}$ and $\sigma_{\text{prot, novo}}$, is shown in Figs. 4.100 to 4.102 in selected energy bins, as example, for the single-track sample.

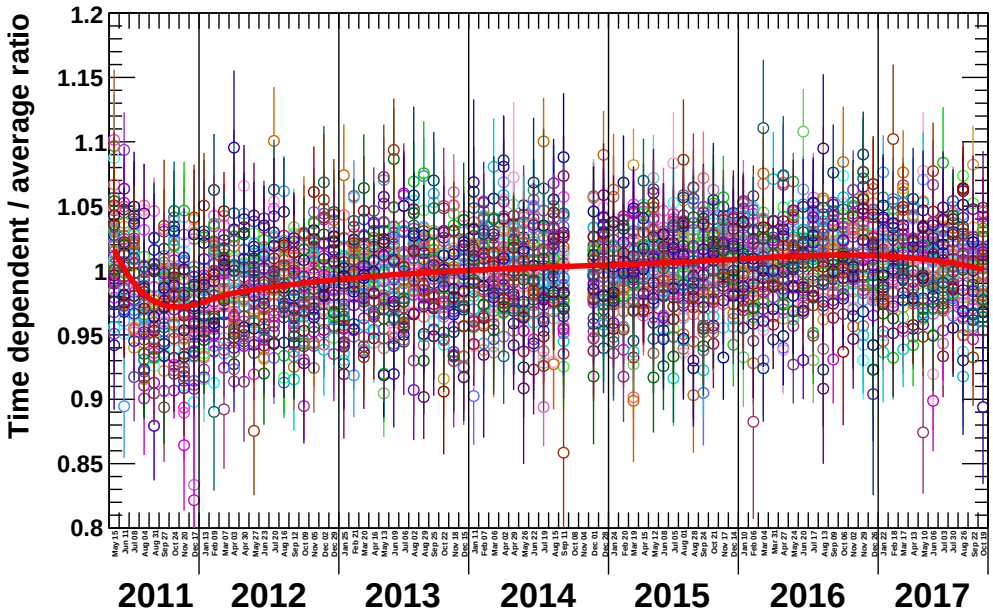

Figure 4.100: Time-dependence of the $\mu_{\text{ccprot, novo}}$ parameter for selected energy bins (1.22 – 52.33 GeV), as example, in the time-dependent analysis for the single-track sample.

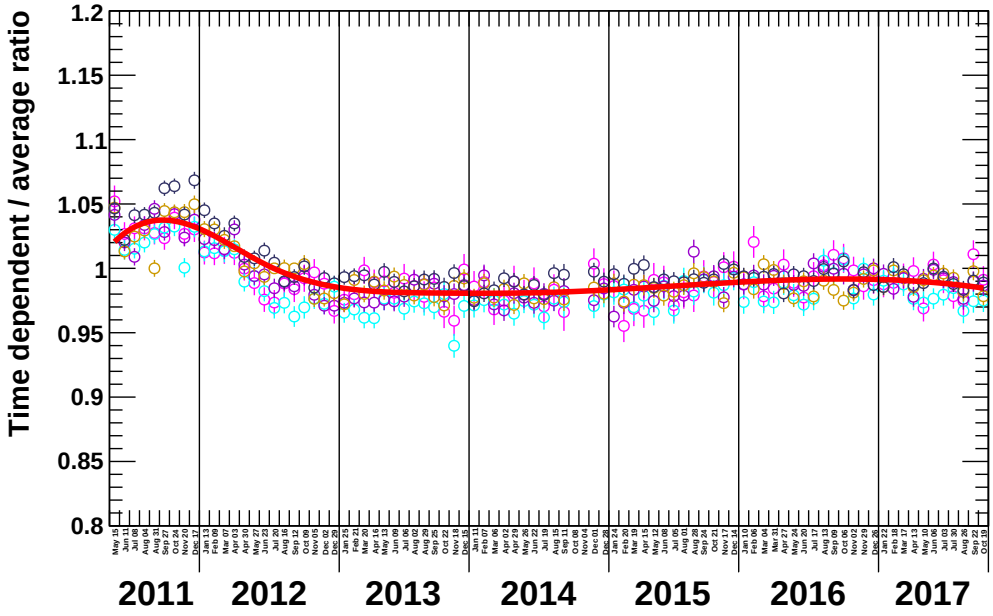

Figure 4.101: Time-dependence of the $\sigma_{\text{elec, novo}}$ parameter for selected energy bins (1.46 – 3.00 GeV), as example, in the time-dependent analysis for the single-track sample.

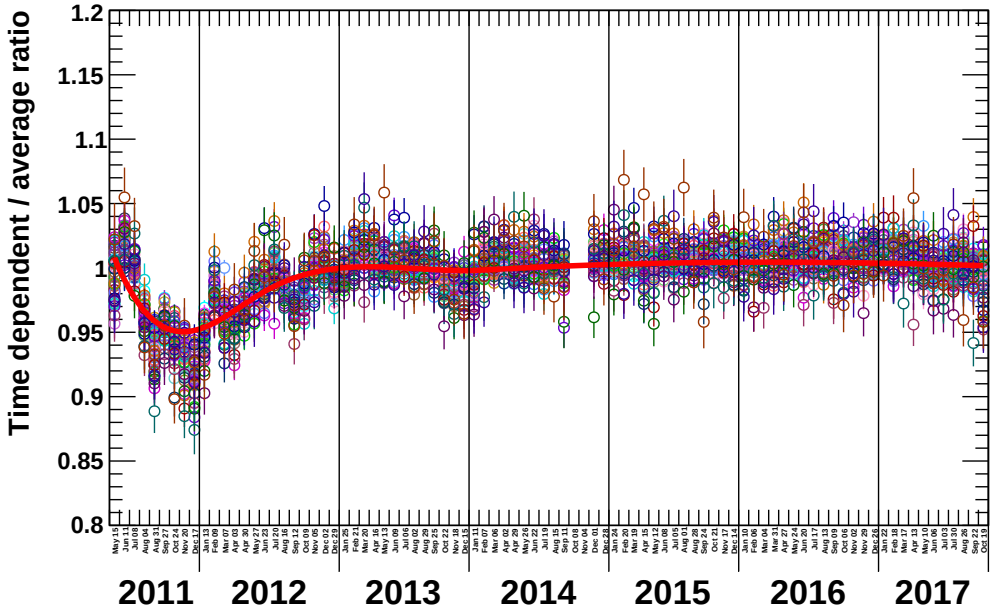

Figure 4.102: Time-dependence of the $\sigma_{\text{prot, novo}}$ parameter for selected energy bins (1.72 – 52.33 GeV), as example, in the time-dependent analysis for the single-track sample.

Since the time-dependence of all TRD template parameters needed to describe both the single-track sample and the multi-tracks sample is known, new time-dependent TRD templates for the all-tracks sample can be constructed, following the recipe given in Section 4.4.5.

To ensure the validity of the time-dependent TRD templates the two-dimensional template fit is performed for all Bartels rotations i and all energy bins j. Figure 4.103 shows the χ^2/dof distribution for the all-tracks sample, encoded as color in the plot. No particular energy or time interval shows a peculiar behaviour. The horizontal stripes appear at energies where the TRD template parameterization changes (certain parameters become constant). The fixation of several parameters does not lead to a bias, but stabilizes the fit procedure.

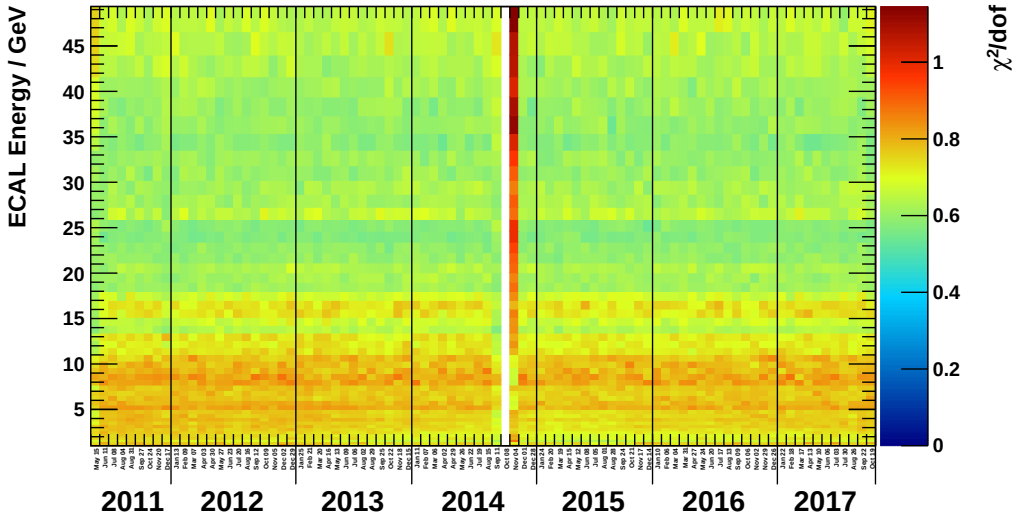

Figure 4.103: Goodness of fit results for the two-dimensional template fit, performed using the time-dependent TRD templates on the all-tracks sample. The color encodes the χ^2/dof value for each Bartels rotation i and each energy bin j of the time-dependent analysis. All χ^2/dof values are acceptable.

To demonstrate the effect of the time-dependent changes of the TRD template parameters on the two-dimensional template fit, the same fit is performed twice: once using the time-averaged templates, Fig. 4.104 and once using the time-dependent templates, Fig. 4.105, or an example energy bin in Bartels rotation $i = 6$. It is evident that only the time-dependent templates correctly describe the data sample. When using the time-averaged templates a bias is exposed, leading to a large χ^2/dof value.

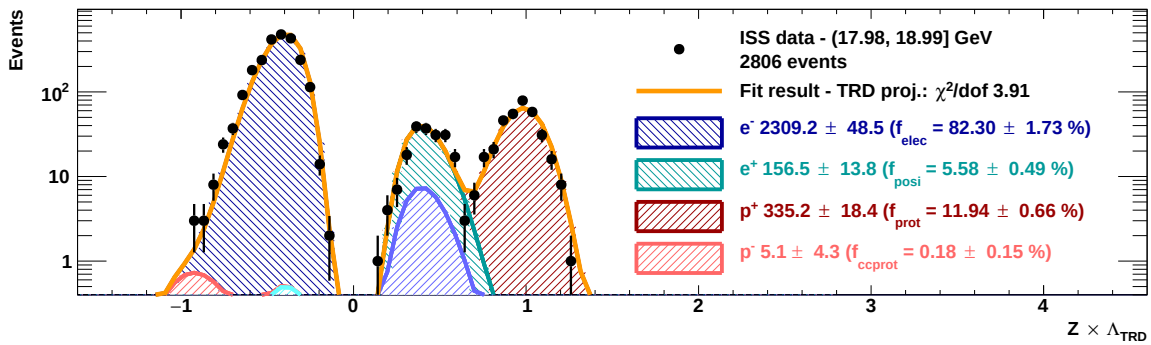

Figure 4.104: Results of the two-dimensional TRD / CCMVA template fit in Bartels rotation $i = 6$ for the energy bin 17.98 – 18.99 GeV (all-tracks sample) using the time-averaged TRD templates.

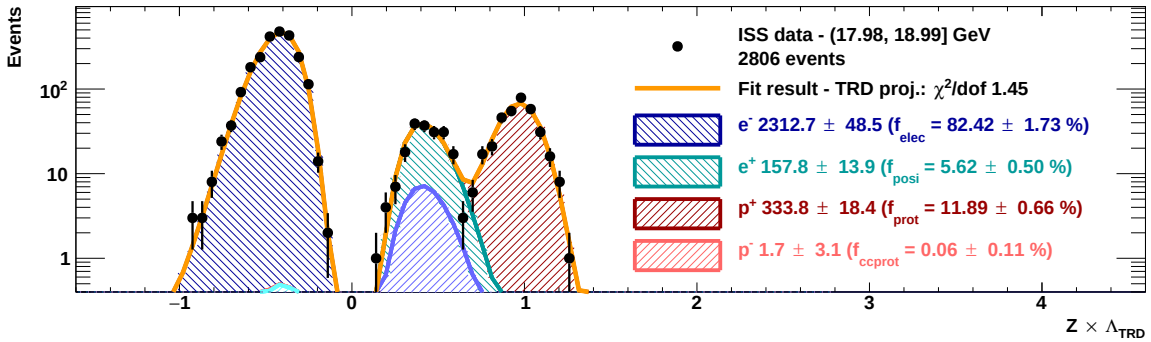

Figure 4.105: Results of the two-dimensional TRD / CCMVA template fit in Bartels rotation $i = 6$ for the energy bin 17.98 – 18.99 GeV (all-tracks sample) using the time-dependent TRD templates.

It was verified that the systematic uncertainty $\sigma_{\text{trd}}(E)/\Phi_{e^\pm}(E)$, derived in Section 4.6.1, is identical when using the time-dependent TRD templates. For that reason, no extra time-dependent systematic uncertainty $\sigma_{\text{trd},\,i}(E)$ is needed.

4.9.6 Energy scale stability

For the time-dependent analysis it is important to ensure that the energy scale (Section 4.2.4) is stable over time. To quantify the stability the $E/|R|$ peak position is analyzed as a function of time.

Assuming the rigidity scale is stable in time - as shown in Ref. [Berdugo2017] - the $E/|R|$ peak position can be used to test if the energy scale E shows a time dependence, such as a drift.

To obtain the time-dependent $E/|R|$ distribution, a negative rigidity ISS data sample is prepared in each Bartels rotation i, by applying the preselection and selection cuts (described in Sections 4.3.2 and 4.3.3) and imposing additional cuts on the ECAL estimator ($\Lambda_{\text{ECAL}} > 0$) and the TRD estimator ($\Lambda_{\text{TRD}} > 0.7$) to select clean electron samples. In these data samples the $E/|R|$ distribution is analyzed from 2 – 50 GeV in six logarithmic energy bins.

For each Bartels rotation i, and each energy bin, the time-dependent $E/|R|$ distribution is shifted along the energy axis, to find the best matching scale factor S_i that leads to best agreement between the resampled time-averaged $E/|R|$ distribution and the time-dependent one. The resampled time-averaged $E/|R|$ distribution, consists of a randomly selected sub-sample of the time-averaged $E/|R|$ distribution, containing ten[17] times as much as events as in the time-dependent $E/|R|$ distribution.

A χ^2 scan (Fig. 4.106(a)) is used to determine the best matching scale factor S_i. After shifting the time-dependent $E/|R|$ distribution along the energy axis, the time-averaged and the time-dependent distributions are on top of each other, as shown in Fig. 4.106(b).

[17] The number needs to be sufficiently large, to smooth statistical fluctuations.

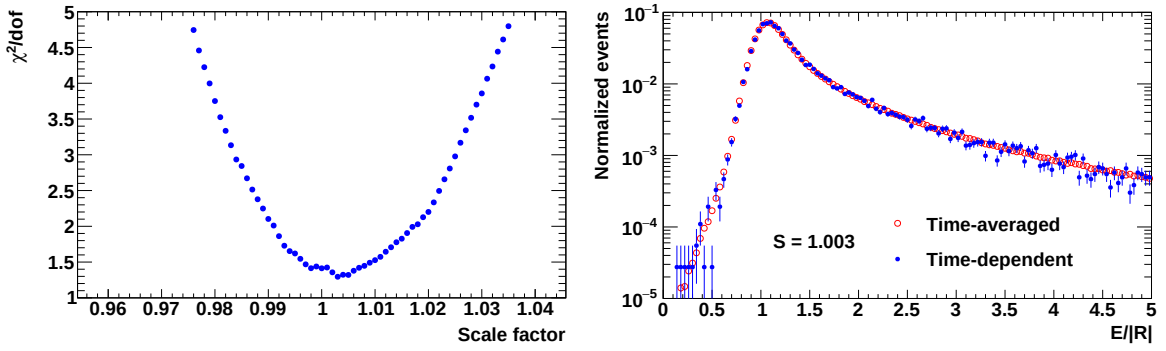

(a) χ^2/dof scan

(b) $E/|R|$ comparison

Figure 4.106: Control plots of the χ^2 scan procedure in the first $E/|R|$ energy bin (2 – 3.42 GeV) to determine the best matching scale factor S, in an example Bartels rotation, that leads to agreement between the time-dependent and the time-averaged $E/|R|$ distribution.

Figure 4.107 shows the result of the χ^2 scan procedure in the first energy bin (2 – 3.42 GeV) as function of time. The procedure is repeated for all energy bins and yields consistent results: acceptable χ^2/dof values and a scale factor close to unity.

There appears to be a slope in the data, as exhibited in Fig. 4.107(b). In a dedicated study it was determined that the cause of the slope is a change in the rigidity reconstruction as function of time. This could either be the result of an improper magnet temperature calibration or the observation of a slightly decreasing magnetic field over time. Both explanations are possible and might induce a slope in the $E/|R|$ distribution as function of time.

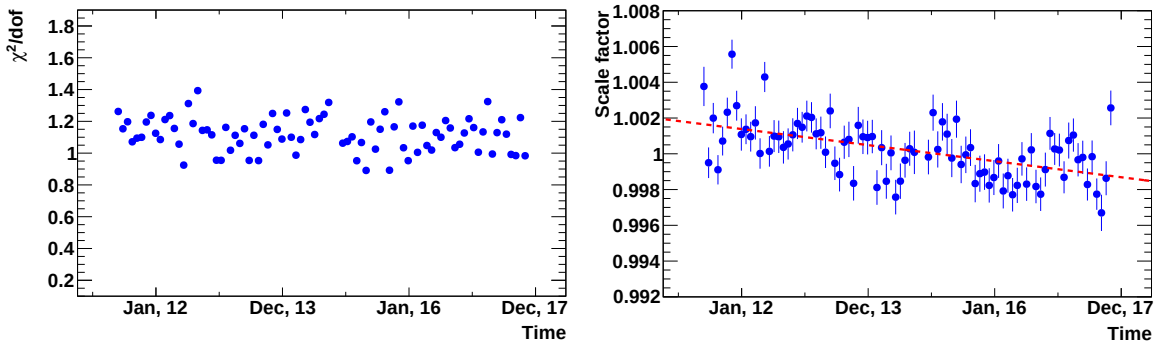

(a) Minimum χ^2/dof vs. time

(b) $E/|R|$ scale factor vs. time

Figure 4.107: Results of the χ^2 scan procedure in the first $E/|R|$ energy bin (2 – 3.42 GeV) as function of time. The left plot shows the minimum χ^2/dof as function of time and the right plot the obtained scale factor S_i for each Bartels rotation i.

The χ^2 scan procedure yields one scaling factor $S_i \pm \sigma_{S_i}$ per energy bin and per Bartels rotation i. A model, parameterizing the time dependence, is fit to the scaling factor vs. time data, as shown in Fig. 4.108 for two example energy bins. For each energy bin, the RMS η_{RMS} is determined from the residual distribution η = data - model: it captures the amount of fluctuations in the given data sample.

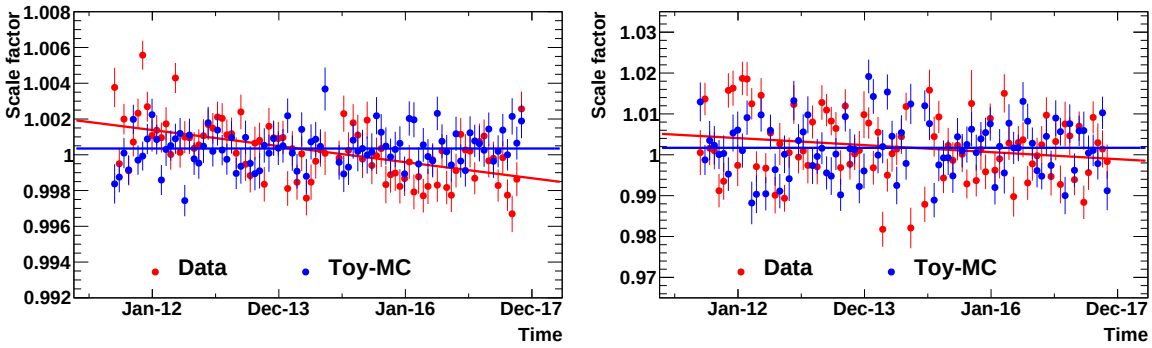

(a) First $E/|R|$ energy bin: 2 – 3.42 GeV

(b) Last $E/|R|$ energy bin: 29.24 – 50.00 GeV

Figure 4.108: Scale factors S_i of both the **ISS data sample** and the **Toy-MC sample** as function of time. The **ISS data sample** time dependence is parameterized using a straight line, and the time dependence in the **Toy-MC sample** using a constant.

The whole χ^2 scan procedure is repeated $M \approx O(200)$ times, each time with a different resampled time-averaged $E/|R|$ distribution. This yields a distribution of M different η_{RMS} values. The mean of this distribution is an estimation of the energy scale stability as function of time: σ_{data} in the **ISS data sample**. The estimated uncertainty σ_{data} may overestimate the true uncertainty σ_{ene}, because of the intrinsic statistical fluctuations in the time-dependent data samples. The intrinsic width of the η distribution, σ_{toy}, needs to be subtracted in order to retrieve the true uncertainty $\sigma_{\text{ene}} = \sqrt{\sigma^2_{\text{data}} - \sigma^2_{\text{toy}}}$.

To determine σ_{toy}, the χ^2 scan procedure is repeated again $M \approx O(200)$ times, but replacing the time-dependent distribution in each iteration m by a randomly selected sub-sample of the time-averaged $E/|R|$ distribution, containing as much events as the time-dependent $E/|R|$ distribution has. This data samples is called **Toy-MC sample**.

The scale factors determined for the both the **ISS data sample** and the **Toy-MC sample** are shown in Fig. 4.108, for an example iteration m in two energy bins, and the η_{RMS} distributions are shown in Fig. 4.109 for the same example energy bins.

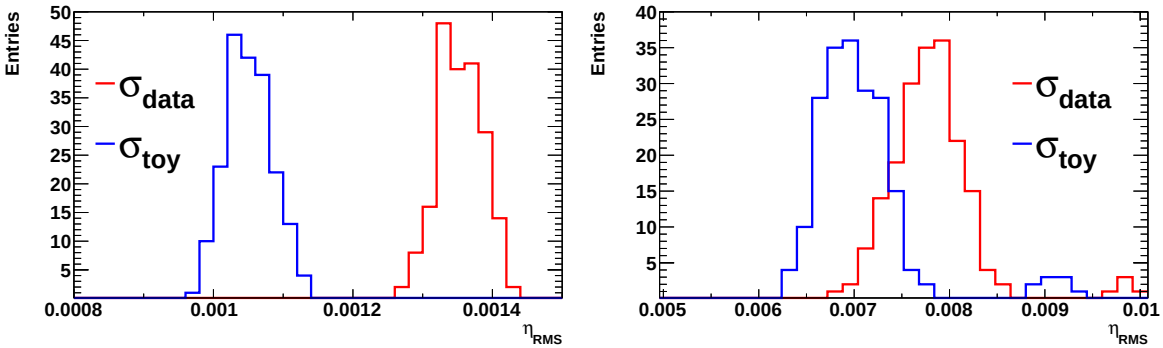

(a) First $E/|R|$ energy bin: 2 – 3.42 GeV

(b) Last $E/|R|$ energy bin: 29.24 – 50.00 GeV

Figure 4.109: η_{RMS} distribution for the **ISS data sample** and the **Toy-MC sample**. The mean of the distributions is denoted as σ_{data} and σ_{toy}, respectively.

Since the origin of the slope in the $E/|R|$ distribution was attributed to the rigidity scale (which was tested in dedicated, extensive studies), one can conclude that the energy scale is stable in time. The deviation of the scale factors S_i from unity, indicating a perfect stable energy scale, leads to an uncertainty of the overall energy scale - independent of energy - of $\sigma_{\text{ene}}/E = (0.101 \pm 0.003)\,\%$, as shown in Fig. 4.110.

The relative uncertainty σ_{ene}/E is propagated to the fluxes as additional systematic uncertainty, which is described in Section 4.10.2. No time-dependent correction of the energy scale is necessary. The next full reproduction of the AMS-02 data (pass7) already implements a time-dependent rigidity correction, which will avoid the slope in the $E/|R|$ distribution as function of time.

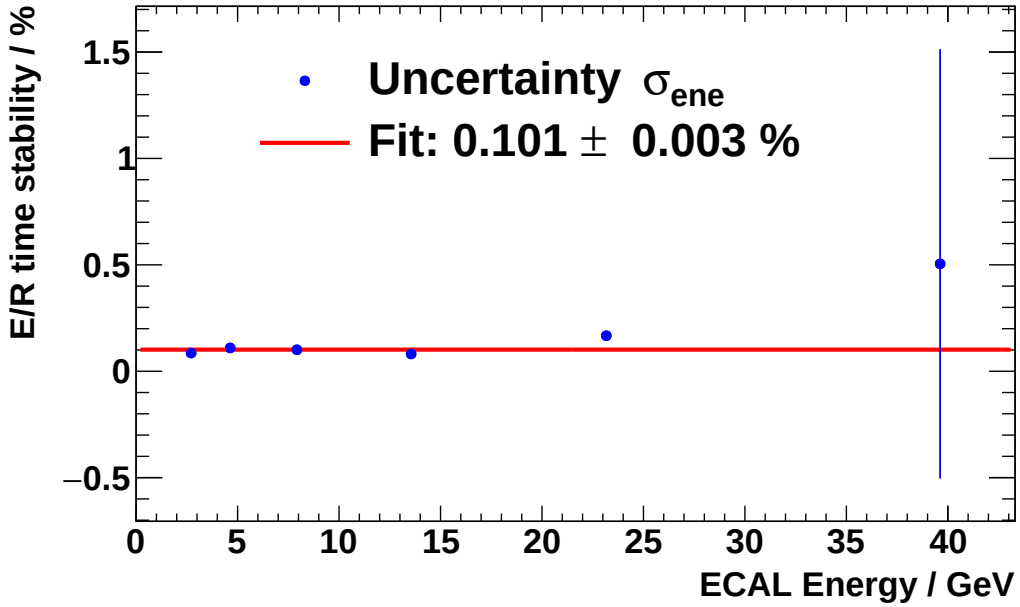

Figure 4.110: Relative energy scale uncertainty σ_{ene}/E as function of energy. It is identical for all Bartels rotations i, since the energy scale is independent of time.

4.10 Time-dependent systematic uncertainties for flux analysis

In this section all systematic uncertainties that contribute to the time-dependent fluxes are summarized. The systematic uncertainties of the time-dependent flux analysis are identical to the time-averaged analysis plus two extra components, that cover the variation with time of the acceptance and the energy scale.

4.10.1 Time-dependent acceptance

The derivation of the time-dependent acceptance including its uncertainty was already discussed in Section 4.9.3. The resulting relative systematic uncertainty $\sigma_{\text{time-acc},\,i}(E)/\Phi_{e^{\pm}}(E)$ is independent of energy and equals to $\approx 0.16\,\%$ in Bartels rotation $i = 26$, as example. The magnitude of the uncertainty is almost identical in all Bartels rotations. Furthermore the uncertainty associated with the electron flux is identical to the uncertainty associated with the positron flux.

4.10.2 Time-dependent energy scale

In Section 4.9.6 it was shown how to derive $\sigma_{\text{ene}}(E)/E$ - the relative uncertainty of the energy scale time stability as function of the energy. In the following it will be shown how to propagate the energy scale uncertainty to an uncertainty on the fluxes.

The flux $\Phi_{e^\pm,i}(E)$ in Bartels rotation i can be locally parameterized using a constant A and a spectral index $\gamma_i^\pm$: $\Phi_{e^\pm,i}(E) = A \cdot E^{-\gamma_i^\pm}$. The integral of the flux in the energy interval $[E_1,\ E_2]$ is given by

$$p_i^\pm(E) = \int_{E_1}^{E_2} \Phi_{e^\pm,i}(E)\,\mathrm{d}E = \frac{A \cdot \left(E_1^{-\gamma_i^\pm+1} - E_2^{-\gamma_i^\pm+1}\right)}{\gamma_i^\pm - 1}.$$

When assuming that the true energy is shifted by a factor $s = \sigma_{\text{ene}}(E)/E$, the integral of the flux needs to be evaluated in the energy interval $[s \cdot E_1,\ s \cdot E_2]$

$$\hat{p}_i^\pm(E) = \int_{E_1(1-s)}^{E_2(1-s)} \Phi_{e^\pm,i}(E)\,\mathrm{d}E.$$

The difference between the integral of the shifted flux and the integral of the original flux, divided by the integral of the original flux is equal to the relative systematic uncertainty $\sigma_{\text{time-ene},\,e^\pm,i}(E)/\Phi_{e^\pm,i}(E)$, which describes the propagation of the energy scale uncertainty to the $e^\pm$ fluxes:

$$\frac{\sigma_{\text{time-ene},\,e^\pm,i}(E)}{\Phi_{e^\pm,i}(E)} = \frac{\hat{p}_i^\pm(E) - p_i^\pm(E)}{p_i^\pm(E)}. \tag{4.34}$$

The difference $\hat{p}_i^\pm(E) - p_i^\pm(E)$ can be approximated using a Taylor expansion, yielding

$$\begin{aligned} &\mathcal{T}(\hat{p}_i^\pm(E) - p_i^\pm(E)) = A \cdot \left(E_1^{-\gamma_i^\pm+1} - E_2^{-\gamma_i^\pm+1}\right) \cdot s + O(s^2) \\ \Rightarrow\ &\frac{\mathcal{T}(\hat{p}_i^\pm(E) - p_i^\pm(E))}{p_i^\pm(E)} = (\gamma_i^\pm - 1) \cdot s + O(s^2). \end{aligned} \tag{4.35}$$

Inserting Eq. (4.35) into Eq. (4.34) yields a simple expression for the energy scale uncertainty, propagated to the $e^\pm$ fluxes:

$$\frac{\sigma_{\text{time-ene},\,e^\pm,i}(E)}{\Phi_{e^\pm,i}(E)} = \left|\gamma_i^\pm - 1\right| \cdot \frac{\sigma_{\text{ene}}}{E}. \tag{4.36}$$

To evaluate the uncertainty in Eq. (4.36) the spectral index $\gamma_i^\pm$ needs to be known. The initial model to derive $\gamma_i^\pm$, described in the derivation of the $\sigma_{\text{time-ene},\,e^\pm,i}(E)$ uncertainty, does not hold at low energies, due to solar modulation, which distorts the simple power law approximation. The force-field approximation [Gleeson1968] allows one to describe the low energy data very well, by introducing another free parameter: the fisk potential ϕ_i. This leads to the following analytical description of the fluxes:

$$\Phi_{e^\pm,i}(E) = A \cdot \left(\frac{E + \phi_i}{E_{\text{ref}}}\right)^{-\gamma_i^\pm} \cdot \frac{T \cdot (T + 2 \cdot m_{e^\pm})}{(T + \phi_i) \cdot ((T + \phi_i) + 2 \cdot m_{e^\pm})}, \tag{4.37}$$

where $m_{e^\pm}$ equals to the electron or positron mass, $T = E - m_{e^\pm}$ and $E_{\text{ref}} = 5\,\text{GeV}$ (arbitrary choice). After fitting the model - Eq. (4.37) - to the $e^\pm$ fluxes, the effective spectral index $\gamma_i^\pm(E)$ can be computed as function of energy by evaluating the spectral derivative

$$\gamma_i^\pm(E) = \mathrm{d}(\log \Phi_{e^\pm,i}(E))/\mathrm{d}(\log E). \tag{4.38}$$

Figure 4.111 shows the spectral indices $\gamma_i^\pm(E)$ obtained by computing the spectral derivative for the electron flux and the positron flux, respectively, as function of energy in an example Bartels rotation.

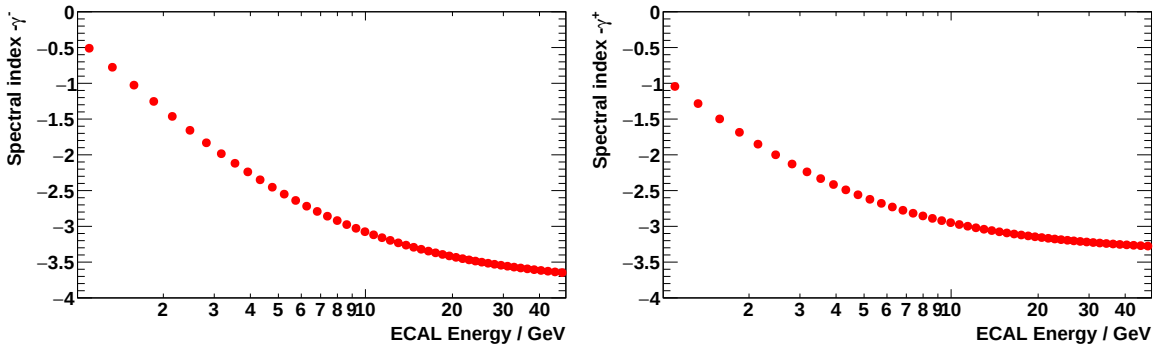

(a) For electron flux **(b)** For positron flux

Figure 4.111: Spectral index of the electron flux (left plot) and the positron flux (right plot), determined via the computation of the spectral derivative, Eq. (4.38), using the flux model - Eq. (4.37) - for the time-dependent $e^\pm$ flux in Bartels rotation $i = 26$ (Apr 16$^{\text{th}}$, 2013 - May 13$^{\text{th}}$, 2013), after unfolding. Note that the y-axis shows $-\gamma_i^\pm$: by convention $\gamma_i^\pm$ is positive.

All ingredients are available to compute the relative systematic uncertainty $\sigma_{\text{time-ene},\,e^\pm,i}(E)/\Phi_{e^\pm,i}(E)$. Figure 4.112 shows the result as function of energy in Bartels rotation $i = 26$, as example. The uncertainty associated with the electron flux is different from the uncertainty associated with the positron flux, due to different spectral indices, that enter the systematic uncertainty calculation.

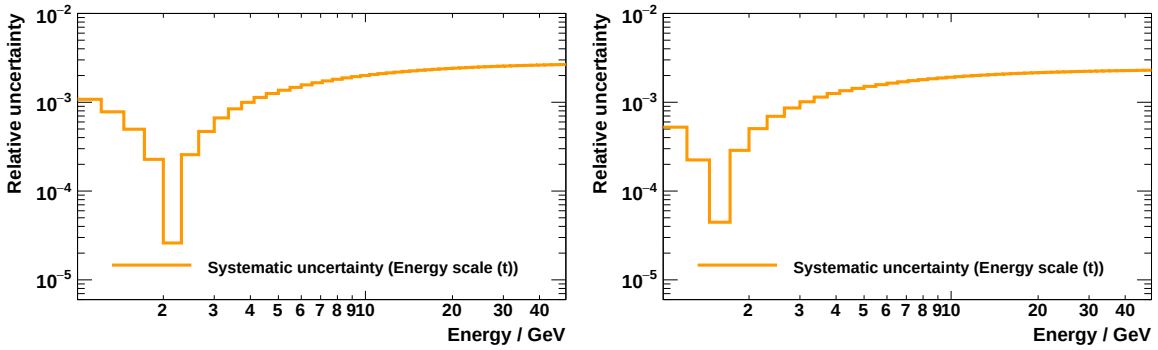

(a) For electron flux **(b)** For positron flux

Figure 4.112: Visualization of the relative systematic uncertainty associated with the electron flux (left plot) and the positron flux (right plot) due to the time-stability of the energy scale, in an example Bartels rotation $i = 26$ (Apr 16$^{\text{th}}$, 2013 - May 13$^{\text{th}}$, 2013).

Between 1 – 2 GeV both uncertainties show a minimum, where the spectral index $\gamma_i^{\pm}(E) \approx 1$, which is consistent with the expectation from Eq. (4.36).

4.10.3 Summary

Figure 4.113 shows the composition of the relative systematic uncertainty $\sigma_i(E)/\Phi_{e^{\pm},i}(E)$ as function of energy for the e^- flux and the e^+ in Bartels rotation $i = 26$, as example.

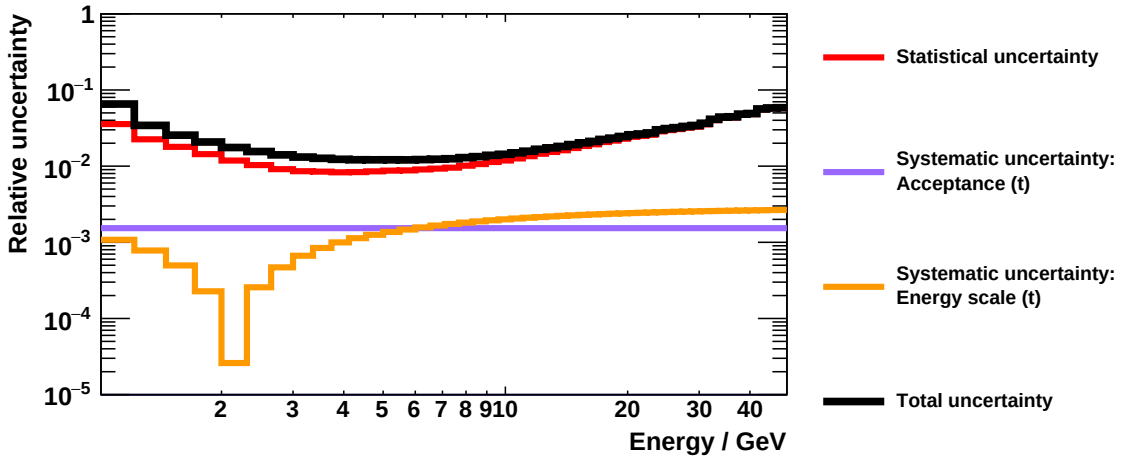

(a) For electron flux

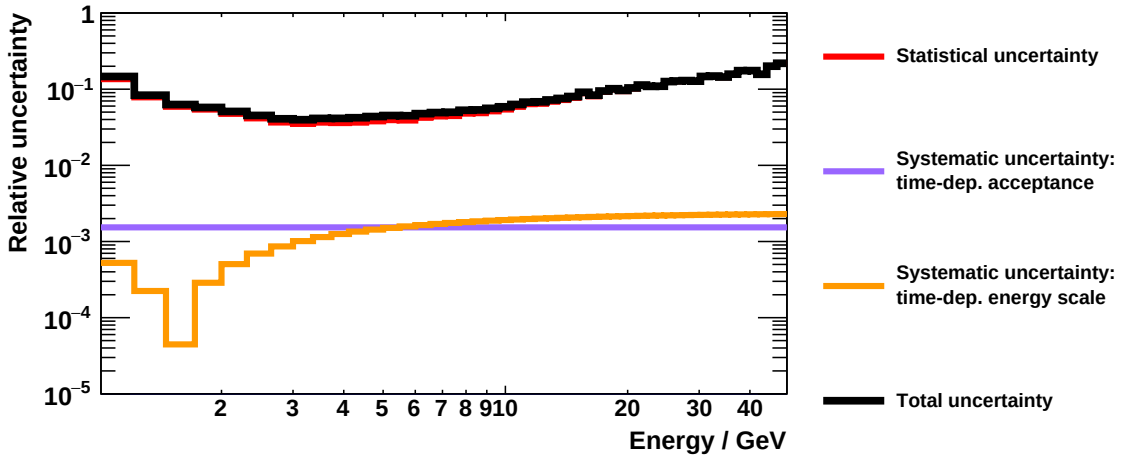

(b) For positron flux

Figure 4.113: Composition of the relative systematic uncertainty associated with the electron flux (upper plot) and the positron flux (lower plot) in Bartels rotation $i = 26$ (Apr 16$^{\text{th}}$, 2013 - May 13$^{\text{th}}$, 2013), as example.

The additional systematic uncertainties due to the time-variation of the acceptance and the energy scale are negligible compared to the statistical uncertainty of both the electron flux and the positron flux, over all energies. The plot does not explicitly show the time-averaged systematic uncertainty, which contributes to the total uncertainty, however it is obvious that the statistical uncertainty dominates the overall uncertainty.

4.11 Time-dependent positron/electron ratio and positron fraction calculation

Following the recipe given in Section 4.7 for the time-averaged analysis the time-dependent ratios for Bartels rotation i are given by

$$R_{e,i}(E) = \frac{N_{e^+,i}(E)}{N_{e^-,i}(E)}; \qquad p_i(E) = \frac{N_{e^+,i}(E)}{N_{e^+,i}(E) + N_{e^-,i}(E)}. \tag{4.39}$$

The results from the two-dimensional template fit for the "single-track sample" are used to extract the number of electrons or positrons $N_{e^\pm,i}$ with the charge-confusion value fixed to the Monte-Carlo prediction, as explained in Section 4.7.

4.12 Time-dependent systematic uncertainties for positron/electron ratio and positron fraction

In this section all systematic uncertainties that contribute to the time-dependent positron/electron ratio and positron fraction are summarized. The systematic uncertainties of the time-dependent positron/electron ratio and positron fraction analysis are the same as for the time-averaged analysis plus one extra component, that covers the energy scale variation with time.

4.12.1 Time-dependent energy scale

In Section 4.10.2 the energy scale stability was derived for the time-dependent flux analysis. Following the same recipe the relative systematic uncertainty $\sigma_{\text{time-ene},\,R_{e,i}}(E)/R_{e,i}(E)$ for the positron/electron ratio and the relative systematic uncertainty $\sigma_{\text{time-ene},\,p_i}(E)/p_i(E)$ can be derived for each Bartels rotation i.

Equation (4.36) can be modified to yield the relative systematic uncertainty for the positron/electron ratio:

$$\frac{\sigma_{\text{time-ene},\,R_{e,i}}(E)}{R_{e,i}(E)} = \left| \left(1 + \frac{\sigma_{\text{ene}}}{E}\right)^{\gamma_i^-(E) - \gamma_i^+(E)} - 1 \right|, \tag{4.40}$$

and for the positron fraction:

$$\frac{\sigma_{\text{time-ene},\,p_i(E)}}{p_i(E)} = \left| \frac{1}{p_i(E) \cdot \left(1 + \frac{1}{R_{e,i}(E)} \cdot \left(1 + \frac{\sigma_{\text{ene}}}{E}\right)^{\gamma_i^+(E) - \gamma_i^-(E)}\right)} - 1 \right|. \tag{4.41}$$

Figure 4.114 shows the result as function of energy in Bartels rotation $i = 26$, as example for the positron/electron ratio. The uncertainty is almost identical for the positron fraction, thus the plot for the positron fraction was omitted.

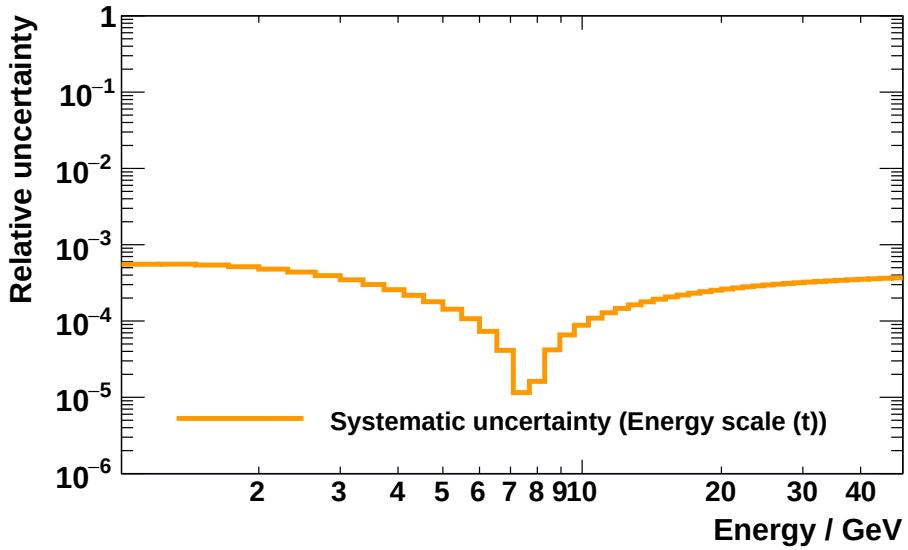

Figure 4.114: Visualization of the relative systematic uncertainty associated with the positron/electron ratio due to the time-stability of the energy scale, in an example Bartels rotation $i = 26$ (Apr 16$^{\text{th}}$, 2013 - May 13$^{\text{th}}$, 2013).

Around $\approx 7\,\text{GeV}$ the uncertainty show a minimum, where the spectral indices of electrons and positrons $\gamma_i^+(E) \approx \gamma_i^-(E)$ are equal, which is consistent with the expectation from Eqs. (4.40) and (4.41).

4.12.2 Summary

The composition of the relative systematic uncertainty $\sigma_i(E)/R_{e,i}(E)$ as function of energy for the positron/electron ratio is shown in Fig. 4.115.

The composition of the relative systematic uncertainty $\sigma_i(E)/p_i(E)$ as function of energy for the positron fraction is almost identical and thus was omitted.

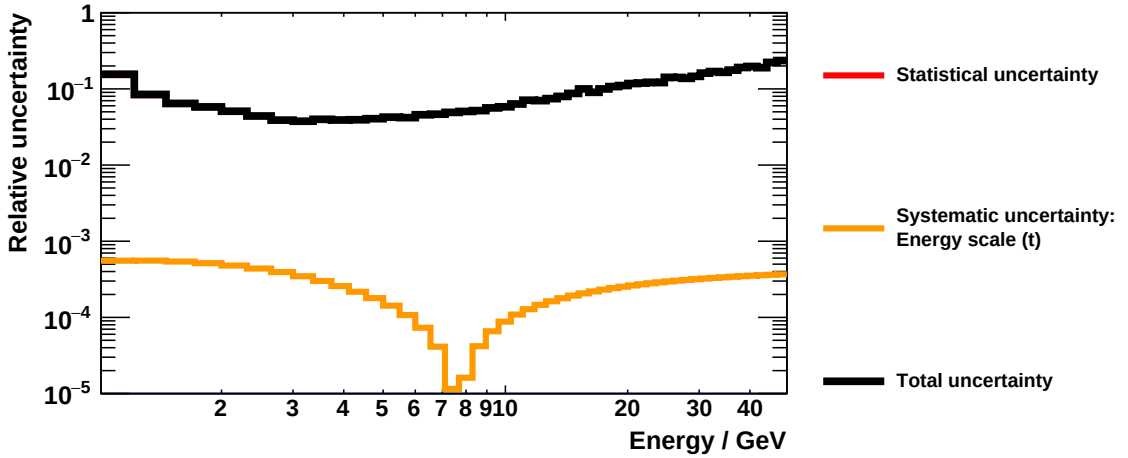

Figure 4.115: Composition of the relative systematic uncertainty associated with the positron/electron ratio.

The additional systematic uncertainties due to the time-variation of the energy scale is negligible compared to the statistical uncertainty of both the positron/electron ratio and the positron fraction, over all energies. The plot does not explicitly show the time-averaged systematic uncertainty, which contributes to the total uncertainty, however it is obvious that the statistical uncertainty dominates the overall uncertainty.

CHAPTER 5

Results

In this chapter the results of the time-averaged and time-dependent analyses are presented. Comparisons against published results and other experiments are shown as well as interpretations of the results.

5.1 Time-averaged results

5.1.1 Electron flux

Figure 5.1 shows the time-averaged electron flux based on **28.39 million** events in the energy range 0.5 – 1,000 GeV, multiplied by energy $\tilde{E}^3$, where $\tilde{E}$ equals to the spectrally weighted mean energy in each energy interval, according to Lafferty & Wyatt [Lafferty1995]. In the following $\tilde{E}$ will be referred to as E - see Appendix B.1 for a discussion of the energy scale.

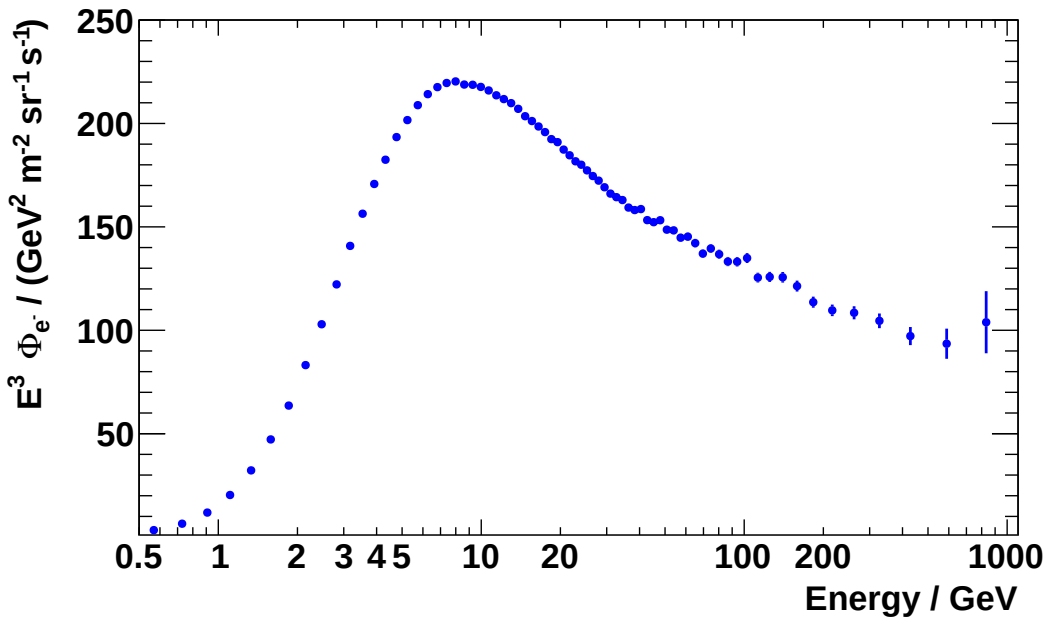

Figure 5.1: The electron flux measured by AMS-02 using the analysis procedure described in this work. The y-axis shows the unfolded flux, multiplied by energy E^3 for illustration purposes.

Figure 5.2 shows a comparison of the electron flux derived in this work with previous experiments. The electron flux was measured by AMS-02 with unprecedented accuracy, up to the TeV regime.

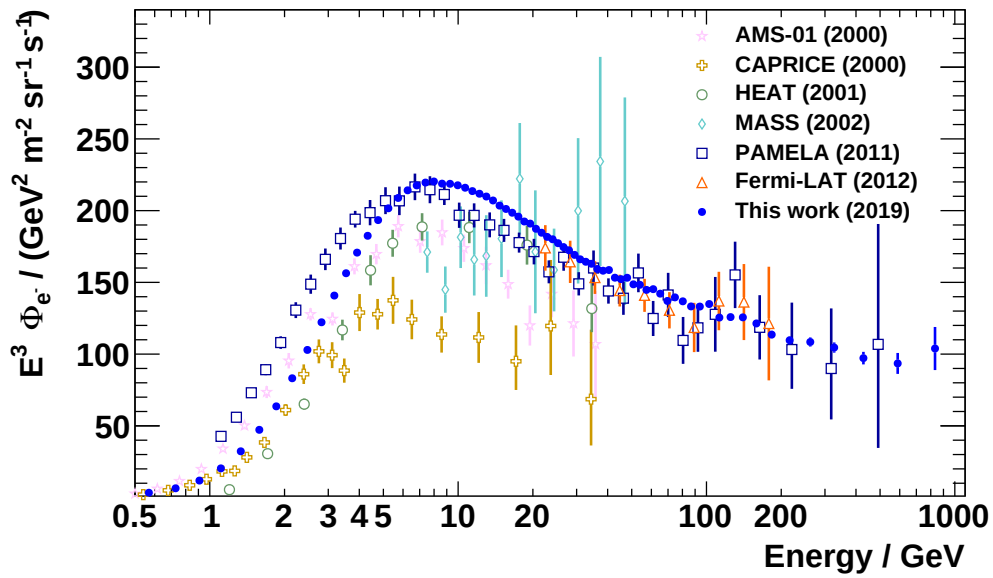

Figure 5.2: Comparison of the electron flux derived in this work with other experiments: AMS-01 [Alcaraz2000], CAPRICE [Boezio2000], HEAT [DuVernois2001], MASS [Grimani2002], PAMELA [Adriani2011] and Fermi-LAT [Ackermann2012].

Figure 5.3 shows a breakdown of the total uncertainty into the statistical and systematic part. Above ≈ 70 GeV the statistical uncertainty dominates the uncertainty of the e^- flux measurement. Below this energy, the systematic uncertainty always exceeds the statistical uncertainty. See Section 4.6.8 for a decomposition of the systematic uncertainties.

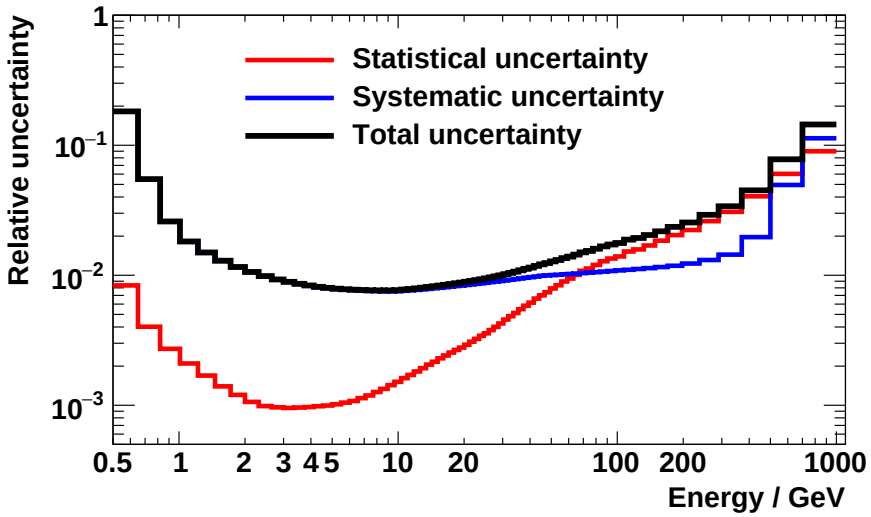

Figure 5.3: Breakdown of the uncertainty of the electron flux into a statistical and systematical part.

The electron flux derived in this work is compatible with the published electron flux [Aguilar2019a] by the AMS-02 collaboration, as shown in Appendix B.2.1.

Spectral analysis

To examine the energy dependence of the electron flux in a model-independent way, the flux spectral index $\gamma^-(E)$ is calculated by evaluating $\gamma^-(E) = \mathrm{d}(\log \Phi_{e^-}(E))/\mathrm{d}(\log E)$ over non-overlapping energy intervals. Following the prescription in Ref. [Aguilar2019a] the energy interval boundaries are 3.36, 5.00, 7.10, 10.32, 17.98, 27.25, 55.58, 90.19, 148.81, 370, and 1,000 GeV, to ensure sufficient sensitivity to the spectral index in each of the energy intervals. The results are shown in Fig. 5.4.

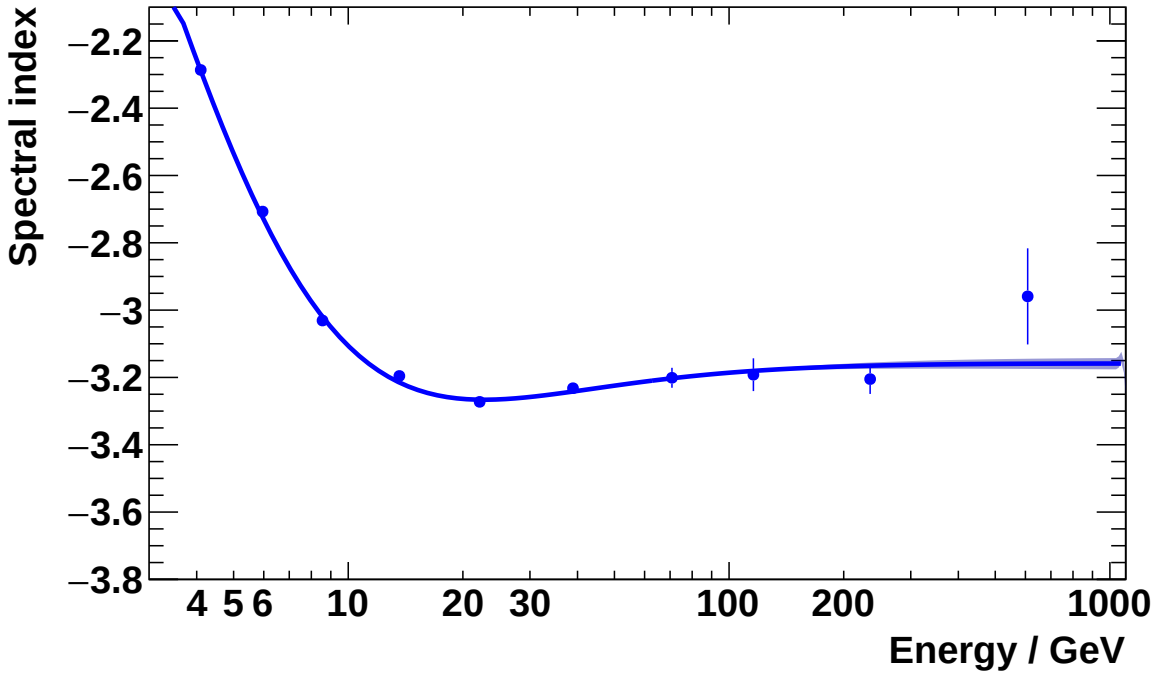

Figure 5.4: The spectral index of the electron flux as function of the energy in non-overlapping energy intervals shown as blue points. The blue band corresponds to the uncertainty determined from a fit of Eq. (5.2) to the data.

The spectral index softens from $\gamma^-(E) \approx -2.2$ at 3 GeV to $\gamma^-(E) \approx -3.2$ above 20 GeV.

To determine the transition energy E_0 where the change of the electron spectral index occurs, a double power law approximation is fit to the data[1] in the range 21.13 – 1,000 GeV:

$$\Phi_{e^-}(E) = \begin{cases} C(E/21.13\,\mathrm{GeV})^{\gamma} & E \leq E_0 \\ C(E/21.13\,\mathrm{GeV})^{\gamma}(E/E_0)^{\Delta\gamma} & E > E_0. \end{cases} \tag{5.1}$$

[1] The AMS-02 electron flux publication [Aguilar2019a] uses 20.04 GeV as normalization constant in Eq. (5.1) and as beginning of the fit range for the transition fit. This work starts the fit procedure one bin later, as it decreases the uncertainty on the transition energy and leads to smaller correlation between the γ and E_0 parameters.

The fit yields $C = (1.973 \pm 0.006) \times 10^{-2}\,[\mathrm{m^2\,sr\,s\,GeV}]^{-1}$, $\gamma = -3.28 \pm 0.01$, $E_0 = 36.26 \pm 1.68\,\mathrm{GeV}$ for the transition energy and $\Delta\gamma = 0.085 \pm 0.012$ for the difference in the spectral index after the transition energy E_0 with respect to the region before the transition with $\chi^2/\mathrm{dof} = 34.7/34 = 1.02$. The results of the double power law fit are shown in Fig. 5.5.

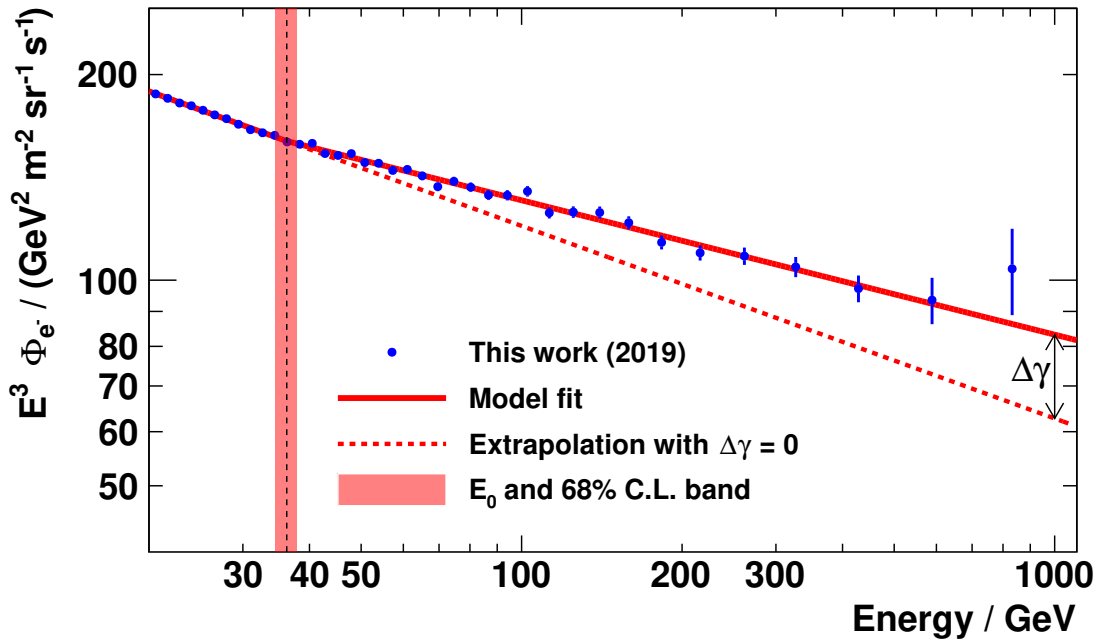

Figure 5.5: Fit of the double power law approximation Eq. (5.1) to the electron flux in the range 21.13 – 1,000 GeV. The electron flux is shown as blue data points, scaled by E^3. The red line corresponds to the fit result of Eq. (5.1). The vertical dashed line indicates the transition energy E_0 and the red band corresponds to the uncertainty. The red dashed line corresponds to an extrapolation of the model, with $\Delta\gamma = 0$.

Model fits

As shown in Ref. [Aguilar2019a], the whole energy range can be described by the sum of two power law components a and b:

$$\Phi_{e^-}(E) = \frac{E^2}{\hat{E}^2}[1 + (\hat{E}/E_t)^{\Delta\gamma_t}]^{-1}[C_a(\hat{E}/E_a)^{\gamma_a} + C_b(\hat{E}/E_b)^{\gamma_b}]. \tag{5.2}$$

In order to account for the effects related to the complex spectral behavior of the electron flux at energies below 10 GeV [Strong2011], an additional transition term, $[1 + (\hat{E}/E_t)^{\Delta\gamma_t}]^{-1}$, is introduced. It is characterized by a transition energy E_t and a spectral index $\Delta\gamma_t$. It has vanishing impact on the flux behavior at energies above E_t (e.g., $< 0.7\,\%$ above 40 GeV).

The two components, a and b, correspond to two power law functions with corresponding normalization factors C_a and C_b, and spectral indices γ_a and γ_b. To account for solar modulation effects, the force-field approximation [Gleeson1968] is used, with the energy of particles in the interstellar space $\hat{E} = E + \phi_{e^-}$ and the effective fisk potential ϕ_{e^-}. The constants $E_a = 20\,\mathrm{GeV}$ and $E_b = 300\,\mathrm{GeV}$ are chosen to minimize the correlation between C_a, C_b and γ_a, γ_b.

A fit to the data yields, $\phi_{e^-} = 1.08 \pm 0.13$ GeV for the effective potential, $E_t = 3.90 \pm 0.18$ GeV and $\Delta\gamma_t = -2.04 \pm 0.11$ for the parameters of the transition term, $C_a = (1.19 \pm 0.08) \times 10^{-2}$ [m^2 sr s GeV]$^{-1}$ and $\gamma_a = -4.46 \pm 0.12$ for the power law a, and $C_b = (3.99 \pm 0.04) \times 10^{-6}$ [m^2 sr s GeV]$^{-1}$, $\gamma_b = -3.16 \pm 0.02$ for the power law b with $\chi^2/\text{dof} = 70.0/67 = 1.04$. The result of the fit is presented in Fig. 5.6.

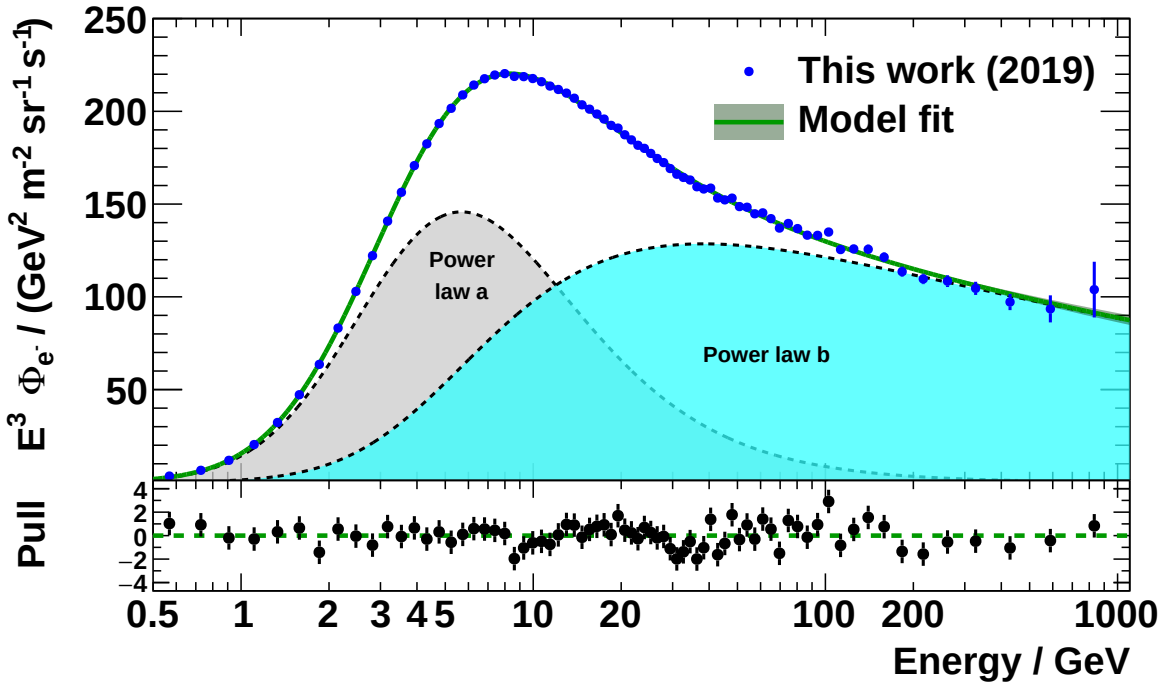

Figure 5.6: The electron flux, scaled with E^3, is shown as blue points. The result of the fit of Eq. (5.2) is shown as green line, enclosed by a green band, indicating the uncertainty of the fit result. The two power law components a and b are indicated by the gray and turquoise areas, respectively. The lower plot shows the pull distribution of the fit (data minus model divided by data uncertainty) – the model describes the data accurately over the whole energy range.

The origin of the low energy break at $E_t = 3.90$ GeV is not clear. The break might already be present in the local interstellar spectrum, or it could be a solar modulation effect. Therefore it is useful to study the low energy data in more detail, to search for low energy breaks as function of time - which is done in the time-dependant analysis, described in Section 5.2.

One can conclude that in the energy range 0.5 – 1,000 GeV the sum of two power law functions with an additional transition term provides an excellent description of the data. This is consistent with the assumption that only a few astrophysical sources of high energy electrons in the vicinity of the Solar System are present, each making a power law contribution to the electron flux.

5.1.2 Positron flux

Figure 5.7 shows the time-averaged positron flux, based on **1.95 million** events in the energy range 0.5 – 1,000 GeV, multiplied by energy E^3.

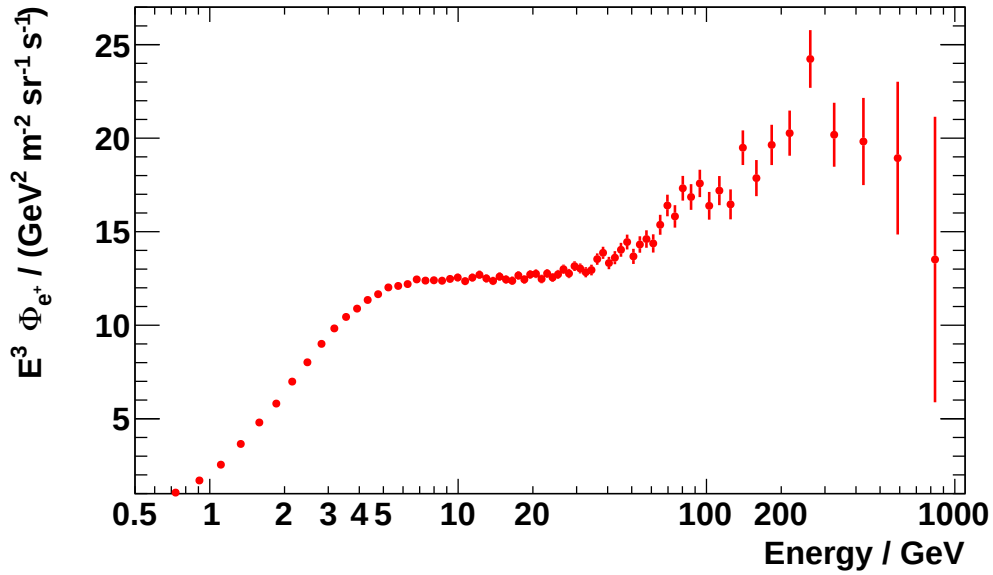

Figure 5.7: The positron flux measured by AMS-02 using the analysis procedure described in this work. The y-axis shows the unfolded flux, multiplied by energy E^3 for illustration purposes.

Figure 5.8 shows a breakdown of the total uncertainty into the statistical and systematic part. Above ≈ 20 GeV the statistical uncertainty dominates the uncertainty of the e^+ flux measurement. Below this energy, the systematic uncertainty always exceeds the statistical uncertainty. See Section 4.6.8 for a decomposition of the systematic uncertainties.

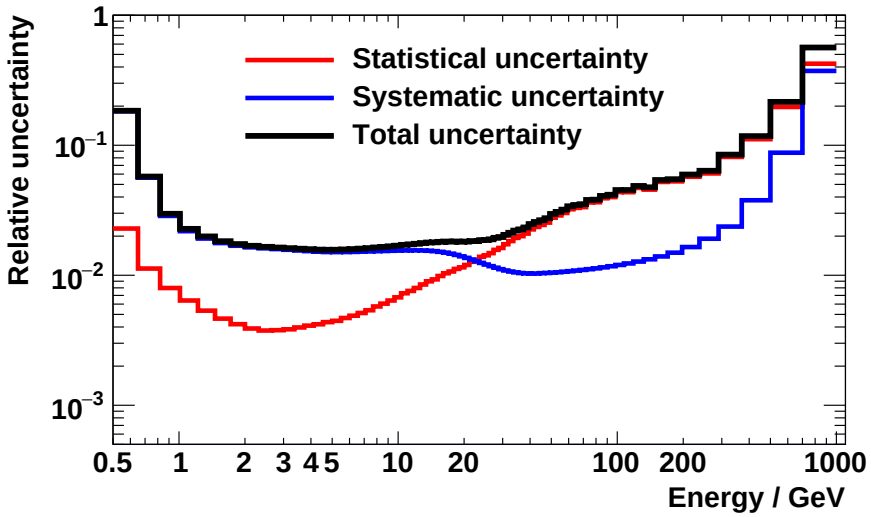

Figure 5.8: Breakdown of the uncertainty of the positron flux into a statistical and systematical part.

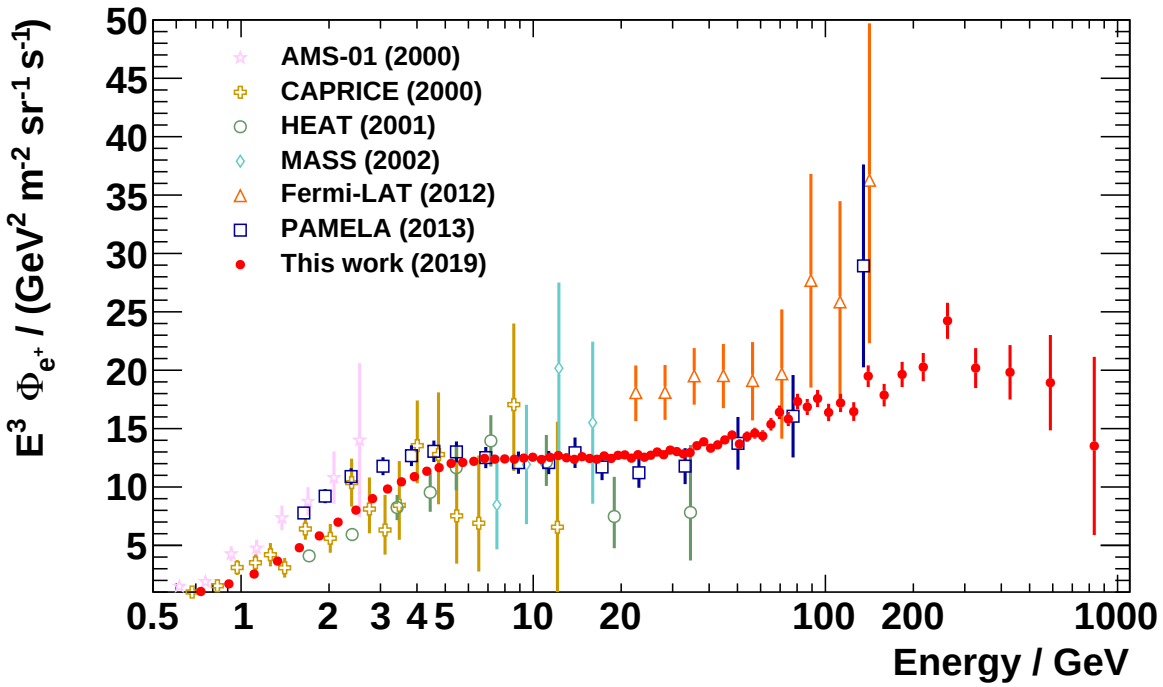

Figure 5.9: Comparison of the positron flux derived in this work with other experiments: AMS-01 [Alcaraz2000], CAPRICE [Boezio2000], HEAT [DuVernois2001], MASS [Grimani2002], Fermi-LAT [Ackermann2012] and PAMELA [Adriani2013].

Figure 5.9 shows a comparison of the positron flux derived in this work with previous experiments. The positron flux was measured by AMS-02 with unprecedented accuracy, up to the TeV regime. The flux derived in this work is compatible with the published positron flux [Aguilar2019b] by the AMS-02 collaboration, as shown in Appendix B.2.1.

Spectral analysis

To examine the energy dependence of the positron flux in a model-independent way, the flux spectral index $\gamma^+(E)$ is calculated by evaluating $\gamma^+(E) = \mathrm{d}(\log \Phi_{e^+}(E))/\mathrm{d}(\log E)$, as described in Section 5.1.1. The results are shown in Fig. 5.10.

The spectral index softens from $\gamma^+(E) \approx -2.3$ at 3 GeV to $\gamma^+(E) \approx -3.0$ at 10 GeV. Above that energy it gradually hardens until it reaches $\gamma^+(E) \approx -2.8$ at ≈ 80 GeV. While approaching TeV energies it gradually softens again.

To determine the transition energy E_0 where the positron spectral index starts rising, a double power law approximation is fit to the data in the range 7.10 – 55.58 GeV:

$$\Phi_{e^-}(E) = \begin{cases} C(E/55.58\,\mathrm{GeV})^{\gamma} & E \leq E_0 \\ C(E/55.58\,\mathrm{GeV})^{\gamma}(E/E_0)^{\Delta\gamma} & E > E_0. \end{cases} \tag{5.3}$$

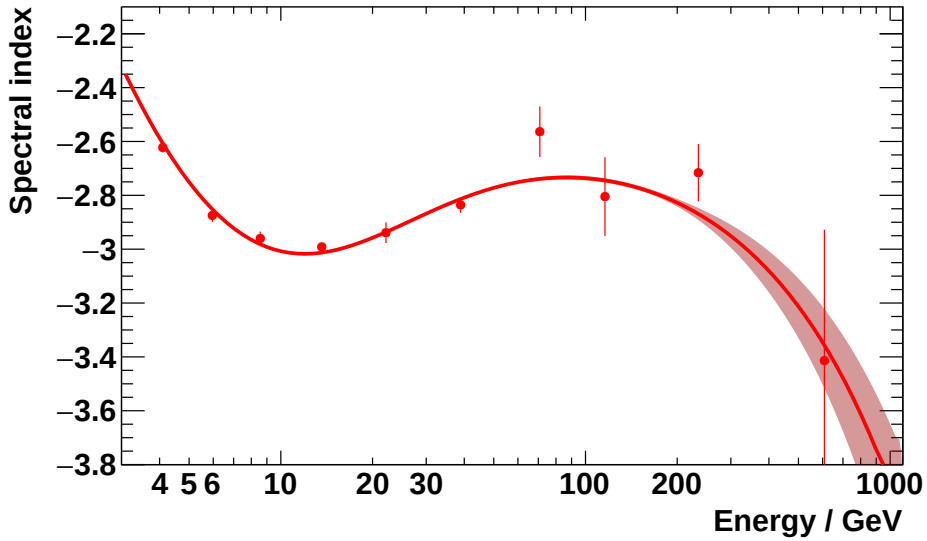

Figure 5.10: The spectral index of the positron flux in non-overlapping energy intervals shown as red points. The red band corresponds to the uncertainty determined from a fit of Eq. (5.4) to the data.

The fit yields, $C = (7.45 \pm 0.11) \times 10^{-5}\,[\mathrm{m^2\,sr\,s\,GeV}]^{-1}$, $\gamma = -2.98 \pm 0.01$, $E_0 = 24.43 \pm 2.87\,\mathrm{GeV}$ for the transition energy and $\Delta\gamma = 0.13 \pm 0.03$ for the difference in the spectral index after the transition energy E_0 with respect to the region before the transition. The results of the double power law fit are compatible with the published results [Aguilar2019b] and shown in Fig. 5.11.

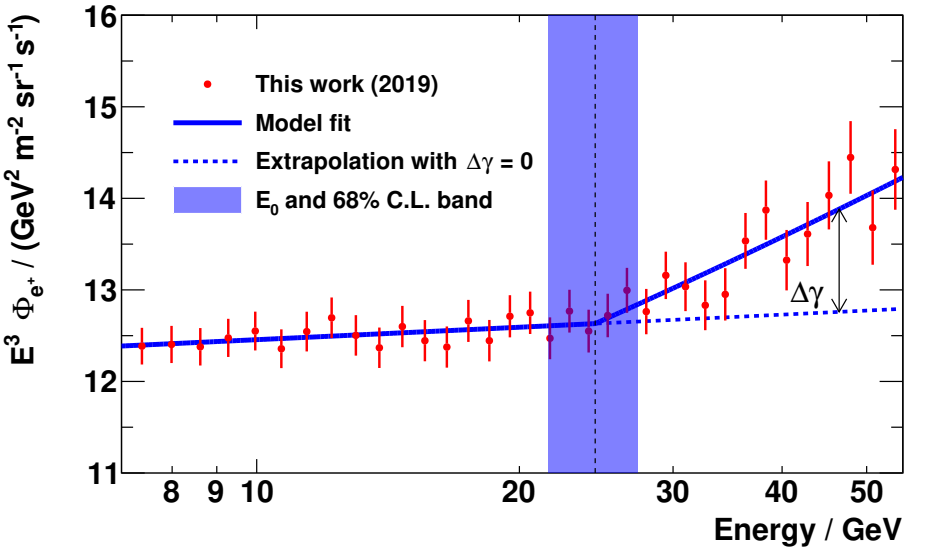

Figure 5.11: Fit of the double power law approximation Eq. (5.3) to the positron flux in the range 7.10 – 55.58 GeV. The positron flux is shown as red data points, scaled by E^3. The blue line corresponds to the fit result of Eq. (5.3). The vertical dashed line indicates the transition energy E_0, where the positron flux starts rising, and the blue band corresponds to the uncertainty. The blue dashed line corresponds to an extrapolation of the model, with $\Delta\gamma = 0$.

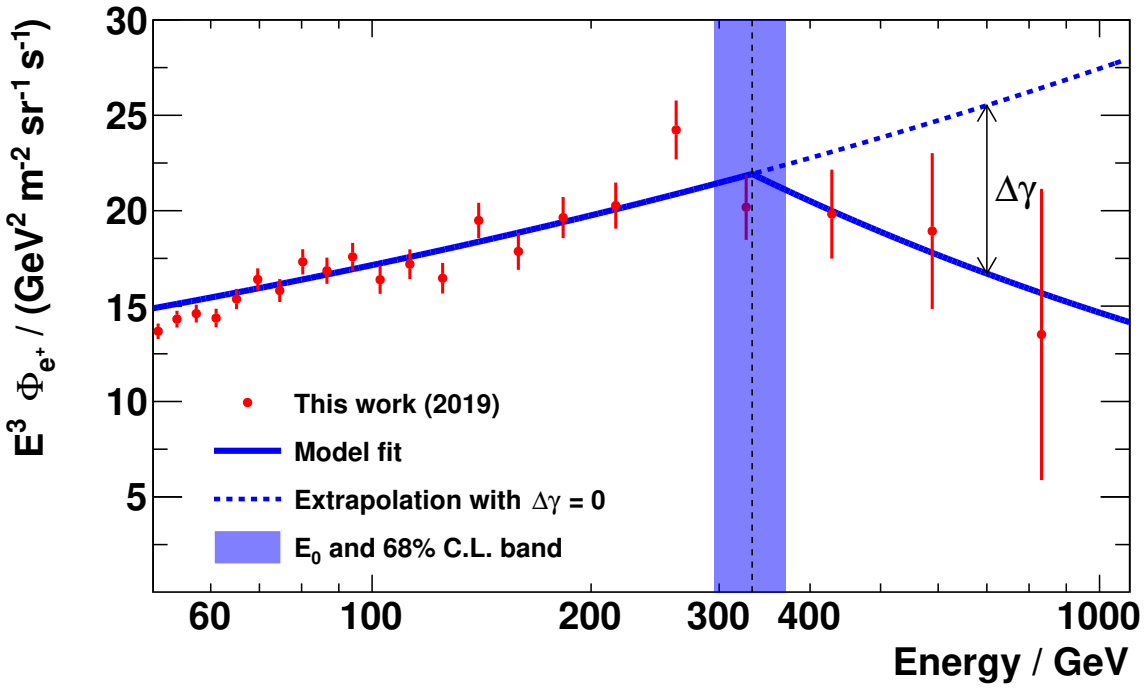

Figure 5.12: Fit of the double power law approximation Eq. (5.3) to the positron flux in the range 63.02 – 1,000 GeV. The positron flux is shown as red data points, scaled by E^3. The blue line corresponds to the fit result of Eq. (5.3). The vertical dashed line indicates the transition energy E_0, where the positron flux starts decreasing and the blue band corresponds to the uncertainty. The blue dashed line corresponds to an extrapolation of the model, with $\Delta\gamma = 0$.

Analogous, the energy where the positron spectral index starts decreasing can be determined, by a fit of Eq. (5.3) to the data[2] in the range 63.02 – 1,000 GeV:

The fit yields, $C = (6.24 \pm 0.11) \times 10^{-5}\ [\mathrm{m^2\ sr\ s\ GeV}]^{-1}$, $\gamma = -2.80 \pm 0.03$, $E_0 = 333^{+61}_{-15}$ GeV for the transition energy and $\Delta\gamma = -0.57 \pm 0.18$ for the difference in the spectral index after the transition energy E_0 with respect to the region before the transition. The results of the double power law fit are compatible with the published results [Aguilar2019b] and shown in Fig. 5.12.

Note that the transition energies cannot be attributed to solar modulation, since the time variation of both the electron and positron flux stop at above 20 GeV - within the measurement accuracy. This will be demonstrated in Section 5.2.

Model fits

As shown in Ref. [Aguilar2019b], the whole energy range can be described by the sum of two terms:

$$\Phi_{e^-}(E) = \frac{E^2}{\hat{E}^2}[C_d(\hat{E}/E_1)^{\gamma_d} + C_s(\hat{E}/E_2)^{\gamma_s} \exp(-\hat{E}/E_s)]. \tag{5.4}$$

[2] The AMS-02 positron flux publication [Aguilar2019b] uses 55.58 GeV as normalization constant in Eq. (5.3) and as beginning of the fit range for the high-energy transition fit. This work starts the fit procedure two bins later, as it improves the uncertainty on the transition energy.

The first term, called **diffuse term**, describes the low-energy part of the flux dominated by the positrons produced in the collisions of ordinary cosmic rays with the interstellar gas. It is characterized by a normalization factor C_d and a spectral index γ_d. The second term, called **source term**, has an exponential cutoff, which describes the high-energy part of the flux dominated by a source. It is characterized by a normalization factor C_s, a spectral index γ_s, and a cutoff energy E_s.

To account for solar modulation effects, the force-field approximation [Gleeson1968] is used, with the energy of particles in the interstellar space $\hat{E} = E + \phi_{e^+}$ and the effective fisk potential ϕ_{e^+}. The constants $E_1 = 7\,\text{GeV}$ and $E_2 = 60\,\text{GeV}$ are chosen to minimize the correlation between C_s and γ_s.

A fit to the data yields $\phi_{e^+} = 1.08 \pm 0.03\,\text{GeV}$, $C_d = (6.61 \pm 0.14) \times 10^{-2}\,[\text{m}^2\,\text{sr}\,\text{s}\,\text{GeV}]^{-1}$, and $\gamma_d = -4.02 \pm 0.07$ for the diffuse component, and $C_s = (6.86 \pm 0.17) \times 10^{-5}\,[\text{m}^2\,\text{sr}\,\text{s}\,\text{GeV}]^{-1}$, $\gamma_s = -2.54 \pm 0.06$ for the source component and $1/E_s = 1.34^{+0.39}_{-0.37}\,\text{TeV}^{-1}$ for the inverse cut-off energy, corresponding to $E_s = 745^{+168}_{-283}\,\text{GeV}$ with $\chi^2/\text{dof} = 50.7/68 = 0.75$. The result of the fit is presented in Fig. 5.13.

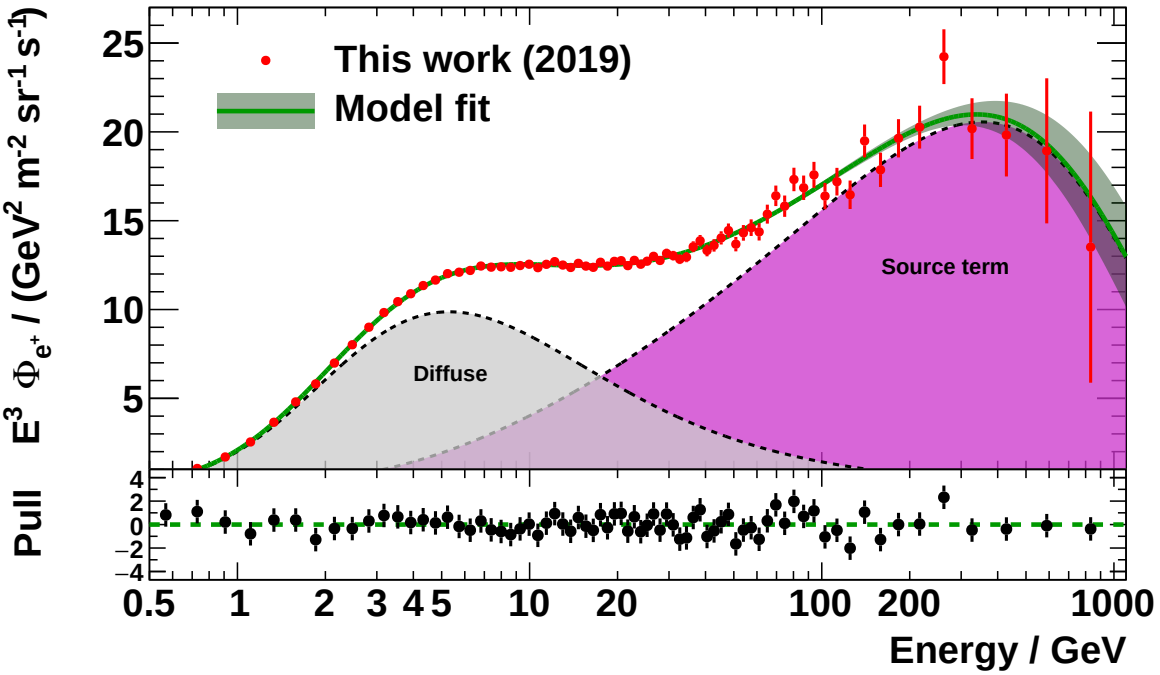

Figure 5.13: The positron flux, scaled with E^3, is shown as red points. The result of the fit of Eq. (5.4) is shown as green line, enclosed by a green band, indicating the uncertainty of the fit result. The diffuse and source components are indicated by the gray and magenta areas, respectively. The lower plot shows the pull distribution of the fit (data minus model divided by data uncertainty) – the model describes the data accurately over the whole energy range.

One can conclude that the positron flux is well described by the sum of a diffuse term associated with positrons produced by collisions, which dominates at low energies, and a new source term, which dominates at high energies.

To study the significance of the $1/E_s$ measurement all six fit parameters were varied, to find regions in the parameter space corresponding to $1-5\ \sigma$ levels. Figure 5.14 shows the projection of the six dimensional parameter space to the $(1/E_s - C_s)$ plane.

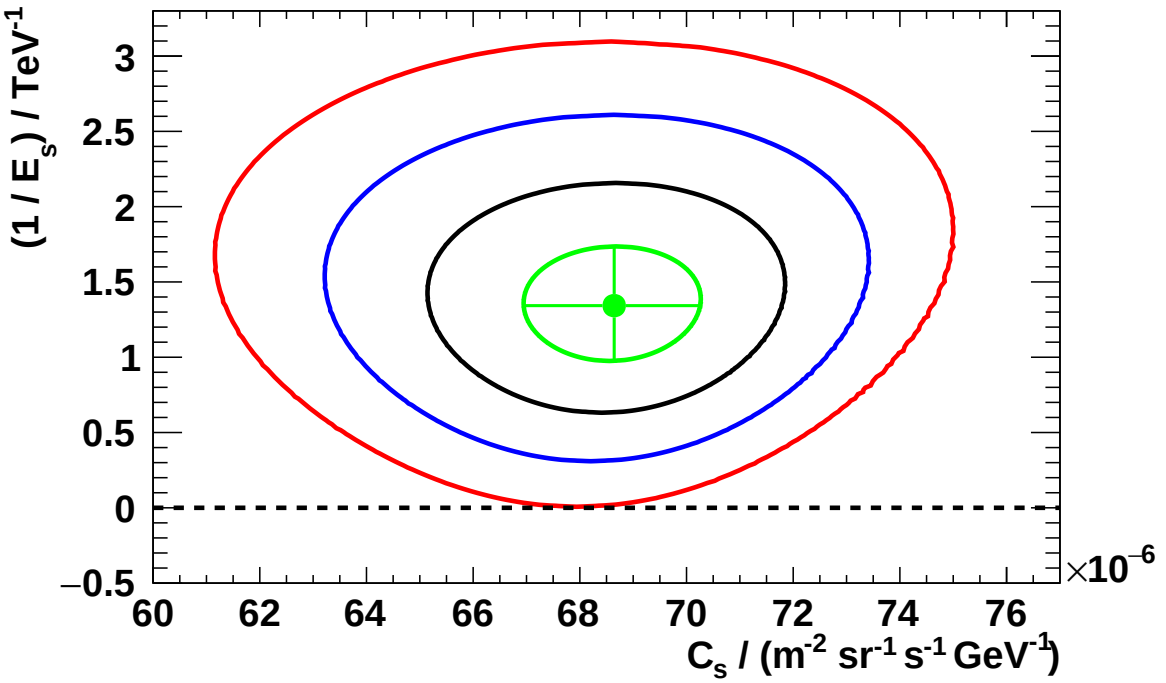

Figure 5.14: The contour plot between the C_s and $1/E_s$ parameters shows that the cut-off significance is established with 4σ. The regions corresponding to 1σ up to 4σ are drawn in green (68.26 % C.L.), black (95.54 % C.L.), blue (99.74 % C.L.) and red (99.99 % C.L.), respectively.

A detailed analysis shows that a point where the parameter, where $1/E_s$ reaches 0 (cut-off at infinity) corresponds to a confidence level of 4.01 σ. The significance of the source term cut-off is established at 4σ: the positron flux in the energy range cannot be described by a sum of two power law functions at the 99.99 % confidence level. This is the first reported evidence for a spectral cut-off in a cosmic-ray flux at these energies.

These experimental data on cosmic-ray positrons show that, at high energies, they predominantly originate from a new source (e.g. from dark matter annihilation or from other astrophysical sources). An important handle to disentangle whether dark matter annihilation or an astrophysical source is responsible for the source term is the *anisotropy* of the arrival directions of the positrons. An astrophysical point source - such as a pulsar - will imprint a larger anisotropy on the arrival directions of the positrons as a smooth dark mater halo. Thus measuring the dipole anisotropy (explained in Ref. [Aguilar2013]) is important to probe the dark matter hypothesis. With the seven year dataset, an upper limit of the dipole anisotropy $\delta < 0.019$ at the 95 % C.L. for energies above 16 GeV is obtained [Aguilar2019b]. This does not yet rule out e.g. a pulsar origin of the high-energetic positrons: depending on the pulsar model, the expected anisotropy is at the level of ≈ 0.5 % [Hooper2009]. More data is needed to be able to uncover the origin of the high-energetic positrons in future (see Chapter 6).

5.1.3 Positron/electron ratio

Figure 5.15 shows the time-averaged positron/electron ratio, determined by a dedicated analysis, using the single-track data sample, not computed from the fluxes themselves, which were derived using the all-tracks sample, as explained in Section 4.4.5.

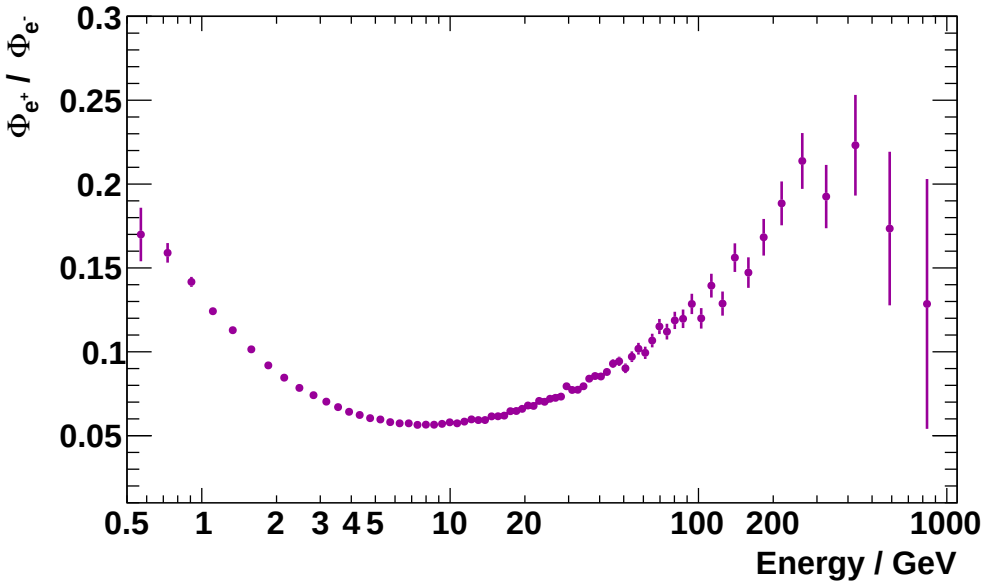

Figure 5.15: The positron/electron ratio measured by AMS-02.

The positron/electron ratio is consistent between the dedicated single-track analysis and the all-tracks flux analysis, as shown in Appendix B.2.4.

Figure 5.16 shows a breakdown of the total uncertainty into the statistical and systematic part.

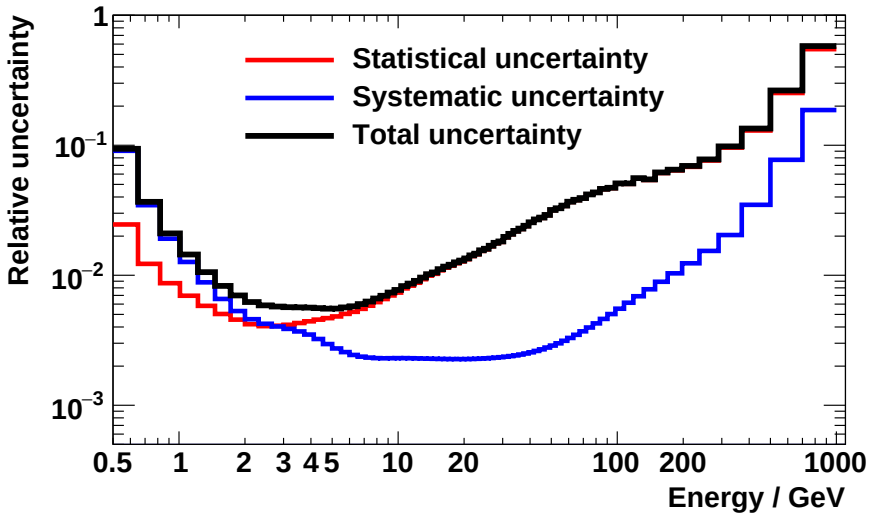

Figure 5.16: Breakdown of the uncertainty of the positron/electron ratio into a statistical and systematical part.

Above ≈ 2 GeV the statistical uncertainty dominates the uncertainty of the positron/electron ratio measurement. Below this energy, the systematic uncertainty always exceeds the statistical uncertainty. See Section 4.8.5 for a decomposition of the systematic uncertainties.

The positron/electron ratio is an important ingredient to interpret the time-dependent flux results, and thus will be discussed in detail in Section 5.2.2. A related quantity, the positron fraction, is derived and discussed in Appendix B.2.2.

5.2 Time-dependent results

5.2.1 Electron and positron flux

The results of the time-dependent analysis were published in *Physical Review Letters* (Ref. [Aguilar2018]) and selected as **Editors suggestion**. The published data is based on this work, covering the first six years of science data from AMS-02 (**May 20th, 2011** until **May 12th, 2017**). The time range of the fluxes in this thesis were extended to **November 12th, 2017**, covering nine more Bartels rotations.

Figure 5.17 shows the extended time-dependent electron and positron flux. Each color represent a flux from a different Bartels rotation period. At low energies a clear time order is exposed: The magnitude of the fluxes, e.g. at ≈ 1 GeV exhibits a maximum in the beginning of the measuring period (BR 2426), then decrease to a minimum, followed by an increase (BR 2513). The same trend is visible in both electrons and positrons.

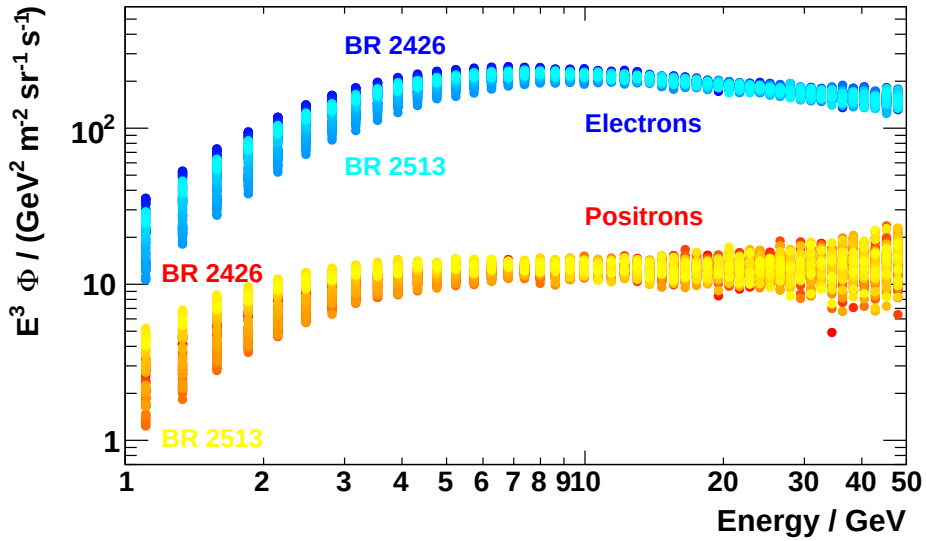

Figure 5.17: The electron / positron fluxes for each Bartels rotation analyzed in this work. The error bars on the individual flux points were omitted for clarity.

Figure 5.18 shows a breakdown of the total uncertainty of the electron and the positron flux into the statistical and systematic part, in an example Bartels rotation. The electron flux is dominated by the statistical uncertainty above ≈ 4 GeV whereas the positron flux is dominated by the statistical uncertainty over the whole energy range. See Section 4.10.3 for a decomposition of the systematic uncertainties.

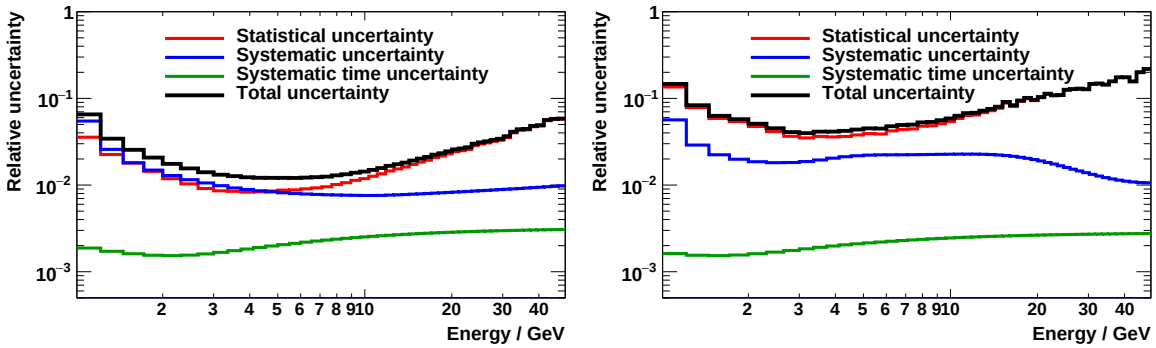

(a) Electron flux **(b)** Positron flux

Figure 5.18: Breakdown of the uncertainty of the electron flux (left) and the positron flux (right) into a statistical and systematical part, in an example Bartels rotation $i = 26$ (Apr 16$^{\text{th}}$, 2013 - May 13$^{\text{th}}$, 2013).

As described in Ref. [Aguilar2018], the model given in Ref. [Cavasonza2017] was fit to the data for each Bartels rotation independently, to search for fine structures in the energy dependence of the fluxes. The positron data show no additional structure, as shown in Appendix B.3.2. Figure 5.19 shows that the electron data reveal a model dependent residual structure in the energy range between 2 – 3 GeV.

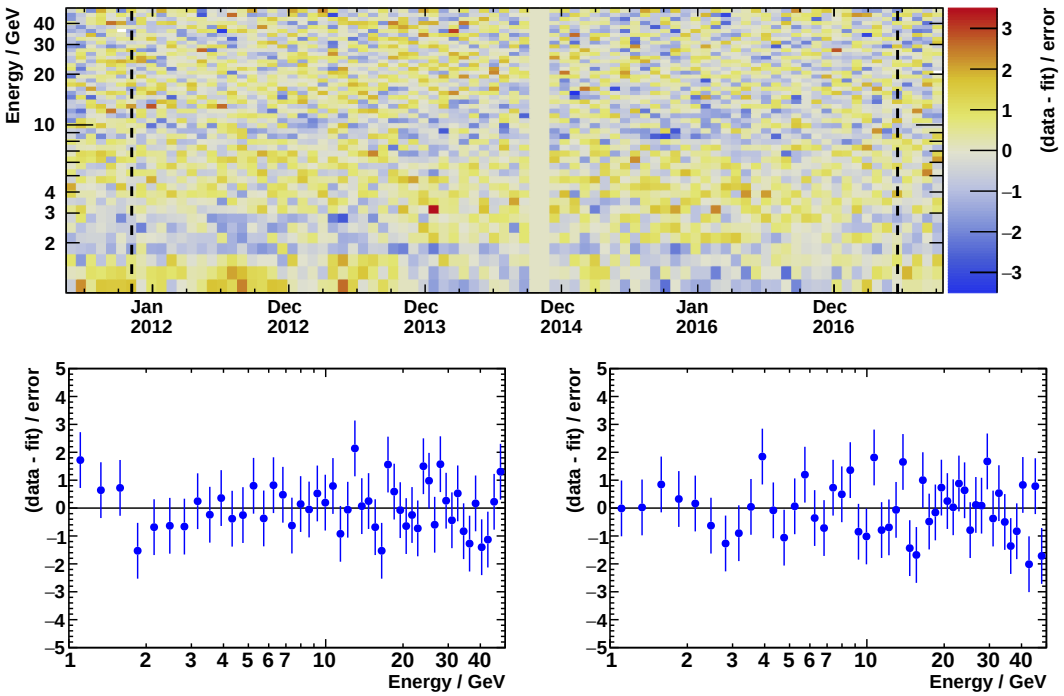

Figure 5.19: For the electron flux, the difference between data and model [Cavasonza2017] fits normalized to the experimental uncertainties: for each Bartels Rotation as a function of energy (upper plot). The distribution for the electrons reveals a model-dependent structure stable in time in the energy range between 2 – 3 GeV, emphasized for Bartels Rotation 2432 (lower left) and Bartels Rotation 2508 (lower right). The times for these two Bartels Rotations are indicated by the vertical dashed lines in the upper graph.

The residual structure is stable in time and consistent with an additional[3] smooth break [Strong2011] in the electron spectral index $\gamma^{-}(E) = \mathrm{d}(\log \Phi_{e^-}(E))/\mathrm{d}(\log E)$ below 10 GeV (Appendix B.3.1), comparable to the local interstellar electron spectrum of Ref. [Potgieter2015].

The fits of the extended model [Cavasonza2017], including the low energy break at ≈ 2 GeV, to the time-dependent electron and positron fluxes yield an average $\chi^2/\mathrm{dof} \approx 1$ for all Bartels rotations and no fine structures in the energy spectra were found.

The time-averaged electron flux and positron flux are shown in Fig. 5.20. To visualize the magnitude of the time variations of the fluxes, the envelopes of all fitted curves are displayed as shaded regions. The amplitude of the shaded regions decreases with increasing energy. At high energies, the statistical bin-to-bin fluctuations are larger than the time variation.

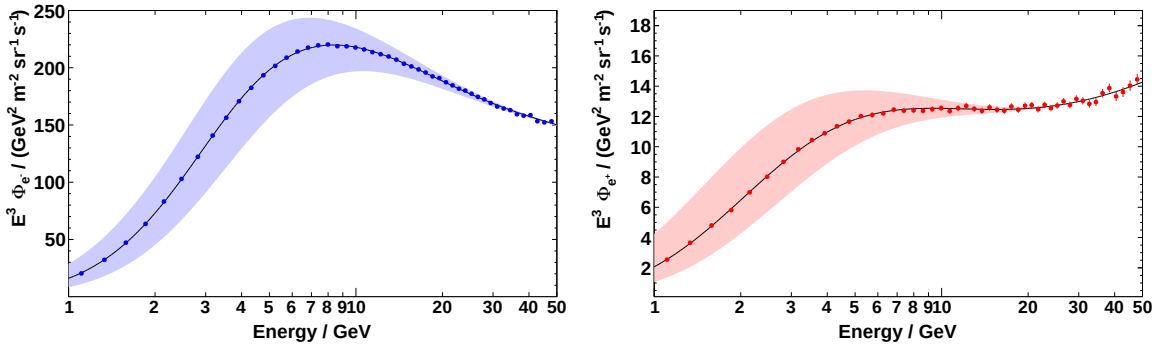

(a) Electron flux

(b) Positron flux

Figure 5.20: Visualization of the time-averaged electron flux (left) and positron flux (right). The time-variation range is indicated by the shaded regions, see text. The fit of the model in Ref. [Cavasonza2017] to the time-averaged data points is shown by the black curves.

To study the time behavior in more detail, the fluxes are shown in Fig. 5.21 as a function of time for five characteristic energy bins. A clear evolution of the fluxes with time at low energies that gradually diminishes towards high energies is exposed. At the lowest energies, the amplitudes of both the electron flux and the positron flux change by a factor of 3. Both fluxes exhibit profound short- and long-term variations. The short-term variations occur simultaneously in both fluxes with approximately the same relative amplitude. On the short term of Bartels rotations, several prominent and distinct structures are observed. They are characterized by minima, visible in both the electron flux and the positron flux across the energy range below $\mathrm{E} \lesssim 10$ GeV. These are marked by dashed vertical lines in Fig. 5.21.

In October 2011 and March 2012, there are sharp drops in the fluxes, followed by a quick recovery. The March 2012 event coincides with a strong Forbush decrease registered on March 8$^{\mathrm{th}}$, 2012 [Cheminet2013]. Another drop occurred in August 2012; this was followed by an extended recovery period. For $\mathrm{E} \lesssim 10$ GeV, May 2013 and April 2015 mark two changes in the long-term trends of the fluxes: From May 2011 to May 2013, the fluxes of both species show a trend to decrease with time. In the period around July 2013 is the time of the solar magnetic field reversal. From May 2013 to April 2015,

[3] Note that the spectral break is less pronounced in this work, than in Ref. [Aguilar2018]. The reason is the unfolding procedure: the fluxes derived in this work are all unfolded, whereas the published fluxes in Ref. [Aguilar2018] have not been unfolded. However the physics conclusions of [Aguilar2018] remain unchanged.

the flux of electrons continues to decrease, but with reduced slope, while the positron flux begins to increase. Then, from April 2015 until November 2017, both fluxes rise steeply. The difference of the rate of the increase is related to the charge-sign dependent solar modulation [Potgieter2001; Heber2009]. At energies above 20 GeV, neither the electron flux nor the positron flux exhibits significant time dependence.

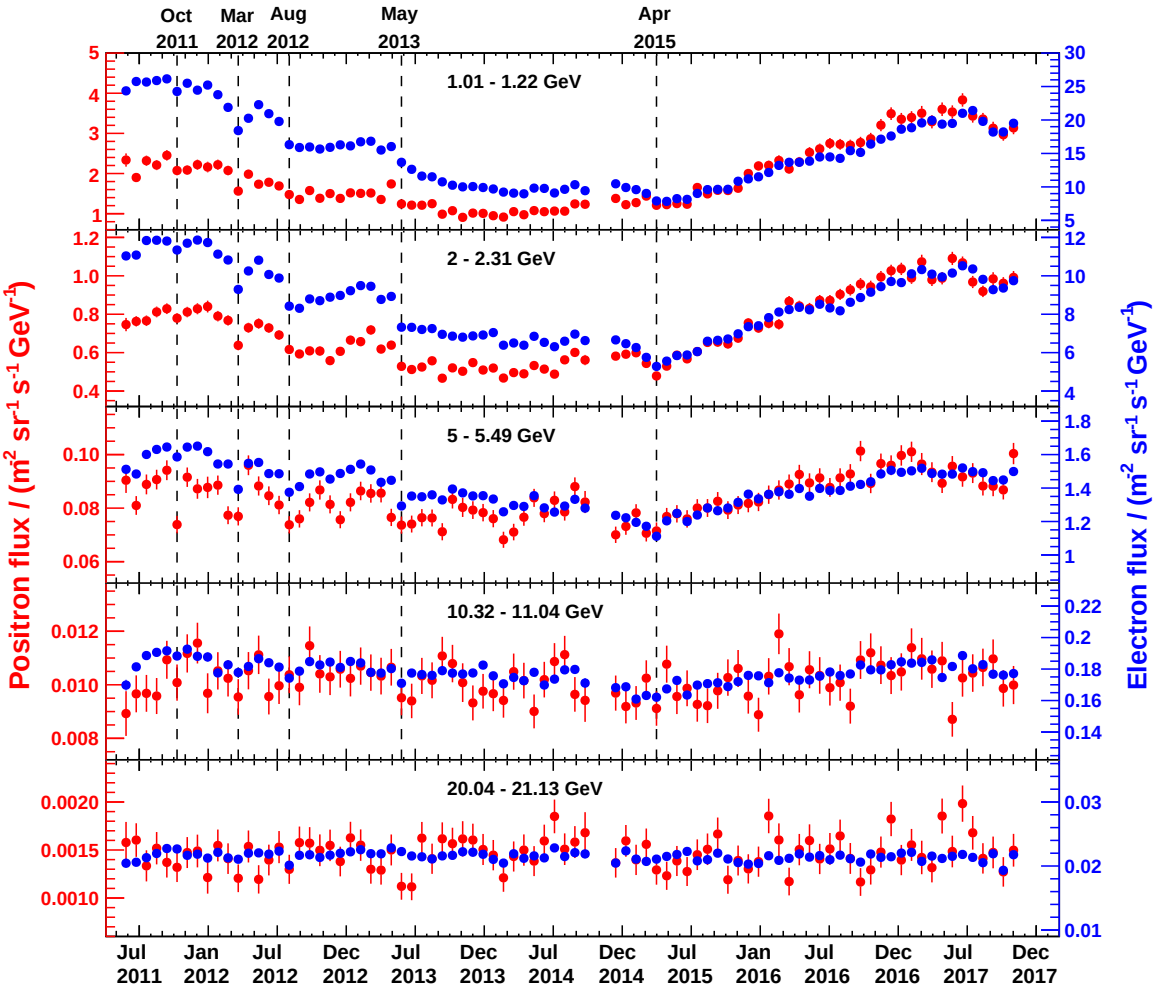

Figure 5.21: Fluxes of primary cosmic-ray positrons (red, left axis) and electrons (blue, right axis) as functions of time, for five of the 49 energy bins. The error bars are the statistical uncertainties. Prominent and distinct time structures visible in both the positron spectrum and the electron spectrum and at different energies are marked by dashed vertical lines.

5.2.2 Positron/electron ratio

The time-averaged positron/electron ratio is shown in Fig. 5.22. To visualize the magnitude of the time variations of the positron/electron ratio, the envelopes of all fitted curves are displayed as shaded regions. The amplitude of the shaded regions decreases with increasing energy. At high energies, the statistical bin-to-bin fluctuations are larger than the time variation.

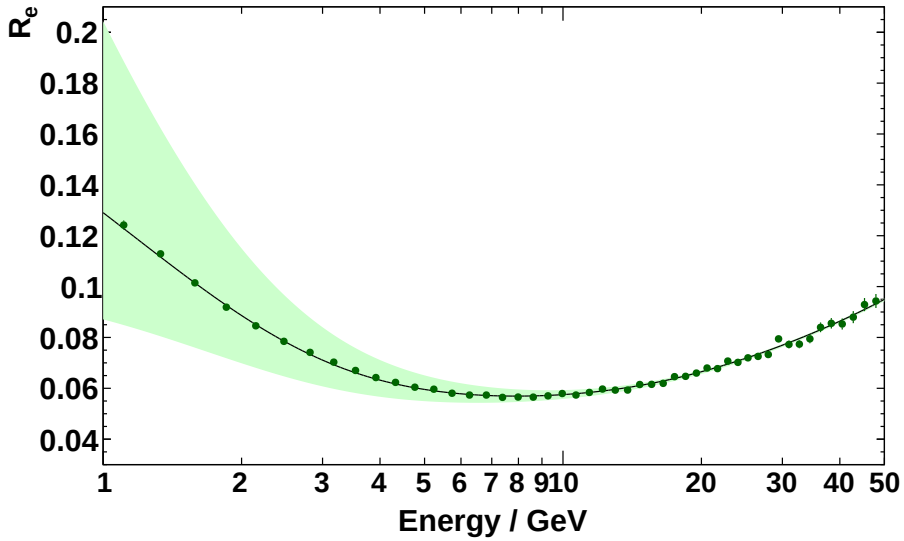

Figure 5.22: Visualization of the time-averaged positron/electron ratio R_e. The time-variation range is indicated by the shaded regions, see text. The fit of the model in Refs. [Corti2016; Cavasonza2017] to the time-averaged data points is shown by the black curves.

The long-term time structure of the data in Fig. 5.21 shows that the changes in relative amplitude are different for electrons and positrons. In the positron/electron ratio R_e, the short-term variations in the fluxes largely cancel, and a clear overall long-term trend appears, as shown in Fig. 5.23.

At low energies, R_e is flat at first, then smoothly increases after the time of the solar magnetic field reversal, to reach a plateau at a higher amplitude. During the extraordinarily quiet solar minimum period from 2006 to 2011, the energy and time dependence of various cosmic-ray measurements [Potgieter2017] are well reproduced by advanced numerical solar modulation models [Tomassetti2017]. But for the following years covered by the new data presented in this work, important and large systematic discrepancies are observed in particular in R_e (see SM of Ref. [Aguilar2018]), which is sensitive to charge-sign dependent effects in the solar modulation process of galactic cosmic rays.

A model-independent approach is used to extract the energy dependence of the quantities that characterize the observed transition in R_e. With a set of four parameters, the 4312 independent R_e measurements as a function of energy and time can be described well with a logistic function:

$$R_e(t,E) = R_0(E)\left[1 + \frac{C(E)}{\exp\left(-\frac{t-t_{1/2}(E)}{\Delta t(E)/\Delta_{80}}\right)+1}\right]. \tag{5.5}$$

At a given energy E, the time-dependence is related to three parameters in the function: the amplitude of the transition C, the midpoint of the transition $t_{1/2}$, and the duration of the transition Δt. Δ_{80} is set to 4.39, such that Δt is the time it takes for the transition to proceed from 10 % to 90 % of the change in magnitude. The results of fitting Eq. (5.5) for each energy bin are shown in Fig. 5.24. A $\chi^2/\mathrm{dof} \approx 1$ was obtained for all fits.

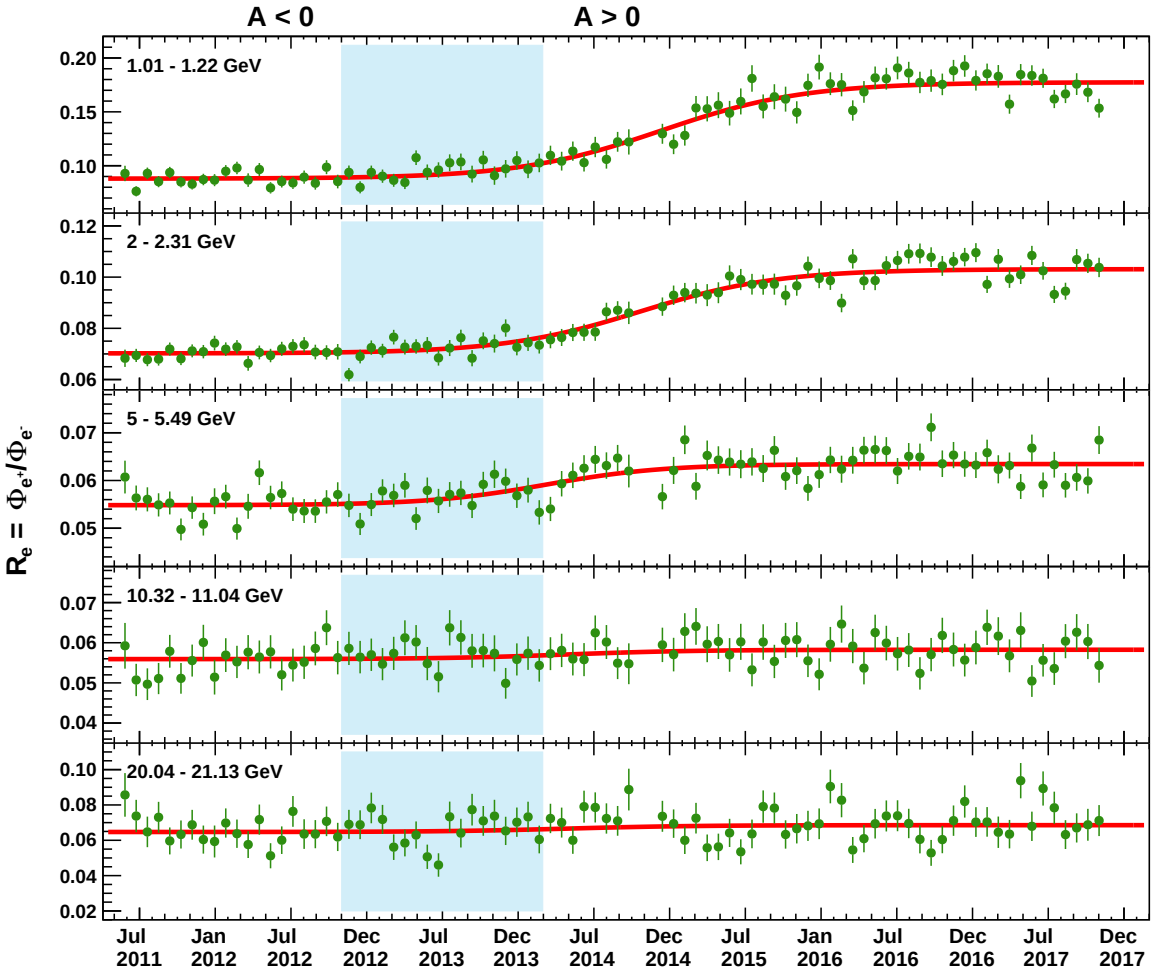

Figure 5.23: The ratio R_e of the positron flux to the electron flux as a function of time. The error bars are statistical. The best-fit parametrization according to Eq. (5.5) is shown by red curves. The polarity of the heliospheric magnetic field is denoted by A < 0 and A > 0. The period without well-defined polarity is marked by the shaded area [Sun2015].

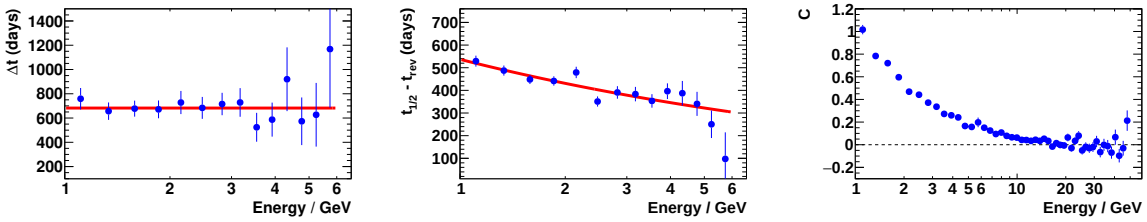

(a) (b) (c)

Figure 5.24: Results of the fits of the parameterization in Eq. (5.5) to the ratio R_e as a function of energy (blue circles): (a) Δt and the best-fit constant value of 682 days (red line), (b) $t_{1/2} - t_{\text{rev}}$ with the parameterization according to Eq. (5.6) (red curve), (c) amplitude C with a dashed line at zero to guide the eye.

The parameters $t_{1/2}$ and Δt can only be determined at low energies, where the amplitude of the transition is large, see Fig. 5.23. As shown in Fig. 5.24(a), the transition duration Δt is independent of energy, and a value of 682 ± 27 days was obtained.

The value differs from the published $\Delta t = 830 \pm 30$ days, presented in Ref. [Aguilar2018]. The difference arises from the additional eight Bartels rotations from May 2017 to December 2017: when excluding the last few Bartels rotations, as shown in Fig. 5.25, Δt will increase, to a value compatible with the previously published result. The difference between the result derived in this work using the full dataset (red point in Fig. 5.25) and the result derived using the reduced dataset (with eight Bartels Rotations removed, blue point in Fig. 5.25) is used as systematic uncertainty: $\Delta t^{\text{syst}} = 148$ days.

Therefore the transition period is determined to be $\Delta t = 682 \pm 27\,(\text{stat}) \pm 148\,(\text{syst})$ days.

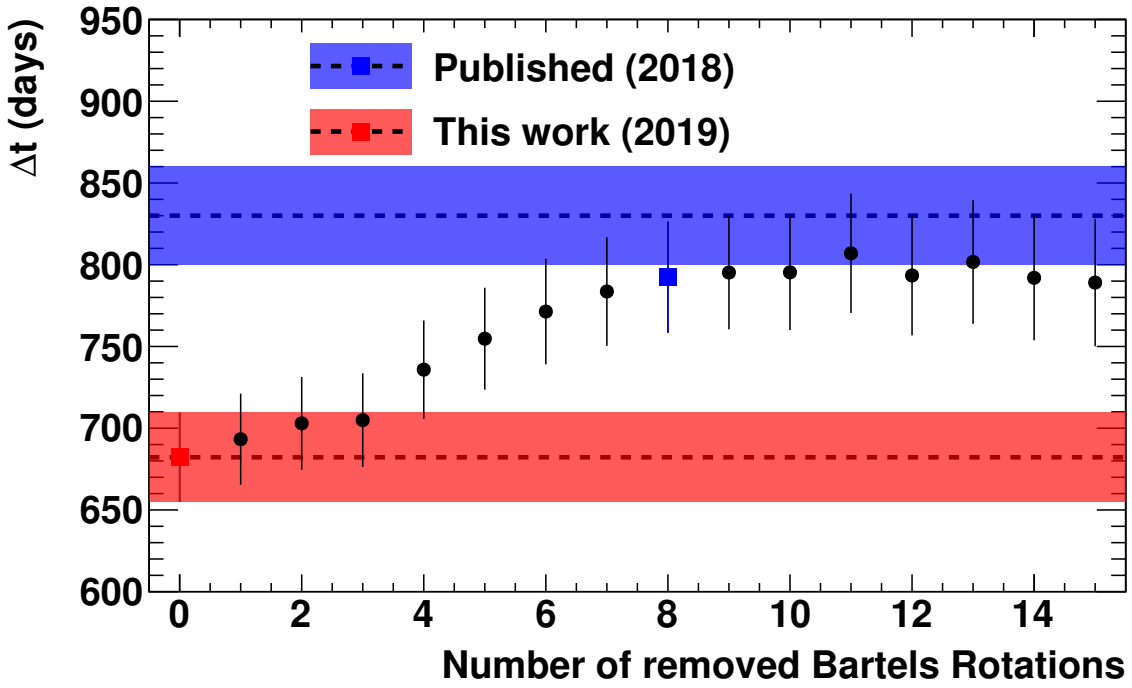

Figure 5.25: Dependence of the Δt parameter on the amount of Bartels Rotations that are included in the fit of Eq. (5.5) to the ratio R_e. The number of excluded Bartels Rotations at the end of the data taking period is correlated with Δt.

Figure 5.24(b) shows the energy dependence of the delay $t_{1/2}$ which is well parameterized by the formula

$$t_{1/2}(E) - t_{\text{rev}} = \tau \cdot (E/\text{GeV})^{\rho}, \tag{5.6}$$

where t_{rev} was fixed to be the effective time of the reversal of the solar magnetic field. For the value of t_{rev}, July 1$^{\text{st}}$, 2013 is used, the center of the period without well defined polarity [Sun2015]. The parameters used to describe the time and energy dependence of R_e in Eqs. (5.5) and (5.6) are illustrated in Fig. 5.26.

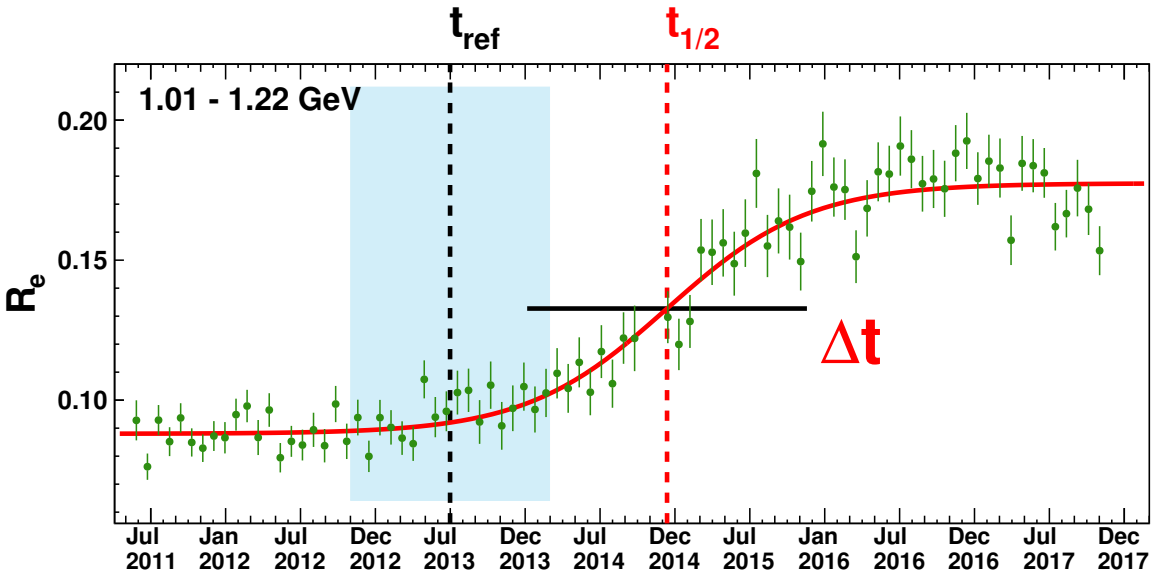

Figure 5.26: Illustration of the parameters in Eqs. (5.5) and (5.6) describing the time and energy dependence of R_e, using two energy bins from Fig. 5.23 as examples. The best-fit parameterizations according to Eq. (5.5) are shown by red curves. The period without well-defined polarity is marked by the shaded area [Sun2015]. The choice for the effective time of the reversal of the solar magnetic field t_{rev} is marked by black dashed vertical lines. The fit results for the midpoint of the transition $t_{1/2}$ are marked by red dashed vertical lines. The value of $t_{1/2}$ is found to be energy dependent. The width of the red horizontal bars indicate the duration of the transition Δt, which is found to be independent of energy at 682 ± 27 days. It takes time Δt for the transition to proceed from 10 % to 90 % of the change in magnitude.

A fit of Eq. (5.6) yields the parameter $\rho = -0.32 \pm 0.04\,(\mathrm{stat})\,^{+0.08}_{-0.16}\,(\mathrm{syst})$ and the amplitude $\tau = 537 \pm 18\,(\mathrm{stat}) \pm 136\,(\mathrm{syst})$ days, and the value of $t_{1/2}$ changes by 233 ± 31 days from 1 – 6 GeV. The systematic uncertainties are due to the uncertainty in t_{rev}. This is an important and unexpected energy dependence of $t_{1/2}$ and reflects the different response of cosmic-ray particles and antiparticles to changing modulation conditions.

To study the amplitude C in Fig. 5.24(c), Δt was fixed to its average value of 682 days and the value of $t_{1/2}$ calculated from Eq. (5.6) for energies above 6 GeV. At high energies, the fit result for the amplitude depends only weakly on the choice of the values for Δt and $t_{1/2}$. As seen in Fig. 5.24(c), the amplitude C is close to 1 at E = 1 GeV and decreases smoothly with energy. This is in qualitative agreement with the expectation from solar modulation models including drift effects [Potgieter1993b] and with the results from Refs. [Heber2002; Ferreira2004; Heber2009; Heber2013]. Above 20 GeV, the amplitude is consistent with zero.

CHAPTER 6

Summary

The presented time-averaged and time-dependent fluxes by AMS-02 are the most accurate measurements of the cosmic-ray electron and positron flux to date. The unprecedented accuracy in the data challenges our understanding of the origin of cosmic-ray positrons. The positron flux - at high energy - shows strong evidence for a source component responsible for the high-energetic positrons. For the first time a cut-off in the positron flux was measured, with a confidence of 4σ. The origin of the cut-off in the positron flux could be an astrophysical source, such as a pulsar. On the other hand the sharp drop-off of the flux could be the manifestation of a *kinematic edge*, related to dark matter annihilation. The electron flux shows no hint of a cut-off: it can be described by the sum of two power laws.

A key handle to differentiate between the dark matter and pulsar hypothesis is the measurement of the anisotropy in the arrival directions. The current limits on the dipole anisotropy of $\delta < 0.019$ at the 95 % confidence level are not competitive to rule out the pulsar origin. A novel large-acceptance analysis is under development, which will measure the fluxes as function of rigidity, not utilizing the ECAL. This allows one to increase the acceptance by a factor ≈ 4.

AMS-02 will continue to measure until the end of the ISS lifetime. Improvements in the analysis techniques [Kounine2017a] will allow us to measure the positron flux beyond the cut-off energy $E_s = 745^{+168}_{-283}$ GeV, up to ≈ 2 TeV and to determine the cut-off with more than 5σ confidence. The model independent search for a spectral index change is currently limited by statistics. With the current dataset the break energy was determined to be $E_0 = 333^{+61}_{-15}$ GeV and the change of the spectral index to $\Delta\gamma = -0.57 \pm 0.18$. With the extended dataset a significance of more than 5σ for the change of the spectral index and the break energy is in reach. Furthermore the gain in statistics and the large-acceptance analysis will allow us to probe the dipole anisotropy on the sub-percent level, allowing to detect either a signature of anisotropy or set the most stringent limits.

As already formulated in Ref. [Aguilar2018], for the first time, the charge-sign dependent modulation during solar maximum has been investigated in detail by electrons and positrons alone, using the time-dependent fluxes. Prominent, distinct, and coincident structures in both the positron flux and the electron flux on a time scale of months were identified, that are not visible in the e^+/e^- flux ratio. Instead a long-term feature in the e^+/e^- flux ratio was revealed: a smooth transition from one value to another, after the polarity reversal of the solar magnetic field. The transition magnitude is decreasing as a function of energy, consistent with expectations from solar modulation models including drift effects. This novel dataset provides accurate input to the understanding of solar modulation. In the past, flux models were often constructed above ≈ 20 GeV, where the influence of solar modulation

plays a minor role. Using the time-dependent precision data presented in this thesis, sophisticated models can be developed, incorporating charge-sign dependent solar modulation, that allows one to describe the electron and positron flux over the whole energy range from 0.5 GeV to 1 TeV.

Final insights on the origin of cosmic-ray positrons will be given by AMS-100 [Schael2019], which offers 1000 times the acceptance of AMS-02, and allows for a measurement of the electron and positron flux up to 10 TeV. The science program could start around the year 2040, which would mark the begin of a new era in astroparticle physics.

APPENDIX A

Appendix - Analysis

A.1 Detector quality cuts

In the following all **detector quality cuts** are listed that are imposed on the ISS data sample for each second of the data taking period.

1. **Nominal reconstruction period**
   The ratio of reconstructed particles over the trigger rate in each second should be nominal. Figure A.1 shows a plot of the trigger rate as function of the ratio: reconstructed particles over the trigger rate. The red dashed line $y = \frac{1600}{0.07} \cdot x$ separates the nominal reconstruction period from the non-nominal reconstruction period, where the reconstruction efficiency is low. All entries left of the line are rejected for further analysis.

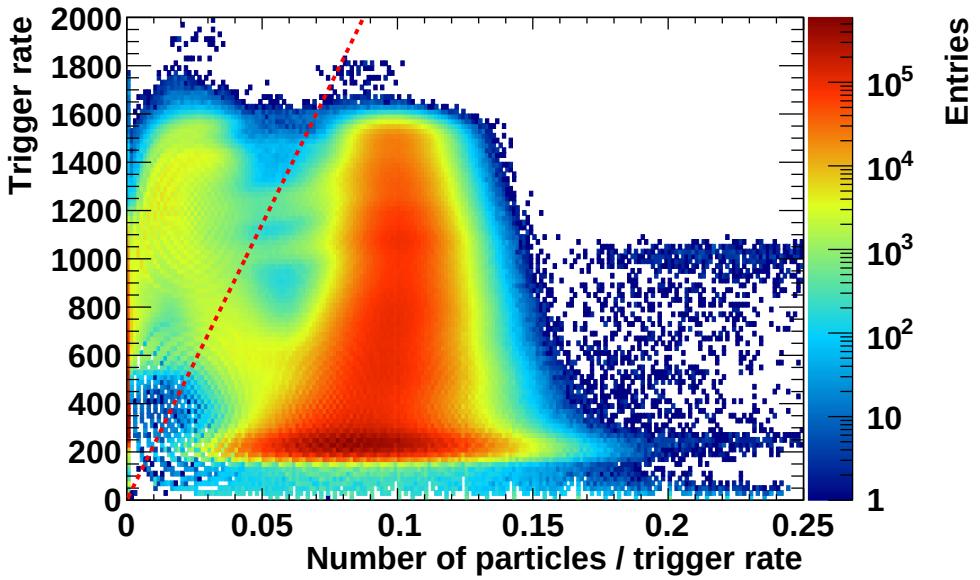

Figure A.1: Plot of the trigger rate as function of the ratio reconstructed particles over trigger rate. The red dashed line illustrates the applied cut. All seconds distributed on the left of the line are rejected for further analysis, due to non-nominal reconstruction quality of that time period.

2. **Nominal data taking period**
   The AMS-02 collaboration keeps track of time intervals in which the detector was in an unstable condition, such as the first weeks of commissioning, all periods where the TRD gas system is refilled, when the DAQ was unavailable, etc. These so-called "bad runs" are excluded when analyzing the ISS data.

3. **Nominal trigger performance**
   The amount of recorded events in each second of ISS data must be compatible with the expectation from the trigger rate: $f_{\text{trigger}}/N_{\text{events}} > 0.98$

4. **Nominal ISS zenith angle**
   The zenith angle of the ISS must be less than 40°. Periods when the ISS was rotated must be excluded for analysis.

5. **No missed events**
   If there are more than 10 % of the events missing in a second, exclude the second for analysis. There are rare reasons that can lead to missing events, for instance transfer problems in the DAQ boards, or buffer overflows on the data reduction boards.

6. **Good tracker alignment**
   The tracker alignment of the external tracker planes (Layer 1 and Layer 9) is performed independently by the Perugia and CIEMAT groups. Both alignment procedures should yield a similar set of alignment parameters for a given time period. Two important parameters are the shifts of the whole tracker plane with respect to the inner tracker: ΔX and ΔY. If the ΔX or ΔY in Layer 1 between the Perugia / CIEMAT method differs by more than 70 µm the time period is excluded. Likewise if the ΔX or ΔY in Layer 9 differs by more than 100 µm the time period is excluded as well.

7. **Too many events in second**
   If the amount of reconstructed events exceeds 1800 in a second, reject the time period. Events in these conditions are mostly taken near the SAA [Kurnosova1962] or in the pole regions, where the detector is filled with low energy particles. These periods should be rejected.

8. **Nominal live-time**
   If the detector was busy for more than 50 % in a second, reject the time period.

9. **Nominal DAQ condition**
   If hardware errors were detected in the second, reject it. Hardware errors might be bit-flips in the electronic boards, or duplicated events that got recorded, due to problems in the DAQ.

10. **Nominal occupancy in TRD**
    Usually the mean number of hits recorded in the TRD in each second is ≈ 60. If the mean number of hits per second exceeds 1000, the second will be rejected. This happens frequently at the edges of the SAA or in the pole regions.

A.2 CCMVA input variables

In the following the remaining nine input variables relevant for the single-track and multi-tracks sample are presented, that were omitted in Section 4.2.8.

1. **Upper TOF charge**

   The TOF clusters belonging to the TOF β measurement associated with the reconstructed primary particle (Section 4.2.5) are used to estimate the charge in the upper TOF. TofUpperCharge is computed by taking the average of the available charge measurements in the TOF clusters.

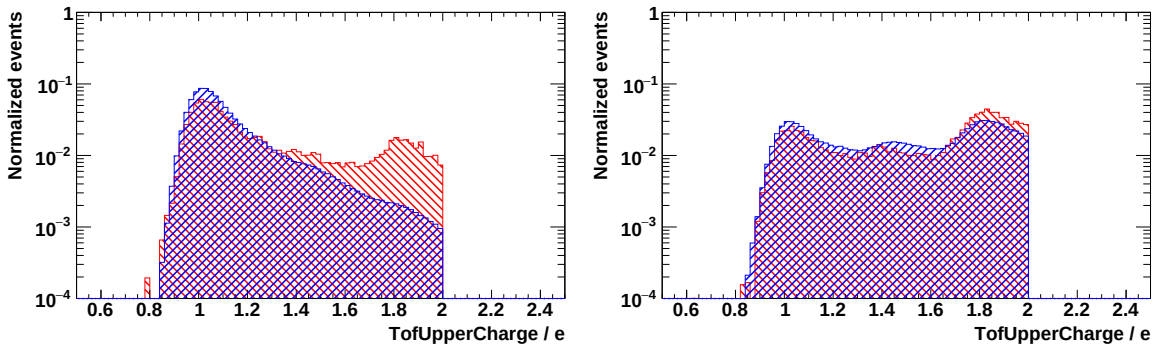

(a) Single-track sample **(b)** Multi-tracks sample

Figure A.2: Example of TofUpperCharge distribution in the energy bin 17.98 – 18.99 GeV in the electron Monte-Carlo simulation. The red histogram shows the charge-confused sample (R > 0) and the blue histogram the correct reconstructed sample (R < 0), after applying all preselection, selection and $e^{\pm}$ identification cuts.

   Figure A.2 shows the TofUpperCharge distribution (as defined in Section 4.3.3 - Item 2) in an example energy bin for both the correct and wrong rigidity sample in the electron Monte-Carlo simulation.

2. **Tracker energy deposition ratio**

   As described in Section 4.2.2, a maximum of one reconstructed hit per tracker layer is associated to a tracker track. If additional particles besides the primary particle traverse the tracker they might produce extra energy depositions in the vicinity of the reconstructed clusters, belonging to the primary reconstructed track. This is a useful information regarding the charge-confusion estimation, as they probability of associating the wrong hit to the primary track increases.

   Therefor it is useful to examine each reconstructed hit belonging to the selected tracker track for additional activity in the neighboring strips, adjacent to the Y clusters. X clusters are less interesting, as a wrong X cluster cannot change the rigidity measurement. Only Y clusters - reconstructed in the bending plane - can alter the sagitta and thus the rigidity measurement.

   The TrkMinSignalRatio quantity captures the information whether extra energy depositions in the vicinity of the reconstructed hits are present, in any of the tracker layers.

The function $i_{\text{seed}}(l)$ yields the seed strip number of the reconstructed hit attached to the selected tracker track in layer l. TrkSignalRatio(l) is defined as the ratio of the sum of the raw amplitudes of the strips in the Y cluster to the sum of all raw Y amplitudes on the same ladder in a 10 channel window, all referring to the reconstructed hit Y cluster associated with the selected tracker track in layer l:

$$\text{TrkSignalRatio}(l) = \left(\sum_{s=i_{\text{seed}}(l)\ -\ \text{nStripsLeft}}^{i_{\text{seed}}(l)\ +\ \text{nStripsRight}} A(s) \right) \Bigg/ \left(\sum_{s=i_{\text{seed}}(l)\ -\ 5}^{i_{\text{seed}}(l)\ +\ 5} A(s) \right).$$

TrkMinSignalRatio denotes the minimum signal ratio TrkSignalRatio(l) in any of the tracker layers l, excluding the outer layers 1 and 9:

$$\text{TrkMinSignalRatio} = \min_{l\ \in\ [2,8]} \text{TrkSignalRatio}(l).$$

Figure A.3 shows the TrkMinSignalRatio distribution in an example energy bin for both the correct and wrong rigidity sample in the electron Monte-Carlo simulation.

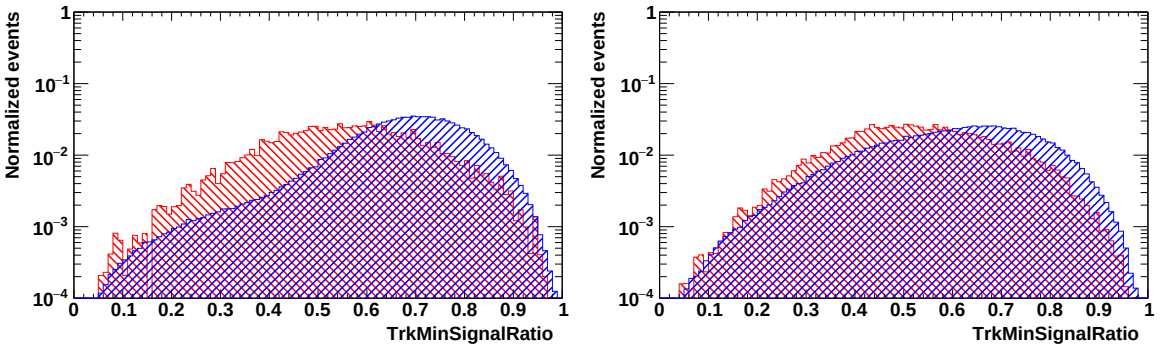

(a) Single-track sample **(b)** Multi-tracks sample

Figure A.3: Example of TrkMinSignalRatio distribution in the energy bin 17.98 – 18.99 GeV in the electron Monte-Carlo simulation.

3. **Additional hits near selected tracker hits**

TrkMinSignalRatio is used to quantify activity of the silicon strips near the reconstructed clusters that are used for the track fit. However it is also possible that there were additional reconstructed clusters nearby, which are not considered in TrkMinSignalRatio: those which are more than 5 channels away from the seed strip. Therefore it is necessary to inspect unused Y clusters, that are not associated to the selected tracker track but are close to the used clusters.

TrkMissClustDist is defined as the closest distance from the cluster used for the track fit to the nearest unused one, in any of the tracker layers. The value is set to zero if there are no unused clusters nearby.

Figure A.4 shows the TrkMissClustDist distribution in an example energy bin for both the correct and wrong rigidity sample in the electron Monte-Carlo simulation.

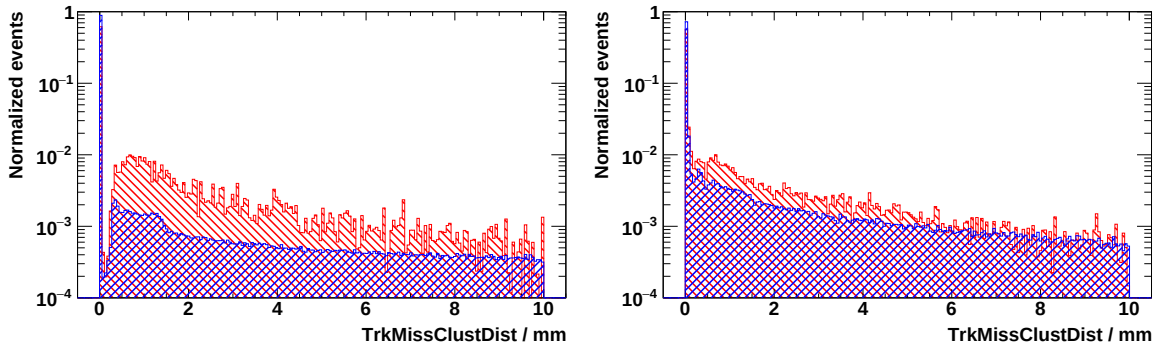

(a) Single-track sample **(b)** Multi-tracks sample

Figure A.4: Example of TrkMissClustDist distribution in the energy bin 17.98 – 18.99 GeV in the electron Monte-Carlo simulation.

4. **Rigidity uncertainty**

LogTrkRigRelError is defined as the logarithm of the uncertainty of the selected primary tracker track rigidity measurement.

$$\text{LogTrkRigRelError} = \log\left(\sigma_{R_{\text{primary}}}\right)$$

Figure A.5 shows the LogTrkRigRelError distribution in an example energy bin for both the correct and wrong rigidity sample in the electron Monte-Carlo simulation.

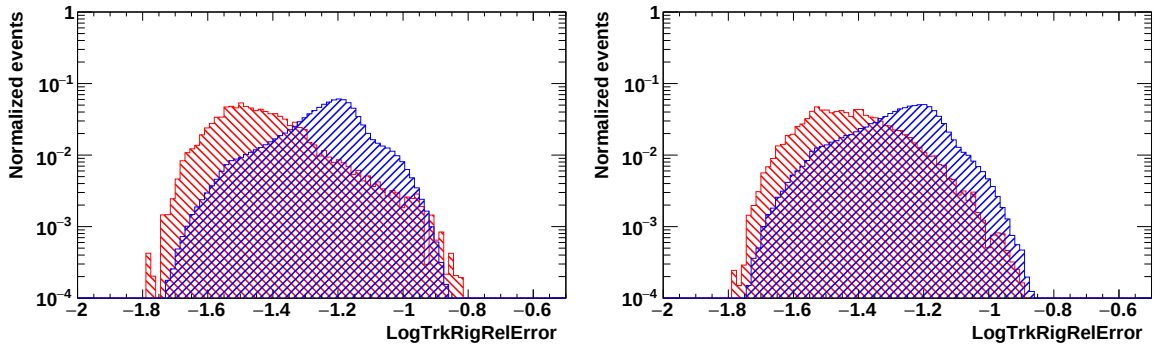

(a) Single-track sample **(b)** Multi-tracks sample

Figure A.5: Example of LogTrkRigRelError distribution in the energy bin 17.98 – 18.99 GeV in the electron Monte-Carlo simulation.

On an event by event basis this quantity is difficult to use for discrimination in a cut based analysis, as its numerical value depends on the tracker pattern and thus is correlated with it. Furthermore the difference between correct and wrong reconstructed sample is not large, but noticeable. Since it offers discrimination power it can be included in this estimator, since correlations are properly handled during the construction of the MVA.

5. **Tracker hit pattern**

The so-called tracker pattern is a classification of the topology of the selected tracker track in disjoint categories, depending on the amount of outer tracker layers associated to the track. Table A.1 shows the numerical value of the tracker pattern and its meaning. The tracker patterns are sorted by MDR. For a single-track electron the tracker pattern where all outer layers contribute to the rigidity measurement (L1 + L9) offers the largest detectable rigidity. The so-called full-span tracker pattern has the largest lever arm to detect the small displacements of the electron trajectory, due to the bending in the magnetic field, which is in the order of less than 20 µm in the TeV regime, between the incident point at L1 and the exit point in L9.

Layer 1	Layer 2	Layer 9	Tracker pattern
x	(x)	x	1
	x	x	2
x	x		3
		x	4
x			5
	x		6

Table A.1: Tracker pattern classification. The cell entry "x" denotes that a hit is associated to the track, "(x)" that a hit might be associated to the track (optional) and an empty cell indicates no hit is associated to the track. The numerical value of the tracker pattern is sorted by MDR - a smaller value corresponds to a higher MDR.

Figure A.6 shows the TrkPattern distribution in an example energy bin for both the correct and wrong rigidity sample in the electron Monte-Carlo simulation.

The two tracker pattern with the smallest MDR are excluded for the analysis, indicated by the two empty bins for tracker pattern 5 and 6.

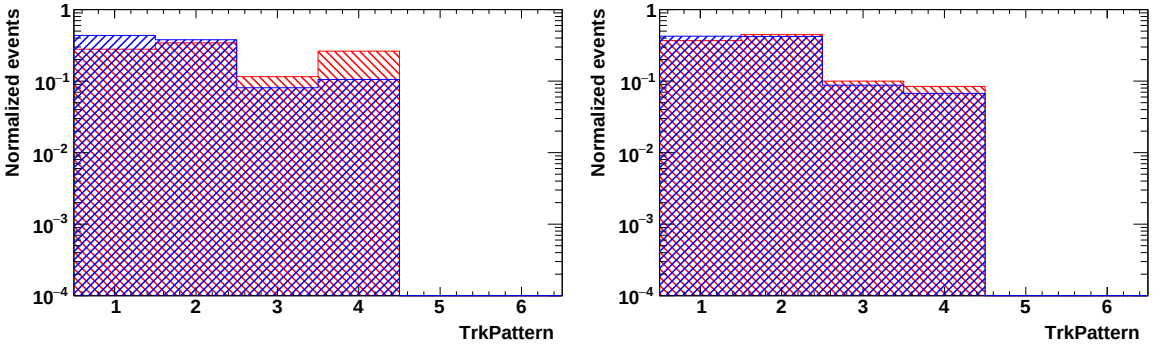

(a) Single-track sample

(b) Multi-tracks sample

Figure A.6: Example of TrkPattern distribution in the energy bin 17.98 – 18.99 GeV in the electron Monte-Carlo simulation.

6. **Tracker fit algorithm compatibility**

The Choutko algorithm - implemented in the AMS-02 track reconstruction - is an iterative track fit procedure, based on a fast global matrix inversion [Hart1984; Choutko2003]. An alternative algorithm - the Chikanian algorithm - aims to improve the multiple scattering treatment at low energies. However the Chikanian fit [Chikanian1996] is also more sensitive to interactions in the detector, therefore it offers a handle to discriminate between events with interactions and those without.

TrkChoutkoVsChikMatching is defined as asymmetry between the two track fit methods:

$$\text{TrkChoutkoVsChikMatching} = \left(\frac{1}{R_{\text{choutko}}} - \frac{1}{R_{\text{chikanian}}}\right) \Big/ \left(\frac{1}{R_{\text{choutko}}} + \frac{1}{R_{\text{chikanian}}}\right).$$

Figure A.7 shows the TrkChoutkoVsChikMatching distribution in an example energy bin for both the correct and wrong rigidity sample in the electron Monte-Carlo simulation.

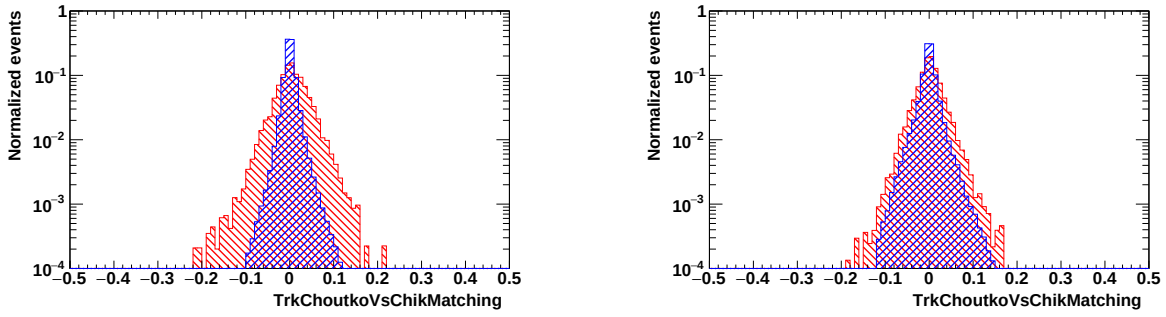

(a) Single-track sample **(b)** Multi-tracks sample

Figure A.7: Example of TrkChoutkoVsChikMatching distribution in the energy bin 17.98 – 18.99 GeV in the electron Monte-Carlo simulation.

7. **Tracker upper/lower half rigidity matching**

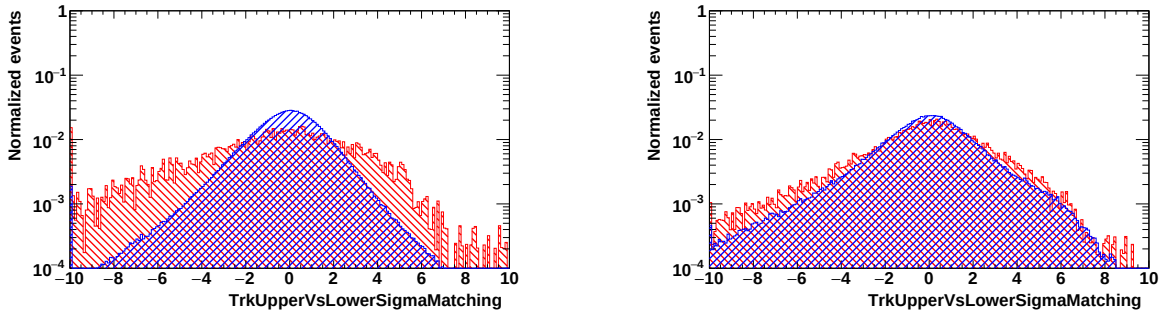

(a) Single-track sample **(b)** Multi-tracks sample

Figure A.8: Example of TrkUpperVsLowerSigmaMatching distribution in the energy bin 17.98 – 18.99 GeV in the electron Monte-Carlo simulation.

Another way to detect interactions in the inner tracker is to perform the track fit once only the upper half of the inner tracker and another time using only the lower half. TrkUpperVsLowerSigmaMatching is defined as the sagitta difference between these track fits, weighted by the quadratic sum of the corresponding relative uncertainties:

$$\text{TrkUpperVsLowerSigmaMatching} = \frac{\text{sgn}(R_{\text{primary}})\left(\frac{1}{R_{\text{upper}}} - \frac{1}{R_{\text{lower}}}\right)}{\sqrt{\left(\frac{\sigma_{R_{\text{upper}}}}{R_{\text{upper}}}\right)^2 + \left(\frac{\sigma_{R_{\text{lower}}}}{R_{\text{lower}}}\right)^2}}.$$

Figure A.8 shows the TrkUpperVsLowerSigmaMatching distribution in an example energy bin for both the correct and wrong rigidity sample in the electron Monte-Carlo simulation.

8. **Tracker all/inner layers rigidity matching**

To study the influence of the outer tracker layers to the reconstructed rigidity, the track fit is performed once only the inner tracker and once with the external layers included. The weighted sagitta difference is defined as TrkAllVsInnerMatching:

$$\text{TrkAllVsInnerMatching} = \frac{\text{sgn}(R_{\text{primary}})\left(\frac{1}{R_{\text{all}}} - \frac{1}{R_{\text{inner}}}\right)}{\frac{1}{2}\sqrt{\left(\frac{\sigma_{R_{\text{all}}}}{R_{\text{all}}}\right)^2 + \left(\frac{\sigma_{R_{\text{inner}}}}{R_{\text{inner}}}\right)^2}}$$

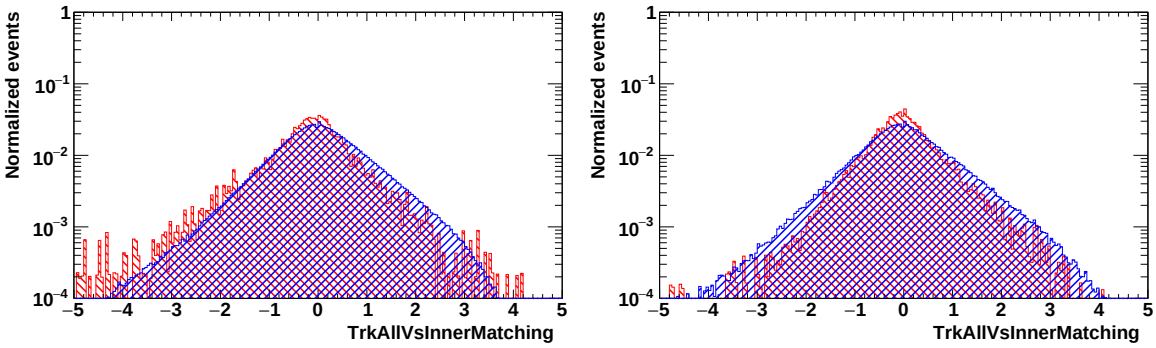

(a) Single-track sample **(b)** Multi-tracks sample

Figure A.9: Example of TrkAllVsInnerMatching distribution in the energy bin 17.98 – 18.99 GeV in the electron Monte-Carlo simulation.

Figure A.9 shows the TrkAllVsInnerMatching distribution in an example energy bin for both the correct and wrong rigidity sample in the electron Monte-Carlo simulation.

9. **Number of inner tracker planes**

   The number of inner layers that contribute a Y hit to the track fit - TrkNLayersInnerY - enters the MVA as input quantity. It is correlated with other variables that enter the MVA (TrkAllVsInnerMatching, TrkUpperVsLowerSigmaMatching). Nevertheless it can be used as input variable, since the MVA can exploit this correlation to achieve more discrimination power.

   Figure A.10 shows the TrkNLayersInnerY distribution in an example energy bin for both the correct and wrong rigidity sample in the electron Monte-Carlo simulation.

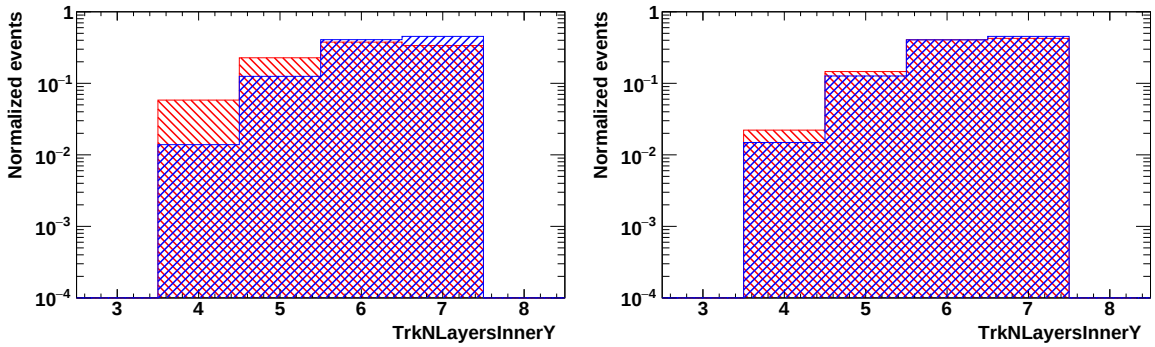

(a) Single-track sample **(b)** Multi-tracks sample

Figure A.10: Example of TrkNLayersInnerY distribution in the energy bin 17.98 – 18.99 GeV in the electron Monte-Carlo simulation.

Three variables were omitted in the description in Section 4.2.8, which enter the MVA estimator for the multi-tracks sample:

10. **Number of tracker tracks**

    Similar to TrkNLayersInnerY, the number of tracker tracks in the event TrkNumTracks has no discrimination power by itself. It still enters the MVA as the MVA can exploit the correlation between this variable and all other input quantities to achieve more discrimination power.

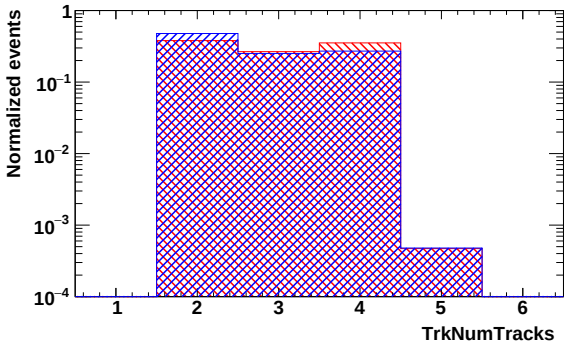

Figure A.11: Example of TrkNumTracks distribution in the energy bin 17.98 – 18.99 GeV in the electron Monte-Carlo simulation.

Figure A.11 shows the TrkNumTracks distribution in an example energy bin for both the correct and wrong rigidity sample in the electron Monte-Carlo simulation. Note that only events with more than one reconstructed tracker track enter the distribution, explaining why the first bin with exactly one track is empty.

11. **Tracker track top distance x-direction &**
12. **Tracker track top distance y-direction**

Using an analogous definition as TrkMinDXBottom / TrkMinDYBottom all tracker tracks are extrapolated to the TRD center position at $z = 113.55\,\text{cm}$.

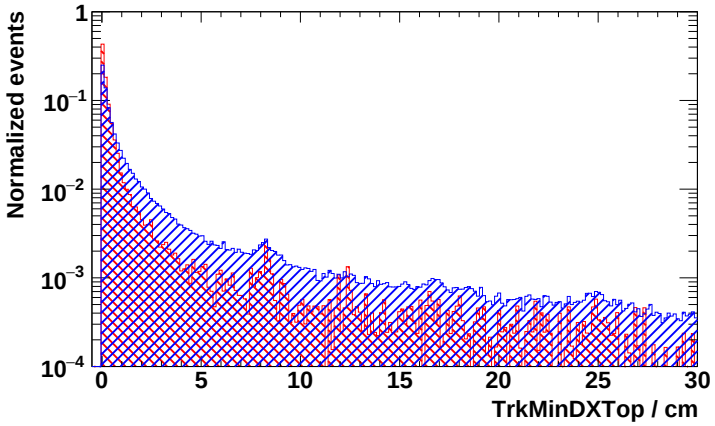

(a) TrkMinDXTop

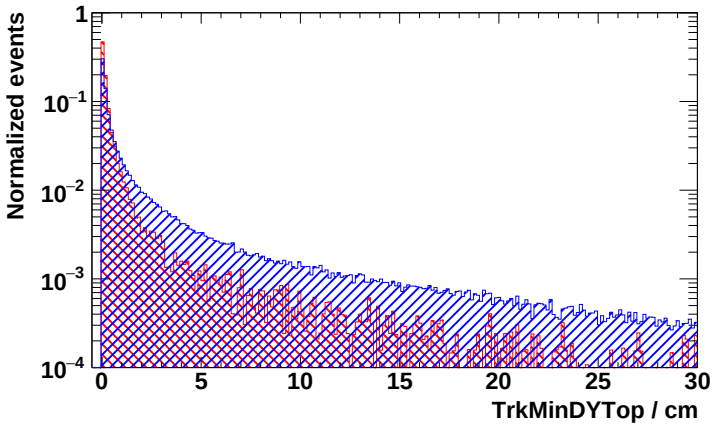

(b) TrkMinDYTop

Figure A.12: Example of TrkMinDXTop / TrkMinDYTop distributions in the energy bin 17.98 – 18.99 GeV in the electron Monte-Carlo simulation.

Figure A.12 shows the TrkMinDXTop / TrkMinDYTop distributions in an example energy bin for both the correct and wrong rigidity sample in the electron Monte-Carlo simulation. The separation power of this quantity is larger at low energies, but vanishes at medium energies above 10 GeV.

All 15 input variables for the single-track sample were compared between the electron Monte-Carlo simulation and the positron Monte-Carlo, as shown in Fig. A.13 for an example energy bin, after applying all preselection, selection and $e^{\pm}$ identification cuts. By construction, there is no difference between electrons and positrons in all energy bins. The same comparison was repeated for the multi-tracks sample, which also shows no differences in any of the variables. The six input variables which are specific to the multi-tracks sample are shown in Fig. A.14.

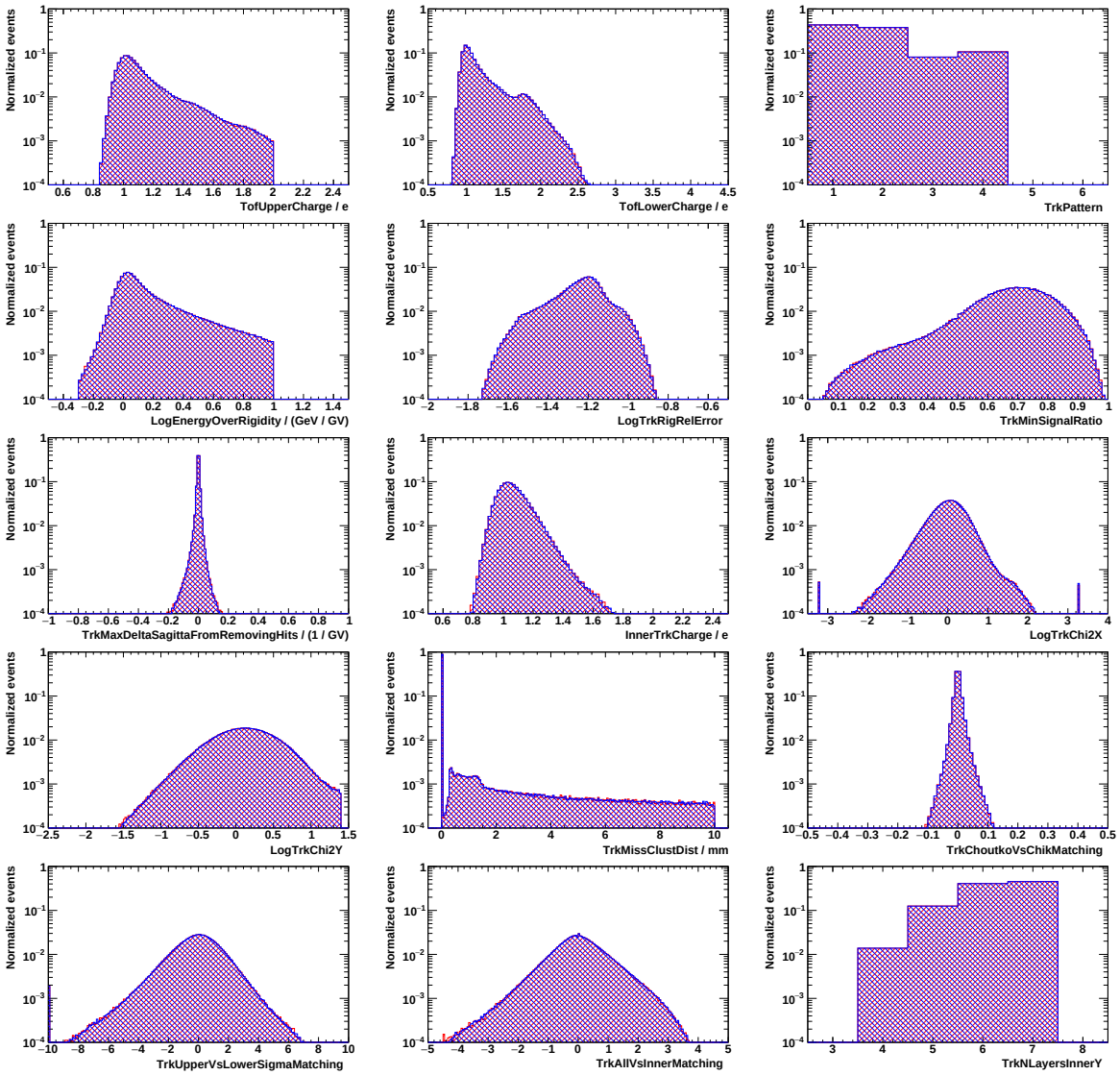

Figure A.13: Comparison of all 15 CCMVA input variables for the single-track sample between the positron Monte-Carlo simulation (red) and the electron Monte-Carlo simulation (blue) in the energy bin 17.98 – 18.99 GeV.

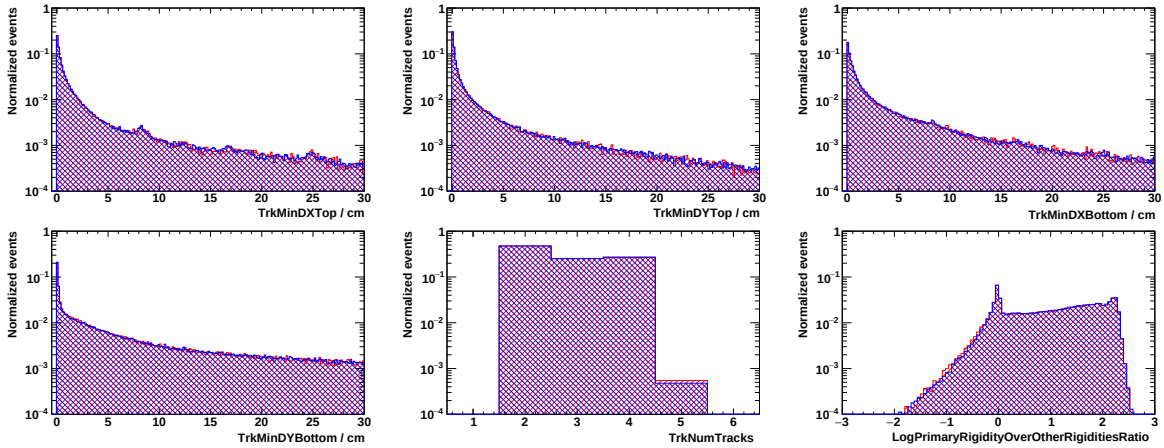

Figure A.14: Comparison of the six multi-tracks sample specific CCMVA input variables between the positron Monte-Carlo simulation (red) and the electron Monte-Carlo simulation (blue) in the energy bin 17.98 – 18.99 GeV. There are no visible differences, except for small fluctuations in the tails, proving the consistency of the input quantities between electron and positrons.

To ensure that the CCMVA is applicable on ISS data, all input variables have to match between ISS data and Monte-Carlo simulation. Figure A.15 shows a comparison in an example energy bin of all relevant variables for the multi-tracks sample between negative rigidity ISS data and the electron Monte-Carlo simulation, after applying all preselection, selection and $e^{\pm}$ identification cuts plus additional cuts to reduce any left-over charge-confused proton background on ISS data. All input quantities show an excellent agreement over all energies.

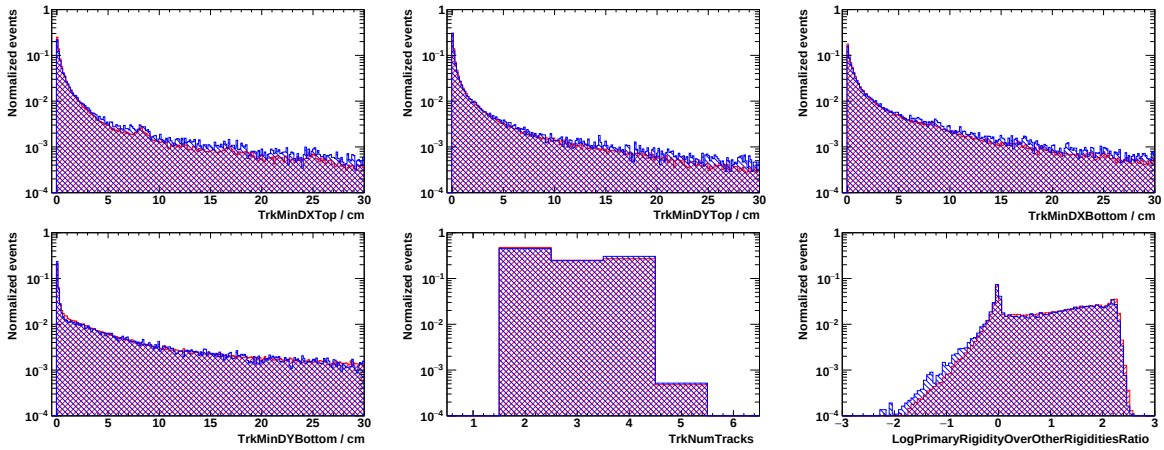

Figure A.15: Comparison of the six multi-tracks sample specific CCMVA input variables between the ISS data (blue) and the electron Monte-Carlo (red) in the energy bin 17.98 – 18.99 GeV. There are no visible differences, except for small fluctuations in the tails, proving the consistency of the input quantities between ISS data and simulation.

Furthermore the single-track sample input variables need to be verified between ISS data and Monte-Carlo simulation, as presented in Figure A.16. All variables except TrkMinSignalRatio show excellent agreement over all energies. The TrkMinSignalRatio quantity requires an accurate simulation

of the energy depositions in the silicon tracker on the strip level. The ISS TrkMinSignalRatio distribution favors slightly higher values and a narrower peak than the Monte-Carlo simulation, which means that the energy is deposited in a wider area in the Monte-Carlo simulation, covering more strips than on ISS data. However this has no impact on the applicability of the MVA on ISS data, as the TrkMinSignalRatio observable is of less importance compared to others and thus does not dominate the discrimination power of the MVA. If it would be an important observable the bias would have an impact on the output shape of the MVA, leading to ISS / Monte-Carlo differences.

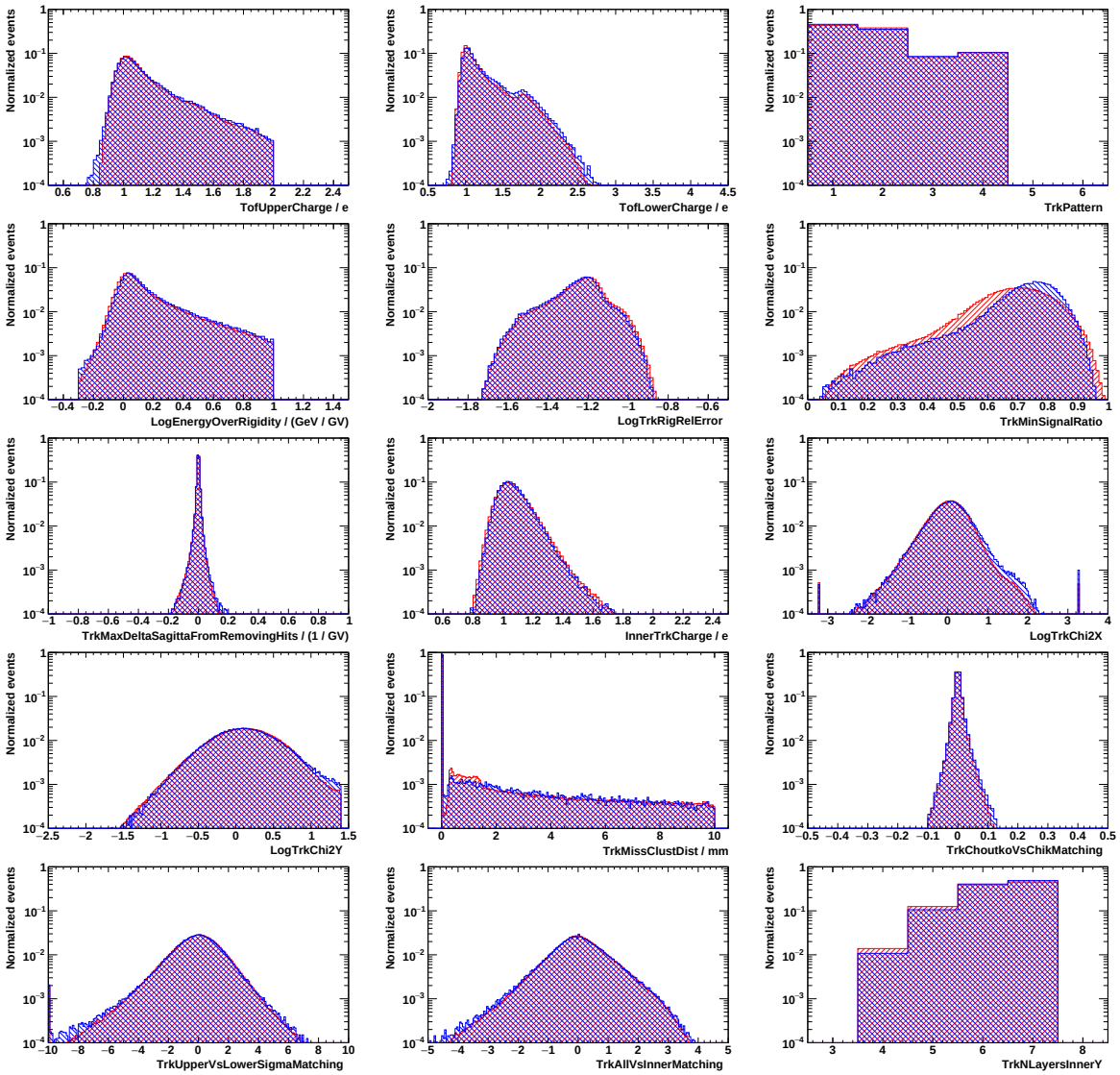

Figure A.16: Comparison of all 15 CCMVA input variables for the single-track sample between the ISS data (blue) and the electron Monte-Carlo (red) in the energy bin 17.98 – 18.99 GeV. There are no visible differences in all variables except TrkMinSignalRatio, except for small fluctuations in the tails, proving the consistency of the input quantities between ISS data and simulation. The whole comparison was performed on a negative rigidity sample, as its impossible to select pure samples of electrons with wrong reconstructed rigidity on ISS data.

A.3 TRD templates (multi-tracks sample)

In Section 4.4.2 the energy dependence of all template parameters was presented for the single-track sample. In this section the TRD template parameters as function of energy are shown for the multi-tracks sample.

Figure A.17 shows the charge-confused proton template parameters as function of energy for the multi-tracks sample.

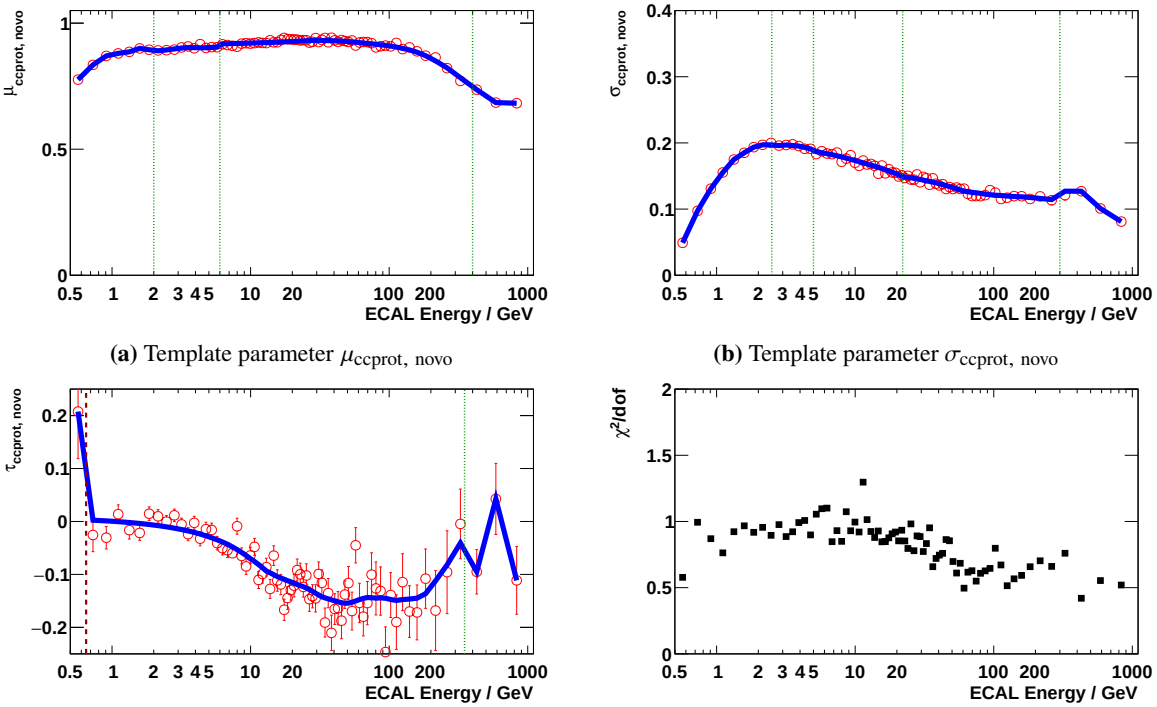

(a) Template parameter $\mu_{\text{ccprot, novo}}$

(b) Template parameter $\sigma_{\text{ccprot, novo}}$

(c) Template parameter $\tau_{\text{ccprot, novo}}$

(d) Goodness-of-fit

Figure A.17: Analytical TRD template parameters describing the evolution of the charge-confused proton template as function of energy for the multi-tracks sample. In each energy bin the analytical function - Eq. (4.7) - is fit to the template data sample, yielding the red points. A smoothing procedure yields the blue curves, which are used as template parameters for the analysis. The vertical dashed green lines mark areas where different isolated smoothing procedures are applied. The goodness-of-fit is indicated by the black points in the lower right plot.

Figure A.18 shows the electron template parameters as function of energy for the multi-tracks sample.

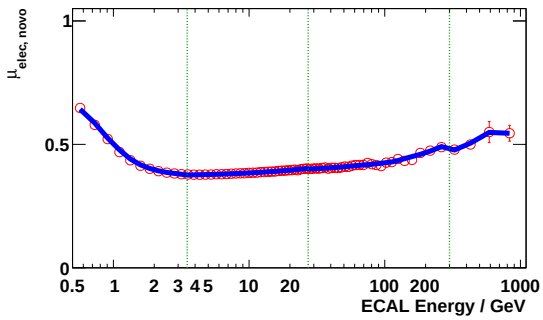

(a) Template parameter $\mu_{\text{elec, novo}}$

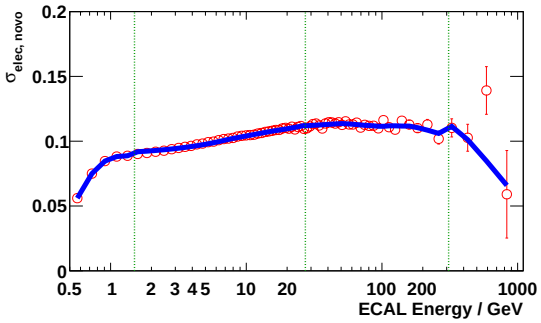

(b) Template parameter $\sigma_{\text{elec, novo}}$

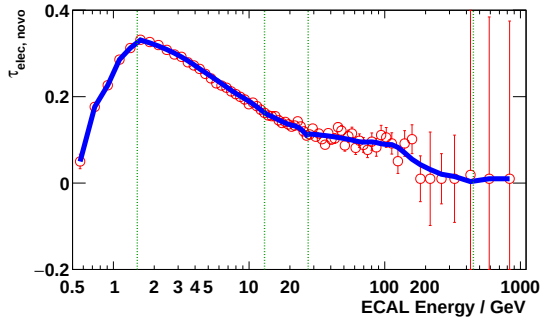

(c) Template parameter $\tau_{\text{elec, novo}}$

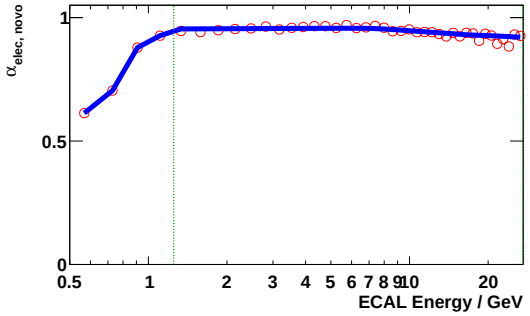

(d) Template parameter $\alpha_{\text{elec, novo}}$

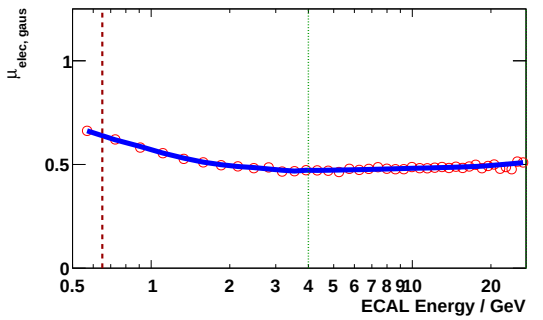

(e) Template parameter $\mu_{\text{elec, gaus}}$

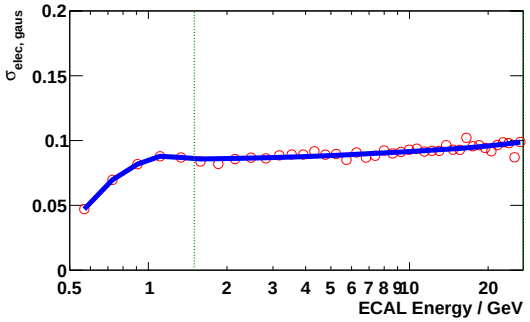

(f) Template parameter $\sigma_{\text{elec, gaus}}$

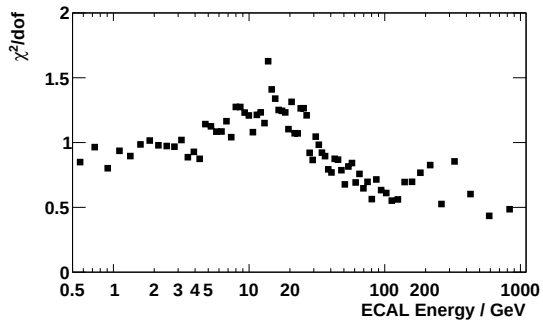

(g) Goodness-of-fit

Figure A.18: Analytical TRD template parameters describing the evolution of the electron template as function of energy for the multi-tracks sample. The meaning of the red points, the blue curve and the dashed lines is given in the caption of Fig. A.17.

Figure A.18(g) shows that between 6 – 20 GeV a tendency towards higher χ^2/dof is revealed. A closer inspection shows that the template data sample contains an additional component, that is not respected in the simultaneous fit procedure: fragmenting helium. In Section 4.4.5 it was shown that this bias is not a practical problem when applying these templates to extract electron and positron counts, as the fragmenting helium component is not present in the final data samples, from which the number of electrons and positrons are extracted. Figure A.19 shows the proton template parameters as function of energy for the multi-tracks sample.

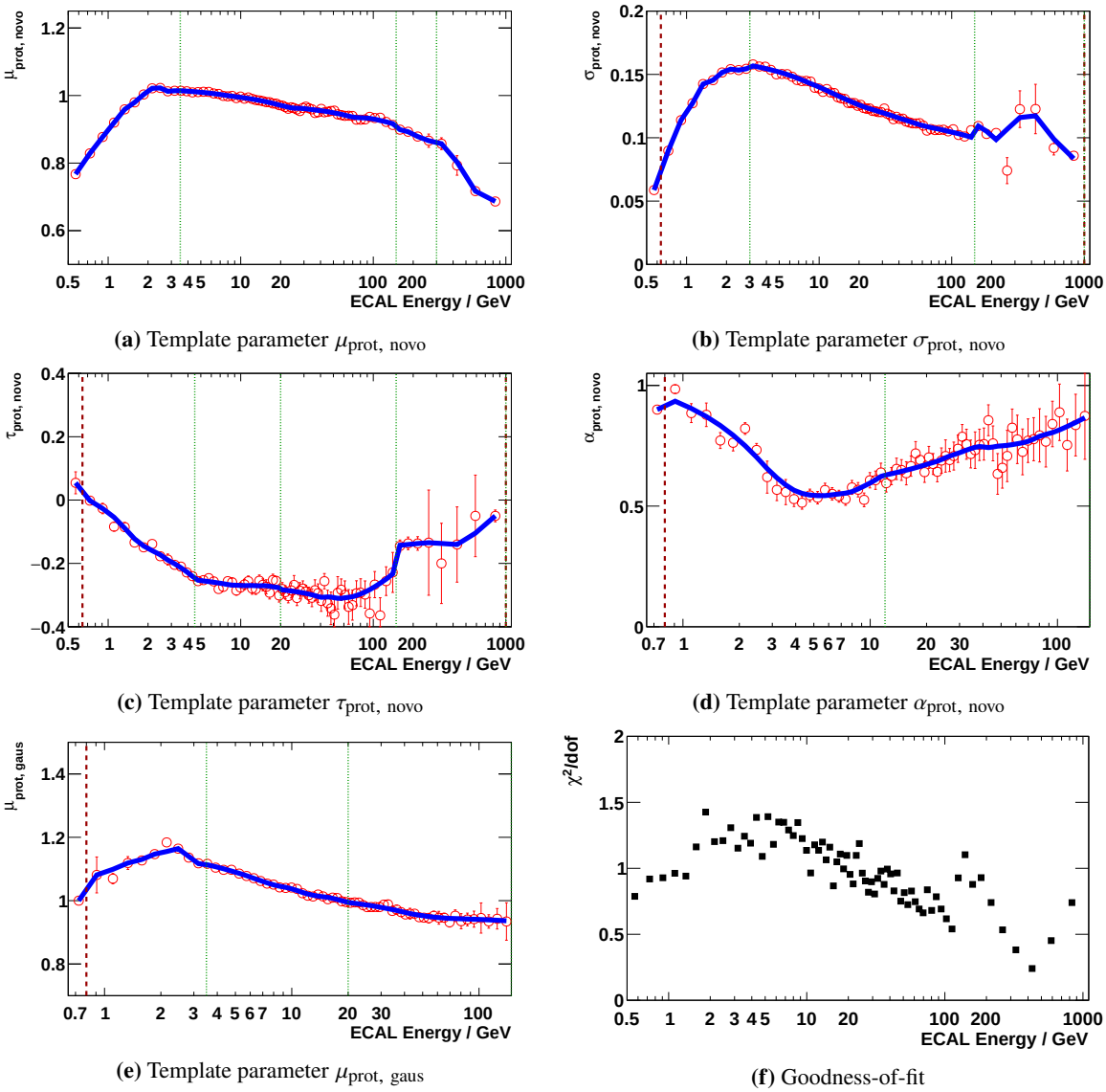

(a) Template parameter $\mu_{\text{prot, novo}}$

(b) Template parameter $\sigma_{\text{prot, novo}}$

(c) Template parameter $\tau_{\text{prot, novo}}$

(d) Template parameter $\alpha_{\text{prot, novo}}$

(e) Template parameter $\mu_{\text{prot, gaus}}$

(f) Goodness-of-fit

Figure A.19: Analytical TRD template parameters describing the evolution of the proton template as function of energy for the multi-tracks sample.

For the multi-tracks sample, Fig. A.19(f), a tendency towards larger χ^2/dof values approaching lower energies is visible, due to the absence of the $\delta_{\sigma\,\text{prot, gaus}}$ parameter. It was shown in Section 4.4.5

that this bias is gone when applying these templates to the multi-tracks data sample, when extracting the final electron and positron counts. The systematic effect at low energies can be safely ignored.

A.4 Construction of two-dimensional TRD / CCMVA templates (multi-tracks sample)

Figure A.20 shows the two-dimensional templates for the multi-tracks sample in an example energy bin, which were omitted in the introduction in Section 4.4.3.

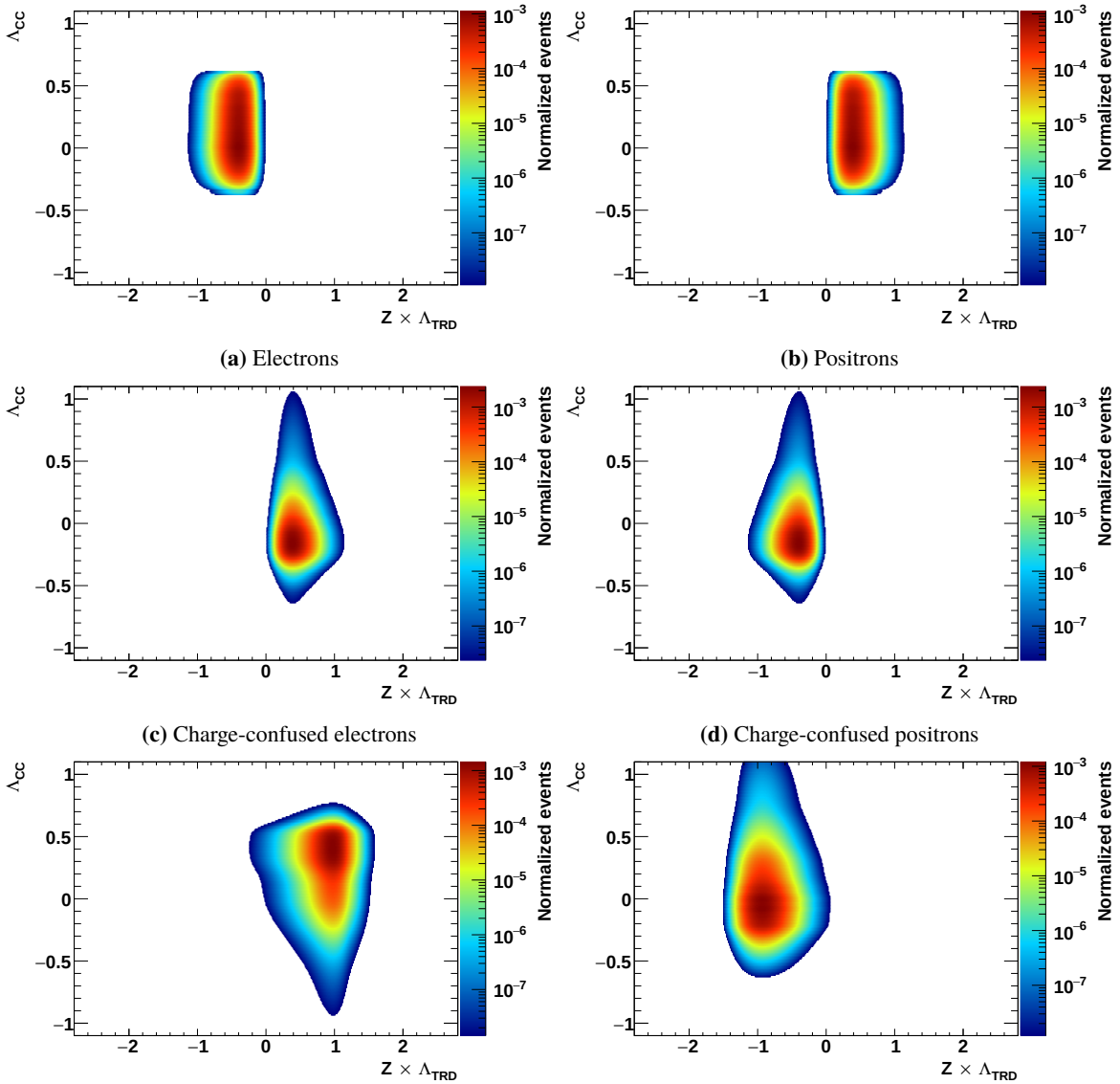

(a) Electrons **(b)** Positrons

(c) Charge-confused electrons **(d)** Charge-confused positrons

(e) Protons **(f)** Charge-confused protons

Figure A.20: Two-dimensional TRD / CCMVA templates in the energy bin 17.98 – 18.99 GeV for the multi-tracks sample.

A.5 Tag cut definitions

In the following a list of all tag sample selection cuts that are used in the analysis is presented. The quantities that appear in the cut conditions refer to branch names in the ROOT [Brun1997] analysis tree used in this work to perform the data analysis.

1. **NegativeRigidityTag**
   - R < 0
     The reconstructed rigidity of the selected tracker track must be negative.
2. **HasTrackerTag**
   - TrkNumTracks = 1
     There must be only one reconstructed tracker track in the event.
   - R ≠ 0
     The reconstructed rigidity must be non-zero.
   - TrkPattern = 1 or TrkPattern = 2
     The tracker track must have a hit in Layer 1 and Layer 9, or the tracker track must have a hit in Layer 2 and Layer 9.
   - 0.5 e < TrkCharge < 1.8 e
     The tracker charge must be compatible with a $Z = 1$ particle.
   - 0.01 < TrackerChiSquareY < 25
     The tracker track goodness-of-fit in Y projection must be in a reasonable range, to filter out wrongly reconstructed tracks.
   - Tracker track must point to the ECAL
     The tracker track extrapolation needs to go through the ECAL.
3. **HasTofTag**
   - 0.5 e < TofUpperCharge < 1.8 e
     The upper TOF charge must be compatible with a $Z = 1$ particle.
   - 0.8 < TofBeta < 1.25
     The reconstructed TOF velocity must be compatible with a relativistic particle.
4. **HasTrdTag**
   - TrdActiveLayers > 15
     At least 15 layers in the TRD must have a hit.
   - $\mathcal{L}_{e^-/\mathrm{He}} > 0.8$
     Helium identified using the TRD must be rejected.
5. **HasEcalTag**
   - Λ_{ECAL} > -1
     The ECAL estimator measurement must be available.

6. **EcalElectronTag**
   - E/R > 0.5
     If both a rigidity and ECAL energy measurement is available, it must be larger than 0.5.
   - EcalShowerDirectionZ > 0
     The ECAL shower must be down-going.
   - $\Lambda_{\mathrm{ECAL}} > 0$
     The ECAL estimator measurement must be electron like.
7. **TofElectronTag**
   - $|1 - 1/\mathrm{TofBeta}| < 0.15$
     The reconstructed TOF velocity must be compatible with a relativistic $e^{\pm}$.
8. **TrdElectronTag**
   - $\Lambda_{\mathrm{TRD}} < 0.75$
     TRD selection of electrons using the log-likelihood ratio estimator.
9. **TrdHasUsefulSegmentsInBothProjectionsTag**
   Note: A TRD segment refers to a partially reconstructed TRD track in two dimensions, utilizing only hits of one projection.
   - Any of the segments in X-Z projection must span at least 6 layers.
   - Any of the segments in Y-Z projection must span at least 4 layers.
   - The first hit of any of the segments in Y-Z projection must be in the upper half of the TRD.
   - The last hit of any of the segments in Y-Z projection must be in the lower half of the TRD.
10. **TrdHasUsefulTrackTag**
    Note: A TRD track is composed from a single X-Z segment and a single Y-Z segment.
    - The TRD track in X-Z projection must span at least 6 layers.
    - The TRD track in Y-Z projection must span at least 4 layers.
    - The first hit of the TRD track must be in the upper half of the TRD.
    - The last hit of the TRD track must be in the lower half of the TRD.
11. **TrdActiveLayersTag**
    - Energy-dependent TrdActiveLayers cut
      Same definition as in the corresponding selection cut (Section 4.3.3 - Item 3).
12. **TrdNoHeliumTag**
    - $\mathcal{L}_{e^-/\mathrm{He}} > 0.8$
      Helium identified using the TRD must be rejected.
13. **TofBetaTag**
    - 0.8 < TofBeta < 1.25
      The reconstructed TOF velocity must be compatible with a relativistic particle.

14. **TofNumberOfLayersTag**
    - TofNumberOfLayers > 2
      At least 3 out of the 4 TOF layers must have a reconstructed cluster.

15. **TofTimeDifferenceTag**
    - 0 ns < TofDeltaT < 20 ns
      The particle passage from upper to lower TOF must not last longer than 20 ns. A relativistic $e^{\pm}$ takes on average 4.3 ns for the passage. This cut only rejects wrongly associated clusters, which might lead to a wrong time difference measurement.

16. **TrackerChargeTag**
    - 0.5 e < TrkCharge < 1.8 e
      The tracker charge must be compatible with a $Z = 1$ particle.

17. **TrackerPatternTag**
    - $1 \leq$ TrkPattern ≤ 4
      Same definition as in the corresponding selection cut (Section 4.3.3 - Item 5).

18. **ElectronUpperEnergyOverRigidityTag**
    - E/R < 10
      This matches the upper cut value of the corresponding $e^{\pm}$ identification cut.

19. **EcalPreselectionTag**
    - |EcalCentreOfGravityX| < 32 cm and |EcalCentreOfGravityY| < 32 cm
      The centre-of-gravity of the reconstructed shower is at least 1.5 Molière radii away from the borders of the ECAL.

20. **EcalTrdPreselectionTag**
    - All cuts from **TrdHasUsefulTrackTag / EcalPreselectionTag** (Items 10 and 19)
    - TRD track / ECAL shower matching
      The TRD track extrapolated to the ECAL Z position must be spatially compatible with the reconstructed ECAL shower centre-of-gravity in X-Z and Y-Z projection.

A.6 Tag sample selection cuts

A.6.1 Tag cuts used for the “At least one useful TRD track” cut

The tag sample for the **“At least one useful TRD track”** cut (Section 4.3.2 - Item 2) is prepared using following cuts:

- **All detector quality cuts** (Section 4.3.1)
- **NegativeRigidityTag** (Appendix A.5 - Item 1)
- **HasTrackerTag** (Appendix A.5 - Item 2)

- **HasTofTag** (Appendix A.5 - Item 3)
- **HasEcalTag** (Appendix A.5 - Item 5)
- **EcalElectronTag** (Appendix A.5 - Item 6)
- **TofElectronTag** (Appendix A.5 - Item 7)
- **TrdHasUsefulSegmentsInBothProjectionsTag** (Appendix A.5 - Item 9)
- **EcalPreselectionTag** (Appendix A.5 - Item 19)

A.6.2 Tag cuts used for the "At least one useful TOF cluster combination" cut

The tag sample for the **"At least one useful TOF cluster combination"** cut (Section 4.3.2 - Item 3) is prepared using following cuts:

- **All detector quality cuts** (Section 4.3.1)
- **NegativeRigidityTag** (Appendix A.5 - Item 1)
- **HasTrackerTag** (Appendix A.5 - Item 2)
- **HasTrdTag** (Appendix A.5 - Item 4)
- **HasEcalTag** (Appendix A.5 - Item 5)
- **EcalElectronTag** (Appendix A.5 - Item 6)
- **TrdElectronTag** (Appendix A.5 - Item 8)
- **TofNumberOfLayersTag** (Appendix A.5 - Item 14)
- **TofTimeDifferenceTag** (Appendix A.5 - Item 15)
- **EcalTrdPreselectionTag** (Appendix A.5 - Item 20)

A.6.3 Tag cuts used for the "Upper TOF charge" cut

The tag sample for the **"Upper TOF charge"** cut (Section 4.3.3 - Item 2) is prepared using following cuts:

- **All detector quality cuts** (Section 4.3.1)
- **All preselection cuts** (Section 4.3.2)
- **NegativeRigidityTag** (Appendix A.5 - Item 1)
- **EcalElectronTag** (Appendix A.5 - Item 6)
- **TrdElectronTag** (Appendix A.5 - Item 8)

- **TrdNoHeliumTag** (Appendix A.5 - Item 12)
- **TofBetaTag** (Appendix A.5 - Item 13)
- **TrackerChargeTag** (Appendix A.5 - Item 16)

A.6.4 Tag cuts used for the "Enough active layers in TRD" cut

The tag sample for the **"Enough active layers in TRD"** cut (Section 4.3.3 - Item 3) is prepared using following cuts:

- **All detector quality cuts** (Section 4.3.1)
- **All preselection cuts** (Section 4.3.2)
- **NegativeRigidityTag** (Appendix A.5 - Item 1)
- **HasTofTag** (Appendix A.5 - Item 3)
- **EcalElectronTag** (Appendix A.5 - Item 6)
- **TrdElectronTag** (Appendix A.5 - Item 8)
- **TrackerChargeTag** (Appendix A.5 - Item 16)

A.6.5 Tag cuts used for the "Tracker track goodness-of-fit in Y-projection" cut

The tag sample for the **"Tracker track goodness-of-fit in Y-projection"** cut (Section 4.3.3 - Item 7) is prepared using following cuts:

- **All detector quality cuts** (Section 4.3.1)
- **All preselection cuts** (Section 4.3.2)
- **NegativeRigidityTag** (Appendix A.5 - Item 1)
- **HasTofTag** (Appendix A.5 - Item 3)
- **EcalElectronTag** (Appendix A.5 - Item 6)
- **TrdElectronTag** (Appendix A.5 - Item 8)
- **TrdActiveLayersTag** (Appendix A.5 - Item 11)
- **TrackerChargeTag** (Appendix A.5 - Item 16)
- **TrackerPatternTag** (Appendix A.5 - Item 17)

A.6.6 Tag cuts used for the "Energy ↔ rigidity matching" cut

The tag sample for the **"Energy ↔ rigidity matching"** cut (Section 4.3.4 - Item 1) is prepared using following cuts:

- **All detector quality cuts** (Section 4.3.1)
- **All preselection cuts** (Section 4.3.2)
- **All selection cuts** (Section 4.3.3)
- **NegativeRigidityTag** (Appendix A.5 - Item 1)
- **EcalElectronTag** (Appendix A.5 - Item 6)
- **TrdElectronTag** (Appendix A.5 - Item 8)

A.6.7 Tag cuts used for the "Tracker ↔ ECAL matching in X-projection" cut

The tag sample for the **"Tracker ↔ ECAL matching in X-projection"** cut (Section 4.3.4 - Item 3) is prepared using following cuts:

- **All detector quality cuts** (Section 4.3.1)
- **All preselection cuts** (Section 4.3.2)
- **All selection cuts** (Section 4.3.3)
- **NegativeRigidityTag** (Appendix A.5 - Item 1)
- **EcalElectronTag** (Appendix A.5 - Item 6)
- **TrdElectronTag** (Appendix A.5 - Item 8)
- **ElectronUpperEnergyOverRigidityTag** (Appendix A.5 - Item 18)

A.7 Iterative Bayesian unfolding method

Mathematically the unfolding process can be written as

$$\hat{\mathbf{n}} = U(\mathbf{n}; \boldsymbol{\theta}), \tag{A.1}$$

where $\mathbf{n}$ denotes the observed distribution in data, $\boldsymbol{\theta}$ the unfolding parameters and $\hat{\mathbf{n}}$ the unfolded, true distribution. The goal of the unfolding procedure is to find a suitable function U and its parameters. Different unfolding methods represent different choices of the U function. Most methods utilize a matrix to represent U and construct U from the migration matrix $\mathbf{M}$. The unfolding parameters $\boldsymbol{\theta}$ have to be estimated (e.g. regularization parameter, number of iterations, etc.).

In this work, after comparing different unfolding methods, the **"iterative Bayesian unfolding"** [DAgostini1995] proposed by D'Agostini - implemented in RooUnfold [Adye2011] - was chosen, as it delivers stable results and a reasonable statistical uncertainty after unfolding.

The fundamental idea behind the iterative Bayesian unfolding method is based on the **Bayes theorem** [Bayes1763], which represents the relation of conditional probabilities:

$$P(A \mid B) = \frac{P(B \mid A) \cdot P(A)}{P(B)}, \tag{A.2}$$

where $P(A)$ and $P(B)$ denote the probabilities of observing event A and B independently of each other, $P(A \mid B)$ the likelihood of event A occurring given that B is true and $P(B \mid A)$ the likelihood of event B occurring given that A is true.

D'Agostini starts introducing his method by defining the terms "causes" and "effect": There are a n_C causes C_i which can produce *one* effect E. If we know the initial probability of the causes $P(C_i)$ and the conditional probability of the i^{th} cause to produce the effect $P(E \mid C_i)$ the Bayes formula can be written as

$$P(C_i \mid E) = \frac{P(E \mid C_i) \cdot P(C_i)}{P(E)} = \frac{P(E \mid C_i) \cdot P(C_i)}{\sum_{k=1}^{n_C} P(E \mid C_k) \cdot P(C_k)}. \tag{A.3}$$

$P(E)$ can be decomposed into conditional probabilities, as there are n_C disjoint causes that can lead to the same effect E, according to the "Law of total probability" [Kokoska2000].

If $n(E)$ events for effect E are observed, the expected number of events assignable to each of the causes C_i ($i = 1, \ldots, n_C$) is

$$\hat{n}(C_i) = P(C_i \mid E) \cdot n(E). \tag{A.4}$$

The outcome of a measurement may have multiple effects E_j ($j = 1, \ldots, n_E$) instead of a single effect E. For each of the effects the Eq. (A.3) holds. Therefore it can be generalized to n_E effects:

$$P(C_i \mid E_j) = \frac{P(E_j \mid C_i) \cdot P_0(C_i)}{\sum_{k=1}^{n_C} P(E_j \mid C_k) \cdot P_0(C_k)}, \tag{A.5}$$

where $P_0(C_i)$ denote the *initial* probabilities of the causes C_i.

After N_{obs} observations a distribution of frequencies is obtained: $\mathbf{n}(E) = \{n(E_1), \ldots, n(E_{n_E})\}$. The expected number of events to be assigned to each of the causes and only due to the observed events can be calculated, by applying Eq. (A.4) to each of the effects:

$$\hat{n}(C_i)|_{\text{obs}} = \sum_{j=1}^{n_E} P(C_i \mid E_j) \cdot n(E_j). \tag{A.6}$$

One needs to take into account that there is no need for each cause to produce at least one effect. The efficiency of detecting the cause C_i in any of the possible effects is given by:

$$\epsilon_i = \sum_{j=1}^{N_E} P(E_j \mid C_i). \tag{A.7}$$

Thus the best estimate of the true number of events is:

$$\hat{n}(C_i) = \frac{1}{\epsilon_i} \cdot \sum_{j=1}^{n_E} P(C_i \mid E_j) \cdot n(E_j). \tag{A.8}$$

Finally the true total number of events and the probabilities of the causes can be extracted:

$$\hat{N}_{\text{true}} = \sum_{i=1}^{n_C} \hat{n}(C_i), \qquad \hat{P}(C_i) = \frac{\hat{n}(C_i)}{\hat{N}_{\text{true}}} \tag{A.9}$$

From Eq. (A.5) it is evident, that the conditional probability $P(C_i \mid E_j)$ depends on the choice of the *initial* probabilities of the causes $P_0(C_i)$. Thus $\hat{n}(C_i)$ and $\hat{P}(C_i)$ also depend on the *initial* probabilities.

If $n_0(C_i) = P_0(C_i) \cdot N_{\text{obs}}$ is not compatible with $\hat{n}(C_i)$, the choice of the *initial* probabilities $P_0(C_i)$ was incorrect. This leads to an **iterative** procedure: $P_0(C_i)$ needs to be refined, by replacing it with $\hat{P}(C_i)$ from Eq. (A.9) and the whole procedure needs to be repeated, until $\hat{n}(C_i)$ agrees with $n_0(C_i)$. If that is the case the true distribution $\hat{n}(C_i)$ was found and the unfolding process is finished.

Coming back to Eq. (A.1), the unfolding function U - suitable of transforming the measured distribution into the true distribution - can be derived. By reformulating Eq. (A.8) the unfolding function U can be identified as matrix $\mathbf{U}$:

$$\begin{aligned}
\hat{n}(C_i) &= \frac{1}{\epsilon_i} \cdot \sum_{j=1}^{n_E} P(C_i \mid E_j) \cdot n(E_j) \\
&\overset{(A.7)}{=} \sum_{j=1}^{n_E} \frac{P(C_i \mid E_j)}{\sum_{k=1}^{N_E} P(E_k \mid C_i)} \cdot n(E_j) \\
&\overset{(A.5)}{=} \sum_{j=1}^{n_E} \underbrace{\frac{P(E_j \mid C_i) \cdot P_0(C_i)}{\left(\sum_{k=1}^{N_E} P(E_k \mid C_i)\right) \cdot \left(\sum_{k=1}^{n_C} P(E_j \mid C_k) \cdot P_0(C_k)\right)}}_{:=\mathbf{U}_{ij}} \cdot n(E_j).
\end{aligned} \tag{A.10}$$

This leads to a simple formulation in matrix style:

$$\hat{\mathbf{n}} = \mathbf{U} \cdot \mathbf{n}.$$

There is only one unfolding parameter $\boldsymbol{\theta}$ for the iterative Bayesian unfolding: the number of iterations N_{iter} needed until convergence is reached. There is no a-priori information how many iterations are sufficient – it depends on the problem. Thus the number of iterations needs to be varied and after each iteration the results should be carefully checked. A high number of iterations might lead to an unfolded distribution that heavily fluctuates around the true distribution, which is not the case for the unfolding of the event counts in this work.

A.8 Time-dependent charge-confusion

Figure A.21 shows the charge-confusion as function of time for an example energy bin of the time-dependent analysis for the all-tracks sample. For all energy bins the average of the charge-confusion value is compatible with the time-averaged charge-confusion and thus $f_{\mathrm{cc},\,i}(E) = f_{\mathrm{cc}}(E)$.

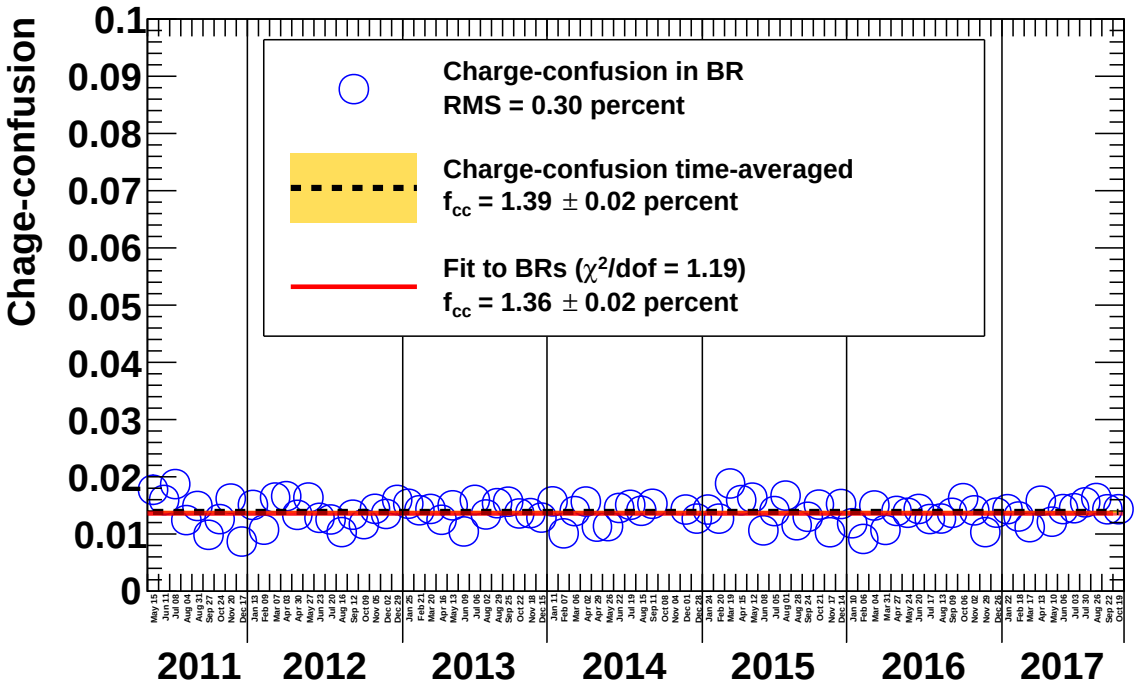

Figure A.21: Time-dependent charge-confusion for the energy bin 9.62 – 10.32 GeV. The x-axis spans 88 Bartels rotations and each bin label denotes the date when the Bartels rotation started (in UTC). The blue symbols show the charge-confusion for the all-tracks sample in the specific energy bin as function of time. The black dashed line shows the time-averaged charge-confusion for comparison. The red line shows a fit of a constant to the red symbols, yielding an acceptable $\chi^2/\mathrm{dof} = 1.19$ value.

A.9 Time-dependent TRD templates (multi-tracks sample)

In Section 4.9.5 the time dependence of the TRD templates was shown for the single-track sample. The results for the multi-tracks samples is shown in the following: Figure A.22 shows the $\mu_{\mathrm{elec,\ novo}}$ parameter, Fig. A.23 for the $\mu_{\mathrm{prot,\ novo}}$ parameter.

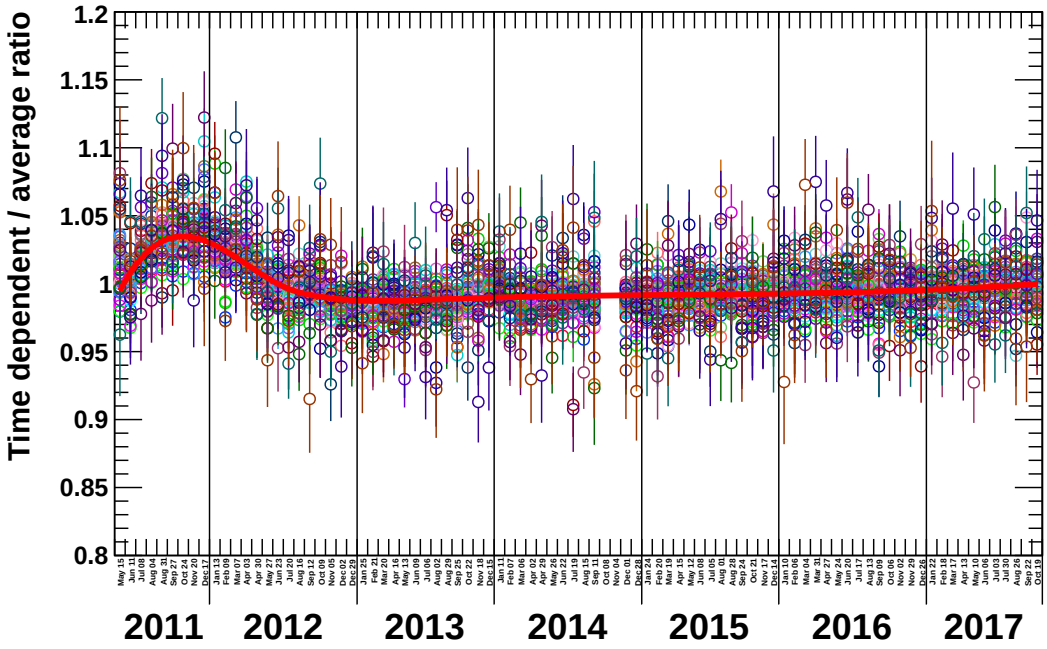

Figure A.22: Time-dependence of the $\mu_{\text{elec, novo}}$ parameter for all energy bins - 0.65 – 52.33 GeV - in the time-dependent analysis for the multi-tracks sample. Each energy bin is represented by a different color. The filled red line denote the result of a spline fit, simultaneously to all data points, describing the average time-dependence of the $\mu_{\text{elec, novo}}$ parameter.

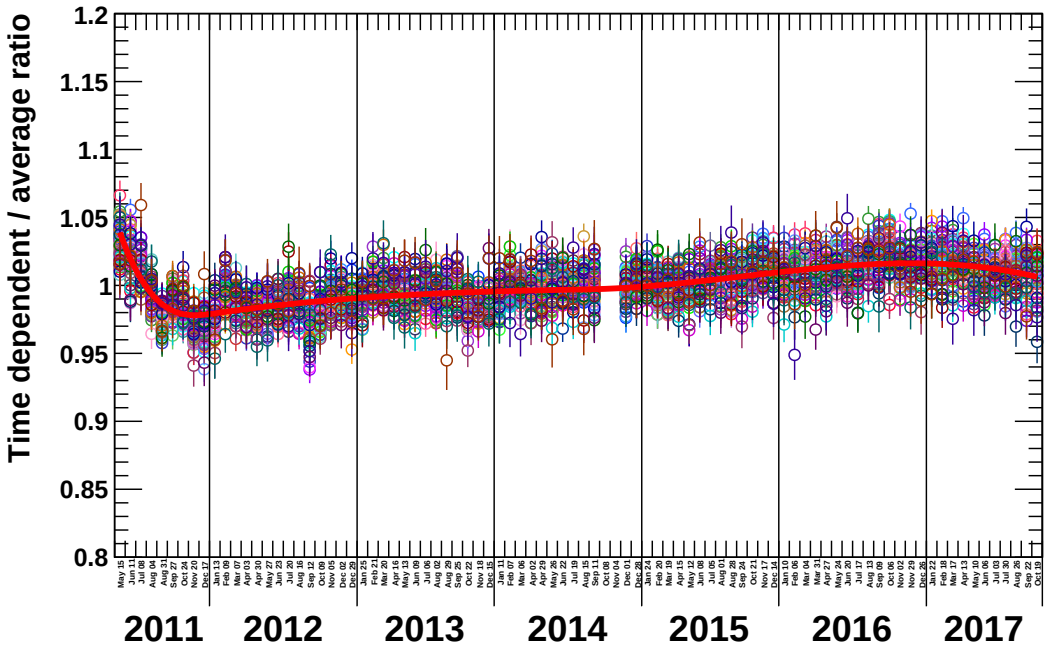

Figure A.23: Time-dependence of the $\mu_{\text{prot, novo}}$ parameter for all energy bins - 0.65 – 52.33 GeV - in the time-dependent analysis for the multi-tracks sample.

The time-dependence of the three remaining parameters - $\mu_{\text{ccprot, novo}}$, $\sigma_{\text{elec, novo}}$ and $\sigma_{\text{prot, novo}}$, is shown in Figs. A.24 to A.26 in selected energy bins, as example, for the multi-tracks sample.

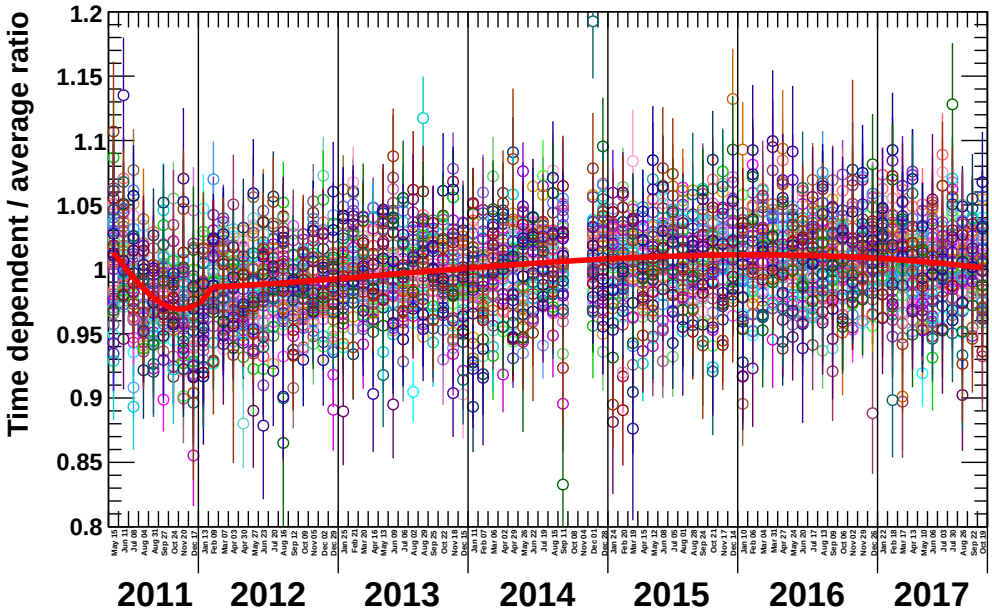

Figure A.24: Time-dependence of the $\mu_{\text{ccprot, novo}}$ parameter for selected energy bins (1.22 – 52.33 GeV), as example, in the time-dependent analysis for the multi-tracks sample.

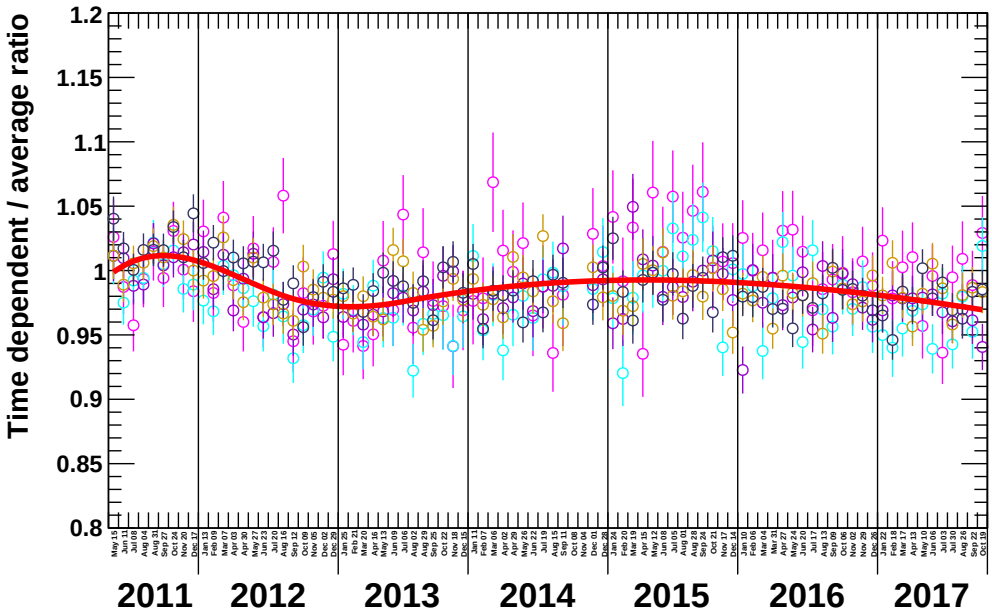

Figure A.25: Time-dependence of the $\sigma_{\text{elec, novo}}$ parameter for selected energy bins (1.46 – 3.00 GeV), as example, in the time-dependent analysis for the multi-tracks sample.

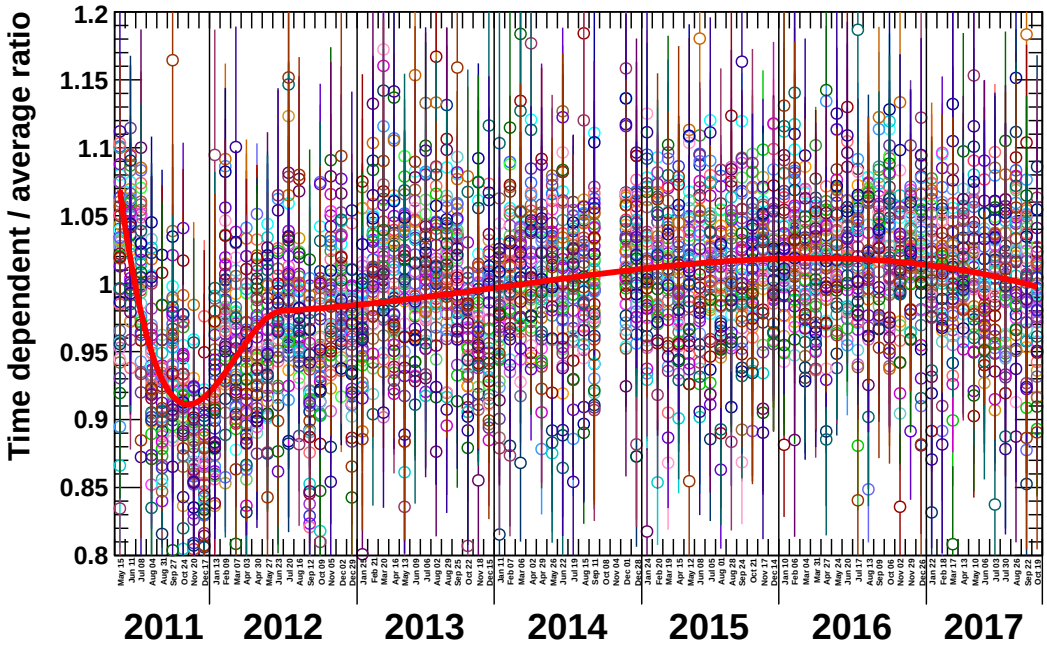

Figure A.26: Time-dependence of the $\sigma_{\text{prot, novo}}$ parameter for selected energy bins (1.72 – 52.33 GeV), as example, in the time-dependent analysis for the multi-tracks sample.

APPENDIX B

Appendix - Results

B.1 Energy scale

It is important to note that the ECAL shower reconstruction used in this work is different compared to the latest AMS-02 publications covering the high-energy electrons [Aguilar2019a] and positrons [Aguilar2019b]. In this work the conventional ECAL shower reconstruction was used, as for the first electron and positron flux publications [Aguilar2014a], but with an improved Top-Of-Instrument correction derived in a dedicated study. This energy scale will be referred to as "Aachen energy scale" in the following.

The improved ECAL shower reconstruction is described in detail in [Kounine2017a] and allows to exploit even higher energies, due to a better positron/proton separation and an improved energy resolution. In the following it will be referred to as "MIT energy scale".

Both ECAL shower reconstruction methods yield slightly different reconstructed energies for the same events, compatible with the quoted absolute energy scale uncertainty (see Ref. [Aguilar2014a]). For a fair comparison of this work with the recent published results, the reconstructed energy scale in this work has to match - on average - the results of improved ECAL shower reconstruction. To achieve this goal the MIT and the Aachen energy scale were compared on the electron Monte-Carlo simulation and migration matrices were obtained using the MIT energy scale and the Aachen energy scale sharing the same true energy axis. By studying the differences between both migration matrices, an effective migration matrix can be deduced, assuring that the unfolded flux is identical when using either the Aachen energy scale and the effective migration matrix or the MIT energy scale and the unmodified migration matrix.

For technical reasons the MIT energy scale and the Aachen energy scale could only be compared on the electron Monte-Carlo simulation and not on the whole time period for the ISS data. As the MIT energy scale is unavailable for the whole ISS time period in this work, it could not be used for the analysis. However it will be shown that the fluxes derived with the Aachen energy scale, unfolded with the effective migration matrix, are fully compatible with the published results, that exclusively use the MIT energy scale. Thus using the Aachen energy scale is acceptable, with the only drawback that energies higher than 1 TeV cannot be exploited.

Figure B.1 shows the average difference of both reconstructed energy scales as function of the true energy. The obtained average correction (red line) is fully compatible with the quoted absolute energy scale uncertainties, limited by the knowledge of AMS-02 beam test.

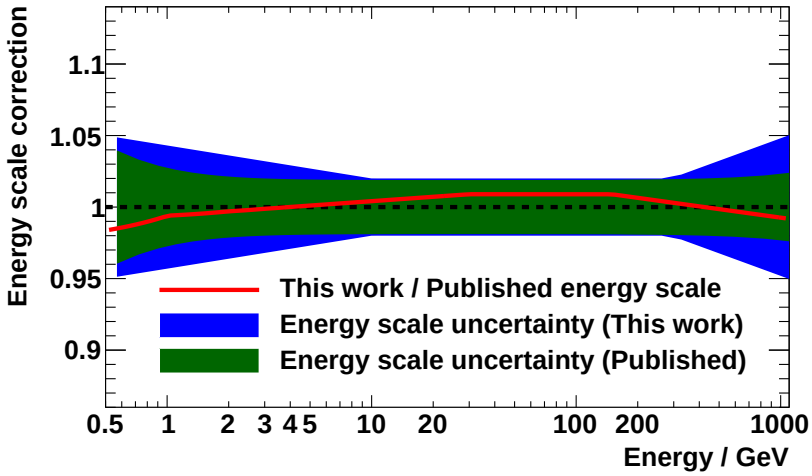

Figure B.1: Correction applied to the Aachen energy scale used in this work to match the MIT energy scale used in recent AMS-02 electron and positron flux publications [Aguilar2019a; Aguilar2019b]. The red line shows the necessary energy scale correction and the colored bands the energy scale uncertainties used for this work (blue band) and for recent publications (green band).

B.2 Time-averaged results

B.2.1 Comparison with published electron and positron fluxes

The electron flux derived in this work is compatible with the recently published AMS-02 electron flux [Aguilar2019a], as shown in Fig. B.2.

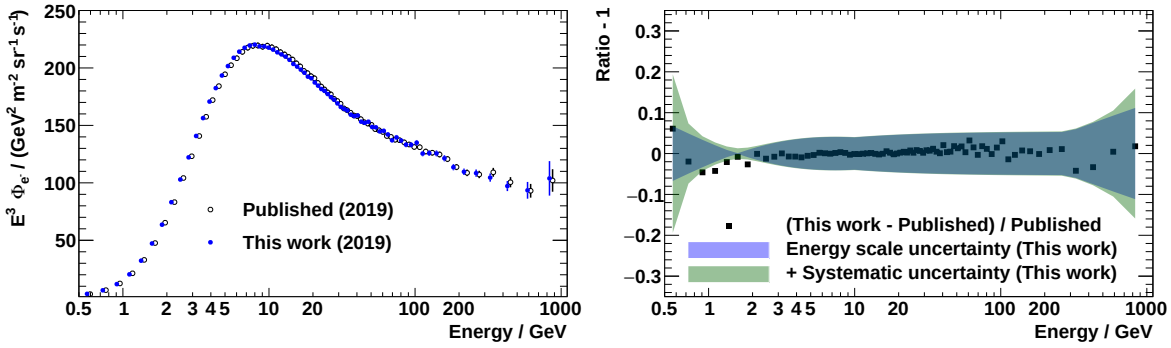

Figure B.2: Comparison of the electron flux derived in this work with the recent AMS-02 electron flux publication [Aguilar2019a]. To ease the comparison the published data points are shifted horizontally by 5 %. Within the quoted systematic uncertainties the results are compatible.

Figure B.3 shows a comparison of the total uncertainty of the electron flux derived in this work and the recently published AMS-02 electron flux [Aguilar2019a].

From 0.7 – 500 GeV the uncertainty of the electron flux derived in this work is smaller than the published result. The recent publication was optimized for the high-energy part and offers a smaller uncertainty in the high-energy regime than the flux derived in this work.

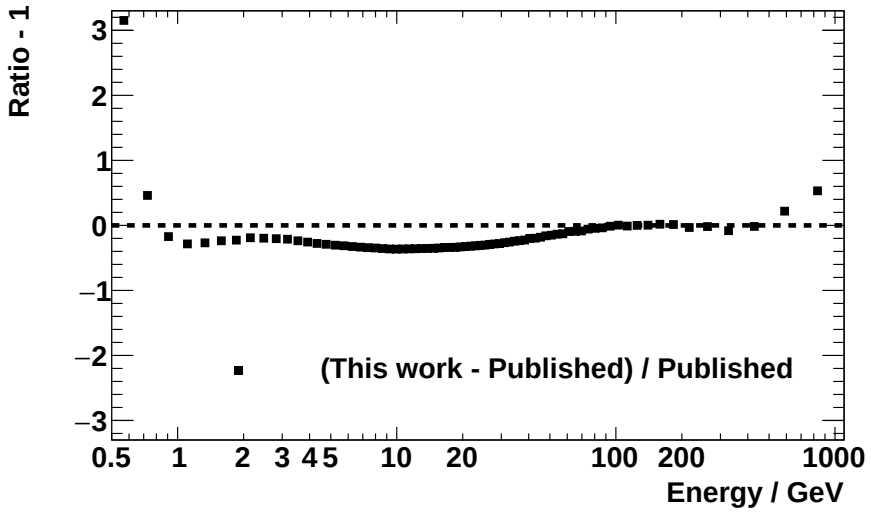

Figure B.3: Ratio of the total uncertainty of the electron flux derived in this work over the uncertainty of the recently published AMS-02 electron flux [Aguilar2019a].

The positron flux derived in this work is compatible with the recently published AMS-02 positron flux [Aguilar2019b], as shown in Fig. B.4.

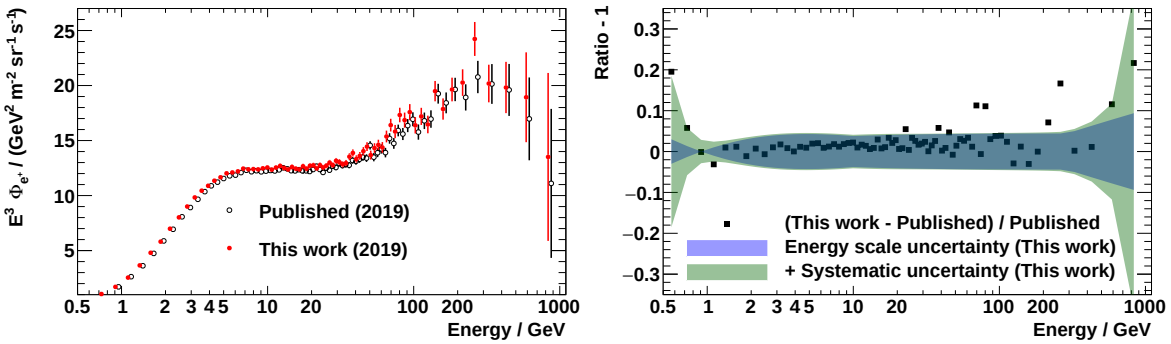

Figure B.4: Comparison of the positron flux derived in this work with the recent AMS-02 positron flux publication [Aguilar2019b]. To ease the comparison the published data points are shifted horizontally by 5 %. Within the quoted systematic uncertainties the results are compatible.

Figure B.5 shows a comparison of the total uncertainty of the positron flux derived in this work and the recently published AMS-02 positron flux [Aguilar2019b].

The uncertainty of the positron flux derived in this work is comparable to the published result above 20 GeV. Below that energy, the uncertainty on the published result is slightly smaller.

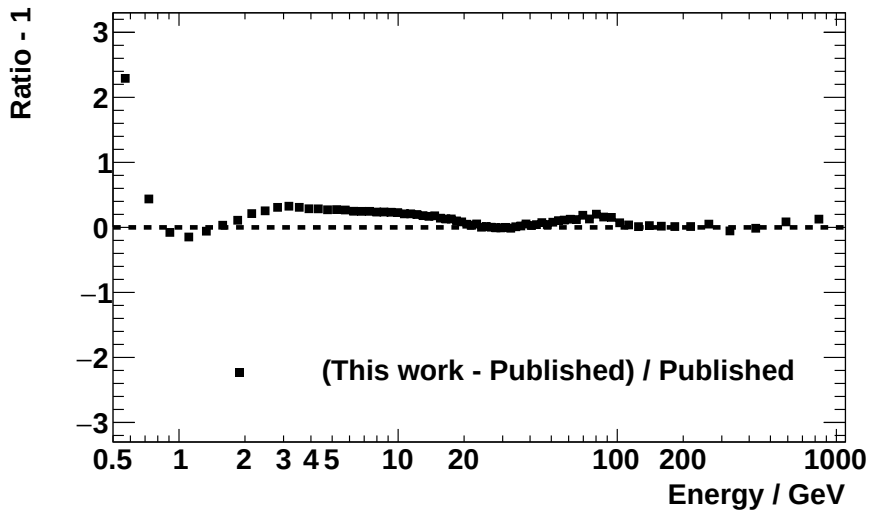

Figure B.5: Ratio of the total uncertainty of the positron flux derived in this work over the uncertainty of the recently published AMS-02 positron flux [Aguilar2019b].

B.2.2 Positron fraction

Figure B.6 shows the time-averaged positron fraction, determined by a dedicated analysis, using the single-track data sample, not computed from the fluxes themselves, which were derived using the all-tracks sample, as explained in Section 4.4.5.

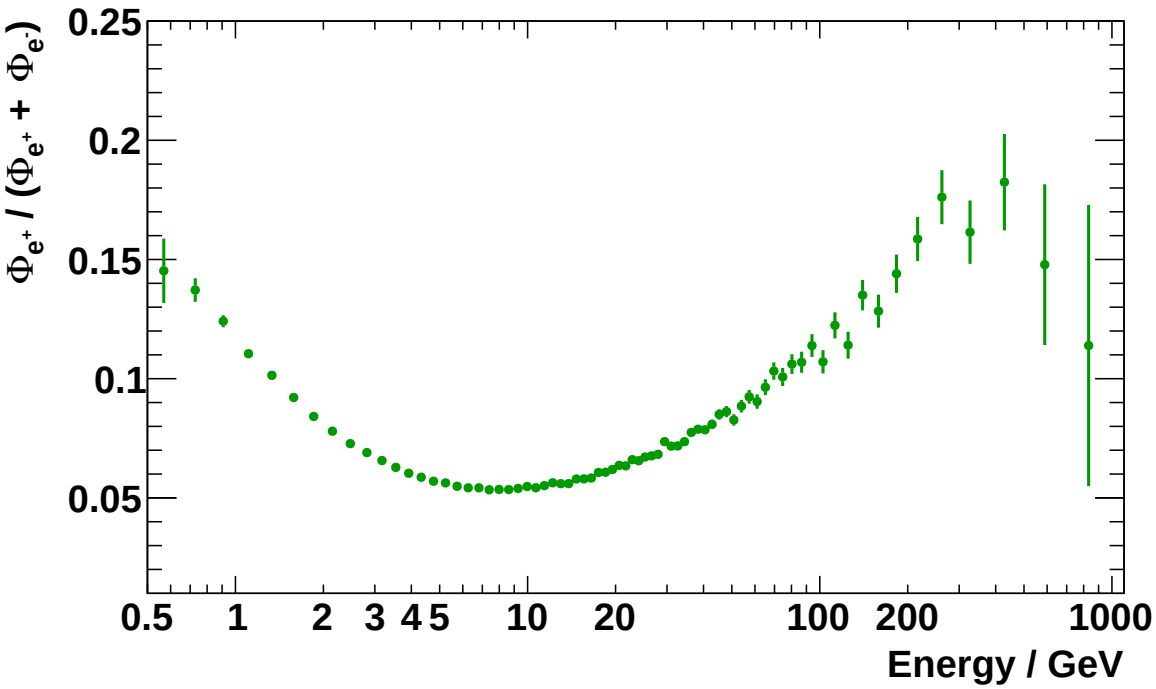

Figure B.6: The positron fraction measured by AMS-02.

The positron fraction derived in this work is compatible with the published positron fraction [Aguilar2019b] by the AMS-02 collaboration, as shown in Appendix B.2.3. Furthermore the positron fraction is consistent between the dedicated single-track analysis and the all-tracks flux analysis, as shown in Appendix B.2.5.

Figure B.7 shows a comparison of the positron fraction derived in this work with previous experiments. The positron fraction was measured by AMS-02 with unprecedented accuracy, up to the TeV regime.

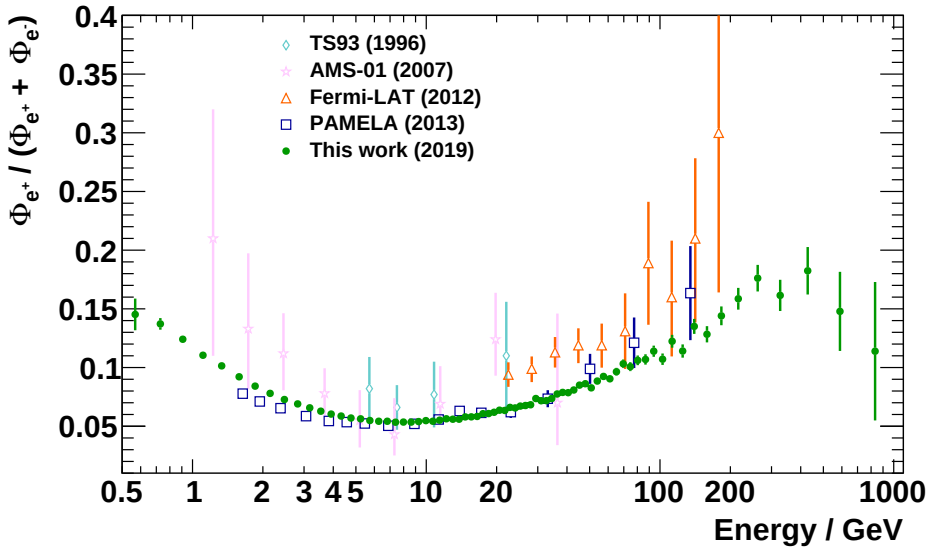

Figure B.7: Comparison of the positron fraction derived in this work with other experiments: TS-93 [Golden1996], AMS-01 [Alcaraz2000], Fermi-LAT [Ackermann2012] and PAMELA [Adriani2013].

Figure B.8 shows a breakdown of the total uncertainty into the statistical and systematic part.

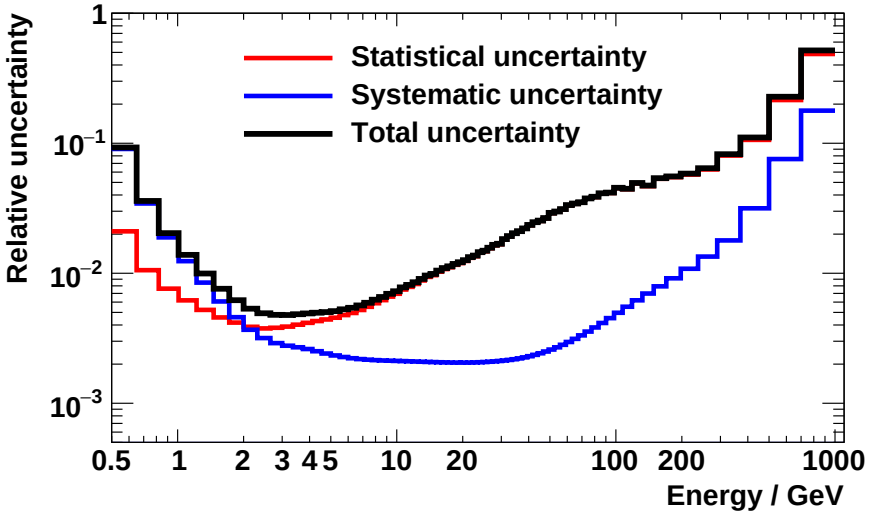

Figure B.8: Breakdown of the uncertainty of the positron fraction into a statistical and systematical part.

Above $\approx 2\,\mathrm{GeV}$ the statistical uncertainty dominates the uncertainty of the positron fraction measurement. Below this energy, the systematic uncertainty always exceeds the statistical uncertainty. See Section 4.8.5 for a decomposition of the systematic uncertainties.

B.2.3 Comparison with published positron fraction

The positron fraction derived in this work is compatible with the recently published AMS-02 positron fraction [Aguilar2019b], as shown in Fig. B.9.

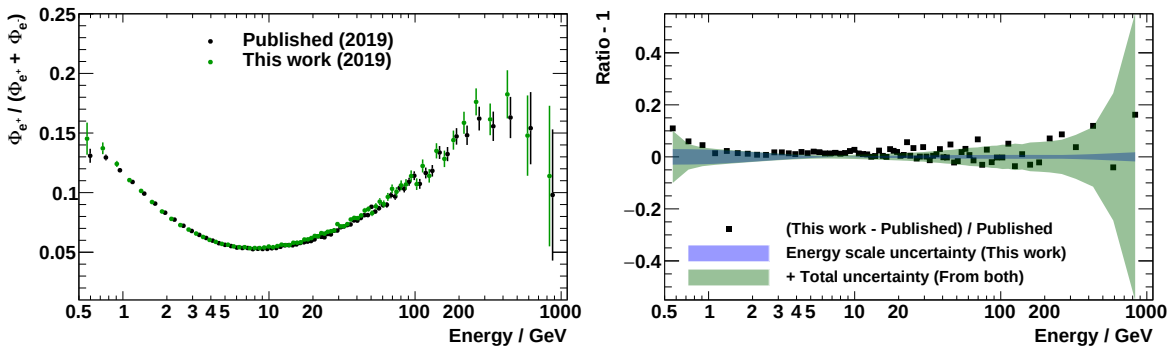

Figure B.9: Comparison of the positron fraction derived in this work with the recent AMS-02 positron fraction publication [Aguilar2019b]. To ease the comparison the published data points are shifted horizontally by 5 %. Within the quoted systematic uncertainties the results are compatible.

Over the whole energy range the uncertainty of the positron fraction derived in this work is larger than the published result[1].

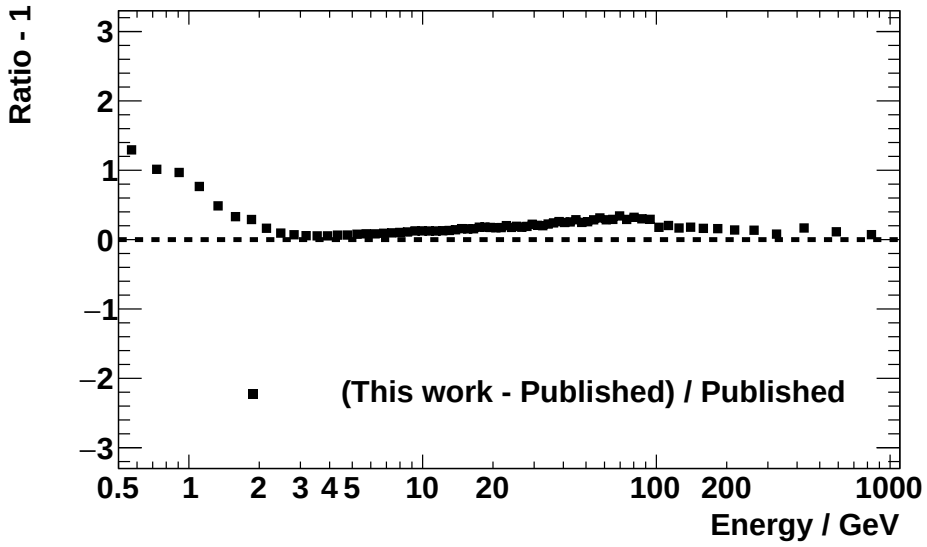

Figure B.10: Ratio of the total uncertainty of the positron fraction derived in this work over the uncertainty of the recently published AMS-02 positron fraction [Aguilar2019b].

[1] The analysis in this work was not tuned specifically for the positron fraction analysis.

B.2.4 Cross-check of the positron/electron ratio between flux / dedicated analysis

As cross-check the positron/electron ratio is also computed from the fluxes, to verify the consistency between the single-track and the all-tracks analyses. As shown in Fig. B.11 the agreement is good.

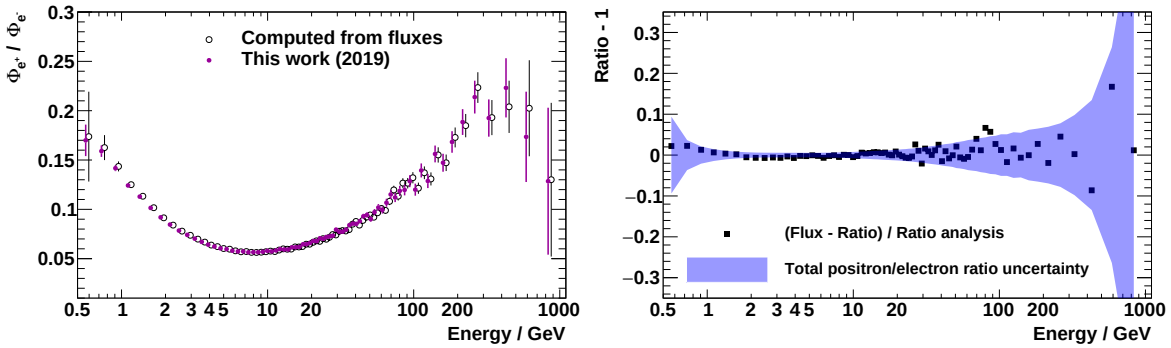

Figure B.11: Comparison of the positron/electron ratio derived using the single-track analysis with the ratio computed from the fluxes, that were derived from the all-track analysis. To ease the comparison the all-track analysis data points are shifted horizontally by 5 %. Within the quoted systematic uncertainties the results are compatible.

Figure B.12 shows the advantage of the single-track analysis for the positron/electron ratio derivation in the low-energy part. Above ≈ 20 GeV the flux analysis yields smaller uncertainties.

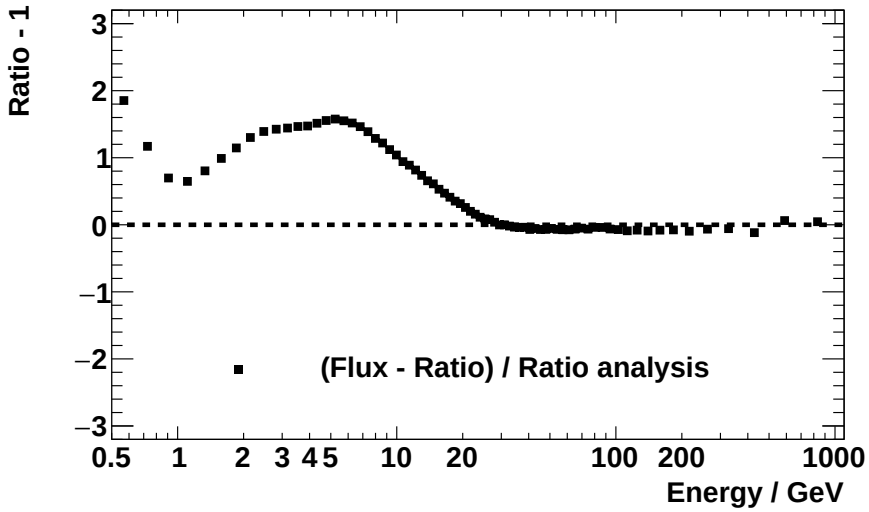

Figure B.12: Ratio of the total uncertainty of the positron/electron ratio derived using the single-track analysis over the positron/electron ratio derived from the all-track analysis.

B.2.5 Cross-check of the positron fraction between flux / dedicated analysis

As cross-check the positron fraction is also computed from the fluxes, to verify the consistency between the single-track and the all-tracks analyses. As shown in Fig. B.13 the agreement is good.

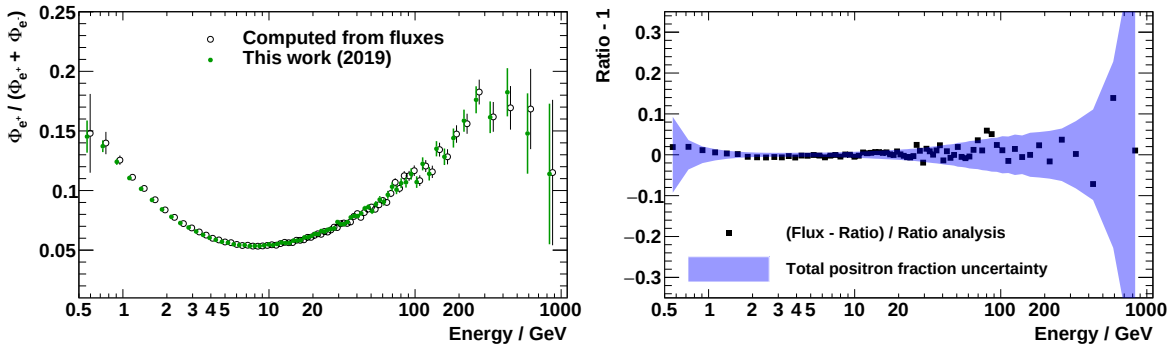

Figure B.13: Comparison of the positron fraction derived using the single-track analysis with the ratio computed from the fluxes, that were derived from the all-track analysis. To ease the comparison the all-track analysis data points are shifted horizontally by 5 %. Within the quoted systematic uncertainties the results are compatible.

Figure B.14 shows the advantage of the single-track analysis for the positron fraction derivation in the low-energy part. Above ≈ 20 GeV the flux analysis yields smaller uncertainties.

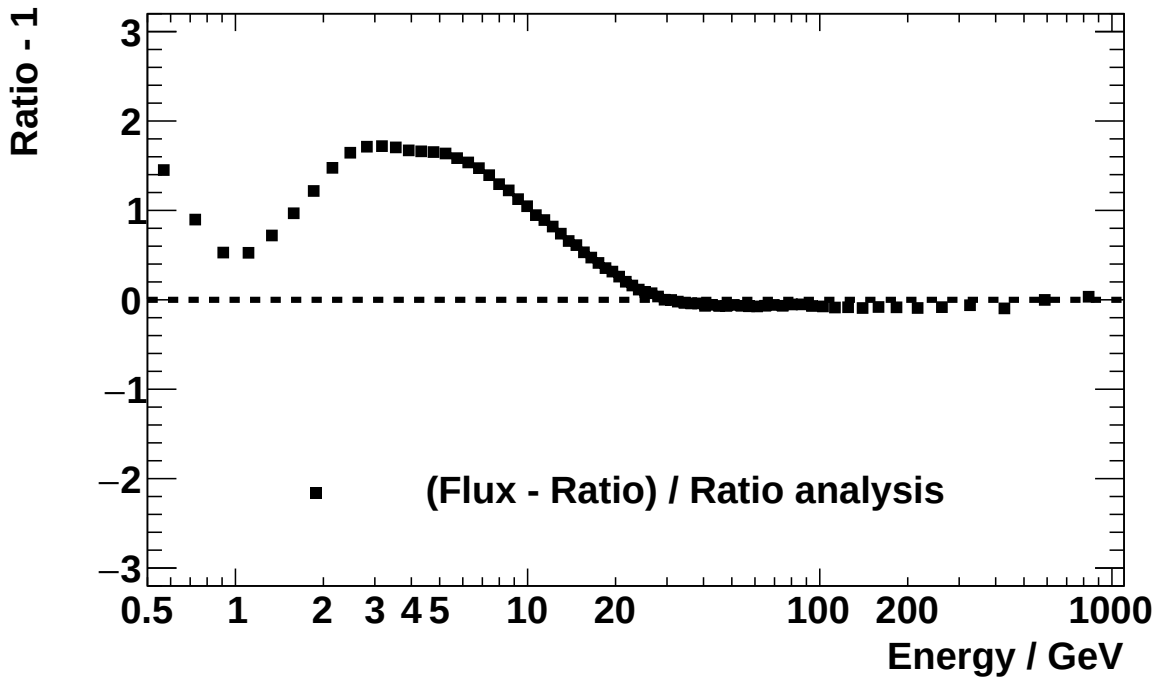

Figure B.14: Ratio of the total uncertainty of the positron fraction derived using the single-track analysis over the positron fraction derived from the all-track analysis.

B.3 Time-dependent results

B.3.1 Energy dependence of the electron spectral index

The energy dependence of the electron spectral index is shown in Fig. B.15.

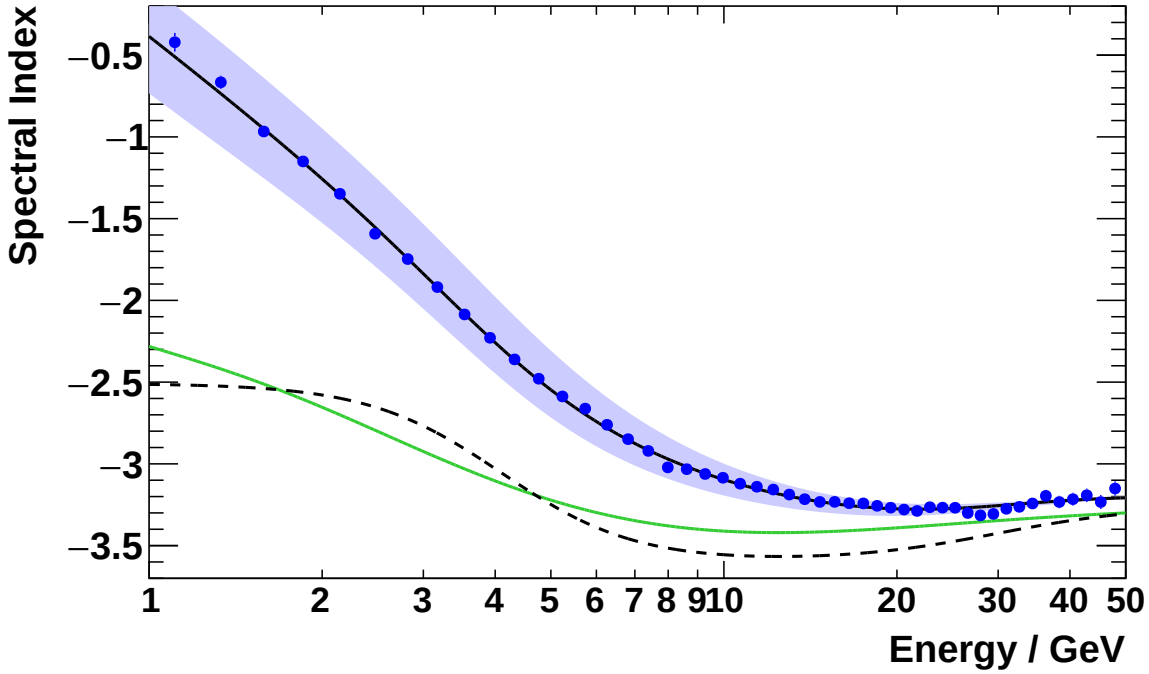

Figure B.15: Energy dependence of the electron spectral index $\gamma^{-}(E) = \mathrm{d}(\log \Phi_{e^-}(E))/\mathrm{d}(\log E)$ obtained in a model independent way (see Section 5.1.1) from the time averaged data and the spectral index obtained from the model described in Ref. [Cavasonza2017] fitted to the time-averaged electron flux data (solid black curve). The shaded band indicates the time-variation. The spectral index from this model without solar modulation (dashed black curve) clearly shows a break in the spectral index between 2 – 10 GeV. A recent model describing the local interstellar electron spectrum [Potgieter2015] is also shown (green curve).

B.3.2 Absence of structures in the positron flux

As described in Ref. [Aguilar2018], the model given in Ref. [Cavasonza2017] was fit to the data for each Bartels rotation independently, to search for fine structures in the energy dependence of the fluxes. The positron data show no additional structure, as shown in Appendix B.3.2.

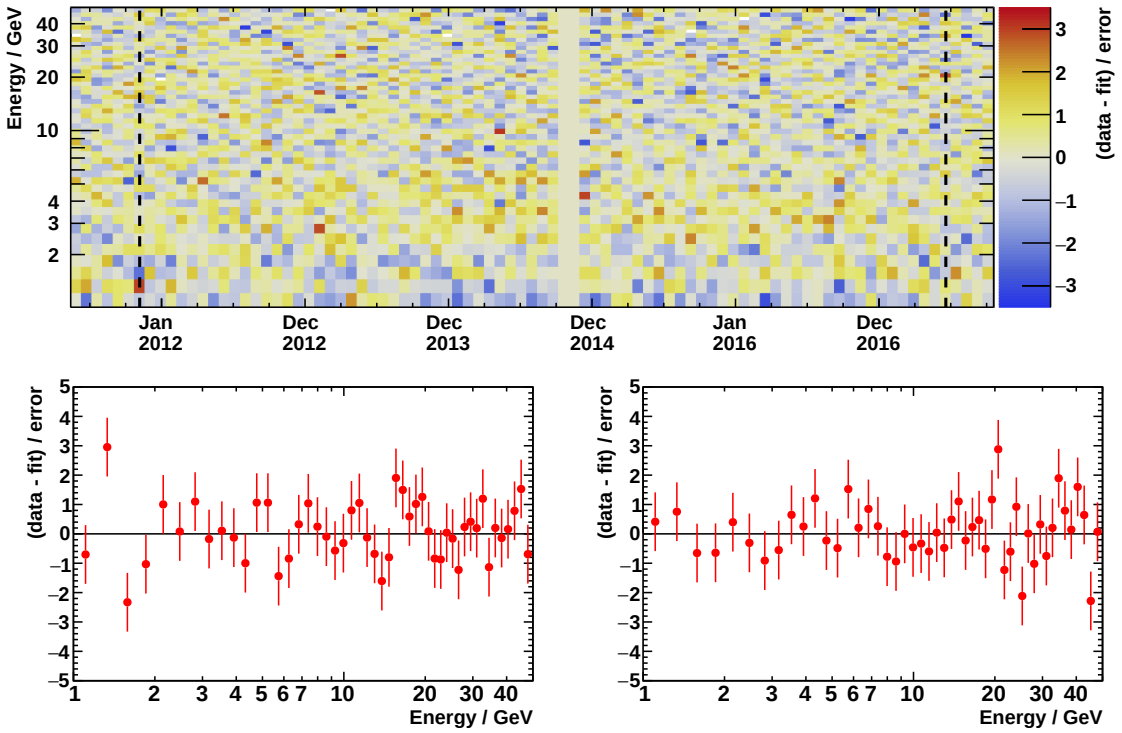

Figure B.16: For the positron flux, the difference between data and model [Cavasonza2017] fits normalized to the experimental uncertainties: for each Bartels Rotation as a function of energy (upper plot). The distribution for the positrons reveals no visible structures, emphasized for Bartels Rotation 2432 (lower left) and Bartels Rotation 2508 (lower right). The times for these two Bartels Rotations are indicated by the vertical dashed lines.

Bibliography

[Ahlen1994] S. Ahlen, V. Balebanov, R. Battiston et al., **An antimatter spectrometer in space**, Nuclear Instruments and Methods in Physics Research Section A: Accelerators, Spectrometers, Detectors and Associated Equipment **350** (1994) 351, DOI: 10.1016/0168-9002(94)91184-3 (cit. on pp. 13, 27).

[Alcaraz2000] J. Alcaraz, B. Alpat, G. Ambrosi et al., **Leptons in near earth orbit**, Physics Letters B **484** (2000) 10, DOI: 10.1016/S0370-2693(00)00588-8 (cit. on pp. 14, 156, 161, 211).

[Aguilar2007] M. Aguilar, J. Alcaraz, J. Allaby et al., **Cosmic-ray positron fraction measurement from 1 to 30 GeV with AMS-01**, Physics Letters B **646** (2007) 145, DOI: 10.1016/j.physletb.2007.01.024 (cit. on p. 14).

[Potgieter1993a] M. Potgieter, **Time-dependent cosmic-ray modulation: Role of drifts and interaction regions**, Advances in Space Research **13** (1993) 239, DOI: 10.1016/0273-1177(93)90415-8 (cit. on p. 14).

[Potgieter1993b] M. S. Potgieter, J. A. Le Roux, L. F. Burlaga and F. B. McDonald, **The role of merged interaction regions and drafts in the heliospheric modulation of cosmic rays beyond 20 AU - A computer simulation**, The Astrophysical Journal **403** (1993) 760, DOI: 10.1086/172247 (cit. on pp. 14, 174).

[Gopalswamy2003] N. Gopalswamy, A. Lara, S. Yashiro, S. Nunes and R. A. Howard, **Coronal mass ejection activity during solar cycle 23**, *Solar Variability as an Input to the Earth's Environment*, ed. by A. Wilson, vol. 535, ESA Special Publication, 2003 403 (cit. on pp. 14, 20).

[Ferreira2003] S. Ferreira and M. Potgieter, **Modulation over a 22-year cosmic ray cycle: On the tilt angles of the heliospheric current sheet**, Advances in Space Research **32** (2003), Heliosphere at Solar Maximum 657, DOI: 10.1016/S0273-1177(03)00360-0 (cit. on pp. 14, 20).

[Potgieter2013] M. S. Potgieter, **Solar Modulation of Cosmic Rays**, Living Reviews in Solar Physics **10** (2013) 3, DOI: 10.12942/lrsp-2013-3 (cit. on p. 14).

[Strong1998] A. W. Strong and I. V. Moskalenko, **Propagation of cosmic-ray nucleons in the galaxy**, The Astrophysical Journal **509** (1998) 212, DOI: 10.1086/306470 (cit. on pp. 14, 19).

[Maurin2001] D. Maurin, F. Donato, R. Taillet and P. Salati, **Cosmic Rays below$Z = 30$ in a Diffusion Model: New Constraints on Propagation Parameters**, The Astrophysical Journal **555** (2001) 585, DOI: 10.1086/321496 (cit. on p. 14).

[Potgieter2014] M. Potgieter, **The charge-sign dependent effect in the solar modulation of cosmic rays**, Advances in Space Research **53** (2014) 1415, DOI: 10.1016/j.asr.2013.04.015 (cit. on p. 14).

[Mathews2017] G. J. Mathews, M. Kusakabe and T. Kajino, **Introduction to Big Bang Nucleosynthesis and Modern Cosmology**, Int. J. Mod. Phys. **E26** (2017) 1741001, DOI: 10.1142/S0218301317410014 (cit. on p. 15).

[Akrami2018] Y. Akrami et al., **Planck 2018 results. I. Overview and the cosmological legacy of Planck** (2018), arXiv: 1807.06205 [astro-ph.CO] (cit. on pp. 15, 24).

[Longair2011] M. S. Longair, **High Energy Astrophysics**, 2011 (cit. on pp. 15, 23).

[Evoli2018] C. Evoli, **The Cosmic-Ray Energy Spectrum**, 2018, DOI: 10.5281/zenodo.2360277 (cit. on p. 16).

[Aab2017] A. Aab, P. Abreu, M. Aglietta et al., **Observation of a large-scale anisotropy in the arrival directions of cosmic rays above 8 × 1018 eV**, Science **357** (2017) 1266, DOI: 10.1126/science.aan4338 (cit. on p. 17).

[Bethe2003] H. A. Bethe, G. E. Brown and C.-H. Lee, **Formation and evolution of black holes in the Galaxy : selected papers with commentary**, 2003, DOI: 10.1142/5142 (cit. on p. 17).

[Raffelt2002] G. G. Raffelt, **Physics with supernovae**, Nucl. Phys. Proc. Suppl. **110** (2002) 254, DOI: 10.1016/S0920-5632(02)01489-5 (cit. on p. 17).

[Chandrasekhar1932] S. Chandrasekhar, **The density of white dwarf stars**, The London, Edinburgh, and Dublin Philosophical Magazine and Journal of Science **11** (1931) 592, DOI: 10.1080/14786443109461710 (cit. on p. 17).

[Berezhko2008] E. G. Berezhko, **Cosmic ray acceleration by supernova shocks**, Adv. Space Res. **41** (2008) 429, DOI: 10.1016/j.asr.2007.04.034 (cit. on p. 17).

[Blasi2011] P. Blasi, **Cosmic Ray Acceleration in Supernova Remnants**, *Cosmic Rays for Particle and Astroparticle Physics*, 2011 493, DOI: 10.1142/9789814329033_0061 (cit. on p. 17).

[Bell1978] A. R. Bell, **The acceleration of cosmic rays in shock fronts – I**, Monthly Notices of the Royal Astronomical Society **182** (1978) 147, DOI: 10.1093/mnras/182.2.147 (cit. on p. 17).

[Blandford1987] R. Blandford and D. Eichler, **Particle acceleration at astrophysical shocks: A theory of cosmic ray origin**, Physics Reports **154** (1987) 1, DOI: 10.1016/0370-1573(87)90134-7 (cit. on p. 17).

[Uchiyama2007] Y. Uchiyama, F. Aharonian, T. Tanaka, T. Takahashi and Y. Maeda, **Extremely fast acceleration of cosmic rays in a supernova remnant**, Nature **449** (2007) 576, DOI: 10.1038/nature06210 (cit. on p. 17).

[CassamChenai2008] G. Cassam-Chenai, J. P. Hughes, E. M. Reynoso, C. Badenes and D. Moffett, **Morphological evidence for azimuthal variations of the cosmic ray ion acceleration at the blast wave of SN 1006**, Astrophys. J. **680** (2008) 1180, DOI: 10.1086/588015 (cit. on p. 17).

[Abdo2010] A. A. Abdo, M. Ackermann, M. Ajello et al., **Observation of Supernova Remnant IC 443 with the Fermi Large Area Telescope**, The Astrophysical Journal **712** (2010) 459, DOI: 10.1088/0004-637x/712/1/459 (cit. on p. 17).

[Penzias1965] A. A. Penzias and R. W. Wilson, **A Measurement of Excess Antenna Temperature at 4080 Mc/s.**, The Astrophysical Journal **142** (1965) 419, DOI: 10.1086/148307 (cit. on p. 18).

[Strong2007] A. W. Strong, I. V. Moskalenko and V. S. Ptuskin, **Cosmic-ray propagation and interactions in the Galaxy**, Ann. Rev. Nucl. Part. Sci. **57** (2007) 285, DOI: 10.1146/annurev.nucl.57.090506.123011 (cit. on pp. 18–19).

[Alfven1942] H. Alfvén, **Existence of Electromagnetic-Hydrodynamic Waves**, Nature **150** (1942) 405, DOI: 10.1038/150405a0 (cit. on p. 18).

[Moskalenko1997] I. V. Moskalenko and A. W. Strong, **Production and propagation of cosmic ray positrons and electrons**, The Astrophysical Journal **493** (1998) 694, DOI: 10.1086/305152 (cit. on p. 19).

[Moskalenko2002] I. V. Moskalenko, A. W. Strong, J. F. Ormes and M. S. Potgieter, **Secondary Antiprotons and Propagation of Cosmic Rays in the Galaxy and Heliosphere**, The Astrophysical Journal **565** (2002) 280, DOI: 10.1086/324402 (cit. on p. 19).

[Ptuskin2006] V. S. Ptuskin, I. V. Moskalenko, F. C. Jones, A. W. Strong and V. N. Zirakashvili, **Dissipation of Magnetohydrodynamic Waves on Energetic Particles: Impact on Interstellar Turbulence and Cosmic-Ray Transport**, The Astrophysical Journal **642** (2006) 902, DOI: 10.1086/501117 (cit. on p. 19).

[Owens2013] M. J. Owens and R. J. Forsyth, **The Heliospheric Magnetic Field**, Living Reviews in Solar Physics **10** (2013) 5, DOI: 10.12942/lrsp-2013-5 (cit. on p. 19).

[Babcock1961] H. W. Babcock, **The Topology of the Sun's Magnetic Field and the 22-year Cycle.**, The Astrophysical Journal **133** (1961) 572, DOI: 10.1086/147060 (cit. on p. 20).

[Gleeson1968] L. J. Gleeson and W. I. Axford, **Solar Modulation of Galactic Cosmic Rays**, The Astrophysical Journal **154** (1968) 1011, DOI: 10.1086/149822 (cit. on pp. 20, 148, 158, 164).

[Stoermer1956] **The polar aurora. By Carl Størmer. Oxford University Press, 1955. Pp. xvii, 403; 216 Figs., 27 Tables. 55s**, Quarterly Journal of the Royal Meteorological Society **82** (1956) 115, DOI: 10.1002/qj.49708235123 (cit. on pp. 21, 116).

[Smart2005] D. Smart and M. Shea, **A review of geomagnetic cutoff rigidities for Earth-orbiting spacecraft**, Advances in Space Research **36** (2005) 2012, DOI: 10.1016/j.asr.2004.09.015 (cit. on p. 21).

[Ogawa1950] S. Ogawa and Y. Nagahara, **On the East-West Effect of the Cosmic-Radiation in the Upper Atmosphere**, Progress of Theoretical Physics **5** (1950) 428, DOI: 10.1143/ptp/5.3.428 (cit. on p. 22).

[Panov2013] A. D. Panov, **Electrons and Positrons in Cosmic Rays**, J. Phys. Conf. Ser. **409** (2013) 012004, DOI: 10.1088/1742-6596/409/1/012004 (cit. on p. 23).

[Kobayashi2004] T. Kobayashi, Y. Komori, K. Yoshida and J. Nishimura, **The Most Likely Sources of High-Energy Cosmic-Ray Electrons in Supernova Remnants**, The Astrophysical Journal **601** (2004) 340, DOI: 10.1086/380431 (cit. on p. 23).

[KatzStone2000] D. M. Katz-Stone, N. E. Kassim, T. J. W. Lazio and R. O'Donnell, **Spatial Variations of the Synchrotron Spectrum within Tycho's Supernova Remnant (3C 10): A Spectral Tomography Analysis of Radio Observations at 20 and 90 Centimeter Wavelengths**, The Astrophysical Journal **529** (2000) 453, DOI: 10.1086/308251 (cit. on p. 23).

[Aharonian2006] F. Aharonian et al., **Discovery of very-high-energy gamma-rays from the galactic centre ridge**, Nature **439** (2006) 695, DOI: 10.1038/nature04467 (cit. on p. 23).

[Ackermann2013] M. Ackermann et al., **Detection of the Characteristic Pion-Decay Signature in Supernova Remnants**, Science **339** (2013) 807, DOI: 10.1126/science.1231160 (cit. on p. 23).

[Aguilar2019a] M. Aguilar, L. Ali Cavasonza, B. Alpat et al., **Towards Understanding the Origin of Cosmic-Ray Electrons**, Phys. Rev. Lett. **122** (10 2019) 101101, DOI: 10.1103/PhysRevLett.122.101101 (cit. on pp. 23, 68, 157–158, 207–209).

[Shen1968] C. S. Shen and G. B. Berkey, **Antiprotons and Positrons in Cosmic Rays**, Phys. Rev. **171** (5 1968) 1344, DOI: 10.1103/PhysRev.171.1344 (cit. on p. 23).

[Adriani2009] O. Adriani et al., **An anomalous positron abundance in cosmic rays with energies 1.5-100 GeV**, Nature **458** (2009) 607, DOI: 10.1038/nature07942 (cit. on p. 24).

[Aguilar2013] M. Aguilar, G. Alberti, B. Alpat et al., **First Result from the Alpha Magnetic Spectrometer on the International Space Station: Precision Measurement of the Positron Fraction in Primary Cosmic Rays of 0.5–350 GeV**, Phys. Rev. Lett. **110** (14 2013) 141102, DOI: 10.1103/PhysRevLett.110.141102 (cit. on pp. 24, 165).

[Hewish1968] A. Hewish, S. J. Bell, J. D. H. Pilkington, P. F. Scott and R. A. Collins, **Observation of a Rapidly Pulsating Radio Source**, Nature **217** (5130 1968) 709, DOI: 10.1038/217709a0 (cit. on p. 24).

[Hooper2009] D. Hooper, P. Blasi and P. D. Serpico, **Pulsars as the sources of high energy cosmic ray positrons**, Journal of Cosmology and Astroparticle Physics **2009** (2009) 025, DOI: 10.1088/1475-7516/2009/01/025 (cit. on pp. 24, 165).

[Verbiest2012] J. P. W. Verbiest, J. M. Weisberg, A. A. Chael, K. J. Lee and D. R. Lorimer, **On Pulsar Distance Measurements and Their Uncertainties**, The Astrophysical Journal **755** (2012) 39, DOI: 10.1088/0004-637X/755/1/39 (cit. on p. 24).

[Rubin1970] V. C. Rubin and J. Ford W. Kent, **Rotation of the Andromeda Nebula from a Spectroscopic Survey of Emission Regions**, The Astrophysical Journal **159** (1970) 379, DOI: 10.1086/150317 (cit. on p. 24).

[Einstein1936] A. Einstein, **Lens-Like Action of a Star by the Deviation of Light in the Gravitational Field**, Science **84** (1936) 506, DOI: 10.1126/science.84.2188.506 (cit. on p. 24).

[Sumner2011] T. J. Sumner, **Direct dark matter searches - recent highlights**, Journal of Physics: Conference Series **312** (2011) 072003, DOI: 10.1088/1742-6596/312/7/072003 (cit. on p. 25).

[Gaskins2016] J. M. Gaskins, **A review of indirect searches for particle dark matter**, Contemp. Phys. **57** (2016) 496, DOI: 10.1080/00107514.2016.1175160 (cit. on p. 25).

[Boyarsky2019] A. Boyarsky, M. Drewes, T. Lasserre, S. Mertens and O. Ruchayskiy, **Sterile neutrino Dark Matter**, Progress in Particle and Nuclear Physics **104** (2019) 1, DOI: 10.1016/j.ppnp.2018.07.004 (cit. on p. 25).

[Steffen2006] F. D. Steffen, **Gravitino dark matter and cosmological constraints**, JCAP **0609** (2006) 001, DOI: 10.1088/1475-7516/2006/09/001 (cit. on p. 25).

[Duffy2009] L. D. Duffy and K. van Bibber, **Axions as Dark Matter Particles**, New J. Phys. **11** (2009) 105008, DOI: 10.1088/1367-2630/11/10/105008 (cit. on p. 25).

[Cheng2002] H.-C. Cheng, J. L. Feng and K. T. Matchev, **Kaluza-Klein dark matter**, Phys. Rev. Lett. **89** (2002) 211301, DOI: 10.1103/PhysRevLett.89.211301 (cit. on p. 25).

[Roszkowski2017] L. Roszkowski, E. M. Sessolo and S. Trojanowski, **WIMP dark matter candidates and searches—current status and future prospects**, Rept. Prog. Phys. **81** (2018) 066201, DOI: 10.1088/1361-6633/aab913 (cit. on p. 25).

[Bergstrom2013] L. Bergström, T. Bringmann, I. Cholis, D. Hooper and C. Weniger, **New Limits on Dark Matter Annihilation from Alpha Magnetic Spectrometer Cosmic Ray Positron Data**, Phys. Rev. Lett. **111** (17 2013) 171101, DOI: 10.1103/PhysRevLett.111.171101 (cit. on p. 25).

[Kounine2011b] A. Kounine, **The Alpha Magnetic Spectrometer on the International Space Station**, International Journal of Modern Physics E **21** (2012) 1230005, DOI: 10.1142/S0218301312300056 (cit. on p. 27).

[Ting2013] S. Ting, **The Alpha Magnetic Spectrometer on the International Space Station**, Nuclear Physics B - Proceedings Supplements **243-244** (2013) 12, DOI: 10.1016/j.nuclphysbps.2013.09.028 (cit. on p. 27).

[AmsWebsite] A. collaboration, **The Alpha Magnetic Spectrometer Experiment**, 2019, URL: https://ams02.space (visited on 15/08/2019) (cit. on pp. 27–34, 36–39).

[Luebelsmeyer2011] K. Lübelsmeyer, A. Schultz von Dratzig, M. Wlochal et al., **Upgrade of the Alpha Magnetic Spectrometer (AMS-02) for long term operation on the International Space Station (ISS)**, Nuclear Instruments and Methods in Physics Research Section A: Accelerators, Spectrometers, Detectors and Associated Equipment **654** (2011) 639, DOI: 10.1016/j.nima.2011.06.051 (cit. on p. 28).

[Hass2004] D. Haas, **The Silicon Tracker of AMS02**, Nuclear Instruments and Methods in Physics Research Section A: Accelerators, Spectrometers, Detectors and Associated Equipment **530** (2004) 173, DOI: 10.1016/j.nima.2004.05.068 (cit. on pp. 29, 45).

[Haino2013] S. Haino, **Performance of the AMS-02 silicon tracker in the ISS mission**, Nuclear Instruments and Methods in Physics Research Section A: Accelerators, Spectrometers, Detectors and Associated Equipment **699** (2013) 221, DOI: 10.1016/j.nima.2012.05.060 (cit. on p. 29).

[Bindi2014] V. Bindi, G. Chen, H. Chen et al., **Calibration and performance of the AMS-02 time of flight detector in space**, Nuclear Instruments and Methods in Physics Research Section A: Accelerators, Spectrometers, Detectors and Associated Equipment **743** (2014) 22, DOI: 10.1016/j.nima.2014.01.002 (cit. on pp. 32, 45).

[Kirn2013] T. Kirn, **The AMS-02 TRD on the international space station**, Nuclear Instruments and Methods in Physics Research Section A: Accelerators, Spectrometers, Detectors and Associated Equipment **706** (2013), TRDs for the Third Millenium 43, DOI: 10.1016/j.nima.2012.05.010 (cit. on pp. 33, 35).

[Heil2013] M. Heil et al., **Operations and Alignment of the AMS-02 Transition Radiation Detector**, *Proceedings, 33rd International Cosmic Ray Conference (ICRC2013): Rio de Janeiro, Brazil, July 2-9, 2013*, 2013 1232 (cit. on p. 33).

[Ginzburg1945] V. L. Ginzburg and I. M. Frank, **Radiation of a uniformly moving electron due to its transition from one medium into another**, J. Phys.(USSR) **9** (1945) 353 (cit. on p. 33).

[Raiha2017] T. Räihä, A. Bachlechner, B. Beischer et al., **Monte Carlo Simulations of the Transition Radiation Detector of the AMS-02 Experiment**, Nucl. Instrum. Meth. **A868** (2017) 10, DOI: 10.1016/j.nima.2017.06.042 (cit. on p. 35).

[Kounine2017b] A. Kounine, **AMS Results on the Properties of the Fluxes of Elementary Particles and Nuclei in Primary Cosmic Rays**, *Proc. ICRC 2017*, vol. PoS(ICRC2017)1093, 2017, DOI: 10.22323/1.301.1093 (cit. on p. 35).

[RosierLees2012] S. Rosier-Lees, **Performance of the AMS02 Electromagnetic Calorimeter in space**, Journal of Physics: Conference Series **404** (2012) 012034, DOI: 10.1088/1742-6596/404/1/012034 (cit. on p. 36).

[Kounine2017a] A. Kounine, Z. Weng, W. Xu and C. Zhang, **Precision measurement of 0.5 GeV–3 TeV electrons and positrons using the AMS Electromagnetic Calorimeter**, Nuclear Instruments and Methods in Physics Research Section A: Accelerators, Spectrometers, Detectors and Associated Equipment **869** (2017), DOI: 10.1016/j.nima.2017.07.013 (cit. on pp. 36, 46, 175, 207).

[Gallucci2015] G. G. and, **Performance of the AMS-02 Electromagnetic Calorimeter in Space**, Journal of Physics: Conference Series **587** (2015) 012028, DOI: 10.1088/1742-6596/587/1/012028 (cit. on pp. 37, 46).

[Doetinchem2009] P. von Doetinchem, T. Kirn, K. Luebelsmeyer and S. Schael, **The Anticoincidence Counter System of AMS-02**, arXiv e-prints (2009), arXiv: 0906.1068 [astro-ph.IM] (cit. on p. 37).

[Giovacchini2014] F. Giovacchini, **Performance in space of the AMS-02 RICH detector**, Nuclear Instruments and Methods in Physics Research Section A: Accelerators, Spectrometers, Detectors and Associated Equipment **766** (2014) 57, DOI: 10.1016/j.nima.2014.04.036 (cit. on p. 39).

[Lin2005] C. Lin, **Trigger Logic Design Specification**, AMS internal notes, 2005 (cit. on p. 40).

[Kounine2009] A. Kounine, **Data Processing in JLV1**, AMS internal notes, 2009 (cit. on p. 40).

[Kounine2011a] A. Kounine, **LV1 Trigger Studies**, AMS reports, 2011 (cit. on pp. 40–41).

[Brun1997] R. Brun and F. Rademakers, **ROOT — An object oriented data analysis framework**, Nuclear Instruments and Methods in Physics Research Section A: Accelerators, Spectrometers, Detectors and Associated Equipment **389** (1997), New Computing Techniques in Physics Research V 81, DOI: 10.1016/S0168-9002(97)00048-X (cit. on pp. 44, 194).

[Aguilar2014a] M. Aguilar, D. Aisa, A. Alvino et al., **Electron and Positron Fluxes in Primary Cosmic Rays Measured with the Alpha Magnetic Spectrometer on the International Space Station**, Phys. Rev. Lett. **113** (12 2014) 121102, DOI: 10.1103/PhysRevLett.113.121102 (cit. on pp. 44, 68, 207).

[Aguilar2018] M. Aguilar, L. A. Cavasonza, G. Ambrosi et al., **Observation of Complex Time Structures in the Cosmic-Ray Electron and Positron Fluxes with the Alpha Magnetic Spectrometer on the International Space Station**, Phys. Rev. Lett. **121** (5 2018) 051102, DOI: 10.1103/PhysRevLett.121.051102 (cit. on pp. 44, 167–169, 171, 173, 175, 216).

[BazoAlba2013] J. L. B. A. and, **In-flight performance of the AMS-02 silicon tracker**, Journal of Physics: Conference Series **409** (2013), DOI: 10.1088/1742-6596/409/1/012032 (cit. on pp. 45, 137).

[Gast2015] H. Gast, **Trd-P: determination of parameterized PDFs for AMS-02 TRD**, Unpublished note, 2015, URL: https://confluence.physik.rwth-aachen.de/download/attachments/1215477/trd_pdfs_confluence.pdf (cit. on pp. 46, 48).

[Neyman1933] J. Neyman, E. S. Pearson and K. Pearson, **IX. On the problem of the most efficient tests of statistical hypotheses**, Philosophical Transactions of the Royal Society of London. Series A, Containing Papers of a Mathematical or Physical Character **231** (1933) 289, DOI: 10.1098/rsta.1933.0009 (cit. on p. 47).

[TMVA2007] A. Hoecker, P. Speckmayer, J. Stelzer et al., **TMVA: Toolkit for Multivariate Data Analysis**, PoS **ACAT** (2007) 040 (cit. on pp. 49, 54).

[Roe2005] B. P. Roe, H.-J. Yang, J. Zhu et al., **Boosted decision trees as an alternative to artificial neural networks for particle identification**, Nuclear Instruments and Methods in Physics Research Section A: Accelerators, Spectrometers, Detectors and Associated Equipment **543** (2005) 577, DOI: 10.1016/j.nima.2004.12.018 (cit. on p. 54).

[Aguilar2019b] M. Aguilar, L. Ali Cavasonza, G. Ambrosi et al., **Towards Understanding the Origin of Cosmic-Ray Positrons**, Phys. Rev. Lett. **122** (4 2019) 041102, DOI: 10.1103/PhysRevLett.122.041102 (cit. on pp. 68, 161–163, 165, 207–212).

[Birkhoff1960] G. Birkhoff and H. L. Garabedian, **Smooth Surface Interpolation**, Journal of Mathematics and Physics **39** (1960) 258, DOI: 10.1002/sapm1960391258 (cit. on p. 71).

[Rosenblatt1956] M. Rosenblatt, **Remarks on Some Nonparametric Estimates of a Density Function**, Ann. Math. Statist. **27** (1956) 832, DOI: 10.1214/aoms/1177728190 (cit. on p. 76).

[Parzen1962] E. Parzen, **On Estimation of a Probability Density Function and Mode**, Ann. Math. Statist. **33** (1962) 1065, DOI: 10.1214/aoms/1177704472 (cit. on p. 76).

[Cowan1998] G. Cowan, **Statistical Data Analysis**, Oxford science publications, Clarendon Press, 1998 (cit. on p. 80).

[James1975] F. James and M. Roos, **Minuit: A System for Function Minimization and Analysis of the Parameter Errors and Correlations**, Comput. Phys. Commun. **10** (1975) 343, DOI: 10.1016/0010-4655(75)90039-9 (cit. on p. 80).

[Efron1979] B. Efron, **Bootstrap Methods: Another Look at the Jackknife**, Ann. Statist. **7** (1979) 1, DOI: 10.1214/aos/1176344552 (cit. on p. 93).

[Kurnosova1962] L. Kurnosova, T. Kolobyanina, V. Logachev et al., **Discovery of radiation anomalies above the south atlantic at heights of 310-340 km**, Planetary and Space Sci. **Vol: 9** (1962), DOI: 10.1016/0032-0633(62)90057-0 (cit. on pp. 96–97, 178).

[Thebault2015] E. Thébault, C. C. Finlay, C. D. Beggan et al., **International Geomagnetic Reference Field: the 12th generation**, Earth, Planets and Space **67** (2015) 79, DOI: 10.1186/s40623-015-0228-9 (cit. on p. 98).

[Fiandrini2015] E. Fiandrini, B. Bertucci, M. Boschini et al., **Time dependent Geomagnetic Cutoff estimation along the ISS orbit**, *Proceedings of the 34th International Cosmic Ray Conference (ICRC2015), July 30 - August 6, 2015 (The Hague, The Netherlands)*, 2015 (cit. on p. 98).

[Agostinelli2003] S. Agostinelli, J. Allison, K. Amako et al., **Geant4—a simulation toolkit**, Nuclear Instruments and Methods in Physics Research Section A: Accelerators, Spectrometers, Detectors and Associated Equipment **506** (2003) 250, DOI: 10.1016/S0168-9002(03)01368-8 (cit. on p. 99).

[Allison2006] J. Allison, K. Amako, J. Apostolakis et al., **Geant4 developments and applications**, IEEE Transactions on Nuclear Science **53** (2006) 270, DOI: 10.1109/TNS.2006.869826 (cit. on p. 99).

[Allison2016] J. Allison, K. Amako, J. Apostolakis et al., **Recent developments in Geant4**, Nuclear Instruments and Methods in Physics Research Section A: Accelerators, Spectrometers, Detectors and Associated Equipment **835** (2016) 186, DOI: 10.1016/j.nima.2016.06.125 (cit. on p. 99).

[Sullivan1971] J. Sullivan, **Geometric factor and directional response of single and multi-element particle telescopes**, Nuclear Instruments and Methods **95** (1971) 5, DOI: 10.1016/0029-554X(71)90033-4 (cit. on p. 99).

[Rohrlich1954] F. Rohrlich and B. C. Carlson, **Positron-Electron Differences in Energy Loss and Multiple Scattering**, Phys. Rev. **93** (1 1954) 38, DOI: 10.1103/PhysRev.93.38 (cit. on p. 106).

[Golub1996] G. Golub and C. Van Loan, **Matrix Computations**, Johns Hopkins Studies in the Mathematical Sciences, Johns Hopkins University Press, 1996 (cit. on p. 111).

[ClopperPearson1934] C. J. CLOPPER and E. S. PEARSON, **THE USE OF CONFIDENCE OR FIDUCIAL LIMITS ILLUSTRATED IN THE CASE OF THE BINOMIAL**, Biometrika **26** (1934) 404, DOI: 10.1093/biomet/26.4.404 (cit. on p. 115).

[Landau1944] L. Landau, **On the energy loss of fast particles by ionization**, J. Phys.(USSR) **8** (1944) 201 (cit. on p. 118).

[Skwarnicki1986] T. Skwarnicki, **A study of the radiative CASCADE transitions between the Upsilon-Prime and Upsilon resonances** (1986) 178, URL: http://www-library.desy.de/cgi-bin/showprep.pl?DESY-F31-86-02 (cit. on p. 118).

[Bartels1934] J. Bartels, **Twenty-seven day recurrences in terrestrial-magnetic and solar activity, 1923–1933**, Terrestrial Magnetism and Atmospheric Electricity **39** (1934) 201, DOI: 10.1029/TE039i003p00201 (cit. on p. 133).

[Kirn2019] T. Kirn, M. Graziani, N. Nikonov, P. Soldin and H. Biss, **TRD Detector Status**, Aachen internal report, 2019 (cit. on p. 138).

[Berdugo2017] J. Berdugo, V. Choutko, C. Delgado and Q. Yan, **Determination of the rigidity scale of the Alpha Magnetic Spectrometer**, Nuclear Instruments and Methods in Physics Research Section A: Accelerators, Spectrometers, Detectors and Associated Equipment **869** (2017) 10, DOI: 10.1016/j.nima.2017.07.012 (cit. on p. 144).

[Lafferty1995] G. Lafferty and T. Wyatt, **Where to stick your data points: The treatment of measurements within wide bins**, Nuclear Instruments and Methods in Physics Research Section A: Accelerators, Spectrometers, Detectors and Associated Equipment **355** (1995) 541, DOI: 10.1016/0168-9002(94)01112-5 (cit. on p. 155).

[Boezio2000] M. Boezio, P. Carlson, T. Francke et al., **The Cosmic-Ray Electron and Positron Spectra Measured at 1 AU during Solar Minimum Activity**, The Astrophysical Journal **532** (2000) 653, DOI: 10.1086/308545 (cit. on pp. 156, 161).

[DuVernois2001] M. A. DuVernois, S. W. Barwick, J. J. Beatty et al., **Cosmic-Ray Electrons and Positrons from 1 to 100 GeV: Measurements with HEAT and Their Interpretation**, The Astrophysical Journal **559** (2001) 296, DOI: 10.1086/322324 (cit. on pp. 156, 161).

[Grimani2002] Grimani, C., Stephens, S. A., Cafagna, F. S. et al., **Measurements of the absolute energy spectra of cosmic-ray positrons and electrons above 7 GeV**, A&A **392** (2002) 287, DOI: 10.1051/0004-6361:20020845 (cit. on pp. 156, 161).

[Adriani2011] O. Adriani, G. C. Barbarino, G. A. Bazilevskaya et al., **Cosmic-Ray Electron Flux Measured by the PAMELA Experiment between 1 and 625 GeV**, Phys. Rev. Lett. **106** (20 2011) 201101, DOI: 10.1103/PhysRevLett.106.201101 (cit. on p. 156).

[Ackermann2012] M. Ackermann, M. Ajello, A. Allafort et al., **Measurement of Separate Cosmic-Ray Electron and Positron Spectra with the Fermi Large Area Telescope**, Phys. Rev. Lett. **108** (1 2012) 011103, DOI: 10.1103/PhysRevLett.108.011103 (cit. on pp. 156, 161, 211).

[Strong2011] Strong, A. W., Orlando, E. and Jaffe, T. R., **The interstellar cosmic-ray electron spectrum from synchrotron radiation and direct measurements**, A&A **534** (2011) A54, DOI: 10.1051/0004-6361/201116828 (cit. on pp. 158, 169).

[Adriani2013] O. Adriani, G. C. Barbarino, G. A. Bazilevskaya et al., **Cosmic-Ray Positron Energy Spectrum Measured by PAMELA**, Phys. Rev. Lett. **111** (8 2013) 081102, DOI: 10.1103/PhysRevLett.111.081102 (cit. on pp. 161, 211).

[Cavasonza2017] L. A. Cavasonza, H. Gast, M. Krämer, M. Pellen and S. Schael, **Constraints on Leptophilic Dark Matter from the AMS-02 Experiment**, The Astrophysical Journal **839** (2017) 36, DOI: 10.3847/1538-4357/aa624d (cit. on pp. 168–169, 171, 215–216).

[Potgieter2015] M. S. Potgieter, E. E. Vos, R. Munini, M. Boezio and V. D. Felice, **MODULATION OF GALACTIC ELECTRONS IN THE HELIOSPHERE DURING THE UNUSUAL SOLAR MINIMUM OF 2006–2009: A MODELING APPROACH**, The Astrophysical Journal **810** (2015) 141, DOI: 10.1088/0004-637x/810/2/141 (cit. on pp. 169, 215).

[Cheminet2013] A. Cheminet, G. Hubert, V. Lacoste, D. Maurin and L. Derome, **Cosmic ray solar modulation and Forbush decrease analyses based on atmospheric neutron spectrometry at mountain altitude and GEANT4 simulations of extensive air showers**, Journal of Geophysical Research: Space Physics **118** (2013) 7488, DOI: 10.1002/2013JA019166 (cit. on p. 169).

[Potgieter2001] M. Potgieter, R. Burger and S. Ferreira, **Modulation of Cosmic Rays in the Heliosphere From Solar Minimum to Maximum: a Theoretical Perspective**, Space Science Reviews **97** (2001) 295, DOI: 10.1023/A:1011837303094 (cit. on p. 170).

[Heber2009] B. Heber, A. Kopp, J. Gieseler et al., **Modulation of Galactic Cosmic Ray Protons and Electrons During an Unusual Solar Minimum**, The Astrophysical Journal **699** (2009) 1956, DOI: 10.1088/0004-637X/699/2/1956 (cit. on pp. 170, 174).

[Corti2016] C. Corti, V. Bindi, C. Consolandi and K. Whitman, **Solar modulation of the local interstellar spectrum with Voyager 1, AMS-02, PAMELA, and BESS**, The Astrophysical Journal **829** (2016) 8, DOI: 10.3847/0004-637x/829/1/8 (cit. on p. 171).

[Potgieter2017] M. Potgieter, **The global modulation of cosmic rays during a quiet heliosphere: A modeling perspective**, Advances in Space Research **60** (2017), Solar Energetic Particles, Solar Modulation and Space Radiation: New Opportunities in the AMS-02 Era 848, DOI: 10.1016/j.asr.2016.09.003 (cit. on p. 171).

[Tomassetti2017] N. Tomassetti, M. Orcinha, F. Barão and B. Bertucci, **Evidence for a Time Lag in Solar Modulation of Galactic Cosmic Rays**, The Astrophysical Journal **849** (2017) L32, DOI: 10.3847/2041-8213/aa9373 (cit. on p. 171).

[Sun2015] X. Sun, J. T. Hoeksema, Y. Liu and J. Zhao, **ON POLAR MAGNETIC FIELD REVERSAL AND SURFACE FLUX TRANSPORT DURING SOLAR CYCLE 24**, The Astrophysical Journal **798** (2015) 114, DOI: 10.1088/0004-637x/798/2/114 (cit. on pp. 172–174).

[Heber2002] B. Heber, G. Wibberenz, M. S. Potgieter et al., **Ulysses Cosmic Ray and Solar Particle Investigation/Kiel Electron Telescope observations: Charge sign dependence and spatial gradients during the 1990–2000 A > 0 solar magnetic cycle**, Journal of Geophysical Research: Space Physics **107** (2002) SSH 2-1-SSH 2, DOI: 10.1029/2001JA000329 (cit. on p. 174).

[Ferreira2004] S. E. S. Ferreira and M. S. Potgieter, **Long-Term Cosmic-Ray Modulation in the Heliosphere**, The Astrophysical Journal **603** (2004) 744, DOI: 10.1086/381649 (cit. on p. 174).

[Heber2013] B. Heber, **Cosmic Rays Through the Solar Hale Cycle**, Space Science Reviews **176** (2013) 265, DOI: 10.1007/s11214-011-9784-x (cit. on p. 174).

[Schael2019] S. Schael et al., **AMS-100: The Next Generation Magnetic Spectrometer in Space – An International Science Platform for Physics and Astrophysics at Lagrange Point 2** (2019), arXiv: 1907.04168 [astro-ph.IM] (cit. on p. 176).

[Hart1984] J. Hart and D. Saxon, **Track and vertex fitting in an inhomogeneous magnetic field**, Nuclear Instruments and Methods in Physics Research **220** (1984) 309, DOI: 10.1016/0167-5087(84)90291-6 (cit. on p. 183).

[Choutko2003] V. Choutko, **Selected AMS Reconstruction Software Issues**, AMS internal notes, 2003, URL: http://ams.cern.ch/AMS/Analysis/hpl3itp1/ams_rec_sel.ps (cit. on p. 183).

[Chikanian1996] A. Chikanian, B. Kumar, N. Smirnov and E. O'Brien, **A momentum reconstruction algorithm for the PHENIX spectrometer at Brookhaven**, Nuclear Instruments and Methods in Physics Research **371** (1996) 480, DOI: 10.1016/0168-9002(95)01000-9 (cit. on p. 183).

[DAgostini1995] G. D'Agostini, **A multidimensional unfolding method based on Bayes' theorem**, Nucl. Instrum. Meth. A **362** (1995) 487, DOI: 10.1016/0168-9002(95)00274-X (cit. on p. 199).

[Adye2011] T. Adye, **Unfolding algorithms and tests using RooUnfold** (2011) 313, URL: http://cds.cern.ch/record/1349242 (cit. on p. 199).

[Bayes1763] T. Bayes, **An essay towards solving a problem in the doctrine of chances**, Phil. Trans. of the Royal Soc. of London **53** (1763) 370 (cit. on p. 200).

[Kokoska2000] S. Kokoska and D. Zwillinger, **CRC standard probability and statistics tables and formulae**, Taylor and Francis, 2000 31 (cit. on p. 200).

[Golden1996] R. L. Golden, S. J. Stochaj, S. A. Stephens et al., **Measurement of the Positron to Electron Ratio in the Cosmic Rays above 5 GeV**, The Astrophysical Journal **457** (1996), DOI: 10.1086/309896 (cit. on p. 211).

Acronyms

AMS . . . . . Alpha Magnetic Spectrometer

BDT . . . . . Boosted Decision Tree

CMB . . . . . Cosmic Microwave Background

CME . . . . . Coronal Mass Ejections

DSA . . . . . Diffusive Shock Acceleration

HCS . . . . . Heliospheric Current Sheet

HMF . . . . . Heliospheric Magnetic Field

HRDL . . . . . High Rate Data Link

ISM . . . . . Interstellar Medium

ISS . . . . . International Space Station

KDE . . . . . Kernel Density Estimation

LHC . . . . . Large Hadron Collider

MDR . . . . . Maximum Detectable Rigidity

MIP . . . . . Minimum Ionizing Particle

MPV . . . . . Most Probable Value

MSFC . . . . . Marshall Space Flight Center

POCC . . . . . Payload Operation Control Center

ROC . . . . . Receiver Operating Characteristic

SAA . . . . . South Atlantic Anomaly

SN . . . . . Supernova

SNRs . . . . . Supernova Remnants

TAS . . . . . Tracker Alignment System

TDRS . . . . . Tracking and Data Relay Satellite

TOF . . . . . Time Of Flight

TOI . . . . . Top-Of-Instrument

TRD . . . . . Transition Radiation Detector

WIMPs . . . . . Weakly Interacting Massive Particles

Acknowledgements

I am very grateful to many people who made the creation of this dissertation possible.

First of all I would like to thanks my advisor Prof. Dr. Schael, who offered me the PhD position after completing my Diploma in his institute. During the past 13 years I learned a lot about physics and data analysis, the interpretation of the results and many soft skills from Prof. Schael. I am sincerely thankful for his continuous support and encouragements in my decisions throughout the thesis. The enthusiasm for astroparticle physics is truly inspiring and made working in his institute a pleasure.

Furthermore, I thankfully acknowledge Prof. Dr. Christopher Wiebusch who kindly agreed to be my second supervisor.

My special thanks goes to my colleagues and friends from the Aachen group with whom I had many fruitful discussions throughout my time as PhD student: Dr. Henning Gast, Dr. Thorsten Siedenburg, Andreas Bachlechner, Bastian Beischer, Fabian Machate and Dr. Leila Ali Cavasonza. Many things became clear after discussions with all of you.

In the first year Dr. Thorsten Siedenburg answered numerous of questions regarding the detector, the reconstruction algorithms and physics in general. Each week he took time for me and patiently explained all things I wanted to know. The *ACQt* data format was inspired by his ideas - thanks for all the time you devoted to me.

Many colleagues and friends shared an office with me over the years: Sarah Beranek, Bastian Beischer, Tobias Verlage, Nikolay Nikonov, Leila Ali Cavasonza, Sichen Li and Robin Sonnabend. Many thanks to all of you for making our office a nice play to stay, discuss and drink coffee. Special thanks go to Bastian and Henning: it was a pleasure to work with you, and design the *ACsoft* software package, the *ACQt* file format and all the surrounding software infrastructure. Discussions with both of you always led to the best possible, most flexible, future-proof solution. Henning patiently took time to read through my thesis and gave excellent comments, which helped me a lot. Many thanks for your time.

I would like to express my deep gratitude to the AMS-02 collaboration, who supported my analysis and encouraged me to go further. Special thanks go to Prof. Dr. Samuel Ting, Dr. Andrei Kounine, Dr. Vitaly Choutko, Dr. Zhili Weng and Dr. Marco Incagli. Many discussions with Andrei and Vitaly helped in understanding the detector, the inner workings of the reconstruction software and the utilized algorithms. The analysis described in this dissertation would not be finished today, without many productive discussion and debates during various analysis meeting, the ideas and suggestions from the collaboration.

Special thanks go to Dr. Marco Incagli who patiently walked me through the whole ECAL calibration sequence, which I carefully rechecked during 2017 (not described in this thesis). I gained many insights during this time. Long and fruitful discussions with Marco at CERN and via numerous mails

helped a lot. Marco always took the time to provide all necessary information necessary to complete the ECAL calibration, thank you very much for your time and help.

The acknowledgements would be incomplete without a big thank you for my parents. During the past three decades you continuously supported me and my decisions and helped me to find my way in life. I am thankful that you bought me a computer when I was 12 years old. This changed my life and the focus for the following decades. It also paved the way for studying physics: to understand the inner workings of such a machine, on the lowest level.

Most importantly, I thank my wife Stefanie, who gave birth to our wonderful sons - Hanno & Bene. There are no words that can describe what I feel for you: without your continuous support this thesis would not have been possible. You always supported me throughout this entire process and made countless sacrifices to help me get to this point. I am thankful to have a women like you by my side. Thanks for sharing your life with me since almost 10 years!